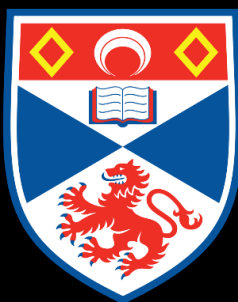




Magnetohydrodynamic waves in the solar corona

A mathematical investigation of the role of
resonant absorption and phase mixing in coronal
heating

Alexander Philip Kofi Prokopyszyn



June 2021

Abstract

Background: The Sun is a massive and highly dynamic ball of plasma, and oscillations in kinetic and magnetic energy are commonplace throughout its atmosphere. Since the plasma conducts electricity, we model the fluid using magnetohydrodynamics (MHD) instead of hydrodynamics which is used for non-ionised fluids. We study two MHD wave phenomena, namely, phase mixing and resonant absorption. These are both phenomena which occur exclusively in MHD fluids and do not occur in hydrodynamic fluids. We study their implications for the coronal heating problem and coronal seismology. The solar surface is significantly denser than the atmosphere and we model it as solid wall. In other words, we impose line-tied boundary conditions at the solar surface where the velocity is set equal to zero.

Aims: 1) The first research chapter (Chapter 2), introduces some of the key properties of footpoint driven Alfvén waves (a type of MHD wave) which are relevant for the rest of this thesis. 2) Chapter 3 calculates an upper bound for the heat that can be produced by linear phase-mixed Alfvén waves at observed frequencies and amplitudes to assess its viability as a coronal heating mechanism. 3) Chapter 4 tests if line-tied boundary conditions still apply in a resonant absorption experiment where the transverse length-scales can be very short.

Methods: We take an analytic and theoretical approach to solving each of these problems and then check the results numerically.

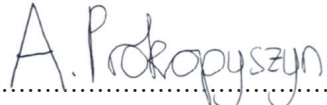
Results: 1) We show that the growth of energy in closed loops for a sinusoidal footpoint driver is highly dependent on the driver frequency. If a resonance is excited, then the energy grows quadratically with time, and for a broadband driver, the energy grows linearly on average. If the loop is partially-closed (i.e. only a fraction of the wave amplitude reflects at the boundary), the energy will converge towards a steady-state in which the energy of the loop remains constant with time. 2) We calculate an upper bound for the heat that can be produced by phase-mixed Alfvén waves and find that it is on average too small to play a significant role in coronal heating. 3) We show that if the length-scales perpendicular or parallel to the boundary is sufficiently short, then imposing line-tied boundary conditions may no longer be valid. However, researchers may wish to continue to use them in their models for their simplicity and ability to significantly reduce computation time if they understand and are aware of their limitations.

Candidate's declaration

I, Alexander Philip Kofi Prokopszyn, do hereby certify that this thesis, submitted for the degree of PhD, which is approximately 30,000 words in length, has been written by me, and that it is the record of work carried out by me, or principally by myself in collaboration with others as acknowledged, and that it has not been submitted in any previous application for any degree. I confirm that any appendices included in my thesis contain only material permitted by the 'Assessment of Postgraduate Research Students' policy.

I was admitted as a research student at the University of St Andrews in September 2017.

I received funding from an organisation or institution and have acknowledged the funder(s) in the full text of my thesis.

Date: 08/03/2021 Signature of candidate: 

Supervisor's declaration

I hereby certify that the candidate has fulfilled the conditions of the Resolution and Regulations appropriate for the degree of PhD in the University of St Andrews and that the candidate is qualified to submit this thesis in application for that degree. I confirm that any appendices included in the thesis contain only material permitted by the 'Assessment of Postgraduate Research Students' policy.

Date: 08/03/2021 Signature of supervisor: 

Permission for publication

In submitting this thesis to the University of St Andrews we understand that we are giving permission for it to be made available for use in accordance with the regulations of the University Library for the time being in force, subject to any copyright vested in the work not being affected thereby. We also understand, unless exempt by an award of an embargo as requested below, that the title and the abstract will be published, and that a copy of the work may be made and supplied to any bona fide library or research worker, that this thesis will be electronically accessible for personal or research use and that the library has the right to migrate this thesis into new electronic forms as required to ensure continued access to the thesis.

I, Alexander Philip Kofi Prokopszyn, confirm that my thesis does not contain any third-party material that requires copyright clearance.

The following is an agreed request by candidate and supervisor regarding the publication of this thesis:

Printed copy

No embargo on print copy.

Electric copy

No embargo on electronic copy.

Date: 08/03/2021..... Signature of candidate: A. Prokopszyn.....

Date: 8/03/2021..... Signature of supervisor: Alan Hood.....

Underpinning research data or digital outputs

I, Alexander Philip Kofi Prokopszyn, hereby certify that no requirements to deposit original research data or digital outputs apply to this thesis and that, where appropriate, secondary data used have been referenced in the full text of my thesis.

Date: 08/03/2021 Signature of candidate: A. Prokopszyn

Financial support

The research leading to the results presented within this thesis has received funding from the Science and Technology Facilities Council (U.K.) through the consolidated grant ST/N000609/1.

Publications

This thesis contains work which has been adapted from the following publications:

1. Prokopyszyn, A. P. K., A. W. Hood, and Ineke De Moortel. “Phase mixing of nonlinear Alfvén waves.” *Astronomy & Astrophysics* 624 (2019): A90.
2. Prokopyszyn, A. P. K., and A. W. Hood. “Investigating the damping rate of phase-mixed Alfvén waves.” *Astronomy & Astrophysics* 632 (2019): A93.
3. Prokopyszyn, A. P. K., A. N. Wright, and A. W. Hood. “Line-tied boundary conditions can cause resonant absorption models to generate unphysically large boundary layers.” *The Astrophysical Journal (in prep)*.

Collaboration statement

The numerical simulations presented in this thesis were carried out by myself under the supervision of Prof. Alan Hood, Prof Ineke De Moortel and Dr Andrew Wright.

Acknowledgements

I want to thank several people for their aid and support in the completion of this thesis.

Firstly, I am incredibly grateful to my primary supervisor, Alan, for his help and guidance throughout my PhD. His enthusiasm and expertise played a crucial role in making this work possible. I want to thank my co-supervisors, Ineke and Andy. I found Ineke's advice really useful, and she ensured I didn't stray off on too many tangents. I found Andy's constructive criticism and ability to think about problems from a physical and a mathematical perspective very insightful.

Secondly, I'd like to thank all of the Maths department members and Steve's football players. A special thanks to my office mates and everyone else for the long lunch breaks and interesting conversations. Thanks to Callan for being a great house/office-mate throughout the COVID-19 pandemic.

Last but not least, I would like to thank my family. Thank you to my parents and siblings for always believing in me and encouraging me through the highs and lows. I am also grateful to Isobel and Ken for their advice and assistance.

Contents

1	Introduction	11
1.1	Solar atmosphere	12
1.2	Coronal heating problem	17
1.3	MHD equations	20
1.3.1	Assumptions	20
1.3.2	Faraday's law	21
1.3.3	Ampère's law	23
1.3.4	Solenoidal constraint	24
1.3.5	Ohm's law	24
1.3.6	Mass continuity	25
1.3.7	Momentum equation	25
1.3.8	Ideal gas law	30
1.3.9	Internal energy equation	30
1.3.10	Induction equation	32
1.3.11	Total energy equation	33
1.4	MHD waves: Dispersion relation	34
1.4.1	Alfvén waves	40
1.4.2	Fast waves	41
1.4.3	Poynting flux	42
1.5	MHD waves: power spectrum	43
1.6	Outline of the thesis	46
2	Ideal footpoint driven Alfvén waves	48
2.1	Introduction	48

2.2	Model and equations	49
2.3	Closed loop: general solution	51
2.4	Closed loop: sinusoidal solution	53
2.4.1	Solution at $z = 0$	54
2.4.2	Resonant case	56
2.4.3	Approximately resonant case	60
2.4.4	Nonresonant case	64
2.5	Closed loop: broadband driver	64
2.5.1	Driven harmonic oscillator	67
2.5.2	General solution	68
2.5.3	Noisy force	71
2.6	Leaky loop: reflection coefficient	78
2.7	Leaky loop: general solution	86
2.8	Leaky loop: steady state solution	89
2.9	Open loop: phase mixing	94
2.10	Discussion and conclusions	97
3	Resistive phase-mixed Alfvén waves	100
3.1	Introduction	100
3.2	Model and equations	104
3.3	Open loop	109
3.3.1	Analytic solution	109
3.3.2	Numerical solution	112
3.4	Closed loop	113
3.4.1	Analytic solution	115
3.4.2	Numerical solution	116
3.4.3	Heating rate	117
3.4.4	Multiple harmonics	122
3.5	Leaky loop	126
3.6	Coronal heating discussion	131
3.7	Conclusions	137

4 Resonant absorption in an oblique field	139
4.1 Introduction	139
4.2 Model and equations	142
4.3 Energy equations	145
4.4 Normal field: Resonant absorption with line-tied BCs	147
4.4.1 Equations	147
4.4.2 Analytic solution	148
4.4.3 Numerical solution	157
4.5 Oblique field: Uniform density profile	160
4.5.1 Dispersion relation	160
4.5.2 Normal mode solution	161
4.6 Oblique field: Piecewise constant density profile	167
4.6.1 Asymptotic expansion: Case where $k_{ +} \ll k_x \ll k_{ -}$	176
4.6.2 Asymptotic expansion: Case where $k_{ -}, k_{ +} \ll k_x$	178
4.7 Oblique field: Resonant absorption	182
4.7.1 Model and equations	183
4.7.2 Eigenfunctions and eigenfrequencies	184
4.7.3 Analytic resonant solution	190
4.7.4 Numerical solution	196
4.8 Summary and conclusions	201
5 Conclusions and future work	205
A Coronal heating by viscous fast waves	209
A.1 Model and assumptions	209
A.2 Damping length	211
A.3 Discussion	213

Chapter 1

Introduction

The Sun is the brightest and most energetic object in the solar system. Despite it being 1.5×10^8 km away, our understanding of how it works has dramatically improved over the last century. Solar physics has played a vital role in some of the most important discoveries of the last century. For example, before the 20th century, the fuel source for the Sun was a complete mystery. It was not until the early 20th century that the fusion of Hydrogen into Helium was first proposed as the dominant process that powers the stars. More recently, the solar neutrino problem was solved due to developments in particle and quantum physics. The solar neutrino problem concerned a large discrepancy between the flux of neutrinos as predicted from the solar luminosity and measured directly. The difference was first observed in the mid-1960s and finally resolved around 2002. Another fundamental discovery was the derivation of the MHD equations (see Section 1.3) which combines the equation of fluid dynamics with electromagnetism. These equations enable the plasma, which makes up the Sun, to be modelled and played a key role in allowing Eugene Parker to predict the existence of the solar wind in 1957. The MHD equations are also currently being used to develop space weather prediction models to give early warnings of dangerous flares and coronal mass ejections, see for example, [Feynman and Gabriel \(2000\)](#).

Over recent decades, due to improvements in our observational instruments, we are now able to measure wave amplitudes and frequencies in the solar atmosphere directly. This thesis focuses on studying linear MHD waves in the solar atmosphere. Improving our understanding of these waves could lead to coronal seismology developments ([Banerjee et al., 2007](#)). It could also provide insight into one of the biggest problems

in solar physics, namely, the coronal heating problem (see Section 1.2). Coronal seismology is a technique where mathematical models are used to infer hard to measure quantities, e.g. the coronal magnetic field strength or density gradients from easier to measure quantities, e.g. wave frequencies and damping time. We take a theoretical, as opposed to an observational approach to build our simple models. We calculate analytic solutions which we verify numerically. Most of the code used for this thesis, including LaTeX files, is available on GitHub via the following URL:

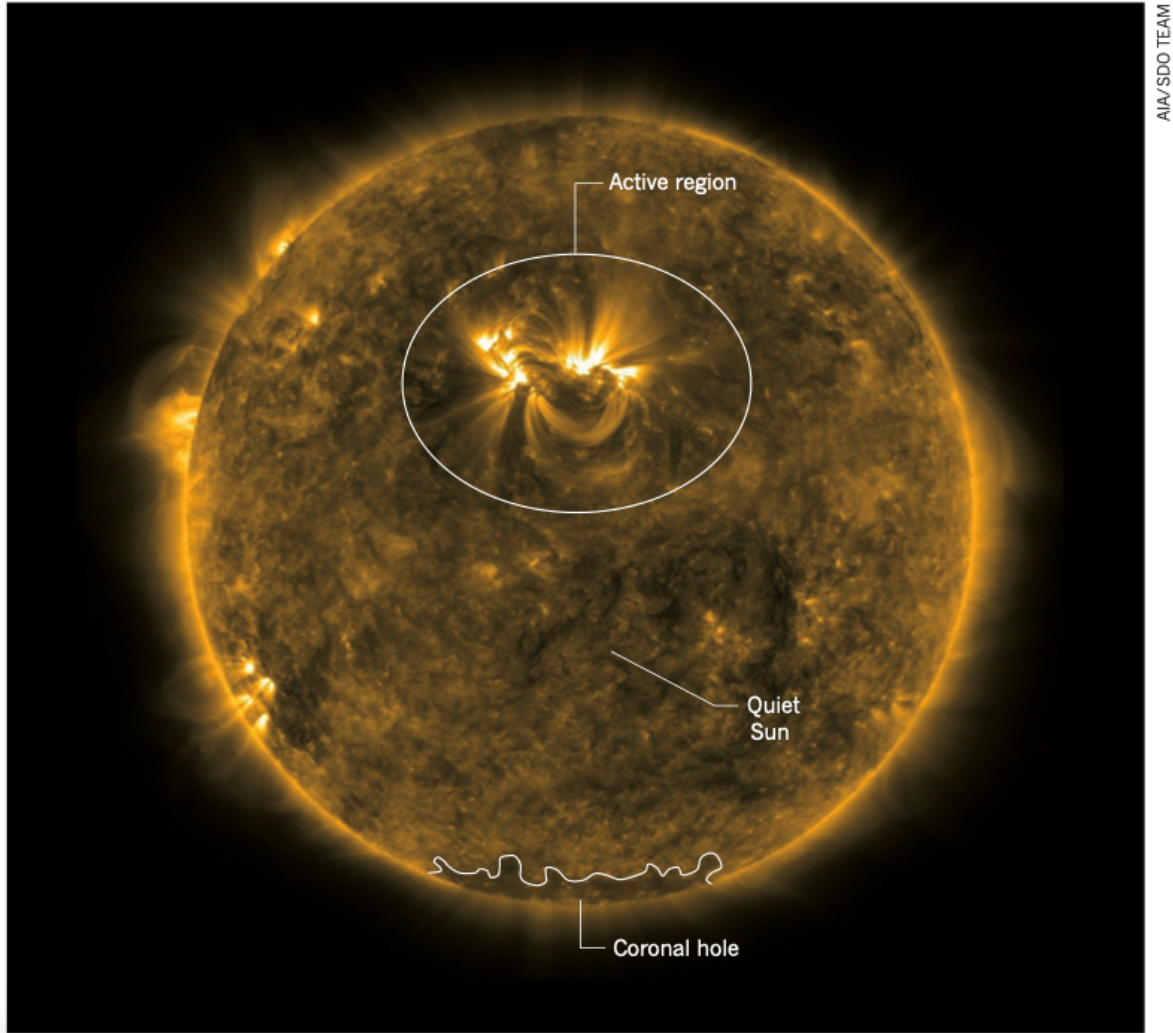
https://github.com/aleksyprok/apkp_thesis

In this chapter, we introduce some of the critical properties of the solar atmosphere which are relevant to this thesis. After that, we will introduce the MHD equations which allow us to accurately model the plasma. In Section 1.4, we model waves in a domain where the background quantities are uniform and introduce some of the key aspects and terminology used in solar MHD wave theory. Nakariakov and Kolotkov (2020) gives a more in-depth introduction to MHD waves in the solar corona and Goossens et al. (2011) focuses on the linear aspects. Finally, in Section 1.5, we discuss recent observations of waves in the solar atmosphere and show how the energy distributes as a function of wave frequency.

1.1 Solar atmosphere

The solar atmosphere refers to the outer layer of gas and plasma surrounding the Sun. It is defined as the part of the Sun from which photons can escape directly into space. We split the atmosphere into four regions: the photosphere, chromosphere, transition region and corona. The regions form approximate concentric spherical shells around the Sun. However, this picture breaks down at, for example, prominences/filaments, which are cool and dense loop structures which can extend high into the corona. With that in mind, when viewing the Sun at a global scale, it is useful to model it in terms of four distinct, but highly coupled layers.

We label different parts of the solar atmosphere as either an active region, coronal hole or quiet sun (see Figure 1.1). An active region is an area with a strong magnetic field. It is common for sunspots to form in active regions. These are usually the



AIA/SDO TEAM

Figure 1.1: At a temperature of about 1 million kelvin, this image of coronal plasma was taken using the Atmospheric Imaging Assembly (AIA) instrument on the Solar Dynamics Observatory (SDO) (courtesy [Cargill and De Moortel 2011](#)). It also offers an example of solar physicists labelling different solar atmosphere parts as either an active region, coronal hole or quiet sun.

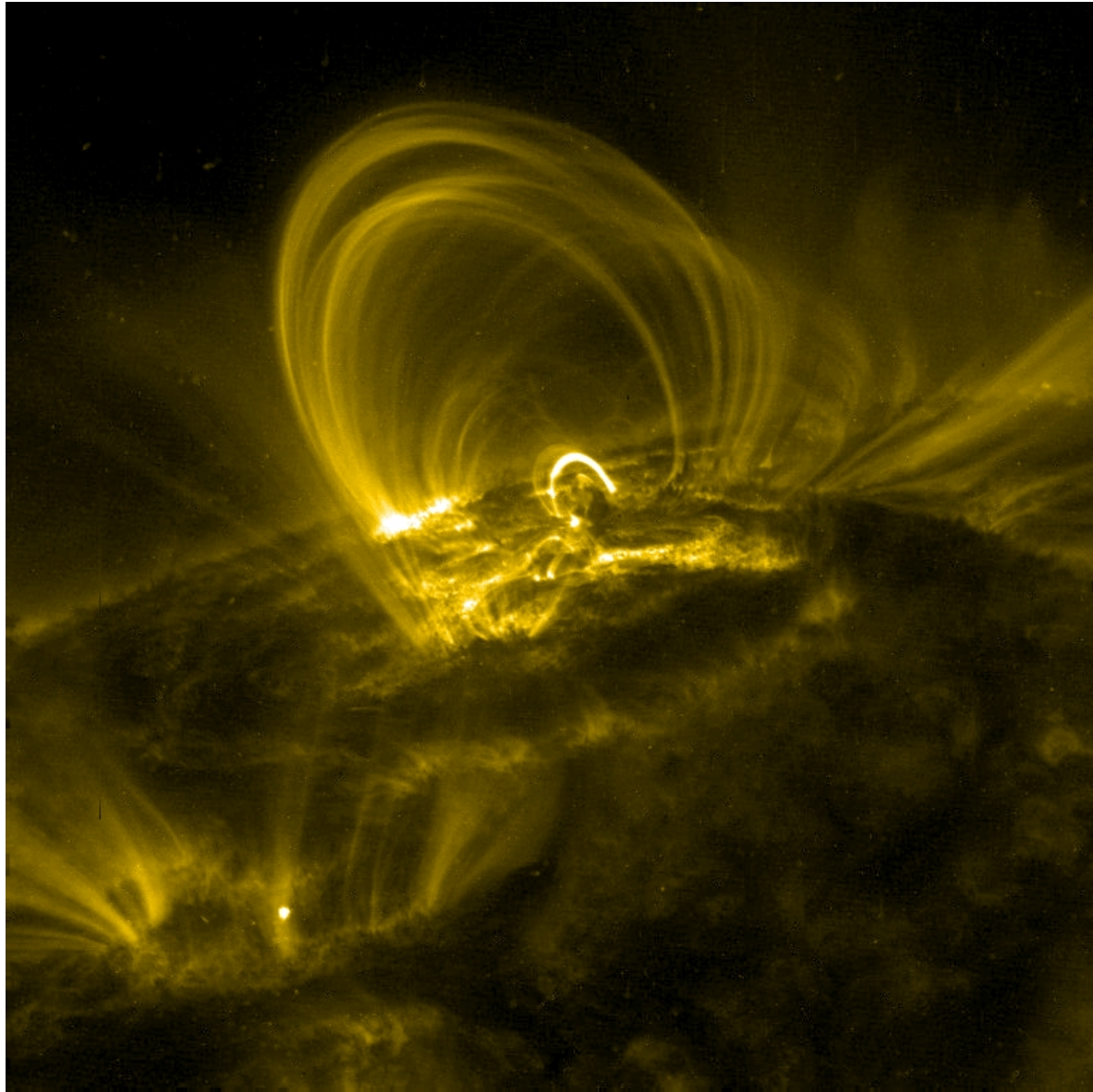


Figure 1.2: This image of coronal loops was taken using the TRACE (Transition Region and Coronal Explorer) instrument (courtesy [Lockheed Martin Solar and Astrophysics Laboratory 2019](#)). It shows coronal plasma at a temperature of about 1 million kelvin.

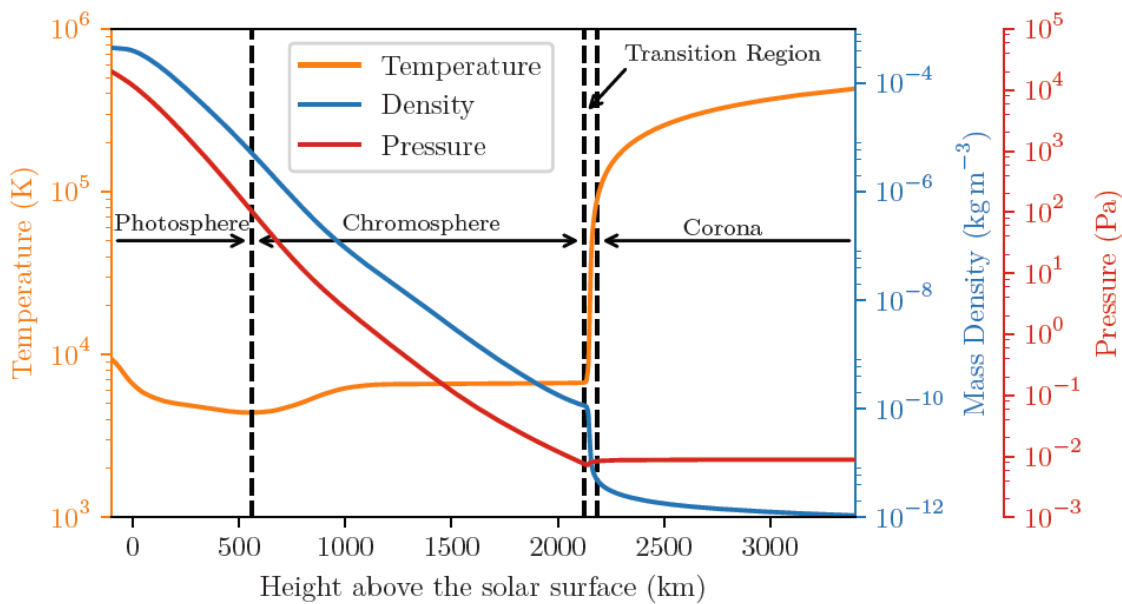


Figure 1.3: The VAL model (Vernazza et al., 1981) of the solar atmosphere (courtesy [Williams 2018](#)).

	Coronal hole	Quiet Sun	Active region
<u>Corona</u>			
Conduction	60	200	$10^3\text{-}10^4$
Radiation	10	100	5000
Solar wind	700	< 50	< 100
Total	800	300	10,000
<u>Chromosphere</u>			
Radiation	4000	4000	20,000

Table 1.1: Order-of-magnitude energy-loss fluxes in W m^{-2} ([Withbroe and Noyes, 1977](#); [Priest, 2014](#)).

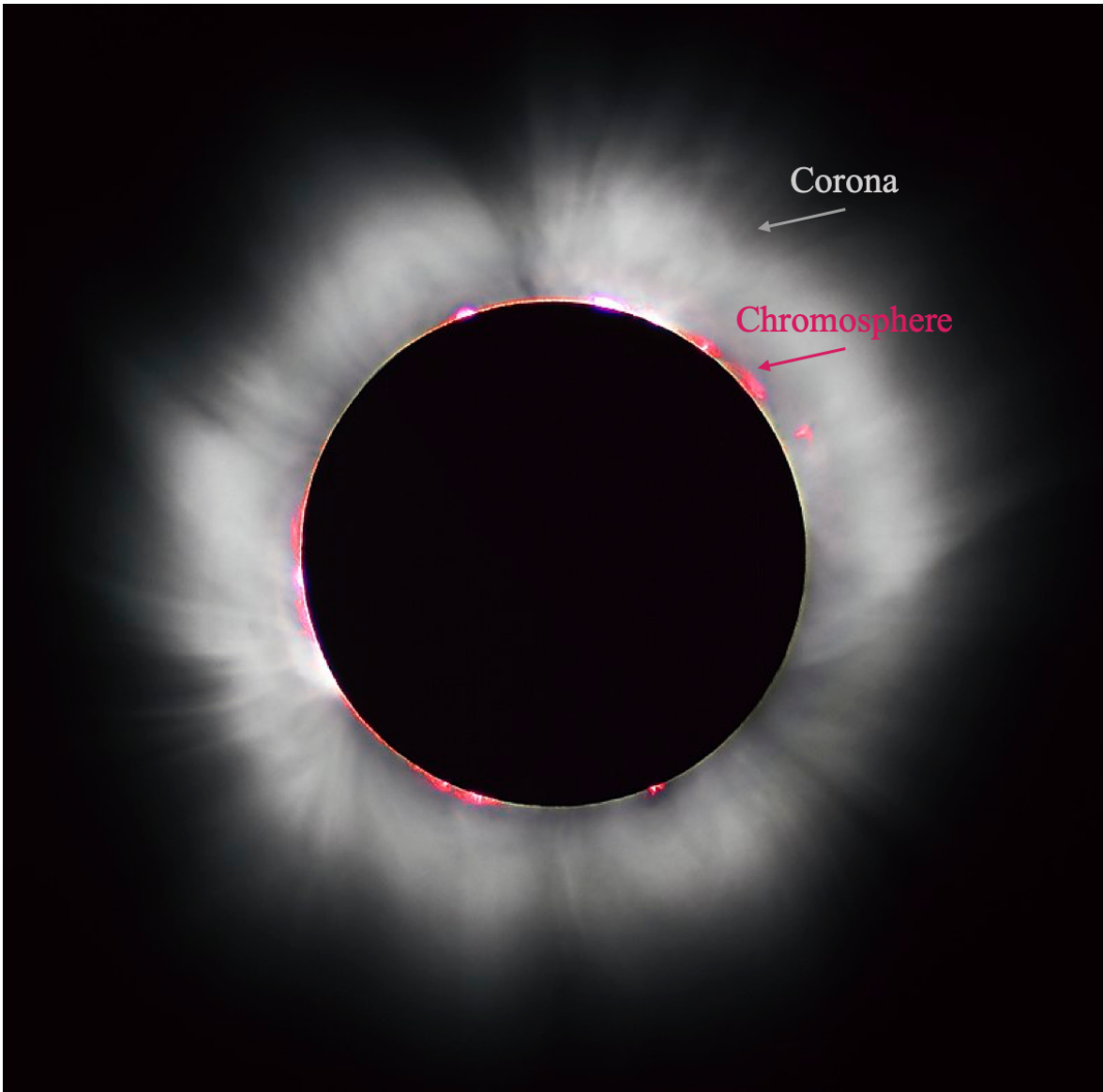


Figure 1.4: This photo taken in France during the 1999 total eclipse (courtesy Wikimedia, User: Luc Viatour). The chromosphere is emitting a pink/red light close to the disc. The faint white glow around the disk shows white light from the photosphere being Thompson scattered by the corona.

locations where the largest flares and coronal mass ejections occur. Coronal holes are the polar regions of the Sun, which look dark in the X-ray emission. In coronal holes, the magnetic field is usually unipolar and opens towards the interplanetary space. Finally, the quiet Sun usually refers to solar regions that do not lie in either active regions or coronal holes. Note that active regions and the quiet Sun often contain closed loops, like those shown in Figure 1.2. We refer to these loops as closed because their magnetic field does not extend beyond the solar atmosphere. In contrast, the field lines in coronal holes are referred to as open because they extend far out into the solar system before eventually looping back or connecting with the interplanetary medium.

Figure 1.3 shows data from what is commonly referred to as the Vernazza Avrett and Loeser (VAL) ([Vernazza et al., 1981](#)) model of the quiet sun. It is useful for approximating average values of physical quantities. However, the solar atmosphere is, in reality, a highly inhomogeneous, time-dependent plasma. Figure 1.3 shows that the lowest region is the photosphere. It is the region where most photons, at visible light frequencies, escape into outer space. The chromosphere lies above the photosphere and emits significantly less light than the photosphere. It is only visible with the naked eye during total solar eclipses (see red/pink light in Figure 1.4). The transition region lies between the chromosphere and the corona. Across the transition region, the temperature changes rapidly from approximately 10^5 K to 10^6 K. Finally, the corona lies above the chromosphere and transition region. As with the chromosphere, it emits significantly less light than the photosphere and is only visible with the naked eye during total solar eclipses as a white glow (see Figure 1.4). Note that the corona Thompson scatters white light from the photosphere. The intrinsic colour of the corona is not white. However, the inherent colour of the chromosphere is indeed the pink/red colour seen in Figure 1.4.

1.2 Coronal heating problem

The chromospheric and coronal heating problem relates to the question; ‘why are they so hot?’ It remains one of the biggest unsolved problems in solar physics. Figure 1.3 shows that the temperature increases with distance from the photosphere in the corona and chromosphere. Looking at Figure 1.3, two questions come to mind. Why does the temperature increase with distance away from the surface of the Sun? Intuitively,

the temperature should decrease away from a heat source. Since the temperature is higher in the corona and chromosphere, this means that conduction is an energy loss mechanism. The plasma is also optically thin (for most bands) in the corona, which means the plasma loses more energy via radiation than it gains. So what is balancing the conductive and radiative losses in the chromosphere and corona? The energy losses are balanced by converting kinetic and magnetic energy into heat via Ohmic and viscous dissipation ([Klimchuk, 2015](#)). However, we do not have a verified model giving a precise description of how the temperatures are maintained.

Regarding the first question, we now understand why the temperature of the solar atmosphere increases with distance from the core of the Sun. For example, [Martens \(2010\)](#) successfully models a similar temperature profile (although a detailed description of the heating source is still unknown). These models use the internal energy equation with a user-defined heating function superimposed. This heating function simulates the Ohmic and viscous dissipation of magnetic and kinetic energy. They find that even if the heating function is more significant at the footpoints, their models still produce the same basic structure as the solar atmosphere. This counter-intuitive temperature profile is partly explained by the fact that for coronal/chromospheric plasma, the radiative losses can decrease with rising temperature (see for example [Klimchuk et al. 2008](#)). However, a detailed description of the primary mechanism(s) by which magnetic and kinetic energy dissipates in the corona has yet to be provided.

In the closed corona, the proposed heating mechanisms can be split into two categories. The first one, relies on the build-up of magnetic energy in the corona which is then suddenly released by magnetic reconnection. The second mechanism brings energy into the corona through MHD waves. In for example [van Ballegooijen et al. \(2011\)](#), [Howson et al. \(2020\)](#) they model both mechanisms and compare them against each other. Reconnection mechanisms rely on the slow stressing of the magnetic field. We define slow motions as having a period longer than the Alfvén travel time of a coronal loop. In Section 2.4.2 we show that if the driving footpoint motions are longer than the Alfvén travel time of the loop then this causes the loop to stretch resulting in a large build-up in magnetic energy compared with a small growth in kinetic energy. We show that if the driving motions period is shorter than the Alfvén travel time of the loop then the growth in kinetic and magnetic energy is approximately equal. Therefore, for reconnection models, the primary dissipation mechanism is resistive since the amount

of free magnetic energy is usually much greater than the amount of free kinetic energy. The amount of free magnetic and kinetic energy associated with the wave is assumed to be approximately equal. Therefore, for wave heating mechanisms the primary dissipation mechanism is usually viscous because the viscous Reynolds number (see Equation 1.3.38) is much smaller than the magnetic Reynolds number (see Equation 1.3.52).

This thesis will investigate the dissipation of phase mixed Alfvén waves and their role in coronal heating. The dissipation of Alfvén waves has been the basis of many coronal heating models (see review by [Arregui 2015](#) and references therein). Phase mixing was first suggested as a coronal heating mechanism by [Heyvaerts and Priest \(1983\)](#). Phase mixing is the process where gradients perpendicular to the field build-up due to Alfvén waves propagating on field lines with a spatial gradient in Alfvén travel time. This process leads to neighbouring waves moving out of phase with each other; hence the name phase mixing. Other notable mechanisms are: resonant absorption ([Ionson, 1982](#)), reflection-driven Alfvén wave turbulence ([Hollweg, 1986a](#); [van Ballegooijen et al., 2011](#); [Shoda et al., 2019](#)), turbulence triggered via the tearing mode or Kelvin-Helmholtz instability ([Browning and Priest, 1984](#); [Antolin et al., 2016, 2018](#)) and coupling with compressive modes ([Kudoh and Shibata, 1999](#); [Antolin and Shibata, 2010](#)).

Table 1.1 shows order-of-magnitude estimates for the power-losses (per unit area) in the corona and chromosphere. Note that the mean radiation from the photosphere is significantly greater at about $0.63 \times 10^8 \text{ W m}^{-2}$. It is sometimes useful to consider the energy losses per unit volume rather than by per area. The chromosphere's per unit volume radiative losses can be calculated from the total radiative losses divided by the volume. Taking the height difference between the top and bottom of the chromosphere as 1500 km gives the average radiative losses in an active region chromosphere per unit volume as $1.33 \times 10^{-2} \text{ W m}^{-3}$. To help get an intuitive idea of how much heat this is, this means that a 1 W light-emitting diode emits about the same radiation as an Olympic sized swimming pool of chromosphere. It is worth noting that the chromosphere and corona are very sparse compared with the photosphere and so a relatively small amount of heat can lead to a large temperature change. Note that Table 1.1 shows the radiative losses are greater in the chromosphere than in the corona. This is interesting as chromospheric and coronal heating problem is usually referred to as simply the coronal heating problem despite the chromospheric radiative losses being greater.

1.3 MHD equations

A large fraction of the solar atmosphere is ionised ([Shimizu et al., 2018](#)) due to the high temperature. The high temperature allows the orbital electrons to break their bonds with their corresponding ions and form free electrons. The medium is a plasma and can therefore conduct electricity. To study the plasma, we use Magnetohydrodynamics (MHD). The MHD equations are formed by combining equations from electromagnetism with equations from fluid dynamics. Different forms of the MHD equations are used in different contexts. In sections [1.3.2-1.3.11](#) we discuss each of the MHD equations in SI base units.

1.3.1 Assumptions

This thesis is primarily concerned with studying waves in the corona which is assumed to be fully ionised. The solar atmosphere is approximately 74% Hydrogen 25% Helium and 1% other elements ([Stanford Solar Center, 2019](#)). At typical coronal temperatures, say 10^6 K, the thermal energy of an electron is approximately 86 eV. This is greater than the ionisation energies of Hydrogen and Helium which have first ionisation energies of approximately 14 eV and 25 eV and the second ionisation energy of Helium is approximately 54 eV ([Lide, 2003](#)). Also, the ionisation fraction as a function of height has been estimated in, for example, [Shimizu et al. \(2018\)](#) and suggests that the plasma in the corona is nearly completely ionised. Therefore, in this thesis, we will often model the plasma as fully ionised Hydrogen plasma.

We model the plasma as collisional and assume that collisional transport theory is valid. In [Richardson \(2019\)](#), they list six conditions for collisional transport theory to be valid. In the strong magnetic field limit, where $\omega_{ce}/\nu_e \gg 1$ (see Table [1.2](#)) we require

$$L_{\parallel} \gg \lambda_{Te}, \lambda_{Ti}, \quad (1.3.1)$$

$$L_{\perp} \gg \sqrt{\lambda_{Te} r_e}, \sqrt{\lambda_{Ti} r_e} \quad (1.3.2)$$

where L_{\parallel} , L_{\perp} denote the macroscopic length scales parallel and perpendicular to the magnetic field respectively. In the absence of a magnetic field, we require

$$L \gg \lambda_{Te}, \lambda_{Ti}, \quad (1.3.3)$$

where L denotes the macroscopic length scales. For fully ionised Hydrogen plasma, typical values in the corona are,

$$\begin{aligned} \frac{\omega_{ce}}{\nu_e} &= \frac{1}{3.64 \times 10^{-6}} \frac{eBT^{3/2}}{m_e n_e \ln \Lambda} \\ &\approx 2.42 \times 10^6 \left(\frac{20}{\ln \Lambda} \right) \left(\frac{B}{10^{-3} \text{ T}} \right) \left(\frac{T_e}{10^6 \text{ K}} \right)^{3/2} \left(\frac{10^{15} \text{ m}^{-3}}{n_e} \right), \end{aligned} \quad (1.3.4)$$

$$\begin{aligned} \lambda_{Te} &= \frac{1}{3.64 \times 10^{-6}} \frac{\sqrt{k_B/m_e}}{\ln \Lambda} \frac{T_e^2}{n_e} \\ &\approx 0.53 \times 10^5 \left(\frac{20}{\ln \Lambda} \right) \left(\frac{T_e}{10^6 \text{ K}} \right)^2 \left(\frac{10^{15} \text{ m}^{-3}}{n_e} \right) \text{ m}, \end{aligned} \quad (1.3.5)$$

$$\begin{aligned} \lambda_{Ti} &= \frac{1}{6.00 \times 10^{-6}} \frac{\sqrt{k_B/m_p}}{\ln \Lambda} \frac{T_i^2}{n_i} \\ &\approx 0.76 \times 10^5 \left(\frac{20}{\ln \Lambda} \right) \left(\frac{T_i}{10^6 \text{ K}} \right)^2 \left(\frac{10^{15} \text{ m}^{-3}}{n_i} \right) \text{ m}, \end{aligned} \quad (1.3.6)$$

$$\begin{aligned} r_e &\approx \frac{\sqrt{m_e k_B T_e}}{eB} \\ &\approx 2.21 \times 10^{-2} \left(\frac{T_e}{10^6 \text{ K}} \right) \left(\frac{10^{-3} \text{ T}}{B} \right) \text{ m}. \end{aligned} \quad (1.3.7)$$

Therefore, provided the macroscopic length scales are greater than about 1 Mm and the parameters are given as above, Equations (1.3.1)-(1.3.3) should be approximately satisfied.

1.3.2 Faraday's law

Faraday's law is given by

$$\boldsymbol{\nabla} \times \mathbf{E} = - \frac{\partial \mathbf{B}}{\partial t}. \quad (1.3.8)$$

\mathbf{B} is the magnetic induction. In solar or astrophysical contexts, it is referred to as the magnetic field strength. In this thesis, \mathbf{B} will hereafter be referred to as the magnetic field strength. \mathbf{E} denotes the electric field. Finally, time is denoted with t .

Name	Symbol	Gaussian units	SI units
Electron gyrofrequency	ω_{ce}	$\frac{eB}{m_e c}$	$\frac{eB}{m_e}$
Ion gyrofrequency	ω_{ci}	$\frac{ZeB}{m_i c}$	$\frac{ZeB}{m_i}$
Electron collision rate	ν_e	$2.91 \times 10^{-6} \frac{n_e \ln \Lambda}{T_e^{3/2}} \text{ s}^{-1}$	$3.64 \times 10^{-6} \frac{n_e \ln \Lambda}{T_e^{3/2}} \text{ s}^{-1}$
Ion collision rate	ν_i	$4.80 \times 10^{-8} \frac{Z^4 n_i \ln \Lambda}{\sqrt{T_i^3 m_i / m_p}} \text{ s}^{-1}$	$6.00 \times 10^{-8} \frac{Z^4 n_i \ln \Lambda}{\sqrt{T_i^3 m_i / m_p}} \text{ s}^{-1}$
Electron thermal speed	v_{Te}	$\sqrt{\frac{k_B T_e}{m_e}}$	$\sqrt{\frac{k_B T_e}{m_e}}$
Ion thermal speed	v_{Ti}	$\sqrt{\frac{k_B T_i}{m_i}}$	$\sqrt{\frac{k_B T_i}{m_i}}$
Electron gyroradius	r_e	$\frac{v_{Te}}{\omega_{ce}}$	$\frac{v_{Te}}{\omega_{ce}}$
Ion gyroradius	r_i	$\frac{v_{Ti}}{\omega_{ci}}$	$\frac{v_{Ti}}{\omega_{ce}}$
Electron mean free path	λ_{Te}	$\frac{v_{Te}}{\nu_e}$	$\frac{v_{Te}}{\nu_e}$
Ion mean free path	λ_{Ti}	$\frac{v_{Ti}}{\nu_i}$	$\frac{v_{Ti}}{\nu_i}$

Table 1.2: This table lists some of the fundamental plasma parameters. The Gaussian formulas were copied from [Richardson \(2019\)](#) which were then converted into SI base units. The collision rates are for completely ionised plasmas. B denotes the magnetic field strength, e denotes the elementary charge, c denotes the speed of light, m_e , m_p denote the mass of an electron and proton respectively, Z gives the charge state, i.e. the number of protons in an ion, n_e , n_i denote the electron and ion number densities respectively, $\ln \Lambda$ denotes the Coulomb logarithm, T_e , T_i denotes the temperature of the electrons and ions respectively and k_B denotes the Boltzmann constant.

1.3.3 Ampère's law

Ampère's law is given by

$$\nabla \times \mathbf{B} = \mu_0 \mathbf{j} + \underbrace{\frac{1}{c^2} \frac{\partial \mathbf{E}}{\partial t}}_{\approx 0} \quad (1.3.9)$$

We approximate the magnetic permeability, μ_0 , by its value in a vacuum, namely,

$$\mu_0 = 4\pi \times 10^{-7} \text{ henry m}^{-1}.$$

The current density is denoted with \mathbf{j} . We approximate the speed of light, c , with its value in a vacuum, namely,

$$c = \frac{1}{\sqrt{\mu_0 \epsilon_0}} \approx 3.00 \times 10^8 \text{ m s}^{-1},$$

where ϵ_0 is the permittivity of free space in a vacuum.

In this thesis, we neglect last term in Equation (1.3.9), called the displacement current. Replacing the time derivative with $1/t_0$, and \mathbf{E} with E_0 means that

$$\left| \frac{1}{c^2} \frac{\partial \mathbf{E}}{\partial t} \right| \approx \frac{1}{c^2} \frac{E_0}{t_0},$$

where E_0 and t_0 denotes the typical size of their respective quantities. From Faraday's law, Equation (1.3.8), it follows that

$$\frac{E_0}{l_0} \approx \frac{B_0}{t_0},$$

where B_0 and l_0 denote the typical size of their respective quantities. Letting

$$v_0 = \frac{l_0}{t_0}, \quad \frac{B_0}{l_0} \rightarrow |\nabla \times \mathbf{B}|,$$

it follows that

$$\left| \frac{1}{c^2} \frac{\partial \mathbf{E}}{\partial t} \right| \approx \frac{v_0^2}{c^2} |\nabla \times \mathbf{B}|,$$

where v_0 here denotes a typical speed. Hence, we can neglect the displacement current, provided

$$v_0 \ll c. \quad (1.3.10)$$

This thesis is interested in waves in the corona. It is very rare for waves to have a velocity amplitude which exceeds the local Alfvén speed, v_A , given by

$$v_A \approx \frac{|\mathbf{B}|}{\sqrt{\mu_0 \rho}}, \quad (1.3.11)$$

where ρ denotes the plasma density. In the corona, the Alfvén speed is approximately 10^6 m s^{-1} and so condition (1.3.10) is satisfied.

1.3.4 Solenoidal constraint

The solenoidal constraint states that

$$\nabla \cdot \mathbf{B} = 0. \quad (1.3.12)$$

Physically, this equation states that a magnetic field can have no sources or sinks, i.e. no monopoles.

1.3.5 Ohm's law

Priest (2014) shows that for fully ionised plasma, Ohm's law is given by

$$\mathbf{E} + \mathbf{v} \times \mathbf{B} = \underbrace{\frac{\mathbf{j}}{\sigma}}_{\text{Direct term}} + \underbrace{\frac{1}{n_e e} \mathbf{j} \times \mathbf{B}}_{\text{Hall term}}, \quad (1.3.13)$$

where the electron inertia and electron pressure gradient terms have been neglected. We denote the plasma velocity with \mathbf{v} . The conductivity, σ , is given by

$$\sigma = \frac{n_e e^2}{m_e \nu_e}. \quad (1.3.14)$$

Substituting in typical coronal values, the resistivity coefficients can be approximated by

$$\frac{1}{\sigma} \approx 2.58 \times 10^{-6} \left(\frac{T}{10^6 \text{ K}} \right)^{-3/2} \text{ ohm}^{-1} \text{ m}^{-1}, \quad (1.3.15)$$

$$\frac{|\mathbf{B}|}{en_e} \approx 6.24 \left(\frac{|\mathbf{B}|}{10^{-3} \text{ T}} \right) \left(\frac{10^{15} \text{ m}^{-3}}{n_e} \right). \quad (1.3.16)$$

The coulomb logarithm, $\ln \Lambda$, lies between 5 and 20 and has a weak temperature dependence. For coronal plasma, a suitable approximation is $\ln \Lambda \approx 20$. It is tempting to neglect the direct current term in favour of the Hall term. However, the Hall term is dependent only on currents parallel to the field. Throughout this thesis, the currents perpendicular to the field dominate.

1.3.6 Mass continuity

The mass continuity equation is given by

$$\frac{\partial \rho}{\partial t} + \nabla \cdot (\rho \mathbf{v}) = 0. \quad (1.3.17)$$

The mass density is denoted by ρ . Physically, this equation states that the rate of mass change in a volume is given by the total flux of mass moving in or out of a fixed volume.

1.3.7 Momentum equation

The most general form of the momentum equation/equation of motion relevant for this thesis is

$$\rho \frac{D\mathbf{v}}{Dt} = \underbrace{\mathbf{j} \times \mathbf{B}}_{\text{Lorentz force}} - \underbrace{\nabla p}_{\text{Pressure force}} - \underbrace{\frac{G\rho}{r^2} \hat{\mathbf{r}}}_{\text{Gravitational force}} + \underbrace{\nabla \cdot \boldsymbol{\sigma}_{\text{Brag}}}_{\text{Viscous force}}. \quad (1.3.18)$$

Here the D/Dt operator denotes the material derivative. The plasma pressure is denoted with p .

The first term on the right-hand side of Equation (1.3.18) is the Lorentz force. The $\rho^* \mathbf{E}$ term in the more general form of the Lorentz force has been neglected, where ρ^*

denotes the charge density. This is because we model the plasma as electrically neutral. Priest (2014) shows that the plasma can be modelled as electrically neutral provided the length scales of the system, l_0 , are greater than the Debye length, λ_D . The Debye length is approximated by

$$\lambda_D \approx 2.18 \times 10^{-3} \left(\frac{T}{10^6 \text{ K}} \right)^{1/2} \left(\frac{10^{15} \text{ m}^{-3}}{n} \right)^{1/2} \text{ m.} \quad (1.3.19)$$

The Lorentz force is commonly split into two components,

$$\mathbf{j} \times \mathbf{B} = \underbrace{\frac{1}{\mu_0} (\mathbf{B} \cdot \nabla) \mathbf{B}}_{\text{Magnetic tension force}} - \underbrace{\nabla \left(\frac{B^2}{2\mu_0} \right)}_{\text{Magnetic pressure force}}, \quad (1.3.20)$$

where

$$\frac{B^2}{2\mu_0} = \frac{\mathbf{B} \cdot \mathbf{B}}{2\mu_0},$$

is commonly called the magnetic energy density.

The gravitational force acts radially inward towards the core of the Sun, where $\hat{\mathbf{r}}$ is the unit vector in the radial direction. The gravitational force in the solar atmosphere is approximated by

$$\frac{G\rho}{r^2} \hat{\mathbf{r}} = \rho g_\odot \hat{\mathbf{r}}, \quad (1.3.21)$$

where

$$g_\odot = \frac{M_\odot G}{R_\odot^2} \approx 274 \text{ m s}^{-2}, \quad (1.3.22)$$

M_\odot denotes the mass of the Sun enclosed by the solar surface, R_\odot is the radius of the solar surface, and G is the universal gravitational constant. Equation (1.3.21) is valid in the solar atmosphere provided the height of the plasma above the solar surface, h , is less than the solar radius, i.e. $h \ll R_\odot$.

The viscous force is given by the divergence of the Braginskii viscous stress tensor, $\boldsymbol{\sigma}_{Brag}$ (Braginskii, 1965). Here we present the viscous stress tensor in the same form as

in MacTaggart et al. (2017),

$$\boldsymbol{\sigma}_{Brag} = \eta_0 \mathbf{W}^{(0)} + \eta_1 \mathbf{W}^{(1)} + \eta_2 \mathbf{W}^{(2)} - (\eta_3 \mathbf{W}^{(3)} + \eta_4 \mathbf{W}^{(4)}), \quad (1.3.23)$$

where

$$\mathbf{W}^{(0)} = \frac{3}{2}(\mathbf{W}\hat{\mathbf{B}} \cdot \hat{\mathbf{B}})(\hat{\mathbf{B}} \otimes \hat{\mathbf{B}} - \frac{1}{3}\mathbf{I}), \quad (1.3.24)$$

$$\mathbf{W}^{(1)} = (\mathbf{I} - \hat{\mathbf{B}} \otimes \hat{\mathbf{B}})\mathbf{W}(\mathbf{I} - \hat{\mathbf{B}} \otimes \hat{\mathbf{B}}) + \frac{1}{2}(\mathbf{W}\hat{\mathbf{B}} \cdot \hat{\mathbf{B}})(\mathbf{I} - \hat{\mathbf{B}} \otimes \hat{\mathbf{B}}), \quad (1.3.25)$$

$$\mathbf{W}^{(2)} = (\mathbf{I} - \hat{\mathbf{B}} \otimes \hat{\mathbf{B}})\mathbf{W}(\hat{\mathbf{B}} \otimes \hat{\mathbf{B}}) + (\hat{\mathbf{B}} \otimes \hat{\mathbf{B}})\mathbf{W}(\mathbf{I} - \hat{\mathbf{B}} \otimes \hat{\mathbf{B}}), \quad (1.3.26)$$

$$\mathbf{W}^{(3)} = \frac{1}{2}\mathbf{Z}\mathbf{W}(\mathbf{I} - \hat{\mathbf{B}} \otimes \hat{\mathbf{B}}) - \frac{1}{2}(\mathbf{I} - \hat{\mathbf{B}} \otimes \hat{\mathbf{B}})\mathbf{W}\mathbf{Z}, \quad (1.3.27)$$

$$\mathbf{W}^{(4)} = (\mathbf{Z}\mathbf{W}\hat{\mathbf{B}}) \otimes \hat{\mathbf{B}} + \hat{\mathbf{B}} \otimes (\mathbf{Z}\mathbf{W}\hat{\mathbf{B}}), \quad (1.3.28)$$

with

$$\mathbf{W} = \nabla \mathbf{v} + (\nabla \mathbf{v})^T - \frac{2}{3}(\nabla \cdot \mathbf{v})\mathbf{I}, \quad (1.3.29)$$

where \mathbf{Z} is the tensor with components $Z_{ij} = \epsilon_{ikj}b_k$, where ϵ_{ikj} are components of the Levi-Civita symbol. $\hat{\mathbf{B}}$ is given by

$$\hat{\mathbf{B}} = \frac{\mathbf{B}}{|\mathbf{B}|}. \quad (1.3.30)$$

Hogan (1984) labels each of the tensors, $\eta_0 \mathbf{W}^{(0)}$, $\eta_1 \mathbf{W}^{(1)}$, $\eta_2 \mathbf{W}^{(2)}$, $\eta_3 \mathbf{W}^{(3)}$ and $\eta_4 \mathbf{W}^{(4)}$ with names based on their physical interpretations. The author labels $\eta_0 \mathbf{W}^{(0)}$ as the viscosity tensor parallel to the magnetic field. $\eta_1 \mathbf{W}^{(1)}$ and $\eta_2 \mathbf{W}^{(2)}$ are labelled as the viscosity tensors perpendicular to the magnetic field. Finally, $\eta_3 \mathbf{W}^{(3)}$ and $\eta_4 \mathbf{W}^{(4)}$ are referred to as the drift contributions. The drift terms are also referred to as the dispersive terms because $\mathbf{W}^3 : \nabla \mathbf{v} = \mathbf{W}^4 : \nabla \mathbf{v} = 0$ which means they do not directly dissipate energy. Note that $\mathbf{W}^{(0)}$ contains a $\nabla \cdot \mathbf{v}$ term, therefore, it is dependent on derivatives parallel to the magnetic field as well as derivatives associated with the compressibility of the velocity. The viscosity coefficients are approximated by

$$\eta_0 = 2.21 \times 10^{-16} \frac{T^{5/2}}{\log \Lambda} \text{ kg m}^{-1} \text{ s}^{-1}, \quad (1.3.31)$$

$$\eta_1 = \frac{3}{10} \eta_0 (\omega_{ci}/\nu_i)^{-2}, \quad (1.3.32)$$

$$\eta_2 = 4\eta_1, \quad (1.3.33)$$

$$\eta_3 = \frac{1}{2} \eta_0 (\omega_{ci}/\nu_i)^{-1}, \quad (1.3.34)$$

$$\eta_4 = 2\eta_3, \quad (1.3.35)$$

in the strong filed limit ($\omega_{ci}/\nu_i \gg 1$). For typical coronal parameters, the product ω_{ci}/ν_i for fully ionised hydrogen plasma is approximated by

$$\begin{aligned} \omega_{ci}/\nu_i &= \frac{1}{6.00 \times 10^{-8}} \frac{eBT_i^{3/2}}{m_i n_i \ln \Lambda} \\ &\approx 0.80 \times 10^5 \left(\frac{20}{\ln \Lambda} \right) \left(\frac{B}{10^{-3} \text{ T}} \right) \left(\frac{T_i}{10^6 \text{ K}} \right)^{3/2} \left(\frac{10^{15} \text{ m}^{-3}}{n_i} \right). \end{aligned} \quad (1.3.36)$$

Hence, in the corona the condition, $\omega_{ci}/\nu_i \gg 1$, is usually satisfied (except near null points). For this reason, authors commonly neglect all of the viscosity tensors except $\mathbf{W}^{(0)}$ (Hollweg, 1986b; MacTaggart et al., 2017). However, in this thesis, we find that the gradients perpendicular to the field can be so strong that the $\mathbf{W}^{(1)}$ tensor cannot be neglected. The Reynolds number associated with $\mathbf{W}^{(0)}$ is given by

$$\begin{aligned} R_e &= \frac{\rho |\mathbf{v} \cdot \nabla \mathbf{v}|}{|\nabla \cdot \eta_0 \mathbf{W}^{(0)}|} \\ &\approx \frac{\rho_0 l_0 V_0}{\eta_0}, \end{aligned} \quad (1.3.37)$$

where ρ_0 denotes the typical density in the system, l_0 denotes the typical length scales of the system and V_0 denotes the typical velocity amplitude of the system. According to McIntosh et al. (2011); McIntosh and De Pontieu (2012), the velocity amplitude can be approximated as about 10 km s^{-1} . In the corona, we approximate the above Reynolds number as

$$R_e \approx 0.90 \times 10^2 \left(\frac{\rho_0}{10^{-12} \text{ kg m}^{-3}} \right) \left(\frac{l_0}{10^8 \text{ m}} \right) \left(\frac{V_0}{10^4 \text{ m s}^{-1}} \right) \left(\frac{10^6 \text{ K}}{T} \right)^{5/2}. \quad (1.3.38)$$

Given that the Reynolds number is significantly greater than unity we will often neglect

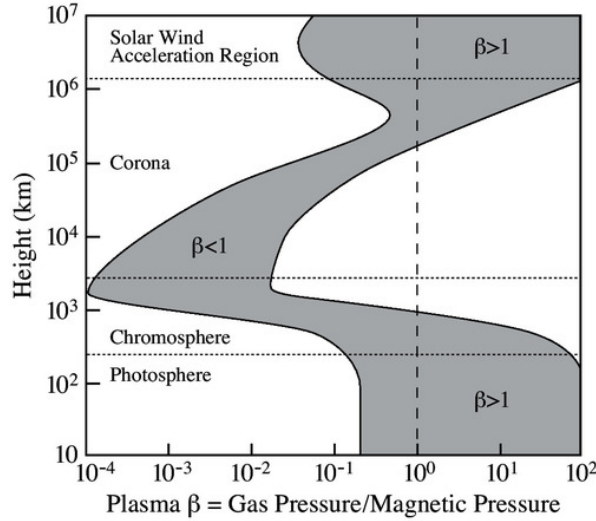


Figure 1.5: The shaded region shows an estimate of the plasma beta in the solar atmosphere as a function of height. This figure was adapted from [Gary \(2001\)](#).

viscosity. Note that if we ignore all viscous and resistive terms, then the equations are ideal.

Consider the ratio of the pressure force term and Lorentz force term in the momentum equation, Equation (1.3.18), given by

$$\frac{|\nabla p|}{|\mathbf{j} \times \mathbf{B}|} \approx \frac{p_0}{B_0^2/\mu} = \frac{\beta}{2},$$

where p_0 and B_0 denotes the typical size of their respective quantities. The plasma beta, β , is defined as the ratio of the plasma pressure over the magnetic pressure given by

$$\beta = \frac{p}{B^2/(2\mu)}. \quad (1.3.39)$$

Figure 1.5 shows an estimate of the plasma beta as a function of height in the solar atmosphere. It shows that in the solar corona $\beta \ll 1$. Since this Thesis is primarily concerned with modelling waves in the corona, we will often approximate $\beta = 0$, which allows us to neglect the pressure force in favour of the Lorentz force.

1.3.8 Ideal gas law

For fully ionised Hydrogen plasma the ideal gas law is approximated by

$$p = 2 \frac{k_B}{m_p} \rho T, \quad (1.3.40)$$

where k_B denotes the Boltzmann constant approximated by

$$k_B \approx 1.38 \times 10^{-23} \text{ m}^2 \text{ kg s}^{-2} \text{ K}^{-1}.$$

1.3.9 Internal energy equation

The most general form of the internal energy equation which we use in this thesis is

$$\frac{\partial}{\partial t} \left(\frac{p}{\gamma - 1} \right) + \nabla \cdot \underbrace{\left(\frac{\gamma p}{\gamma - 1} \mathbf{v} + \mathbf{q} \right)}_{\text{Enthalpy flux + Heat flux}} = \underbrace{\frac{j^2}{\sigma}}_{\text{Ohmic}} + \underbrace{\boldsymbol{\sigma}_{Brag} : \nabla \mathbf{v}}_{\text{Viscous heating}} - \underbrace{n^2 Q(T)}_{\text{Radiation}} - \underbrace{\mathbf{v} \cdot \nabla p}_{\text{Work done}}. \quad (1.3.41)$$

The internal energy per unit volume is given by $p/(\gamma - 1)$, where γ is the ratio of specific heats, also known as the adiabatic index.

The conduction term is given by the divergence of the heat flux vector, \mathbf{q} , where

$$\mathbf{q} = -\boldsymbol{\kappa} \nabla T, \quad (1.3.42)$$

where $\boldsymbol{\kappa}$ is the thermal conduction tensor. The divergence of the heat flux may be split into two parts,

$$\nabla \cdot \mathbf{q} = \nabla_{||} \cdot (\kappa_{||} \nabla_{||} T) + \nabla_{\perp} \cdot (\kappa_{\perp} \nabla_{\perp} T), \quad (1.3.43)$$

where $\nabla_{||}$ is given by

$$\nabla_{||} = \hat{\mathbf{B}} (\hat{\mathbf{B}} \cdot \nabla), \quad (1.3.44)$$

and ∇_{\perp} is given by

$$\nabla_{\perp} = \nabla - \nabla_{||}. \quad (1.3.45)$$

The thermal conductivity parallel/perpendicular to the field is denoted with $\kappa_{\parallel}/\kappa_{\perp}$ respectively. In coronal plasma, the conductivity is usually much stronger along the field than it is perpendicular to the field. The parallel conductivity is approximated by

$$\kappa_{\parallel} = 1.8 \times 10^{-10} \frac{T^{5/2}}{\ln \Lambda} \text{ W m}^{-1} \text{ K}^{-1}, \quad (1.3.46)$$

and the ratio $\kappa_{\perp}/\kappa_{\parallel}$, for typical coronal parameters, is approximated by

$$\frac{\kappa_{\perp}}{\kappa_{\parallel}} = 2 \times 10^{-13} \left(\frac{n}{10^{15} \text{ m}^{-3}} \right)^2 \left(\frac{10^6 \text{ K}}{T} \right)^3 \left(\frac{10^{-3} \text{ T}}{B} \right)^2 \quad (1.3.47)$$

(in the strong field limit, where $\omega_{ci}/\nu_i \gg 1$, see Spitzer 1965; Braginskii 1965; Priest 2014). In the corona, the parallel conductivity dominates (except near null points), so we usually neglect the perpendicular conduction.

$Q(T)$ denotes the optically thin radiative loss function. See for example Rosner et al. (1978); Klimchuk et al. (2008); Dere et al. (2009); Priest (2014) for details on the radiative loss function in the solar corona. Klimchuk (2015) (and references therein) shows that the temperature evolution of coronal loops is dependent on the time interval, Δt , between nanoflares/heating events. If the timescale between nanoflares is significantly shorter than the cooling timescale of a loop through conduction and radiation, i.e. $\Delta t \ll \tau_{cool}$, then the temperature evolution can be approximately isothermal. However, if the heating concentrates near the loop footpoints then a loop may be in a state of thermal non-equilibrium, see e.g. Antiochos et al. (2000); Johnston et al. (2019). If the time interval between nanoflares is significantly longer than the cooling timescale, i.e. $\Delta t \gg \tau_{cool}$, then a loop can change in temperature significantly. For simplicity, in this thesis, we will model the plasma as isothermal.

1.3.10 Induction equation

Faraday's law, Equation (1.3.8), can be combined with Ohm's law, Equation (1.3.13), to give the induction equation,

$$\frac{\partial \mathbf{B}}{\partial t} = \underbrace{\nabla \times (\mathbf{v} \times \mathbf{B})}_{\text{Ideal term}} - \underbrace{\nabla \times \left(\frac{\mathbf{j}}{\sigma} + \frac{1}{n_e e} \mathbf{j} \times \mathbf{B} \right)}_{\text{Non-ideal term + Hall term}}. \quad (1.3.48)$$

In Section 1.3.5, we showed that if $B_0/(n_e e) \ll \sigma^{-1}$ or $\mathbf{j}_{||} \gg \mathbf{j}_{\perp}$ then we can neglect the Hall term. Additionally, if we assume that the spatial derivatives of σ can be neglected then by using Ampère's law, Equation (1.3.9) (the induction equation), may be written as

$$\frac{\partial \mathbf{B}}{\partial t} = \underbrace{\nabla \times (\mathbf{v} \times \mathbf{B})}_{\text{Advection term}} + \underbrace{\eta \nabla^2 \mathbf{B}}_{\text{Diffusive term}}, \quad (1.3.49)$$

where η is the magnetic diffusivity, given by

$$\begin{aligned} \eta &= \frac{1}{\mu_0 \sigma} \\ &\approx 2.06 \left(\frac{T}{10^6 \text{ K}} \right)^{-3/2} \text{ m}^2 \text{ s}^{-1}, \end{aligned} \quad (1.3.50)$$

for typical coronal temperatures. The magnetic Reynolds number is defined as

$$R_m = \frac{l_0 V_0}{\eta} \sim \frac{\text{Advection term}}{\text{Diffusive term}}, \quad (1.3.51)$$

where l_0 denotes the typical length scales of the system and V_0 denotes the typical velocity in the system. In the corona, the magnetic Reynolds number can be approximated by

$$R_m \approx 4.86 \times 10^9 \left(\frac{l_0}{10^6 \text{ m}} \right) \left(\frac{V_0}{10^4 \text{ m s}^{-1}} \right) \left(\frac{T_0}{10^6 \text{ K}} \right)^{3/2}. \quad (1.3.52)$$

We usually neglect the diffusive term in the induction equation in favour of the advective term. However, sometimes the length scales can become sufficiently small that we

cannot ignore the diffusion term. Note that our approximation for the coronal velocities uses results from [McIntosh et al. \(2011\)](#); [McIntosh and De Pontieu \(2012\)](#).

For typical values, R_m , given by Equation [\(1.3.52\)](#), is approximately 8 orders of magnitude larger than R_e , given by Equation [\(1.3.38\)](#). This suggests viscous dissipation dominates over resistive. However, this order of magnitude analysis does not consider the fact that gradients perpendicular to the field may be orders of magnitude greater than gradients parallel to the magnetic field. Moreover, there could be significantly more free magnetic energy to dissipate compared with kinetic energy. Note that [Van Doorsselaere et al. \(2007\)](#) uses observations to suggest that resistive heating dominates over viscous.

1.3.11 Total energy equation

Taking the dot product of Equation [\(1.3.18\)](#) with \mathbf{v} gives

$$\rho \frac{\partial}{\partial t} \left(\frac{v^2}{2} \right) + \rho \mathbf{v} \cdot \nabla \left(\frac{1}{2} v^2 \right) = \mathbf{v} \cdot \nabla p + \mathbf{v} \cdot (\mathbf{j} \times \mathbf{B}) - \mathbf{v} \cdot (\rho \nabla \Phi) + \mathbf{v} \cdot \nabla \cdot \boldsymbol{\sigma}_{Brag},$$

where $\rho\Phi = \rho g_{\odot} r$ gives the gravitational potential energy density (assuming the gravitational force is given by Equation [1.3.21](#)). We can simplify this by using the following identity

$$\nabla \cdot (\boldsymbol{\sigma}_{Brag} \mathbf{v}) = \mathbf{v} \cdot \nabla \cdot \boldsymbol{\sigma}_{Brag}^T + \boldsymbol{\sigma}_{Brag} : \mathbf{v},$$

from Equation (1.11.16) of [Kelly \(2020\)](#), where $\boldsymbol{\sigma}_{Brag} : \mathbf{v} = \text{tr}(\boldsymbol{\sigma}_{Brag} \nabla \mathbf{v})$ denotes the double-dot product. Note that $\boldsymbol{\sigma}_{Brag}$ is symmetric, i.e. $\boldsymbol{\sigma}_{Brag} = \boldsymbol{\sigma}_{Brag}^T$. Multiplying Equation [\(1.3.17\)](#) with $v^2/2$ gives

$$\frac{v^2}{2} \frac{\partial \rho}{\partial t} + \frac{v^2}{2} \nabla \cdot (\rho \mathbf{v}) = 0.$$

The time-derivative of the gravitational potential energy density gives

$$\frac{\partial \rho \Phi}{\partial t} = -\Phi \nabla \cdot \rho \mathbf{v}.$$

Combining the above equations gives the equation for the kinetic and gravitational energy,

$$\frac{\partial}{\partial t} \left(\frac{1}{2} \rho v^2 + \rho \Phi \right) + \nabla \cdot \left(\frac{1}{2} \rho v^2 \mathbf{v} + \rho \Phi \mathbf{v} - \boldsymbol{\sigma}_{Brag} \mathbf{v} \right) = -\mathbf{v} \cdot \nabla p + \mathbf{v} \cdot (\mathbf{j} \times \mathbf{B}) - \boldsymbol{\sigma}_{Brag} : \mathbf{v}.$$

Taking the dot product of Equation (1.3.8) with \mathbf{B}/μ gives

$$\begin{aligned} \frac{\partial}{\partial t} \left(\frac{B^2}{2\mu} \right) &= -\frac{\mathbf{B}}{\mu} \cdot \nabla \times \mathbf{E} \\ &= -\nabla \cdot \left(\frac{\mathbf{E} \times \mathbf{B}}{\mu} \right) - \mathbf{E} \cdot \mathbf{j}. \end{aligned}$$

Substituting Equation (1.3.13) gives the equations for the magnetic energy density,

$$\frac{\partial}{\partial t} \left(\frac{B^2}{2\mu} \right) + \nabla \cdot \left(\frac{\mathbf{E} \times \mathbf{B}}{\mu} \right) = -\mathbf{v} \cdot (\mathbf{j} \times \mathbf{B}) - \frac{j^2}{\sigma}.$$

Therefore the rate of change of total energy is given by

$$\frac{\partial}{\partial t} \left(\frac{1}{2} \rho v^2 + \frac{B^2}{2\mu} + \frac{p}{\gamma - 1} + \rho \Phi \right) + \nabla \cdot \mathbf{S} = -n^2 Q(T), \quad (1.3.53)$$

where

$$\mathbf{S} = \frac{1}{2} \rho v^2 \mathbf{v} + \frac{\mathbf{E} \times \mathbf{B}}{\mu} + \frac{\gamma p}{\gamma - 1} \mathbf{v} + \mathbf{q} + \rho \Phi \mathbf{v} - \boldsymbol{\sigma}_{Brag} \mathbf{v}. \quad (1.3.54)$$

1.4 MHD waves: Dispersion relation

Solving the MHD equations is notoriously difficult. Some of the basic properties of the Navier-Stokes equations, which is a subset of the MHD equations, are not known. There is a famous problem known as the Navier-Stokes existence and smoothness problem. The Clay Mathematics Institute in May 2000 made this problem one of its seven Millennium Prize problems in mathematics. It offered a \$1,000,000 prize to the first person to solve the problem. The challenge is to prove or give a counter-example of the following statement:

In three space dimensions and time, given an initial velocity field, there

exists a vector velocity and a scalar pressure field, which are both smooth and globally defined, that solve the Navier–Stokes equations.

Due to the difficulty in solving the MHD equations, solutions are usually calculated numerically. To obtain an analytic solution, we study a simplified plasma. Analytical solutions are useful as a starting point for understanding plasma dynamics. Moreover, parameters can be arbitrary constants which allows a large parameter space to be studied simultaneously. Typically, numerical simulations only calculate the solution for a single set of parameters, and then the simulation has to be restarted for different parameter values.

Given that the corona has a large Reynolds number (see Equations 1.3.38 and 1.3.52) we model the plasma as ideal. Additionally, the plasma beta in the corona is small (see Figure 1.5) so we assume the only force in the momentum equation is the Lorentz force. This gives the momentum equation as

$$\rho \frac{D\mathbf{v}}{Dt} = \frac{1}{\mu} (\nabla \times \mathbf{B}) \times \mathbf{B}, \quad (1.4.1)$$

the induction equation as

$$\frac{\partial \mathbf{B}}{\partial t} = \nabla \times (\mathbf{v} \times \mathbf{B}), \quad (1.4.2)$$

and mass continuity equation as,

$$\frac{\partial \rho}{\partial t} + \nabla \cdot (\rho \mathbf{v}) = 0. \quad (1.3.17)$$

We model small perturbations on a static background equilibrium in other words we assume

$$\mathbf{v}(\mathbf{x}, t) = \mathbf{u}(\mathbf{x}, t), \text{ where } u \ll v_A, \quad (1.4.3)$$

$$\mathbf{B}(\mathbf{x}, t) = \mathbf{B}_0(\mathbf{x}) + \mathbf{b}(\mathbf{x}, t), \text{ where } b \ll B_0, \quad (1.4.4)$$

$$\rho(\mathbf{x}, t) = \rho_0(\mathbf{x}) + \rho_1(\mathbf{x}, t), \text{ where } \rho_1 \ll \rho_0, \quad (1.4.5)$$

where

$$u = |\mathbf{v}|, \quad B_0 = |\mathbf{B}_0|, \quad b = |\mathbf{b}|.$$

Note that \mathbf{B}_0 and ρ_0 are referred to as the background quantities which are specified beforehand and \mathbf{v} , \mathbf{b} and ρ_1 are the perturbed quantities which need to be calculated. We assume $u \ll v_A$ because observations suggest u/v_A to be approximately in the range $[10^{-2}, 10^{-1}]$ (McIntosh et al., 2011; McIntosh and De Pontieu, 2012). We approximate $\partial\mathbf{B}_0/\partial t = 0$ since magnetic structures can last much longer than the typical frequency and Alfvén travel time of waves in a coronal loop. If we take the Alfvén speed in the corona as about 1 Mm s^{-1} and assume that coronal loops have a characteristic length of about 100 Mm (O'Neill and Li, 2005) then this gives an Alfvén travel time of about 100 s . Magnetic structures can last much longer than this, for example, active region prominences can last a few hours or a day, while quiescent prominences can last between a few and 300 days (Priest, 2014). We assume that $\partial\rho_0/\partial t = 0$ and this approximately holds in coronal loops which are isothermal and isobaric. Klimchuk (2015) shows that loops can be approximated as isothermal if the time interval between heating events/nanoflares in the loops is sufficiently small.

The final assumption we make, in this section, is to assume the background quantities are uniform, primarily because this allows the equations to be solved analytically more easily. Without loss of generality, we can model the background magnetic field as being directed in the z -direction, i.e.

$$\mathbf{B}_0 = B_0 \hat{\mathbf{z}}. \tag{1.4.6}$$

With these assumptions in place we can simplify Equation (1.4.1) and (1.4.2) via a linearization procedure. This is where we neglect terms involving the product of small terms i.e. \mathbf{u} , \mathbf{b} or ρ_1 and neglect the time-derivatives of the background terms \mathbf{B}_0 , ρ_0 . The momentum equation reduces to

$$\begin{aligned} \frac{\partial \mathbf{u}}{\partial t} &= \frac{1}{\mu\rho_0} (\nabla \times \mathbf{b}) \times \mathbf{B}_0 \\ &= \frac{B_0}{\mu\rho_0} \left[(\mathbf{B}_0 \cdot \nabla) \mathbf{b} - \nabla \left(\frac{\mathbf{b} \cdot \mathbf{B}_0}{2\mu} \right) \right]. \end{aligned} \tag{1.4.7}$$

The induction equation simplifies to

$$\begin{aligned}\frac{\partial \mathbf{b}}{\partial t} &= \nabla \times (\mathbf{u} \times \mathbf{B}_0) \\ &= (\mathbf{B}_0 \cdot \nabla) \mathbf{u} - \mathbf{B}_0 \nabla \cdot \mathbf{u},\end{aligned}\tag{1.4.8}$$

and the mass continuity equation is given by

$$\frac{\partial \rho_1}{\partial t} + \nabla \cdot (\rho_0 \mathbf{v}) = 0.\tag{1.4.9}$$

Note that \mathbf{u} and \mathbf{b} are independent of ρ_1 and so we only need to solve for \mathbf{u} and \mathbf{b} . Written out component-wise the above equations become

$$\frac{\partial u_x}{\partial t} = v_{A0}^2 \left[\frac{\partial \hat{b}_x}{\partial z} - \frac{\partial \hat{b}_z}{\partial x} \right],\tag{1.4.10}$$

$$\frac{\partial u_y}{\partial t} = v_{A0}^2 \left[\frac{\partial \hat{b}_y}{\partial z} - \frac{\partial \hat{b}_z}{\partial y} \right],\tag{1.4.11}$$

$$\frac{\partial \hat{b}_x}{\partial t} = \frac{\partial u_x}{\partial z},\tag{1.4.12}$$

$$\frac{\partial \hat{b}_y}{\partial t} = \frac{\partial u_y}{\partial z},\tag{1.4.13}$$

$$\frac{\partial \hat{b}_z}{\partial t} = - \left[\frac{\partial u_x}{\partial x} + \frac{\partial u_y}{\partial y} \right],\tag{1.4.14}$$

where

$$\hat{\mathbf{b}} = \frac{\mathbf{b}}{B_0} = (\hat{b}_x, \hat{b}_y, \hat{b}_z),\tag{1.4.15}$$

$$v_{A0} = \frac{B_0}{\sqrt{\mu \rho_0}}.\tag{1.4.16}$$

Since the Lorentz force is perpendicular to the background field, u_z , is decoupled and can be treated separately. We can eliminate \hat{b}_x and \hat{b}_y from the above equations to give

$$\left(\frac{\partial^2}{\partial t^2} - v_{A0}^2 \frac{\partial^2}{\partial z^2} \right) u_x = -v_{A0}^2 \frac{\partial^2 \hat{b}_z}{\partial x \partial t},\tag{1.4.17}$$

$$\left(\frac{\partial^2}{\partial t^2} - v_{A0}^2 \frac{\partial^2}{\partial z^2} \right) u_y = -v_{A0}^2 \frac{\partial^2 \hat{b}_z}{\partial y \partial t}. \quad (1.4.18)$$

Eliminating \hat{b}_z gives

$$\left[\frac{\partial^2}{\partial t^2} - v_{A0}^2 \left(\frac{\partial^2}{\partial x^2} + \frac{\partial^2}{\partial z^2} \right) \right] u_x = v_{A0}^2 \frac{\partial^2 u_y}{\partial x \partial y}, \quad (1.4.19)$$

$$\left[\frac{\partial^2}{\partial t^2} - v_{A0}^2 \left(\frac{\partial^2}{\partial y^2} + \frac{\partial^2}{\partial z^2} \right) \right] u_y = v_{A0}^2 \frac{\partial^2 u_x}{\partial x \partial y}. \quad (1.4.20)$$

Eliminating u_y gives

$$\left[\frac{\partial^2}{\partial t^2} - v_{A0}^2 \left(\frac{\partial^2}{\partial y^2} + \frac{\partial^2}{\partial z^2} \right) \right] \left[\frac{\partial^2}{\partial t^2} - v_{A0}^2 \left(\frac{\partial^2}{\partial x^2} + \frac{\partial^2}{\partial z^2} \right) \right] u_x = v_{A0}^4 \frac{\partial^4 u_x}{\partial x^2 \partial y^2},$$

$$\begin{aligned} & \Rightarrow \left[\frac{\partial^2}{\partial t^2} - v_{A0}^2 \frac{\partial^2}{\partial z^2} \right] \left[\frac{\partial^2}{\partial t^2} - v_{A0}^2 \left(\frac{\partial^2}{\partial x^2} + \frac{\partial^2}{\partial z^2} \right) \right] u_x = \\ & v_{A0}^2 \frac{\partial^2}{\partial y^2} \left\{ v_{A0}^2 \frac{\partial^2}{\partial x^2} + \left[\frac{\partial^2}{\partial t^2} - v_{A0}^2 \left(\frac{\partial^2}{\partial x^2} + \frac{\partial^2}{\partial z^2} \right) \right] \right\} u_x, \end{aligned}$$

hence

$$\Rightarrow \left[\frac{\partial^2}{\partial t^2} - v_{A0}^2 \frac{\partial^2}{\partial z^2} \right] \left[\frac{\partial^2}{\partial t^2} - v_{A0}^2 \left(\frac{\partial^2}{\partial x^2} + \frac{\partial^2}{\partial y^2} + \frac{\partial^2}{\partial z^2} \right) \right] u_x = 0. \quad (1.4.21)$$

Since all the coefficients are constant, we can use Fourier analysis to calculate an analytic solution which satisfies the above equation. We assume u_x is of the form

$$u_x = u_{x0} \exp[i(k_x x + k_y y + k_z z + \omega_n t)],$$

where k_x, k_y, k_z and $\omega_n \in \mathbb{C}$. This reduces our PDE to the following algebraic equation

$$[\omega_n^2 - v_{A0}^2 k_z^2][\omega_n^2 - v_{A0}^2 (k_x^2 + k_y^2 + k_z^2)] = 0. \quad (1.4.22)$$

The above dispersion equation shows that four types of solution can exist. The solutions are given by

$$\omega_1 = v_{A0} k_z,$$

$$\begin{aligned}\omega_2 &= -v_{A0}k_z, \\ \omega_3 &= v_{A0}\sqrt{k_x^2 + k_y^2 + k_z^2}, \\ \omega_4 &= -v_{A0}\sqrt{k_x^2 + k_y^2 + k_z^2}.\end{aligned}$$

Solutions where $\omega = \omega_1$ or ω_2 are called Alfvén wave solutions and solutions where $\omega = \omega_3$ or ω_4 are fast wave solutions. The next two subsections go into further detail about each wave, respectively.

For now, we calculate the solution for the case where the perturbed quantities, u_x , u_y , \hat{b}_x , \hat{b}_y and \hat{b}_z have an x , y , z and t dependence of the form

$$f(x, y, z, t) = f_0 \exp[i(k_x x + k_y y + k_z z + \omega_n t)],$$

where

$$\omega = \pm v_{A0}k_z.$$

Let u_{x0} be fixed, from Equation (1.4.20) we know that

$$u_{y0} = \frac{v_{A0}^2 k_x k_y}{\omega^2 - v_{A0}^2 (k_y^2 + k_z^2)} u_{x0}. \quad (1.4.23)$$

From Equations (1.4.12) and (1.4.13) we know that

$$\hat{b}_{x0} = \frac{k_z}{\omega} u_{x0}, \quad (1.4.24)$$

$$\hat{b}_{y0} = \frac{k_z}{\omega} u_{y0}. \quad (1.4.25)$$

From Equation (1.4.17) we know that

$$\hat{b}_z = -\frac{\omega^2 - v_{A0}^2 k_z^2}{k_x \omega} u_{x0}. \quad (1.4.26)$$

1.4.1 Alfvén waves

We define Alfvén waves (Alfvén, 1942) as waves with a velocity amplitude, \mathbf{u} , which satisfy the Alfvén wave equation, which is given by

$$\mathcal{L}\mathbf{u} = \left(\frac{\partial^2}{\partial t^2} - \frac{1}{\mu\rho} (\mathbf{B}_0 \cdot \nabla)^2 \right) \mathbf{u} = 0, \quad (1.4.27)$$

(see e.g. Prokopszyn et al. 2019) where \mathcal{L} denotes the Alfvén wave equation operator and \mathbf{B}_0 denotes the background magnetic field. This shows that Alfvén waves propagate parallel to the background magnetic field with speed given by the Alfvén speed. Note that for our configuration above the Alfvén wave equation operator, \mathcal{L} , becomes

$$\mathcal{L} = \frac{\partial^2}{\partial t^2} - v_{A0}^2 \frac{\partial^2}{\partial z^2}. \quad (1.4.28)$$

Equations (1.4.17) and (1.4.18) show that if $\mathcal{L}u_x = \mathcal{L}u_y = 0$ then $b_z = b_z(z)$. Therefore, applying the initial condition that b_z is initially zero ensures $b_z = 0 \ \forall t$. Note that b_z gives the perturbation in magnetic pressure. For this reason, Alfvén waves can be thought of as an oscillation in kinetic and magnetic tension energy. Very much like waves on a guitar string but with magnetic tension replaced with tension in the string.

Note that if $\omega = \pm k_z v_A$ then Equations (1.4.23)-(1.4.26) simplify to

$$u_{y0} = -\frac{k_x}{k_y} u_{x0}, \quad (1.4.29)$$

$$\hat{b}_{x0} = \pm \frac{u_{x0}}{v_{A0}}, \quad (1.4.30)$$

$$\hat{b}_{y0} = \pm \frac{u_{y0}}{v_{A0}}, \quad (1.4.31)$$

$$\hat{b}_{z0} = 0. \quad (1.4.32)$$

This shows that the magnetic pressure perturbation is zero and so all the energy is contained within the magnetic tension.

It is also worth noting that our Alfvén wave is invariant in the \mathbf{u} -direction, in other

words,

$$\begin{aligned}\nabla \cdot \mathbf{u} &= i(u_x k_x + u_y k_y) \\ &= 0 \text{ (using Equation 1.4.29).}\end{aligned}\tag{1.4.33}$$

This means the Alfvén wave is incompressible.

1.4.2 Fast waves

We define fast waves in $\beta = 0$ plasma as waves with velocity amplitude, \mathbf{u} , which satisfy the classical wave equation,

$$\left(\frac{\partial^2}{\partial t^2} + v_A^2 \nabla^2 \right) \mathbf{u} = 0.\tag{1.4.34}$$

This shows that fast waves propagate isotropically with a speed given by the Alfvén speed. Note that this is only valid for $\beta = 0$ plasma, for $\beta \ll 1$ then the fast wave propagates perpendicular to the field at a speed of approximately $v_A + c_s$, where c_s gives the background sound speed. In the limit where the fast wave propagates parallel to the field, it degenerates into an Alfvén wave and moves at a speed of v_A . For a derivation of the dispersion relation of fast waves (and its sibling slow waves) in a $\beta > 0$ plasma, see for example [Priest \(2014\)](#); [Roberts \(2019\)](#).

Note that if $\omega = \pm v_{A0} \sqrt{k_x^2 + k_y^2 + k_z^2}$, then Equations (1.4.23)-(1.4.26) simplify to

$$u_{y0} = \frac{k_y}{k_x} u_{x0},\tag{1.4.35}$$

$$\hat{b}_{x0} = \pm \frac{k_z}{\sqrt{k_x^2 + k_y^2 + k_z^2}} \frac{u_{x0}}{v_{A0}},\tag{1.4.36}$$

$$\hat{b}_{y0} = \pm \frac{k_z}{\sqrt{k_x^2 + k_y^2 + k_z^2}} \frac{u_{y0}}{v_{A0}},\tag{1.4.37}$$

$$\hat{b}_{z0} = \mp \frac{k_x^2 + k_y^2}{k_x \sqrt{k_x^2 + k_y^2 + k_z^2}} \frac{u_{x0}}{v_{A0}},\tag{1.4.38}$$

The above equation shows that, unlike Alfvén waves, the magnetic pressure perturbation, b_z , is in general non-zero. Fast waves are oscillations in kinetic and magnetic energy, where the restoring force can be magnetic tension and the magnetic pressure.

More generally, in a $\beta > 0$ plasma, the plasma pressure also acts as a restoring force and contributes towards the energy associated with the fast wave.

The fast wave is compressible, however, it is invariant in the $\hat{\mathbf{B}}_0 \times \mathbf{u}$, direction, in other words,

$$\begin{aligned} (\hat{\mathbf{z}} \times \mathbf{u}) \cdot \nabla &= (-u_y \hat{\mathbf{x}} + u_x \hat{\mathbf{y}}) \cdot \nabla \\ &= i(-u_y k_x + u_x k_y) \\ &= 0 \text{ (using Equation (1.4.35))}. \end{aligned} \tag{1.4.39}$$

In the last section we showed that the Alfvén waves are invariant in the \mathbf{u} direction. Therefore, there is always at least one invariant direction for both our fast and Alfvén waves.

1.4.3 Poynting flux

The Poynting flux, \mathbf{S} is given by

$$\begin{aligned} \mathbf{S} &= \frac{\mathbf{E} \times \mathbf{b}}{\mu} \\ &= \frac{1}{\mu} [(\mathbf{B}_0 \cdot \mathbf{b}) \mathbf{u} - (\mathbf{u} \cdot \mathbf{b}) \mathbf{B}_0]. \end{aligned} \tag{1.4.40}$$

where \mathbf{E} denotes the electric field and we approximate it by linearizing Ohm's law (Equation (1.3.13)) and assuming ideal MHD to give

$$\mathbf{E} = -\mathbf{u} \times \mathbf{B}_0. \tag{1.4.41}$$

\mathbf{S} gives the directional energy flux, to see this consider the following. Taking the dot product of Equation (1.4.7) with $\rho_0 \mathbf{u}$ gives

$$\frac{\partial}{\partial t} \left(\frac{1}{2} \rho_0 u^2 \right) = \frac{1}{\mu} \mathbf{u} \cdot [(\mathbf{B}_0 \cdot \nabla) \mathbf{b} - \nabla(\mathbf{B}_0 \cdot \mathbf{b})].$$

Taking the dot product of Equation (1.4.2) with \mathbf{b} gives

$$\frac{\partial}{\partial t} \left(\frac{b^2}{2\mu} \right) = \frac{1}{\mu} \mathbf{b} \cdot [(\mathbf{B}_0 \cdot \nabla) \mathbf{u} - \mathbf{B}_0(\nabla \cdot \mathbf{u})].$$

Note that

$$\frac{\partial}{\partial t} \left(\frac{1}{2} \rho_0 u^2 + \frac{b^2}{2\mu} \right) = -\frac{1}{\mu} \nabla \cdot [(\mathbf{B}_0 \cdot \mathbf{b}) \mathbf{u} - (\mathbf{u} \cdot \mathbf{b}) \mathbf{B}_0],$$

Hence, the energy equation is given by

$$\frac{\partial}{\partial t} \left(\frac{1}{2} \rho u^2 + \frac{b^2}{2\mu} \right) + \nabla \cdot \mathbf{S} = 0. \quad (1.4.42)$$

This confirms that \mathbf{S} does indeed give the energy flux for the magnetic and kinetic energy. For Alfvén waves, the magnetic pressure perturbation is zero. Therefore, the Poynting flux points along the magnetic field (see Equation (1.4.40)).

1.5 MHD waves: power spectrum

MHD waves are ubiquitous and have been observed in for example Tomczyk et al. (2007); McIntosh et al. (2011); De Moortel and Nakariakov (2012). These observations are useful for constraining theoretical models and may help answer unsolved problems such as the coronal heating problem. Measurements of the waves' amplitude and wavelength could play an important role in deciding whether MHD waves play an essential or negligible role in coronal heating. Note that the Ohmic and viscous heat provided by MHD waves typically increases with larger wave amplitudes and shorter wavelengths. A power spectrum can represent the wave amplitude and frequency. This section aims to give a brief overview of the power spectrum of velocity fluctuations in the corona and explain how we calculate it.

In for example Morton et al. (2016, 2019), the power spectrum of velocity fluctuations in the solar corona is calculated. They produce a time sequence, $\{v_n\}$, of the Doppler velocities on the limb of the corona using data from the Coronal Multi-channel Polarimeter (CoMP). CoMP only has a finite cadence and they can only observe the fluctuations for a finite time. Therefore, the observed velocities, $\{v_n\}$, can only be measured at a finite discrete sequence of times $\{t_n\}$. If N measurements are made, i.e.

$$\{v_n\} = v_0, v_1, \dots v_{N-1},$$

then we can write

$$\begin{aligned} v_n &= \frac{1}{N} \sum_{k=0}^{N-1} V_k \exp(2i\pi kn/N) \\ &= \frac{1}{N} \sum_{k=0}^{N-1} V_k \exp(2i\pi f_k t_n), \end{aligned}$$

where

$$t_n = n\Delta t,$$

$$f_k = \frac{k}{N\Delta t},$$

and $\{V_k\}$ is the discrete Fourier transform of $\{v_n\}$, given by

$$\begin{aligned} V_k &= \sum_{n=0}^{N-1} v_n \exp(-2i\pi kn/N) \\ &= \sum_{n=0}^{N-1} v_n \exp(-2i\pi f_k t_n). \end{aligned}$$

Note that a measure of the average energy associated with the velocity fluctuations is given by

$$\langle v^2 \rangle = \frac{1}{N} \sum_{n=0}^{N-1} v_n^2. \quad (1.5.1)$$

By the Plancheral theorem

$$\langle v^2 \rangle = \frac{1}{N^2} \sum_{k=0}^{N-1} |V_k|^2. \quad (1.5.2)$$

Therefore, $|V_k|^2/N^2$ gives a useful measure of the average energy associated with each frequency, f_k , for the signal, $\{v_n\}$. Note that $|V_k|$ is Hermitian-symmetric because $\{v_n\}$ is strictly real, i.e.

$$V_k = \bar{V}_{N-k}, \quad \text{for } 1 \leq k \leq N-1, \quad (1.5.3)$$

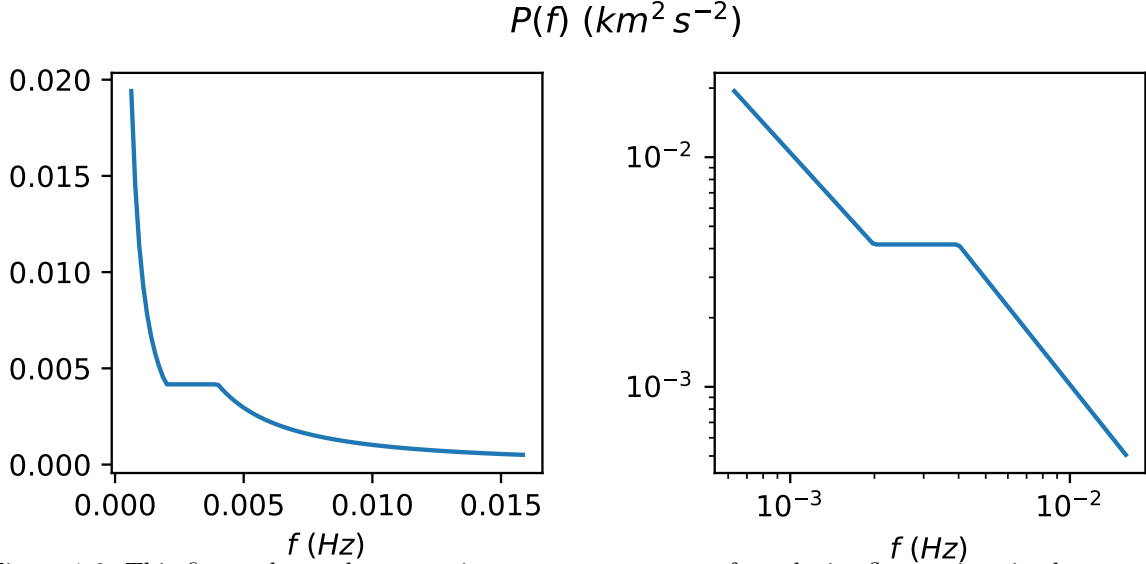


Figure 1.6: This figure shows the approximate power spectrum for velocity fluctuations in the corona using data from [Morton et al. \(2016\)](#) and an approximation used in [Pagano and De Moortel \(2019\)](#). The left-hand side uses a linear axis while the right-hand side uses a log-log axis. The code used to make this figure is available on GitHub in the following directory:

[→ Python/Introduction/power_spectrum.py](#)

where \bar{V}_{N-k} denotes the complex conjugate and $\lfloor \cdot \rfloor$ denotes the floor function which rounds down to the nearest integer. Therefore, we define the power spectrum, $P_k[\{v_n\}]$, as

$$P_k[\{v_n\}] = \frac{1}{N^2} \begin{cases} |V_0|^2, & \text{for } k = 0, \\ |V_k|^2, & \text{for } k = N/2 \text{ and } N \text{ even}, \\ 2|V_k|^2, & \text{otherwise,} \end{cases} \quad (1.5.4)$$

where $k = 0, 1, \dots, \lfloor N/2 \rfloor$. This ensures that $P_k[\{v_n\}]$ satisfies

$$\langle v^2 \rangle = \sum_{k=0}^{\lfloor N/2 \rfloor} P_k[\{v_n\}]. \quad (1.5.5)$$

To plot the average power spectrum, $P(f) = P_k[\{v_n\}]$, we will use an approximation given in [Pagano and De Moortel \(2019\)](#) which uses data from [Morton et al. \(2016\)](#). They

state that the power spectrum in $\text{km}^2 \text{s}^{-2}$ can be approximated as

$$P(f) = \begin{cases} 10^{-6} f^{-1.34}, & 10^{-3.2} \leq f \leq 10^{-2.7}, \\ 10^{-2.38}, & 10^{-2.7} \leq f \leq 10^{-2.4}, \\ 10^{-6.05} f^{-1.53}, & 10^{-2.4} \leq f \leq 10^{-1.8}, \end{cases} \quad (1.5.6)$$

where the frequency is measured in Hz. Note that the dimensions of $P(f)$ are somewhat meaningless without knowledge of the number of points used, however, for now, we are only interested in the shape of the power spectrum. [McIntosh et al. \(2011\)](#); [McIntosh and De Pontieu \(2012\)](#) measured the average amplitude of velocity fluctuations in the corona. They show that observed amplitudes are of the order 10 km s^{-1} . $P(f)$ is plotted in Figure 1.6. We can only plot the power spectrum for a finite range of frequencies because the equipment's cadence is limited. Moreover, we can only observe features for about half a solar rotation before moving out of view. Here the frequency range is $10^{-3.2} \text{ Hz} \leq f \leq 10^{-1.8} \text{ Hz}$. [Podesta et al. \(2007\)](#) is able to observe higher frequency waves in the solar wind.

1.6 Outline of the thesis

This thesis aims to improve our understanding of the dynamics of MHD waves in the solar atmosphere by using models which are complex enough to build our intuition and simple enough to easily be comprehended. In Chapter 2 we study the simplest type of MHD wave, namely, Alfvén waves. These are waves with a velocity amplitude which satisfies the Alfvén wave equation (Equation 1.4.27). Our goal is to introduce some of the key concepts relevant to the rest of the thesis. We calculate the solutions for the case where we impose a footpoint driver as a boundary condition. We aim to calculate the solution for when the driver is sinusoidal and a white/red noise force. After that, we extend the model by allowing waves to leak out of the corona.

In Chapter 3 our goal is to assess the viability of a process called phase mixing as a heating mechanism. We study linear Alfvén waves with resistivity and viscosity included in the model with the y -direction assumed invariant. We show that if neighbouring field lines have different natural frequencies, this can lead to the formation of steep gradients across the field via phase mixing. To test if this is a viable heating mechanism, we

introduce a quantity called the heating rate per unit of wave energy which we denote with γ . We estimate the required heating rate by assuming it must balance our estimates of the coronal conductive and radiative losses. We also use observational data of velocity fluctuations to estimate the average wave energy in the corona. Using these values, we calculate that γ needs to equal about 10^{-1} s^{-1} for a wave heating mechanism to play a major role in coronal heating. We calculate a theoretical upper bound for γ and use this to test if the dissipation of phase-mixed Alfvén wave is a viable heating mechanism. Our model also includes partial reflection and allows for a power spectrum of harmonics to be excited.

Chapter 4 allows for $\partial/\partial y \neq 0$. This enables a phenomenon called resonant absorption to occur. This is where a propagating fast wave with a given frequency gets absorbed by a magnetic field line, called the resonant field line, with the same natural Alfvén frequency. Energy concentrates at the resonant field line and the waves form a standing Alfvén wave. We model the magnetic field to be at an arbitrary angle, α , to the transition region. In for example, [Halberstadt and Goedbloed \(1993, 1995\)](#); [Arregui et al. \(2003\)](#), they show that in general, steep boundary layers/evanescent fast waves form. However, their model only includes the corona, and they impose line-tied boundary conditions. This chapter includes the chromosphere and corona and tests if the boundary layers still form if we do not impose line-tied boundary conditions. This allows us to test if the boundary layers are physical or fictitious artefacts generated by using line-tied boundary conditions.

Finally, in Chapter 5 a summary of results from each of the chapters is given, and we discuss ideas for further study.

Chapter 2

Ideal footpoint driven Alfvén waves

2.1 Introduction

Before we can discuss the results from our more technical research in Chapters 3 and 4 we need to first understand the dynamics of waves in a more simple domain. This chapter models footpoint driven linear Alfvén waves in a uniform domain to establish some of the key ideas we will use throughout this thesis. We will see in Chapter 3 that if an invariant direction is assumed, in this case, $\partial/\partial y = 0$, then the velocity perturbations in the invariant direction (in this case, v_y), must satisfy the Alfvén wave equation. Chapter 4 shows that propagating fast waves with a given frequency will mode convert at a field line with the same natural frequency to form standing Alfvén waves. This phenomenon is called resonant absorption. Moreover, a similar effect was demonstrated in more general three-dimensional domains (see for example, [Wright and Elsden 2016](#); [Elsden and Wright 2017, 2018](#)). This suggests that Alfvén waves and approximate Alfvén waves are ubiquitous throughout the solar atmosphere.

The outline of this chapter is as follows. In Section 2.2 we introduce the model we use and discuss the assumptions we will make. In Sections 2.3-2.4 we calculate the solution for a closed loop with a footpoint driver. We show how a footpoint driver can excite resonances along the loop. We will calculate the solutions for the case where the driver is sinusoidal and excites resonant frequencies, nearly resonant frequencies and frequencies halfway in between different resonant frequencies. After that, in Section 2.5, we will study the solution when we use a noisy driver. We think of a noisy driver

as a superposition of an infinite number of sinusoidal drivers. We use a white and red noise force driver where the slope of its power spectrum defines the colour of the noise, and this is explained further in Section 2.5. One of the goals in this section is to determine if the energy of a randomly driven loop will grow to infinity or oscillate about a finite value. In Section 2.6-2.8 we consider the case where waves can leak out of the loop. To estimate the reflection coefficient at the transition region, we approximate the corona and chromosphere using a similar model to that used in Hollweg (1984b). In Section 2.8, we show that leakage prevents the energy from growing to infinity, even if a natural frequency is excited. We show that the system tends towards a state where the whole system oscillates at the driver frequency, called the steady-state solution. Finally, Section 2.9 introduces phase mixing to show some of the key results which are used in Chapter 3.

2.2 Model and equations

In this chapter, we will model perturbations on a background medium. We will make the same assumption as described by Equations (1.4.3)-(1.4.5), namely, that we will model linear perturbations on a static background medium. We assume the velocity amplitude satisfies the Alfvén wave equation, see Equation (1.4.27). We model the domain as ideal, which means we neglect resistivity and viscosity. As in Section 1.4 we will model the background quantities as uniform. In reality, the coronal field is non-uniform, and the density is stratified due to gravity. The propagation of Alfvén waves through a divergent and stratified coronal structure is investigated in, for example, Smith et al. (2007). The effects of loop curvature on coronal kink oscillations are investigated in, for example, van Doorsselaere et al. (2009). In the next chapter, we will study waves in a domain where the background density has a transverse density profile. Modelling the background quantities as uniform means the background field must be straight. Without loss of generality, we model the background field, \mathbf{B}_0 , as

$$\mathbf{B}_0 = B_0 \hat{\mathbf{z}}. \tag{1.4.6}$$

In Section 1.4 we showed that with these assumptions and assuming $\beta = 0$, two types of solutions exist, namely fast and Alfvén waves. In this chapter we choose only

to investigate Alfvén waves, i.e. waves with a velocity amplitude \mathbf{u} which satisfies

$$\mathcal{L}\mathbf{u} = \left(\frac{\partial^2}{\partial t^2} + v_{A0}^2 \frac{\partial^2}{\partial z^2} \right) \mathbf{u} = 0, \quad (2.2.1)$$

where \mathcal{L} is given by Equation (1.4.28). Let

$$\mathbf{u}(z, t) = u(z, t)\hat{\mathbf{y}}, \quad (2.2.2)$$

$$\mathbf{b}(z, t) = b(z, t)\hat{\mathbf{y}}. \quad (2.2.3)$$

We choose our domain to be given by

$$z \in [-l_z, l_z],$$

where

$$L_z = 2l_z,$$

gives the length of the loop. To begin with, we impose line-tied boundary conditions at the ends of the loop, i.e.

$$u(-l_z, t) = f_{driv}(t), \quad u(l_z, t) = 0, \quad (2.2.4)$$

however, in Section 2.7 we consider a partially confined loop. Additionally, we impose the following initial condition

$$u(z, 0) = 0, \quad \left. \frac{\partial u}{\partial t} \right|_{t=0} = 0, \quad \text{for } z \neq -l_z \quad (2.2.5)$$

Without loss of generality, we impose the driver at only the bottom boundary. We do not lose generality because the system is linear and is symmetric about $z = 0$. Therefore, we can construct a general solution by superimposing solutions with the driver imposed at only one of the boundaries. We impose zero velocity at $z = l_z$; in other words, we impose line-tied boundary conditions. The chromosphere and photosphere are orders of magnitude denser than the corona (see Figure 1.3) over a length scale of just a few Mm, this means that the amplitude of waves propagating from the corona

to the chromosphere and photosphere typically reduces significantly. Line-tied ($\mathbf{u} = 0$) boundary conditions are convenient to simulate this behaviour. We approximate the transmission and reflection coefficients in Section 2.6.

2.3 Closed loop: general solution

In this section, we will construct the general solution to Equation (2.2.1) with boundary and initial conditions described by Equation (2.2.4) and (2.2.5). We will construct this solution step-by step via a method of images approach. By d'Alembert's formula we can write solutions to the 1D wave equation, Equation (2.2.1), as

$$u(z, t) = F\left(t - \frac{z}{v_{A0}}\right) + G\left(t + \frac{z}{v_{A0}}\right). \quad (2.3.1)$$

Although this section aims to calculate the solution for a closed loop we find that it is convenient to first consider the solution in an open loop. For now, we impose the condition that only waves propagating in the positive z direction can exist. Hence, a valid solution is nearly given by

$$u(z, t) = f_{driv}\left(t - \frac{z + l_z}{v_{A0}}\right).$$

however, this does not satisfy our initial condition. We need u and $\partial u / \partial t$ to be initially equal to zero for $z > -l_z$. A solution which satisfies the initial condition is given by

$$u(z, t) = f_{driv}\left(t - \frac{z + l_z}{v_{A0}}\right)H\left(t - \frac{z + l_z}{v_{A0}}\right),$$

where $H(x)$ is the Heaviside step function.

Note that the line-tied boundary condition, $u(l_z, t)$, causes any waves propagating in the positive z -direction to reflect at $z = l_z$. We can simulate this reflection by allowing the real wave to leave the domain and introducing a ‘ghost’ wave that propagates in the negative z -direction. The superposition of the domain wave and ‘ghost’ wave cancels to give zero. This ghost wave needs to propagate in the negative z -direction and needs to start at coordinate $z = 3l_z$ so at time $t = 2l_z/v_{A0}$ it cancels with the real wave at

$z = l_z$ to give the reflection. Therefore, a solution which reflects at $z = l_z$ is given by

$$u(z, t) = f_{driv} \left(t - \frac{z + l_z}{v_{A0}} \right) H \left(t - \frac{z + l_z}{v_{A0}} \right) - f_{driv} \left(t + \frac{z - 3l_z}{v_{A0}} \right) H \left(t + \frac{z - 3l_z}{v_{A0}} \right).$$

Unfortunately, this solution does not in general satisfy $u(-l_z, t) = f_{driv}(t)$. We need waves propagating in the negative z -direction to reflect at the $z = -l_z$ boundary. We need waves to reflect back and forth forever between $z = -l_z$ and $z = l_z$. This means we need an infinite number of ‘ghost’ waves to simulate reflection, an infinite number of times. A solution which satisfies this condition is given by

$$u(z, t) = \sum_{k=0}^{\infty} (-1)^k H(\theta_k) f_{driv}(\theta_k), \quad (2.3.2)$$

where

$$\theta_k = t - (-1)^k \frac{z}{v_{A0}} - \frac{(2k+1)l}{v_{A0}}. \quad (2.3.3)$$

This equation is a valid solution to our problem. However, we can simplify it further. Note that the k 'th term in the series only enters the domain after k reflections have occurred. Therefore, if t is finite, only a limited number of terms in the series are needed. Note that each reflection occurs at times

$$t = \frac{nL_z}{v_{A0}}, \quad (2.3.4)$$

where $n \in \mathbb{N}$. Therefore, at time t the number of reflections which have occurred, m , is given by

$$m = \left\lfloor \frac{tv_{A0}}{L_z} \right\rfloor, \quad (2.3.5)$$

where $\lfloor \cdot \rfloor$ denotes the floor function which rounds the input down to the nearest integer.

Hence, we can simplify Equation (2.3.2) to give

$$\begin{aligned} u(z, t) &= \sum_{k=0}^m (-1)^k H(\theta_k) f_{driv}(\theta_k) \\ &= \sum_{k=0}^{m-1} (-1)^k f_{driv}(\theta_k) + (-1)^m H(\theta_m) f_{driv}(\theta_m). \end{aligned} \quad (2.3.6)$$

To see more clearly that Equation (2.3.6) is indeed a valid solution satisfying our boundary conditions consider the following. We know that each term satisfies the wave equation as they are of the form given by d'Alembert's formula. We can check u does indeed equal 0 at $z = l_z$ and $u = f_{driv}(t)$ at the $z = -l_z$ either numerically or analytically.

2.4 Closed loop: sinusoidal solution

Equation (2.3.6) gives the solution for a general driver, f_{driv} . In this section, we investigate the solution for the case where

$$f_{driv}(t) = u_0 \exp(i\omega t). \quad (2.4.1)$$

Substituting Equation (2.4.1) into Equation (2.3.6) gives

$$u(z, t) = u_0 \sum_{k=0}^m (-1)^k H(\theta_k) \exp(i\omega\theta_k). \quad (2.4.2)$$

From Equation (1.4.13) we can infer that

$$i\omega b = B_0 \frac{\partial u}{\partial z}. \quad (2.4.3)$$

Note that

$$\frac{\partial \theta_k}{\partial z} = -\frac{(-1)^k}{v_{A0}},$$

therefore, substituting Equation (2.4.2) into Equation (2.4.3) gives

$$b = -\frac{B_0 u_0}{v_{A0}} \sum_{k=0}^m H(\theta_k) \exp(i\omega\theta_k). \quad (2.4.4)$$

The equations above describe the solution for all z and t . Section 2.4.1 uses the geometric series formula to simplify the above series. We see that the time evolution can vary significantly depending on the driver frequency, ω .

2.4.1 Solution at $z = 0$

Note that the wave-front reaches $z = 0$ at times

$$t = \left(n + \frac{1}{2}\right) \frac{L_z}{v_{A0}}, \quad (2.4.5)$$

for $n \in \mathbb{N}$. Therefore, the number of times the wave-front has reached $z = 0$ is given by $m' + 1$ where

$$m' = \left\lfloor \frac{tv_{A0}}{L_z} - \frac{1}{2} \right\rfloor. \quad (2.4.6)$$

Hence,

$$\begin{aligned} u(0, t) &= u_0 \sum_{k=0}^{m'} (-1)^k \exp(i\omega\theta_k) \\ &= u_0 \exp[i\omega(t - l_z/v_{A0})] \sum_{k=0}^{m'} (-1)^k \exp(-2ik\omega l_z/v_{A0}). \end{aligned} \quad (2.4.7)$$

Let

$$r = \exp(-2i\omega l_z/v_{A0}). \quad (2.4.8)$$

Therefore, for $r \neq -1$, using the formula for the geometric series, the above series can be simplified as

$$\begin{aligned} u(0, t) &= u_0 \exp[i\omega(t - l_z/v_{A0})] \sum_{k=0}^{m'} (-r)^k \\ &= u_0 \exp[i\omega(t - l_z/v_{A0})] \frac{1 - (-r)^{m'+1}}{1 + r}. \end{aligned} \quad (2.4.9)$$

If $r = -1$ then

$$u(0, t) = u_0 \exp[i\omega(t - l_z/v_{A0})](m' + 1). \quad (2.4.10)$$

Hence, for $r \neq 1$

$$\begin{aligned} b(0, t) &= -\frac{B_0 u_0}{v_{A0}} \exp[i\omega(t - l_z/v_{A0})] \sum_{k=0}^{m'} \exp(-2ik\omega l_z/v_{A0}) \\ &= -\frac{B_0 u_0}{v_{A0}} \exp[i\omega(t - l_z/v_{A0})] \frac{1 - r^{m'+1}}{1 - r}. \end{aligned} \quad (2.4.11)$$

and for $r = 1$,

$$b(0, t) = -\frac{B_0 u_0}{v_{A0}} \exp[i\omega(t - l_z/v_{A0})](1 + m'). \quad (2.4.12)$$

Using the identities that

$$|1 + \exp(ix)| = 2 \left| \cos\left(\frac{x}{2}\right) \right|,$$

$$|1 - \exp(ix)| = 2 \left| \sin\left(\frac{x}{2}\right) \right|,$$

we calculate that for $r \neq -1$, the absolute value of $u(0, t)$ is given by

$$|u(0, t)| = u_0 \begin{cases} |\sin\{(m' + 1)\omega l_z/v_{A0}\}/\cos(\omega l_z/v_{A0})|, & \text{for } m' + 1 \text{ even}, \\ |\cos\{(m' + 1)\omega l_z/v_{A0}\}/\cos(\omega l_z/v_{A0})|, & \text{for } m' + 1 \text{ odd}, \end{cases} \quad (2.4.13)$$

which is equivalent to

$$|u(0, t)| = u_0 \left| \frac{\sin\{(m' + 1)(\omega l_z/v_{A0} + \pi/2)\}}{\cos(\omega l_z/v_{A0})} \right|. \quad (2.4.14)$$

For $r = -1$

$$|u(0, t)| = u_0(m' + 1). \quad (2.4.15)$$

For $r \neq 1$, the absolute value of $b(0, t)$ is given by

$$|b(0, t)| = \frac{u_0 B_0}{v_{A0}} \left| \frac{\sin\{(m' + 1)\omega l_z/v_{A0}\}}{\sin(\omega l_z/v_{A0})} \right|. \quad (2.4.16)$$

For $r = 1$

$$|b(0, t)| = \frac{B_0 u_0}{v_{A0}} (m' + 1). \quad (2.4.17)$$

We call ω_n for $n \in \mathbb{Z}$ the resonant frequencies which satisfy

$$\frac{\omega_n l_z}{v_{A0}} = \frac{n\pi}{2}, \quad (2.4.18)$$

$$\implies \omega_n = \frac{n\pi v_{A0}}{L_z}. \quad (2.4.19)$$

Equations (2.4.14)-(2.4.17) show that for $\omega \neq \omega_n$, the solutions oscillate about a finite value, but for $\omega = \omega_n$, then the amplitude of either u or b at the loop apex grows linearly with time depending on whether n is odd or even. In Sections 2.4.2-2.4.4 we investigate the solutions for the cases where $\omega = \omega_n$, $\omega \approx \omega_n$ and $\omega \neq \omega_n$, where $\omega \neq \omega_n$ is the case where the driver frequency is as far away from the resonant frequencies as possible.

2.4.2 Resonant case

In this section, we investigate solutions for the case where $\omega = \omega_n$. If n is odd, then we say the odd harmonic has been excited, if n is even then we say an even harmonic has been excited.

Note that

$$u(0, t) = u_0 \exp[i\omega_n(t - l_z/v_{A0})] \begin{cases} (m' + 1), & n \text{ odd}, \\ [1 - (-1)^{m'+1}]/2, & n \text{ even}. \end{cases} \quad (2.4.20)$$

$$b(0, t) = -\frac{B_0 u_0}{v_{A0}} \exp[i\omega_n(t - l_z/v_{A0})] \begin{cases} [1 - (-1)^{m'+1}]/2, & n \text{ odd}, \\ (m' + 1), & n \text{ even}. \end{cases} \quad (2.4.21)$$

The Poynting flux at $z = 0$, directed in the z -direction, S_{z0} , is given by

$$S_{z0} = \mathbf{S} \cdot \hat{\mathbf{z}}|_{z=0}, \quad (2.4.22)$$

since, $\mathbf{u} = 0$ at $z = 0$. Hence, using Equation (1.4.40), S_{z0} is given by

$$S_{z0} = -\frac{B_0}{\mu} \operatorname{Im}[u(0, t)] \operatorname{Im}[b(0, t)], \quad (2.4.23)$$

where $\operatorname{Im}[]$ returns the imaginary component of the input. Using the divergence theorem, and the fact that $\mathbf{u} = 0$ at $z = l_z$, we know that $-S_{z0}$ gives the rate of change of energy in the top half the loop. Using Equations (2.4.20) and (2.4.21) we can show that S_{z0} is given by

$$S_{z0} = \frac{B_0 u_0^2}{2\mu v_{A0}} \sin^2[\omega_n(t - l_z/v_{A0})] (m' + 1) (1 - (-1)^{m'+1}). \quad (2.4.24)$$

Figures 2.1 and 2.2 show plots of u and b for $\omega = 0$, $\omega = \omega_1$ and ω_2 . The time is normalised by t_0 given by

$$t_0 = \frac{L_z}{v_{A0}}. \quad (2.4.25)$$

The magnetic field is normalised by b_0 , given by

$$b_0 = \frac{B_0 u_0}{v_{A0}}. \quad (2.4.26)$$

Note that the real component is plotted for $\omega = 0$ because the imaginary component

$$\omega = \omega_n$$

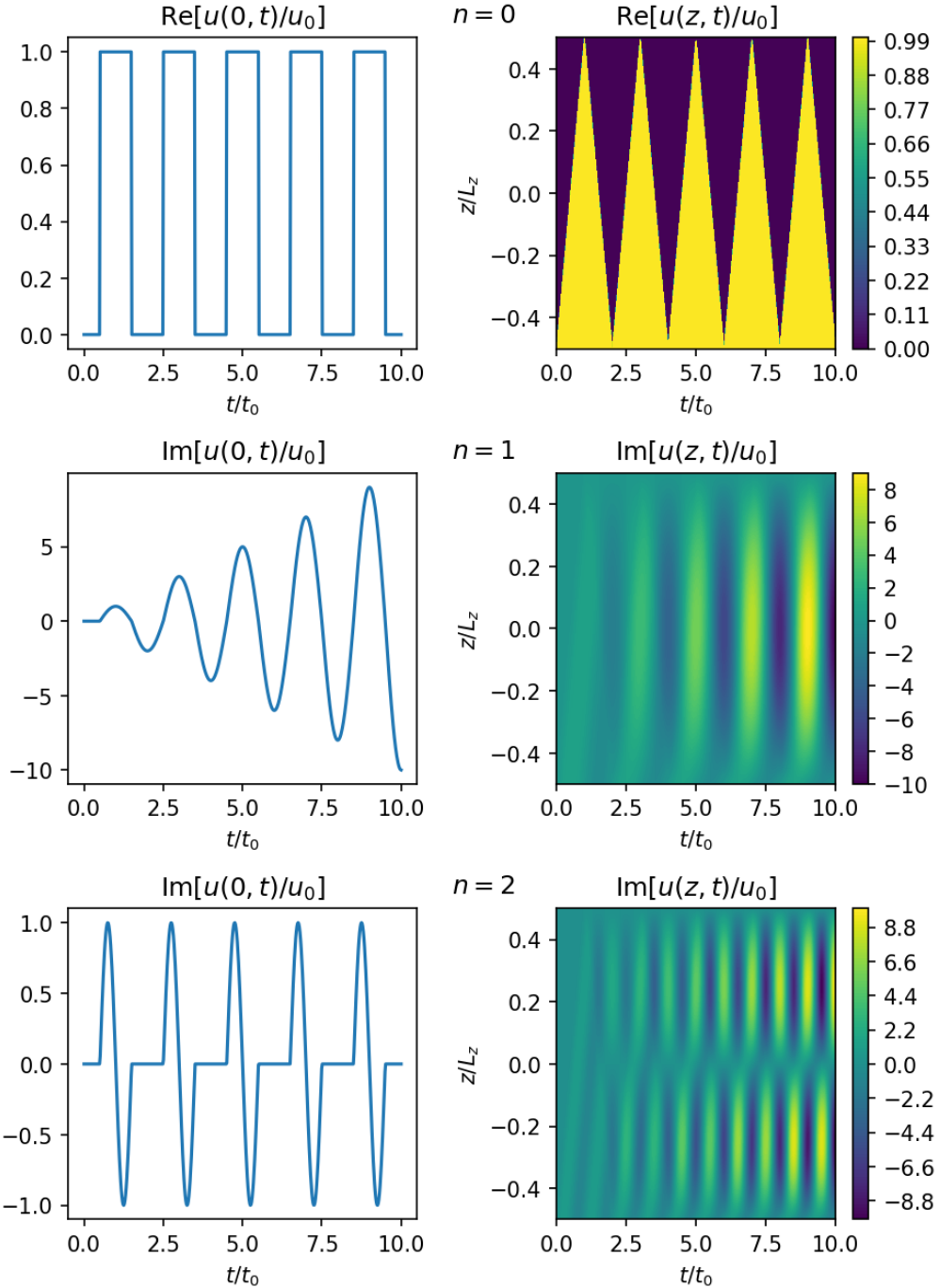


Figure 2.1: This figure shows contour plots of the velocity, u , and line plots at $z = 0$. The driver frequency is given by $\omega = \omega_n$. Each row shows the solution for different values of n . The top row shows the real part and the other rows show the imaginary part. The normalising constant, t_0 , is given by Equation (2.4.25). The code used to make this figure is available on GitHub in the following directory:

→ [Python/Chapter2/case_where_omega=omega_n.py](#)

$$\omega = \omega_n$$

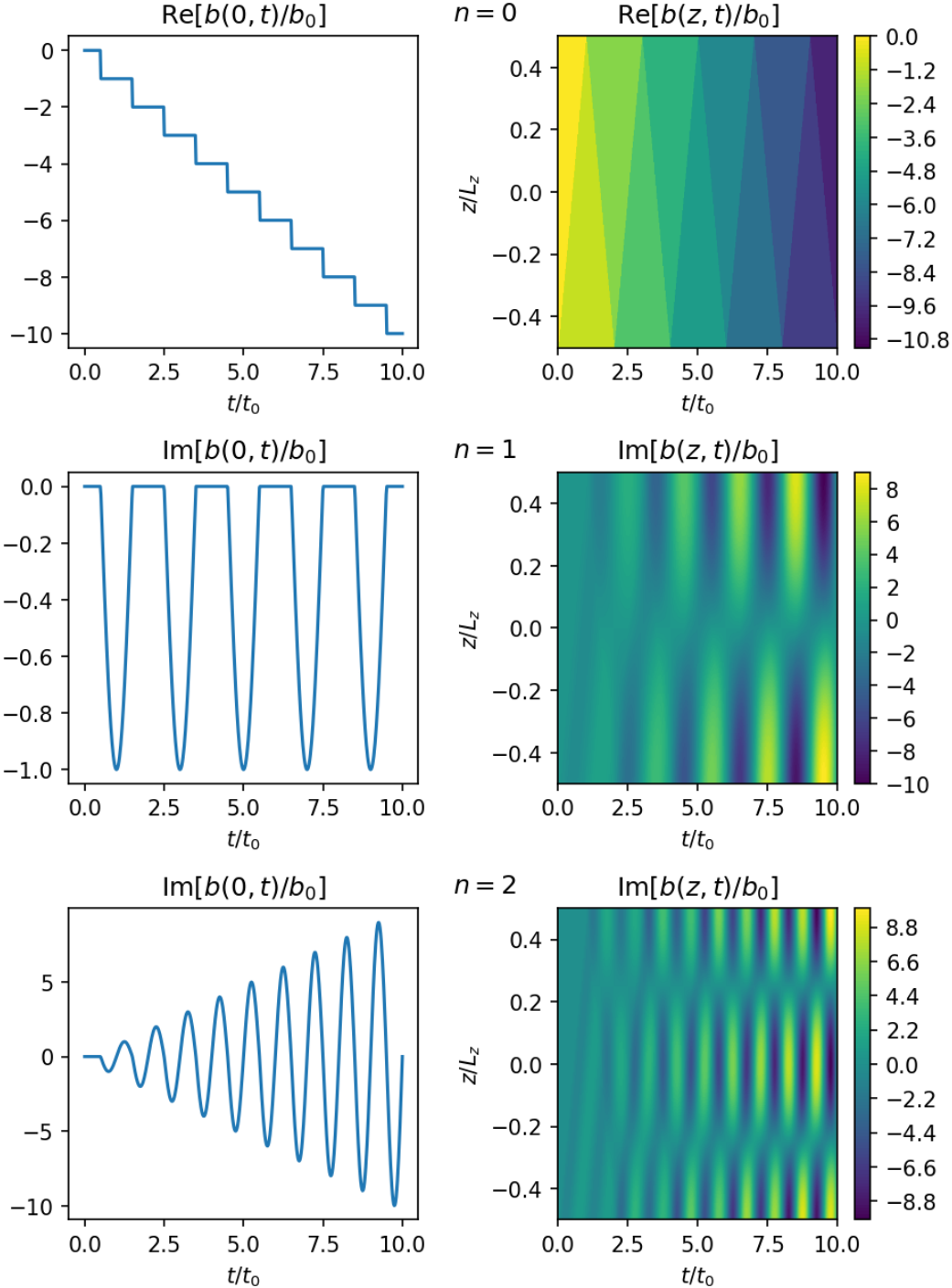


Figure 2.2: This figure is very similar to Figure 2.1 except it shows the magnetic field, b , instead of the velocity. The normalising constant, b_0 , is given by Equation (2.4.26). The code used to make this figure is available on GitHub in the following directory:

→ [Python/Chapter2/case_where_omega=omega_n.py](#)

gives the trivial solution. The imaginary part is plotted for $n \geq 1$ because this ensures u and b are continuous. However, their derivatives are not continuous. In all three plots, the amplitude grows linearly with time, which means the energy grows quadratically. For $n \geq 1$, the driver generates approximate standing Alfvén waves. They are not perfect standing waves as they contain a propagating component due to the driver. The time and space averaged kinetic and magnetic energies are approximately equal. For $n = 0$, the driver shears the magnetic field, and the amplitude grows linearly with time, whereas the kinetic energy oscillates about a finite value. It is convenient to categorise oscillatory motions into fast and slow motions: Slow motions are where the frequency, f , is smaller than v_{A0}/L_z , where L_z gives the length of the loop. Fast motions are where the frequency is greater than v_{A0}/L_z . A key difference between fast and slow motions is that slow motions can generate a large build-up in magnetic energy with relatively little kinetic energy. For fast motions, the build-up in magnetic energy is approximately equal to the build-up in kinetic energy. The plots show if u has an antinode at a given point in space, then b has a node and vice versa.

2.4.3 Approximately resonant case

In this section, we investigate the solutions for the case where $\omega = \omega_n + \epsilon\omega_1$, where $\epsilon \ll 1$, i.e. we look at the solution where the driving frequency is nearly equal to one of the resonant frequencies.

From Equation (2.4.14) we know that the absolute value of the velocity at $z = 0$ is given by

$$|u(0, t)| = u_0 \left| \sec \left(\frac{\omega l_z}{v_{A0}} \right) \sin \left\{ (m' + 1) \left(\frac{l_z}{v_{A0}} (\omega - \omega_n) + \frac{l_z \omega_n}{v_{A0}} + \frac{\pi}{2} \right) \right\} \right|.$$

Since $m' + 1 \in \mathbb{Z}$, then for n odd we know that

$$\left| \sin \left\{ (m' + 1) \left(x + \frac{\omega_n l_z}{v_{A0}} + \frac{\pi}{2} \right) \right\} \right| = |\sin\{(m' + 1)x\}|.$$

Therefore, approximating $m' + 1$ with

$$m' + 1 \approx \frac{v_{A0}t}{L_z},$$

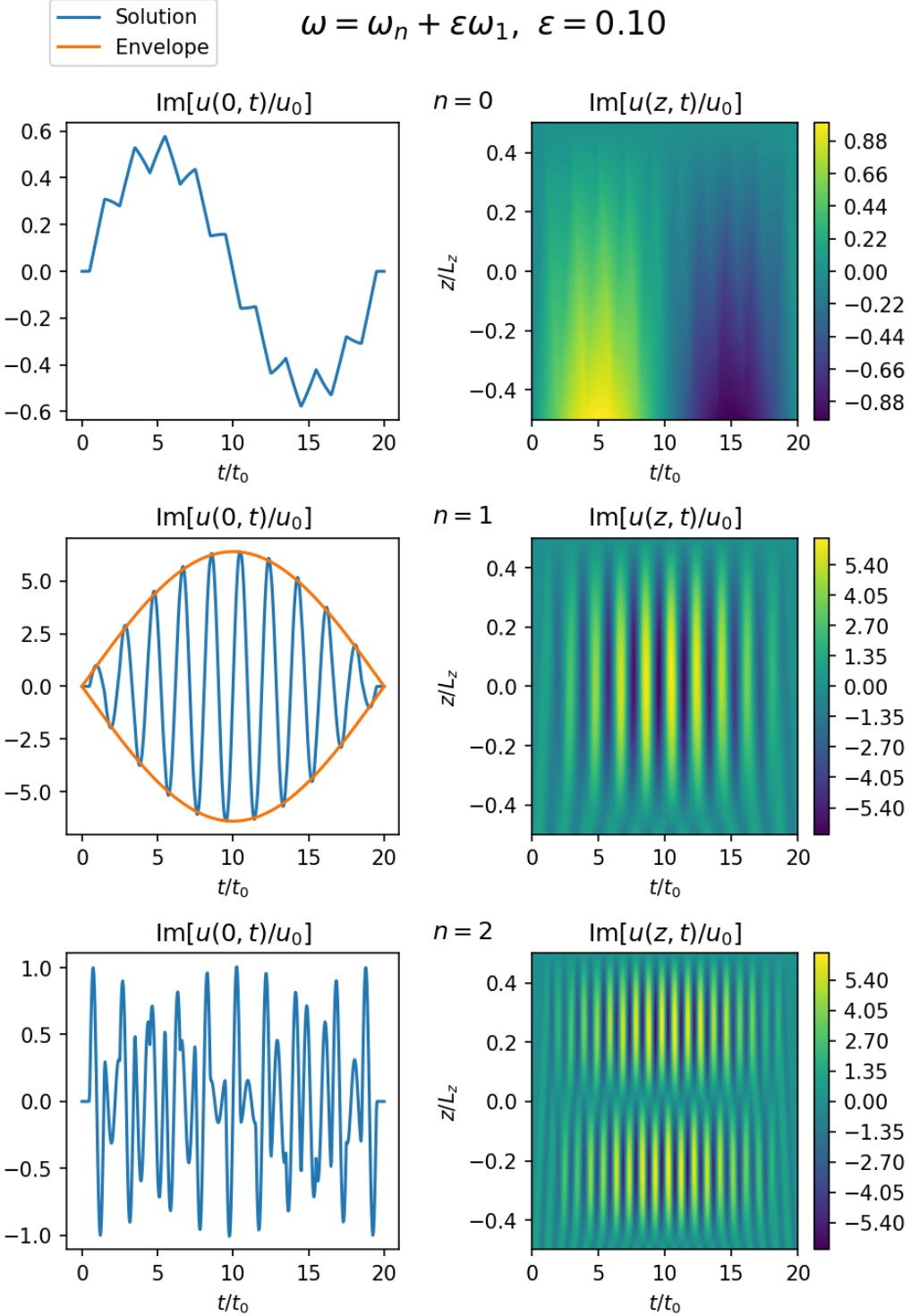


Figure 2.3: This figure is similar to Figure 2.1 except now the frequency is given by $\omega = \omega_n + \epsilon\omega_1$ for $\epsilon = 0.1$. Also, the imaginary component is taken for all values of n . Note that the velocity at $z = 0$ is plotted in blue and the envelope, given by Equation (2.4.27), is plotted in orange. The code used to make this figure is available on GitHub in the following directory:

→ [Python/Chapter2/case_where_omega_approx_omega_n.py](#)

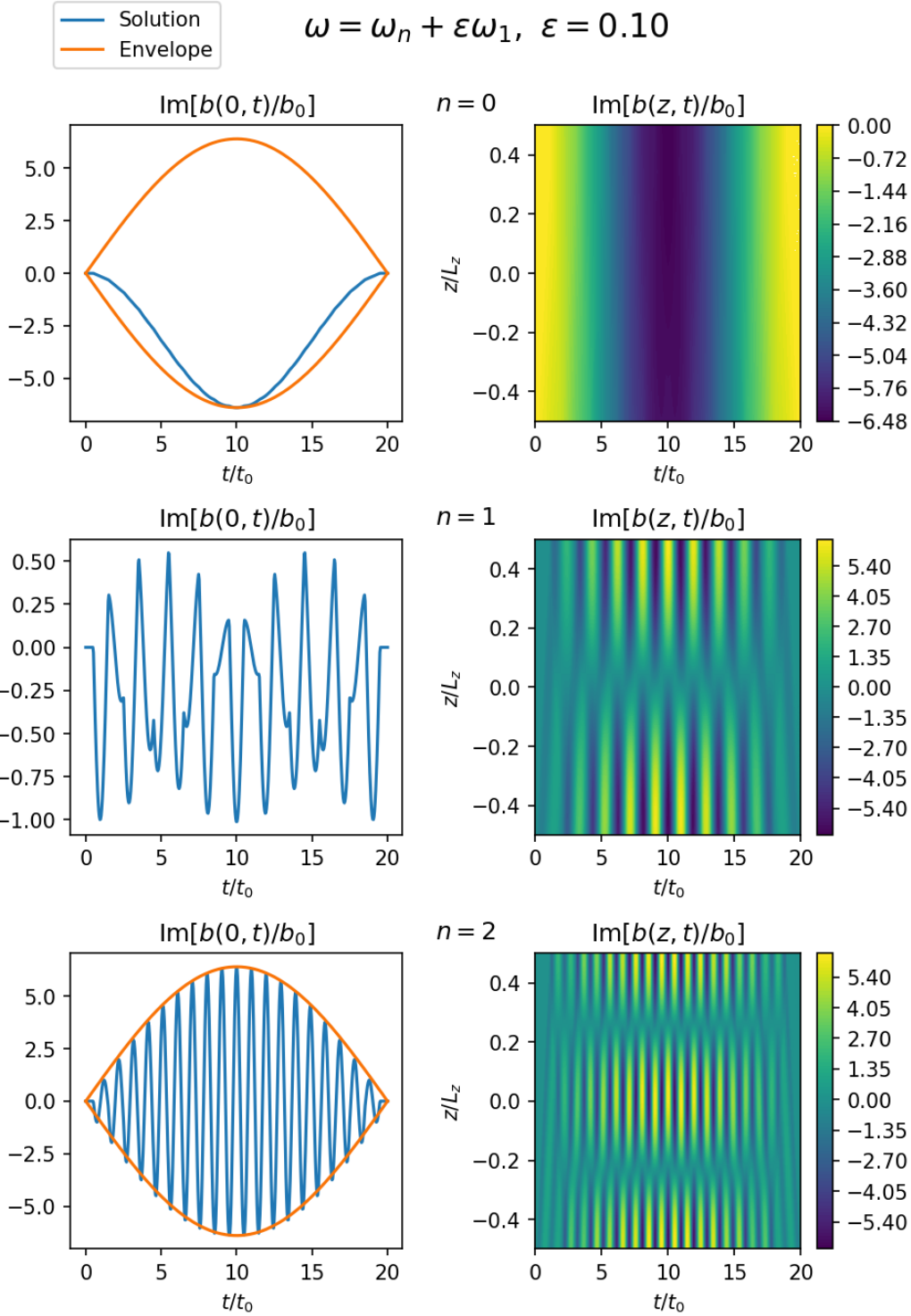


Figure 2.4: This figure is similar to Figure 2.3 except the magnetic field is plotted instead of the velocity. The equation for the envelope is given by Equation (2.4.28). The code used to make this figure is available on GitHub in the following directory:

→ [Python/Chapter2/case_where_omega_approx_omega_n.py](#)

we can derive an equation for an envelope, $u_{e0}(t)$, that the real and imaginary components of the velocity at $z = 0$ approximately lies inside

$$u_{e0}(t) = \pm u_0 \sec\left(\frac{\omega l_z}{v_{A0}}\right) \sin\left\{\frac{\omega - \omega_n}{2}t\right\}, \quad (2.4.27)$$

for n odd. Using Equation (2.4.16) we can derive a similar envelope, $b_{e0}(t)$ for the magnetic field at $z = 0$, given by

$$b_{e0}(t) = \pm \frac{u_0 B_0}{v_{A0}} \csc\left(\frac{\omega l_z}{v_{A0}}\right) \sin\left\{\frac{\omega - \omega_n}{2}t\right\}, \quad (2.4.28)$$

for n even.

Figures 2.3 and 2.4 plot the solutions for the case where $\omega = \omega_n + \epsilon\omega_1$. In all the plots the imaginary part is shown instead of the real part because it is continuous. The plots display an interference pattern called a beat. The beating angular frequency, ω_b , is given by

$$\omega_b = \frac{\omega - \omega_n}{2}. \quad (2.4.29)$$

The beat is a concept from acoustics. It is an interference pattern between two sounds of slightly different frequencies, perceived as a periodic variation in magnitude with a rate which is the difference of the two frequencies. The beat effect is perhaps counterintuitive because it means the energy of the system can sometimes decrease (this is the case for $t/t_0 > 10$ in Figures 2.3 and 2.4). Therefore, the driver can be responsible for removing energy from the system. The driver sends waves into the system which can sometimes constructively interfere with the system and sometimes destructively interfere. If the resonant frequency is not excited, the waves will constructively interfere with the system 50% of the time and destructively interfere 50% of the time. The times where the waves destructively interfere results in the energy decreasing at those times. Hence, the energy of the system oscillates about a finite value.

2.4.4 Nonresonant case

In this section we consider the least resonant case, i.e. the case where

$$\omega = \frac{\omega_n + \omega_{n+1}}{2}.$$

This represents the least resonant case because the frequency is as far away from any of the resonant frequencies as possible. The solutions are plotted in Figure 2.5 and 2.6. As expected, the maximum energy of the solution is significantly smaller than the maximum energies reached in Figures 2.1-2.4. This is because the driver frequency is far away from the resonant and so constructive interference is quickly followed up by destructive interference which prevents the build-up of energy. For $n = 3$ and $n = 6$ the waves oscillate at a fixed amplitude, then after a time interval of length, L_z/v_{A0} , the waves oscillate at a different amplitude.

2.5 Closed loop: broadband driver

This section takes a statistical approach to study the solutions for a broadband driver, i.e. a driver which excites a wide range of frequencies. The previous section calculated the solution for a single frequency driver. Figure 1.6 shows that velocity fluctuations in the corona oscillate at a wide range of frequencies. We think of the previous section as the case where the driver includes only one term in its Fourier series. In contrast, this section contains many terms, even an infinite number of terms. We can constrain the amplitude of the terms using observed power spectra, e.g. Figure 1.6. However, the phase of each term cannot be constrained. Therefore, we need to consider all possible phases associated with each term in the Fourier series. Given the infinite number of possibilities, we take a statistical approach to study the solutions. We aim to study the average behaviour and answer the question: do the solutions grow to infinity or oscillate about a finite value? In the previous section, we calculated that for a sinusoidal driver, the energy of the solution either oscillates about a finite value if $\omega \neq \omega_n$ or grows to infinity if $\omega = \omega_n$. To answer this question for the broadband driver, we first reduce Equation (2.2.1) to a system of ODEs, corresponding to the equation of a driven harmonic oscillator. After that, we calculate the general solution to the ODE, and then we study the case where the driver gives a red noise and white noise force.

$$\omega = (\omega_n + \omega_{n+1})/2$$

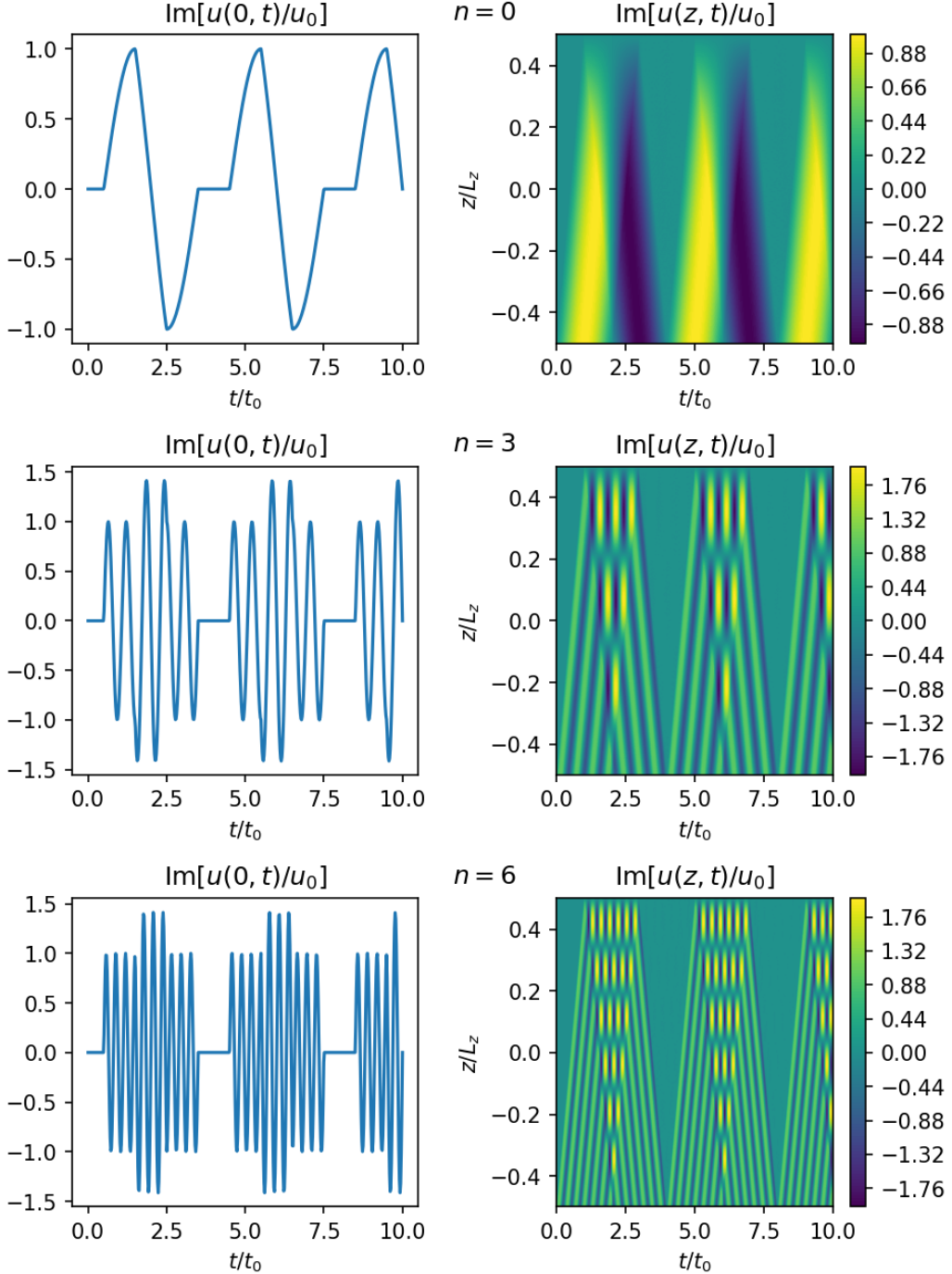


Figure 2.5: This figure is similar to Figure 2.1 except now the frequency is given by $\omega = (\omega_n + \omega_{n+1})/2$. These are the least resonant frequencies because they are as far away from any of the resonant frequencies as possible. The code used to make this figure is available on GitHub in the following directory:

→ [Python/Chapter2/case_where_omega_ne_omega_n.py](#)

$$\omega = (\omega_n + \omega_{n+1})/2$$

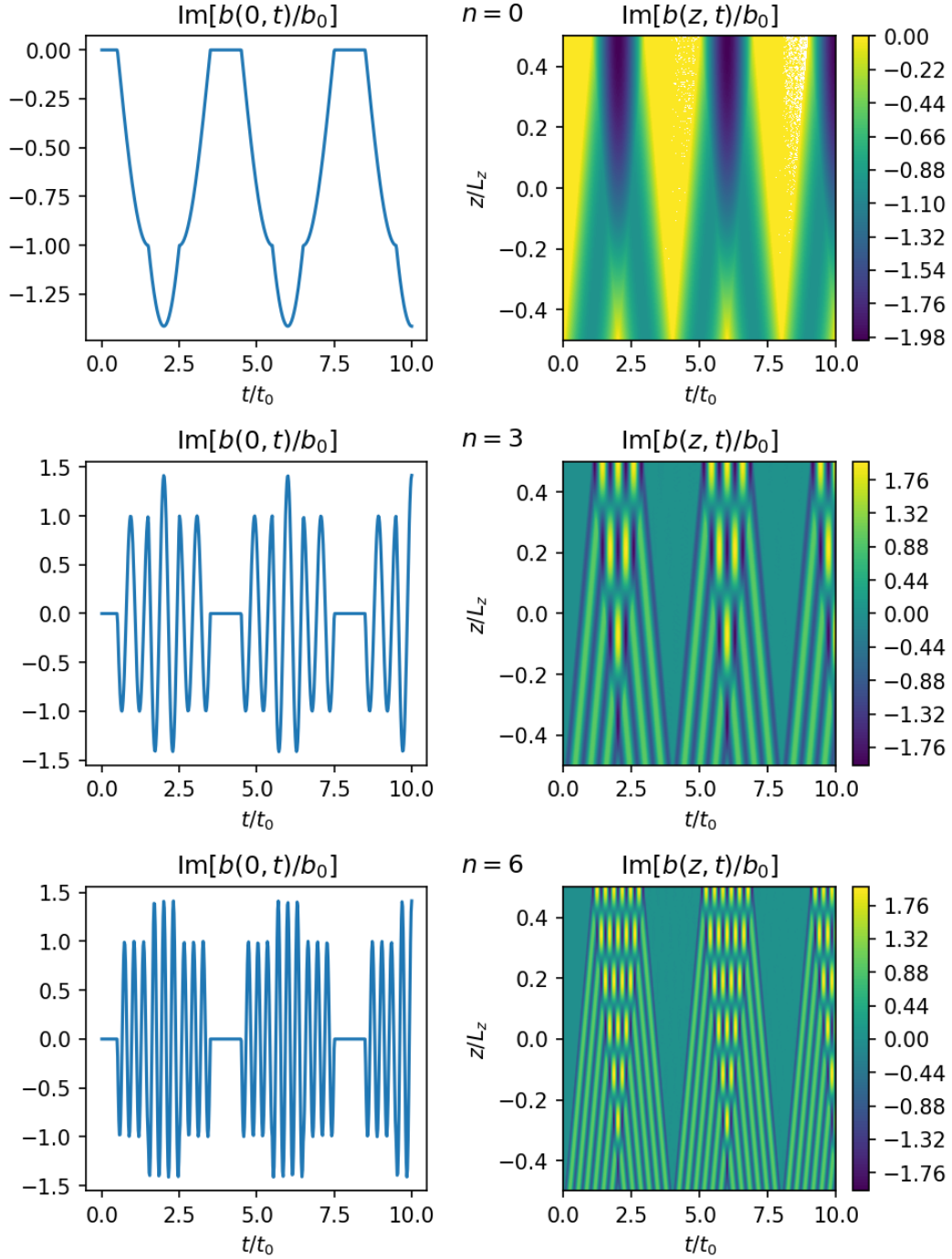


Figure 2.6: This figure is similar to Figure 2.1 except the magnetic field is plotted instead of the velocity. The code used to make this figure is available on GitHub in the following directory:

→ [Python/Chapter2/case_where_omega_ne_omega_n.py](#)

2.5.1 Driven harmonic oscillator

We define our z -range to be given by $0 \leq z \leq L_z$ with the boundary conditions given by

$$u(0, t) = f_{driv}(t), \quad u(L_z, t) = 0. \quad (2.5.1)$$

Let

$$u(z, t) = y(z, t) + \frac{L_z - z}{L_z} f_{driv}(t). \quad (2.5.2)$$

Substituting this into Equation (2.2.1) gives

$$\frac{\partial^2 y}{\partial t^2} - v_{A0}^2 \frac{\partial^2 y}{\partial z^2} = -\frac{L_z - z}{L_z} \frac{d^2 f_{driv}}{dt^2} \quad (2.5.3)$$

Hence, the boundary conditions for $y(z, t)$ are

$$y(0, t) = y(L_z, t) = 0. \quad (2.5.4)$$

We can equate the right-hand side with the following Fourier series

$$-\frac{L_z - z}{L_z} f''_{driv}(t) = -2 f''_{driv}(t) \sum_{n=1}^{\infty} \frac{\sin(k_{zn} z)}{n\pi}, \quad (2.5.5)$$

for $0 < z \leq L_z$, where

$$k_{zn} = \frac{n\pi}{L_z}. \quad (2.5.6)$$

Let

$$y(z, t) = \sum_{n=1}^{\infty} y_n(t) \sin(k_{zn} z), \quad (2.5.7)$$

therefore, each y_n satisfies

$$\frac{d^2 y_n}{dt^2} + \omega_n^2 y_n = f_n(t), \quad (2.5.8)$$

where

$$\omega_n = \frac{n\pi}{L_z} v_{A0}, \quad (2.5.9)$$

$$f_n(t) = -2 \frac{f''_{driv}(t)}{n\pi}. \quad (2.5.10)$$

Note that Equation (2.5.8) is the equation for a driven harmonic oscillator.

2.5.2 General solution

In this section we calculate the general solution to Equation (2.5.8). We first calculate a general solution using a Green's function. After that, we calculate the mean and variance of the solution for a driver with a Fourier series where each coefficient is a random number from a Gaussian probability distribution.

The Green's function, $G(t)$ for Equation (2.5.8) is

$$G(t) = H(t) \frac{\sin(\omega_n t)}{\omega_n}, \quad (2.5.11)$$

where $H(t)$ is the Heaviside step function. We impose the initial condition

$$y_n(0) = \left. \frac{dy_n}{dt} \right|_{t=0} = 0, \quad (2.5.12)$$

therefore, the complementary component of the solution is zero. Hence, the general solution is given by

$$y_n = \frac{1}{\omega_n} \int_0^t \sin[\omega_n(t-t')] f_n(t') dt'. \quad (2.5.13)$$

Equation (2.5.13) works for any smooth function. Now we will consider the solution where we know the Fourier series of the driver up to a statistical average. Let the following Fourier series describe $f_n(t)$,

$$f_n(t) = a_0 X_0 + \sum_{k=1}^{\infty} a_k X_k \cos(\omega_k t) + b_k Y_k \sin(\omega_k t), \quad (2.5.14)$$

for $t \in [0, P]$, where

$$\omega_k = \frac{k\pi}{2P}, \quad (2.5.15)$$

X_k, Y_k are independent random Gaussian variables with mean,

$$\langle X_k \rangle = \langle Y_k \rangle = 0,$$

and variance

$$\langle X_k^2 \rangle = \langle Y_k^2 \rangle = 1.$$

Therefore, by Parseval's theorem,

$$\frac{1}{2P} \int_0^{2P} f_n^2(t) dt = a_0^2 X_0^2 + \frac{1}{2} \sum_{k=1}^{\infty} a_k^2 X_k^2 + b_k^2 Y_k^2. \quad (2.5.16)$$

Hence,

$$\begin{aligned} \left\langle \frac{1}{2P} \int_0^{2P} f_n^2(t) dt \right\rangle &= \langle a_0^2 X_0^2 \rangle + \frac{1}{2} \sum_{k=1}^{\infty} \langle a_k^2 X_k^2 \rangle + \langle b_k^2 Y_k^2 \rangle \\ &= a_0^2 + \frac{1}{2} \sum_{k=1}^{\infty} a_k^2 + b_k^2. \end{aligned} \quad (2.5.17)$$

Therefore, the coefficients a_k, b_k give the average power spectrum of $f_n(t)$. We can use data from observations, e.g. Figure 1.6 to determine the values of a_k, b_k .

Using Equations (2.5.13) and (2.5.14), as well as the Maple file located at

[→ Maple/Chapter 2/driven_harmonic_oscillator.pdf](#),

(to assist with the algebra), we calculate that the solution for $y_n(t)$ is given by

$$y_n(t) = \sum_{k=0}^{\infty} y_n^{(k)}(t), \quad (2.5.18)$$

where

$$y_n^{(k)}(t) = \frac{a_k X_k \omega_n [\cos(\omega_n t) - \cos(\omega_k t)] + b_k Y_k [\omega_k \sin(\omega_n t) - \omega_n \sin(\omega_k t)]}{\omega_n (\omega_k^2 - \omega_n^2)}, \quad (2.5.19)$$

for $\omega_k \neq \omega_n$ and

$$y_n^{(k)}(t) = \frac{a_k X_k \omega_n t \sin(\omega_n t) + b_k Y_k [\sin(\omega_n t) - \omega_n t \cos(\omega_n t)]}{2\omega_n^2}, \quad (2.5.20)$$

for $\omega_k = \omega_n$. Therefore, the mean, $\langle y_n(t) \rangle$, equals zero and the variance is given by

$$\langle y_n^2(t) \rangle = \sum_{k=0}^{\infty} \left\langle [y_n^{(k)}(t)]^2 \right\rangle, \quad (2.5.21)$$

where

$$\left\langle [y_n^{(k)}(t)]^2 \right\rangle = \frac{a_k^2 \omega_n^2 [\cos(\omega_n t) - \cos(\omega_k t)]^2 + b_k^2 [\omega_k \sin(\omega_n t) - \omega_n \sin(\omega_k t)]^2}{\omega_n^2 (\omega_k^2 - \omega_n^2)^2}, \quad (2.5.22)$$

for $\omega_k \neq \omega_n$ and

$$\left\langle [y_n^{(k)}(t)]^2 \right\rangle = \frac{a_k^2 \omega_n^2 t^2 \sin^2(\omega_n t) + b_k^2 [\sin(\omega_n t) - \omega_n t \cos(\omega_n t)]^2}{4\omega_n^4}, \quad (2.5.23)$$

if $\omega_k = \omega_n$. This shows that in general, the power spectrum will have a peak at the resonant frequencies.

Here we calculate the time-derivative of the variance because we will need it in Section 2.5.3. The time-derivative of $y_n(t)$ is given by

$$\frac{dy_n}{dt} = \sum_{k=0}^{\infty} \frac{dy_n^{(k)}}{dt}, \quad (2.5.24)$$

where

$$\frac{dy_n^{(k)}}{dt} = \frac{a_k X_k [\omega_k \sin(\omega_k t) - \omega_n \sin(\omega_n t)] + b_k Y_k \omega_k [\cos(\omega_n t) - \cos(\omega_k t)]}{\omega_k^2 - \omega_n^2}, \quad (2.5.25)$$

for $\omega_k \neq \omega_n$ and

$$\frac{dy_n^{(k)}}{dt} = \frac{a_k X_k [\sin(\omega_n t) + \omega_n t \cos(\omega_n t)] + b_k Y_k \omega_n t \sin(\omega_n t)}{2\omega_n}, \quad (2.5.26)$$

for $\omega_k = \omega_n$. Therefore, the mean, $\langle dy_n/dt \rangle$, equals zero and the variance is given by

$$\left\langle \left[\frac{dy_n}{dt} \right]^2 \right\rangle = \sum_{k=0}^{\infty} \left\langle \left[\frac{dy_n^{(k)}}{dt} \right]^2 \right\rangle, \quad (2.5.27)$$

where

$$\left\langle \left[\frac{dy_n^{(k)}}{dt} \right]^2 \right\rangle = \frac{a_k^2 [\omega_k \sin(\omega_k t) - \omega_n \sin(\omega_n t)]^2 + b_k^2 \omega_k^2 [\cos(\omega_n t) - \cos(\omega_k t)]^2}{(\omega_k^2 - \omega_n^2)^2}, \quad (2.5.28)$$

for $\omega_k \neq \omega_n$ and

$$\left\langle \left[\frac{dy_n^{(k)}}{dt} \right]^2 \right\rangle = \frac{a_k^2 [\sin(\omega_n t) + \omega_n t \cos(\omega_n t)]^2 + b_k^2 \omega_n^2 t^2 \sin^2(\omega_n t)}{4\omega_n^2}, \quad (2.5.29)$$

if $\omega_k = \omega_n$.

2.5.3 Noisy force

Let $\eta(t)$ be a noisy signal, given by

$$\eta(t) = \int_{-\infty}^{\infty} \hat{\eta}(f) \exp(2\pi i t f) df, \quad (2.5.30)$$

where its Fourier transform in the sense of distributions, $\hat{\eta}(f)$, is given by

$$\hat{\eta}(f) = \int_{-\infty}^{\infty} \eta(t) \exp(-2\pi i t f) dt, \quad (2.5.31)$$

where f denotes the frequency. We define $\eta(t)$ to be a white noise signal of strength D . The value of $\eta(t)$ for any time t is a random Gaussian variable that is statistically

independent of its entire history before. Its power spectrum is given by

$$\langle |\hat{\eta}(f)|^2 \rangle = D, \quad (2.5.32)$$

where D is a constant. Similarly, we define $W(t)$ to be red noise of strength E if it is a random signal with a power spectrum given by

$$\langle |\hat{W}(f)|^2 \rangle = Ef^{-2}, \quad (2.5.33)$$

where E is a constant. Red noise is often called brown noise due to its association with Brownian motion. We think of it as the integral of white noise in time, and it is closely related to the Wiener process. The colour of the noise takes its name from its power spectrum. White noise excites all frequencies equally and is analogous to visible white light which contains all frequencies in the rainbow. Red noise has more energy in the lower frequencies, similar to visible red light, which is at the lower end of the visible light frequency spectrum.

Let the displacement, x_n , be given by

$$\frac{dx_n}{dt} = y_n. \quad (2.5.34)$$

Let the acceleration, g_n , be given by

$$\frac{dg_n}{dt} = f_n. \quad (2.5.35)$$

Substituting the above two equations into Equation (2.5.8) and integrating in time gives

$$\frac{d^2x_n}{dt^2} + \omega_n^2 x_n = g_n(t) + C, \quad (2.5.36)$$

where C is an integration constant. We consider the case where the integration constant C equals 0 as the solution associated with this term can be superimposed if needed. Equation (2.5.36) shows that $g_n(t)$ has the dimensions of a force (divided by mass). Therefore, if $g_n(t) = \eta(t)$ we say the system is driven by a white noise force and if $g_n(t) = W(t)$ then the system is driven by a red noise force. We are interested in red

and white noise because they produce power spectra with slopes f^0 and f^{-2} . Fitting Figure 1.6 with a single power law shows the velocity fluctuations in the solar corona have a power spectrum which goes as f^p , where $-2 < p < 0$. If $g_n(t) = \eta(t)$, then we solve Equation (2.5.36). If $g_n(t) = W(t)$, then $f_n(t) = \eta(t)$ and so we solve Equation (2.5.8). In other words, we solve the equation where white noise is on the right hand side. In this section we will solve for the case where $g_n(t) = W(t)$, then we will substitute $dy_n/dt \rightarrow y_n$ to quickly calculate the solution for the case where $g_n = \eta(t)$. Note that this substitution causes the initial conditions, see Equation (2.5.12), to change to

$$x_n(0) = \frac{dx_n}{dt} = 0. \quad (2.5.37)$$

By the Wiener–Khinchin theorem, $\eta(t)$ has an autocorrelation given by the Fourier transform of the power spectral density, i.e.

$$\begin{aligned} \langle \eta(t)\eta(t') \rangle &= \int_{-\infty}^{\infty} \langle |\hat{\eta}(\xi)|^2 \rangle \exp[2\pi i \xi(t - t')] d\xi \\ &= D\delta(t - t'), \end{aligned} \quad (2.5.38)$$

where $\delta(t - t')$ is the Dirac delta function. If $f_n(t)$ is a white noise signal then Equation (2.5.8) gives a Langevin equation where an exact solution can be calculated with a simpler solution compared with Equation (2.5.8). Substituting $f_n(t) = \eta(t)$ into Equation (2.5.8) gives the following Langevin equation

$$\frac{d^2y_n}{dt^2} + \omega_n^2 y_n = \eta(t). \quad (2.5.39)$$

Note that $\eta(t)$ has a mean of

$$\langle \eta(t) \rangle = 0. \quad (2.5.40)$$

Using Equation (2.5.13), the solution is given by

$$y_n = \frac{1}{\omega_n} \int_0^t \sin[\omega_n(t - t')] \eta(t') dt', \quad (2.5.41)$$

and

$$\frac{dy_n}{dt} = \int_0^t \cos[\omega_n(t-t')] \eta(t') dt'. \quad (2.5.42)$$

Hence, the mean of y_n is given by

$$\begin{aligned} \langle y_n \rangle &= \frac{1}{\omega_n} \int_0^t \sin[\omega_n(t-t')] \langle \eta(t') \rangle dt' \\ &= 0. \end{aligned} \quad (2.5.43)$$

The square of y_n is given by

$$y_n^2 = \frac{D^2}{\omega_n^2} \int_0^t \int_0^t \sin[\omega_n(t-t')] \sin[\omega_n(t-t'')] \eta(t') \eta(t'') dt' dt''. \quad (2.5.44)$$

Therefore, the variance of y_n is given by

$$\begin{aligned} \langle y_n^2 \rangle &= \frac{1}{\omega_n^2} \int_0^t \int_0^t \sin[\omega_n(t-t')] \sin[\omega_n(t-t'')] \langle \eta(t') \eta(t'') \rangle dt' dt'' \\ &= \frac{D}{\omega_n^2} \int_0^t \int_0^t \sin[\omega_n(t-t')] \sin[\omega_n(t-t'')] \delta(t'-t'') dt' dt'' \\ &= \frac{D}{\omega_n^2} \int_0^t \sin^2[\omega_n(t-t')] dt' \\ &= \frac{D}{2\omega_n^3} [\omega_n t - \sin(\omega_n t) \cos(\omega_n t)]. \end{aligned} \quad (2.5.45)$$

Similarly, the mean of dy_n/dt is

$$\left\langle \frac{dy_n}{dt} \right\rangle = 0. \quad (2.5.46)$$

The variance is given by

$$\left\langle \left[\frac{dy_n}{dt} \right]^2 \right\rangle = \frac{D}{2\omega_n} [\omega_n t + \sin(\omega_n t) \cos(\omega_n t)]. \quad (2.5.47)$$

This shows that for both red/white noise drivers the energy on average goes to infinity. For a single frequency resonant driver the amplitude grows linearly with time whereas

for a white/red noise driver, the standard deviation grows as \sqrt{t} . However, white noise drivers are unphysical because they have an infinite variance. The variance of $\eta(t)$ is given by its autocorrelation for $t = t'$. Equation (2.5.38) shows that the variance is infinite, and this is because white noise excites all the frequencies from 0 to ∞ . Equation (2.5.22) shows that the variance associated with the higher frequency drivers goes to 0 as $f \rightarrow \infty$. For this reason, we predict that the solutions above provide a good approximation for solutions where the driver only excites frequencies up to a finite value, provided the resonant frequency is excited. To test this prediction, the next paragraph calculates the solution for a more physical driver which excites a finite range of frequencies causing it to have a finite variance.

Our goal is to ensure $f_n(t)$ excites each frequency with the same strength as $\eta(t)$ but only for a finite number of frequencies. Note that Equation (2.5.14) can be written as

$$f_n(t) = \sum_{k=-\infty}^{\infty} C_k \exp[2\pi i f_k t] \Delta f, \quad (2.5.48)$$

where

$$C_k = \begin{cases} 4P a_0 X_0, & k = 0, \\ 2P(a_k X_k - i b_k Y_k), & k > 0, \\ C_{|k|}^*, & k < 0, \end{cases} \quad (2.5.49)$$

$$f_k = \frac{k}{4P}, \quad (2.5.50)$$

$$\Delta f = \frac{1}{4P}. \quad (2.5.51)$$

For $P \rightarrow \infty$:

$$f_k \rightarrow f,$$

$$\Delta f \rightarrow df,$$

$$C_k \rightarrow C(f),$$

hence,

$$f_n(t) \rightarrow \int_{-\infty}^{\infty} C(f) \exp[2\pi i f t] df. \quad (2.5.52)$$

By the Wiener–Khinchin theorem,

$$\begin{aligned} \implies \langle f_n^2(t) \rangle &= \sum_{k=-\infty}^{\infty} \langle |C_k|^2 \rangle \exp[2\pi i f t] \\ &\rightarrow \int_{-\infty}^{\infty} \langle |C(f)|^2 \rangle \exp[2\pi i f t] df. \end{aligned} \quad (2.5.53)$$

Hence, we require

$$\langle |C_k|^2 \rangle = \frac{D}{\Delta f}. \quad (2.5.54)$$

Note that

$$\langle |C_k|^2 \rangle = \begin{cases} (4P a_0)^2, & k = 0, \\ 4P^2(a_k^2 + b_k^2), & k \neq 0, \end{cases} \quad (2.5.55)$$

therefore, letting $a_k = b_k$ gives

$$\implies \begin{pmatrix} a_0 \\ a_k \\ b_k \end{pmatrix} = \frac{1}{2} \sqrt{\frac{D}{P}} \begin{pmatrix} 1 \\ \sqrt{2} \\ \sqrt{2} \end{pmatrix}. \quad (2.5.56)$$

Equation (2.5.21), with the a_k , b_k given above, gives an $f_n(t)$ which excites each frequency with the same strength as $\eta(t)$ but only for a finite number of frequencies.

Our goal now is to test our prediction that Equation (2.5.21) gives the same solution as Equation (2.5.45) with the coefficients given by Equation (2.5.56). We approximate the sum given by Equation (2.5.21) numerically and so the series is truncated at $k = N$. We denote the truncated approximation of Equation (2.5.21) with

$$\langle y_{n,N}(t) \rangle = \sum_{k=0}^N \langle y_n^{(k)} \rangle. \quad (2.5.57)$$

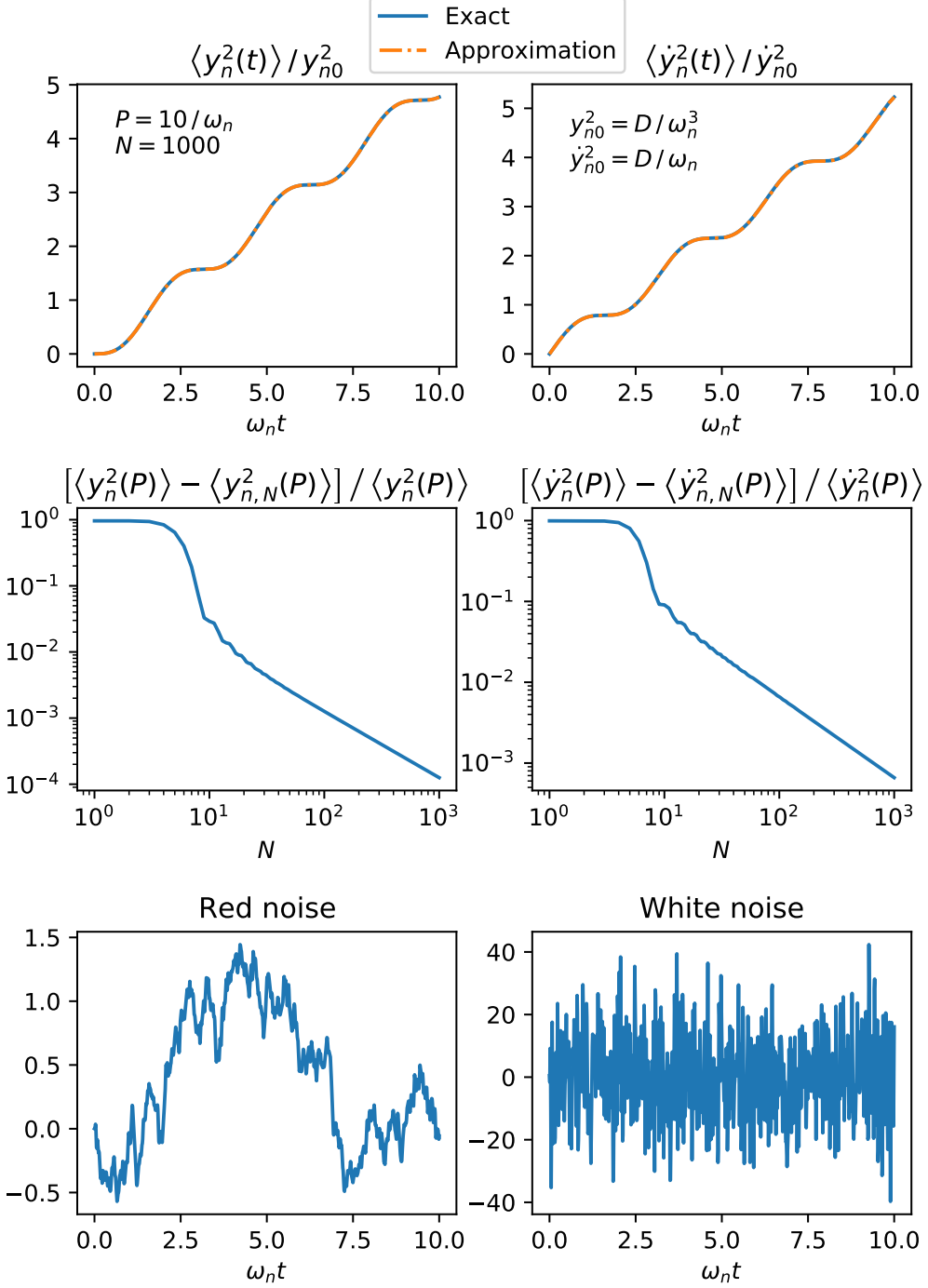


Figure 2.7: This top row of this figure shows the normalised variance of y_n and \dot{y}_n , where we use Newton's dot notation to denote the time derivative. They plot the exact solution and the Fourier approximations. The equations for the normalising constants, y_{n0} and \dot{y}_{n0} is also shown. The middle row shows the error at $t = P$ between the exact solution and the Fourier approximation as a function of the number of terms in the approximation. Finally, the bottom row illustrates an example of red and white noise. The code used to make this figure is available on GitHub in the following directory:
[→ Python/Chapter2/random_driver.py](#)

We refer to the solution given by Equation (2.5.57) as the Fourier approximation and the solution given by Equation (2.5.45) as the exact solution. The top row of Figure 2.7 shows the variance of y_n and its time derivative. It shows that for $P = 10/\omega_n$ and $N = 1000$ that the exact solution and Fourier approximation are in approximate agreement. The second row shows the error for the variance at $t = P$ between the exact solution and the Fourier approximation as a function of the number of terms in the truncated Fourier series. It shows that increasing the number of terms causes the error to decrease. Note that $P = 10/\omega_n$, therefore, from Equation (2.5.15) we know that

$$\omega_k = \frac{k\pi}{20}\omega_n,$$

hence, $\omega_k > \omega_n$ for $k > 6$. The middle row of Figure 2.7 shows that for $N \approx 6$, the accuracy sharply improves for increasing N . This suggests that provided the resonant frequency is excited then the exact solution and Fourier approximation show approximate agreement. Therefore, the solution given by white noise which only excites frequencies over a finite range can approximate the solution given by $\eta(t)$ which excites all the frequencies from 0 to ∞ . Finally, the bottom row of Figure 2.7 shows an illustration of red and white noise. The white noise plot was produced using a truncated approximation of Equation (2.5.14), with $N = 1000$. The red noise plots show the time integral of the white noise plot. The white noise plot shows an example of white noise where only a finite range of frequencies is excited. Note that it has a finite variance, whereas, $\eta(t)$, which excites all frequencies, has an infinite variance.

2.6 Leaky loop: reflection coefficient

In previous sections, we modelled the boundary of the domain as a solid wall. This is a good leading order approximation for the boundary between the corona and the lower layers of the atmosphere. Figure 1.3 shows that the chromosphere and photosphere are orders of magnitude denser than the corona. We can approximate this as a solid wall, provided the wavelength of the waves is significantly longer than length-scale of the density variations. In this section, we aim to calculate an approximation for the Alfvén wave reflection coefficient at the corona/chromosphere interface. In other words, we

aim to calculate on average how much energy is reflected and transmitted for waves at the boundary of the corona. In previous sections, we modelled perfect reflection, i.e. we assumed 100% of the energy reflects at the boundary. Therefore, we described the loops as closed. In this section, the reflection coefficient is less than unity so that some energy can escape. Therefore, we describe the loops as leaky.

To estimate the reflection coefficient, we use a method very similar to that described in [Hollweg \(1984b\)](#). We model the background Alfvén speed as

$$v_A(z) = \begin{cases} v_{A0} \exp(z/(2h)), & z < 0, \\ v_{A0}, & z \geq 0, \end{cases} \quad (2.6.1)$$

where h gives the pressure scale height which is defined as

$$h = \frac{k_B T}{mg_\odot}, \quad (2.6.2)$$

where k_B is the Boltzmann constant, T is the mean plasma temperature, m is the mean mass of a molecule, and g_\odot is the gravitational acceleration given by Equation [\(1.3.22\)](#). We choose the Alfvén speed (see Equation [2.6.1](#)), to approximate the Alfvén speed profile in the solar atmosphere, where $z < 0$ corresponds to the photosphere and chromosphere and $z > 0$ corresponds to the corona. We model the corona as uniform for convenience and because the pressure scale height is much greater there due to the higher temperature.

To estimate the reflection coefficient, we calculate the general normal mode solution for $z < 0$ and $z \geq 0$ and apply the boundary condition that the source of the waves lies in $z > 0$. After that we calculate the coefficients which ensure continuity of u and $\partial u / \partial z$ at $z = 0$. First, we prove that u and $\partial u / \partial z$ must be continuous at $z = 0$. To see this, write the Alfvén wave equation, Equation [\(2.2.1\)](#), as

$$\frac{\partial^2 u}{\partial z^2} = \frac{1}{v_A^2(z)} \frac{\partial^2 u}{\partial t^2}.$$

Integrate from $z = -\epsilon$ to $z = \epsilon$,

$$\left[\frac{\partial u}{\partial z} \right]_{-\epsilon}^{\epsilon} = \int_{-\epsilon}^{\epsilon} \frac{1}{v_A^2(z)} \frac{\partial^2 u}{\partial t^2} dz.$$

Let $\epsilon \rightarrow 0$. Note that u and v_A are finite and so the right-hand-side must go to zero as $\epsilon \rightarrow 0$. Therefore,

$$\frac{\partial u}{\partial z} \Big|_{\epsilon} = \frac{\partial u}{\partial z} \Big|_{-\epsilon}, \quad \epsilon \rightarrow 0,$$

which implies u and $\partial u / \partial z$ must be continuous.

We calculate normal mode solutions, i.e. we assume a time-dependence of the form $\exp(i\omega t)$. Hence, Equation (2.2.1) can be written as

$$\frac{d^2 u}{dz^2} + \frac{\omega^2}{v_A^2(z)} u = 0, \quad (2.6.3)$$

where to keep the notation tidy we assume the time-dependence implicitly.

Here we calculate the normal mode solution for $z < 0$. Let

$$\xi(z) = \frac{2h\omega}{v_A(z)}. \quad (2.6.4)$$

Note that

$$\frac{d\xi}{dz} = -\frac{\xi}{2h},$$

$$\frac{d^2\xi}{dz^2} = \frac{\xi}{4h^2}.$$

Hence,

$$\frac{d}{dz} = \frac{d\xi}{dz} \frac{d}{d\xi}$$

$$\begin{aligned} \frac{d^2}{dz^2} &= \left(\frac{d\xi}{dz} \right)^2 \frac{d^2}{d\xi^2} + \frac{d\xi}{dz} \frac{d}{d\xi} \left(\frac{d\xi}{dz} \right) \frac{d}{d\xi} \\ &= \frac{\xi^2}{4h^2} \frac{d^2}{d\xi^2} + \frac{\xi}{4h^2} \frac{d}{d\xi}. \end{aligned}$$

Therefore, multiplying Equation (2.6.3) through by $4h^2$ gives

$$\xi^2 \frac{d^2 u}{d\xi^2} + \xi \frac{du}{d\xi} + \xi^2 u = 0. \quad (2.6.5)$$

This is the zeroth order Bessel's equation which has the general solution

$$u(\xi) = C_1 J_0(\xi) + C_2 Y_0(\xi), \quad z < 0, \quad (2.6.6)$$

where $J_0(x)$ is the Bessel function of the first kind of order 0 and $Y_0(x)$ is the Bessel function of the second kind of order 0.

To apply boundary conditions to Equation (2.6.6) we need to know which component of the solution corresponds to outward going waves (away from the corona) and inward going waves (towards the corona). To work this out, we need to calculate the Poynting flux. Using Equation (1.4.13) we know that $b(\xi)$ is given by

$$\begin{aligned} b(\xi) &= \frac{B_0}{i\omega} \frac{du}{dz} \\ &= \frac{iB_0\xi}{2h\omega} \frac{d}{d\xi} [C_1 J_0(\xi) + C_2 Y_0(\xi)], \quad z < 0. \end{aligned} \quad (2.6.7)$$

Using Equation (1.4.40), we know that the Poynting flux in the z -direction, $S_z = \mathbf{S} \cdot \hat{\mathbf{z}}$ is given by

$$\begin{aligned} S_z &= -\frac{B_0}{\mu} \operatorname{Re}(u) \operatorname{Re}(b) \\ &= -\frac{B_0}{\mu} \left(\frac{u + \bar{u}}{2} \right) \left(\frac{b + \bar{b}}{2} \right), \end{aligned} \quad (2.6.8)$$

where \bar{u} denotes the complex conjugate of u . Therefore, the component which does not time-average to zero is

$$\begin{aligned} \langle S_z \rangle &= -\frac{B_0}{4\mu} (u\bar{b} + \bar{u}b) \\ &= -\frac{iB_0^2\xi}{8\mu h\omega} [(\bar{C}_1 J_0 + \bar{C}_2 Y_0)(C_1 J'_0 + C_2 Y'_0) - (C_1 J_0 + C_2 Y_0)(\bar{C}_1 J'_0 + \bar{C}_2 Y'_0)] \\ &= -\frac{iB_0^2\xi}{8\mu h\omega} (\bar{C}_1 C_2 - C_1 \bar{C}_2)(J_0 Y'_0 - J'_0 Y_0). \end{aligned}$$

Note that the Wronskian, $W(J_0, Y_0)(\xi)$, is given by

$$W(J_0, Y_0)(\xi) = J_0 Y'_0 - J'_0 Y_0 = \frac{2}{\pi\xi}. \quad (2.6.9)$$

Let

$$\begin{aligned} C_1 &= c_1 + c_2, \\ C_2 &= i(c_1 - c_2), \end{aligned} \tag{2.6.10}$$

therefore,

$$\bar{C}_1 C_2 - C_1 \bar{C}_2 = 2i(|c_1|^2 - |c_2|^2)$$

Hence, the time-averaged Poynting flux is given by

$$\langle S_z \rangle = \frac{B_0^2}{8\pi\mu h\omega} (|c_1|^2 - |c_2|^2), \tag{2.6.11}$$

where

$$u(\xi) = c_1 H_0^{(1)}(z) + c_2 H_0^{(2)}(z), \tag{2.6.12}$$

where $H_0^{(1)}$, $H_0^{(2)}$ are zeroth-order Hankel functions of the first and second kind. From the form of Equation (2.6.11), we identify the $H_0^{(1)}$ and $H_0^{(2)}$ parts of the equations as the inward (towards the corona) and outward (away from the corona) propagating waves respectively. Therefore, applying boundary conditions, we set $c_1 = 0$ as we assume the source of the waves lies inside the corona.

Hence, the full solution for $u(z)$ is given by

$$u(z) = \begin{cases} c_2 H_0^{(2)}(\xi), & \text{for } z < 0, \\ c_3 \exp(ik_z z) + c_4 \exp(-ik_z z), & \text{for } z \geq 0, \end{cases} \tag{2.6.13}$$

where k_z is given by

$$k_z = \frac{\omega}{v_{A0}}. \tag{2.6.14}$$

Using the identity

$$\frac{dJ_0}{d\xi} = -J_0(\xi), \quad \frac{dY_0}{d\xi} = -Y_0(\xi) \implies \frac{dH_0^{(2)}}{d\xi} = -H_1^{(2)}(\xi), \tag{2.6.15}$$

we can show that

$$\frac{du}{dz} = \begin{cases} c_2(\omega/v_A)H_1^{(2)}(\xi), & \text{for } z < 0, \\ ic_3k_z \exp(ik_z z) - ic_4k_z \exp(-ik_z z), & \text{for } z \geq 0. \end{cases} \quad (2.6.16)$$

Note that c_3 gives the amplitude of the coronal incident wave which we arbitrarily choose to have an amplitude u_0 . We require continuity of u and du/dz , this gives 2 equations and we have 2 unknowns, therefore, we can calculate c_2 and c_4 . Written as a matrix equation, the continuity equations become

$$\begin{pmatrix} H_0^{(2)}(\xi_0) & -1 \\ k_z H_1^{(2)}(\xi_0) & ik_z \end{pmatrix} \begin{pmatrix} c_2 \\ c_4 \end{pmatrix} = u_0 \begin{pmatrix} 1 \\ ik_z \end{pmatrix}, \quad (2.6.17)$$

where

$$\xi_0 = \frac{2h\omega}{v_{A0}} \quad (2.6.18)$$

Solving the above matrix equation gives

$$c_2 = \frac{2u_0}{H_0^{(2)}(\xi_0) - iH_1^{(2)}(\xi_0)}, \quad (2.6.19)$$

$$c_4 = u_0 \frac{H_0^{(2)}(\xi_0) + iH_1^{(2)}(\xi_0)}{H_0^{(2)}(\xi_0) - iH_1^{(2)}(\xi_0)}. \quad (2.6.20)$$

In Figure 2.8 we plot the real and imaginary components of u . It suggests that the solution given by Equation (2.6.13) is probably accurate as it agrees with the numerical solution. The numerical solution was calculated using a Runge-Kutta algorithm. More precisely, we used `solve_ivp` from [Virtanen et al. \(2020\)](#). We initialised the code with the values of u and du/dz at $z = z_{min}$ using Equations (2.6.13) and (2.6.16). In the plots we let $h = 150$ km, this value is used in for example [Hollweg \(1984b\)](#). Note that, if the mean mass of a molecule is given by m_p , g_\odot is given by (1.3.22) then from Equation

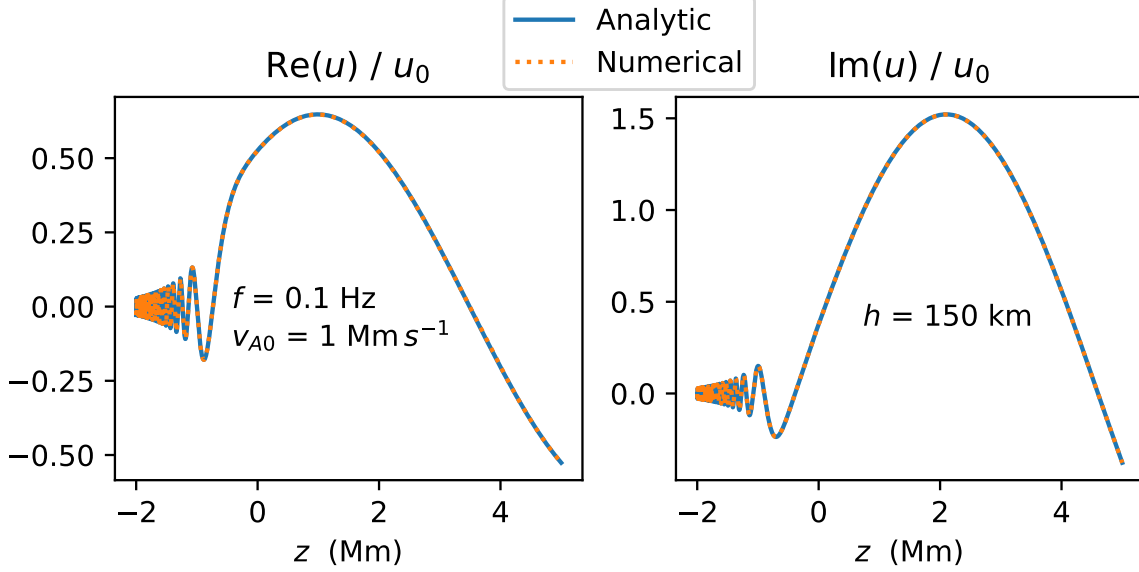


Figure 2.8: This figure shows the real and imaginary parts of the normal mode velocity solution. The plots compare the solution calculated using Equation (2.6.13) with the solution calculated numerically. The parameters, f , v_{A0} , h , are listed as well. The code used to make this figure is available on GitHub in the following directory:

[→ Python/Chapter2/reflection_coefficient_u.py](#)

(2.6.2) we know that

$$h \approx 1.51 \times 10^2 \text{ km} \left(\frac{T}{5 \times 10^3 \text{ K}} \right).$$

We used a frequency of $f = 0.1 \text{ Hz}$, from Figure 1.6 we can see that this is on the high end of the observed frequencies.

We are mainly interested in the reflection coefficient which we define as

$$R = \left| \frac{c_4}{u_0} \right|. \quad (2.6.21)$$

Note that

$$\bar{H}_0^{(2)}(\xi_0) = H_0^{(1)}(\xi_0), \quad (2.6.22)$$

and the Wronskian, $W(H_0^{(1)}, H_0^{(2)})(\xi)$, is given by

$$W(H_0^{(1)}, H_0^{(2)})(\xi) = H_0^{(1)}H_0^{(2)} - H_0'^{(1)}H_0^{(2)} = -\frac{4i}{\pi\xi} \quad (2.6.23)$$

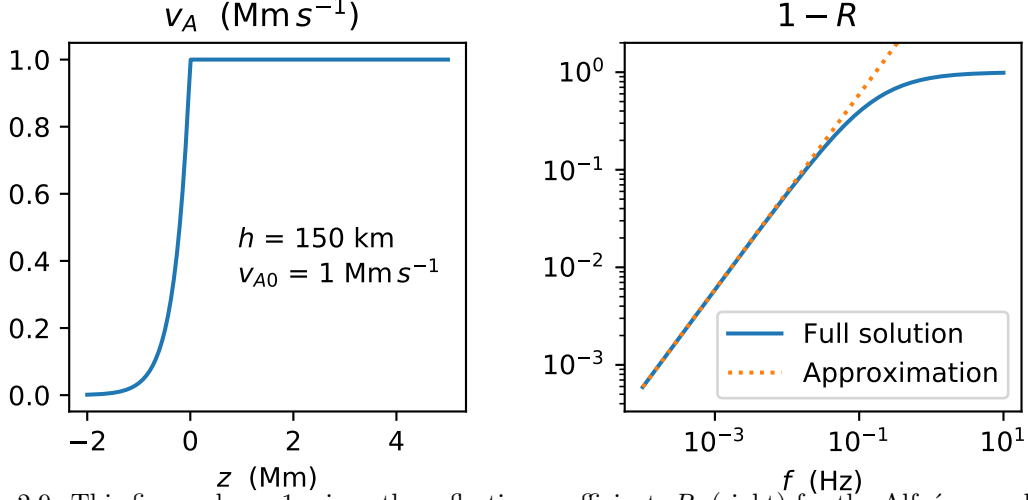


Figure 2.9: This figure shows 1 minus the reflection coefficient, R , (right) for the Alfvén speed shown on the left. We show the full solution in blue and the approximation, given by Equation (2.6.25), is shown in dotted orange. The code used to make this figure is available on GitHub in the following directory:

[→ Python/Chapter2/reflection_coefficient_u.py](#)

therefore,

$$\begin{aligned} |c_4|^2 &= u_0^2 \frac{\left|H_0^{(2)}\right|^2 + \left|H_1^{(2)}\right|^2 + i(-H_0^{(2)}\bar{H}_1^{(2)} + H_1^{(2)}\bar{H}_0^{(2)})}{\left|H_0^{(2)}\right|^2 + \left|H_1^{(2)}\right|^2 + i(H_0^{(2)}\bar{H}_1^{(2)} - H_1^{(2)}\bar{H}_0^{(2)})} \\ &= u_0^2 \frac{\left|H_0^{(2)}\right|^2 + \left|H_1^{(2)}\right|^2 - 4/(\pi\xi_0)}{\left|H_0^{(2)}\right|^2 + \left|H_1^{(2)}\right|^2 + 4/(\pi\xi_0)}. \end{aligned} \quad (2.6.24)$$

For typical values, ξ_0 is given by

$$\xi_0 \approx 0.57 \times 10^{-2} \left(\frac{h}{150 \text{ km}} \right) \left(\frac{\omega}{6\pi \times 10^{-3} \text{ Hz}} \right) \left(\frac{1 \text{ Mm s}^{-1}}{v_{A0}} \right).$$

For $\xi_0 \ll 1$, R can be approximated as

$$R = 1 - \pi\xi_0 + O(\xi_0^2), \quad (2.6.25)$$

where we use the maple file located at

[→ Maple/Chapter 2/reflection_coefficient.pdf](#),

to assist with the algebra.

Unity minus the reflection coefficient and its approximation are plotted in Figure 2.9. It shows that longer wavelength (or lower frequency) waves have larger reflection coefficients. If the wavelength of the wave is longer than the pressure scale height, h , then a large fraction of the wave energy will reflect at $z = 0$. If the wavelength is shorter than h , the waves mostly leak out of the corona into the chromosphere and photosphere.

2.7 Leaky loop: general solution

This section aims to calculate the general solution for a leaky loop, i.e. a loop where the reflection coefficient of the boundary is less than 1 and energy is able to leak out of the loop.

Since the loop is leaky, the boundary conditions can no longer be given by Equation (2.2.4). To precisely define our boundary conditions, we introduce a set of variables called Elsässer variables \mathcal{Z}^+ , \mathcal{Z}^- which are defined as

$$\mathcal{Z}^\pm = u \pm v_{A0} \frac{b}{B_0}. \quad (2.7.1)$$

From Equations (1.4.11) and (1.4.13) we know that

$$\begin{aligned} \frac{\partial u}{\partial t} &= \frac{v_{A0}^2}{B_0} \frac{\partial b}{\partial z}, \\ \frac{v_{A0}}{B_0} \frac{\partial b}{\partial t} &= v_{A0} \frac{\partial u}{\partial z}. \end{aligned} \quad (2.7.2)$$

Adding and subtracting the above equations gives

$$\frac{\partial \mathcal{Z}^\pm}{\partial t} \mp v_{A0} \frac{\partial \mathcal{Z}^\pm}{\partial z} = 0, \quad (2.7.3)$$

respectively. Equation (2.7.3) gives the 1D advection equation for negative propagating and positive propagating waves, respectively, where positive propagating waves travel in the positive z -direction. It shows that \mathcal{Z}^+ travels in the negative direction and \mathcal{Z}^-

travels in the positive direction. We define the boundary conditions as

$$\begin{aligned}\mathcal{Z}^+(-l_z, t) &= 2f_{driv}(t) - R\mathcal{Z}^+(-l_z, t), \\ \mathcal{Z}^+(l_z, t) &= -R\mathcal{Z}^-(l_z, t)\end{aligned}\tag{2.7.4}$$

where R is the reflection coefficient. Note that for $R = 1$ we recover Equation (2.2.4) since $u = (\mathcal{Z}^+ + \mathcal{Z}^-)/2$. The motivation for these boundary conditions is that each time a wave reaches $\pm l_z$ a fraction R of the amplitude is reflected.

The full solution with the boundary conditions given by (2.7.4) and initial conditions given by (2.2.5) is given by

$$u(z, t) = \sum_{k=0}^m (-1)^k R^k H(\theta_k) f_{driv}(\theta_k),\tag{2.7.5}$$

where θ_k is given by Equation (2.3.3) and m is given by Equation (2.3.5) which for convenience we write again here

$$\theta_k = t - (-1)^k \frac{z}{v_{A0}} - \frac{(2k+1)l}{v_{A0}},\tag{2.3.3}$$

$$m = \left\lfloor \frac{tv_{A0}}{L_z} \right\rfloor.\tag{2.3.5}$$

Note that this is almost the same as Equation (2.3.6) except a factor R^k has been introduced. From Equation (1.4.13) we know that b is given by

$$b(z, t) = -\frac{B_0}{v_{A0}} \sum_{k=0}^m R^k H(\theta_k) f_{driv}(\theta_k).\tag{2.7.6}$$

The solution is plotted in Figure 2.10 for the case where f_{driv} produces a pulse. The driver is given by

$$f_{driv} = u_0 \begin{cases} \sin^2(2\pi t/t_0), & t \leq t_0/2, \\ 0, & t > t_0/2, \end{cases}\tag{2.7.7}$$

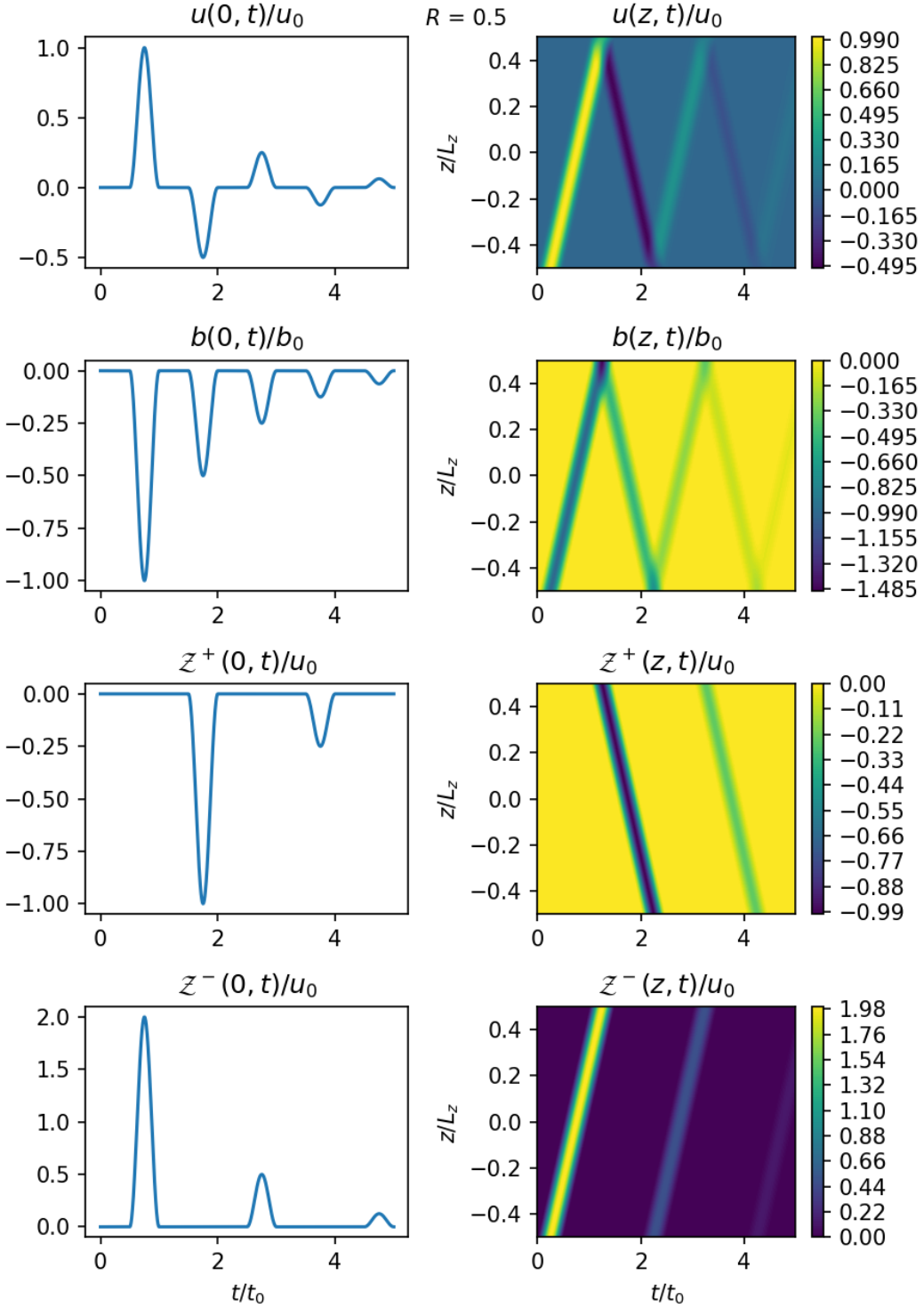


Figure 2.10: This figure plots u , b , \mathcal{Z}^+ , \mathcal{Z}^- for the case where $f_{driv}(t)$ is given by Equation (2.7.7) and this gives a pulse wave. Here the reflection coefficient is given by $R = 0.5$. Note that b_0 is given by Equation (2.4.26). The code used to make this figure is available on GitHub in the following directory:
[→ Python/Chapter2/leaky_pulse.py](#)

where t_0 is given by Equation (2.4.25). The reflection coefficient is given by $R = 0.5$. It shows that the amplitude of the waves reduces by a factor R each time it reflects at one of the boundaries. The figure confirms that \mathcal{Z}^- does indeed correspond to positive propagating waves and \mathcal{Z}^+ corresponds to negative propagating waves.

Figure 2.11 plots the solution for the case where f_{driv} produces a continuous sinusoidal wave. The driver is given by

$$f_{driv} = u_0 \sin(\pi t/t_0). \quad (2.7.8)$$

It confirms that the boundary conditions are satisfied since Equation (2.7.4) implies that

$$\begin{aligned} u(-l_z, t) &= f_{driv}(t) + \frac{1}{2}(1 - R)\mathcal{Z}^+(-l_z, t) \\ u(l_z, t) &= \frac{1}{2}(1 - R)\mathcal{Z}^-(l_z, t). \end{aligned} \quad (2.7.9)$$

The plots also suggest that waves saturate at a maximum amplitude despite being driven at the resonant frequency for $R < 1$. For $t \rightarrow \infty$ the amplitude of the waves saturates and the system oscillates at the driver frequency and we say it is at steady-state. The period in which the amplitude of the wave is changing is called the transient phase.

2.8 Leaky loop: steady state solution

At the end of the previous section, we suggested that for a continuous sinusoidal driver and $R < 1$, the system will evolve towards a steady-state. At steady-state, the system oscillates at the driver frequency, and the amplitude saturates at a constant value. This section aims to prove that this is true for all frequencies and calculate the amplitude of the waves at steady-state for a continuous sinusoidal driver.

Let f_{driv} be given by

$$f_{driv}(t) = u_0 \exp(i\omega t). \quad (2.4.1)$$

We seek the solution for $t \rightarrow \infty$, therefore, from Equation (2.7.5), we know that u is

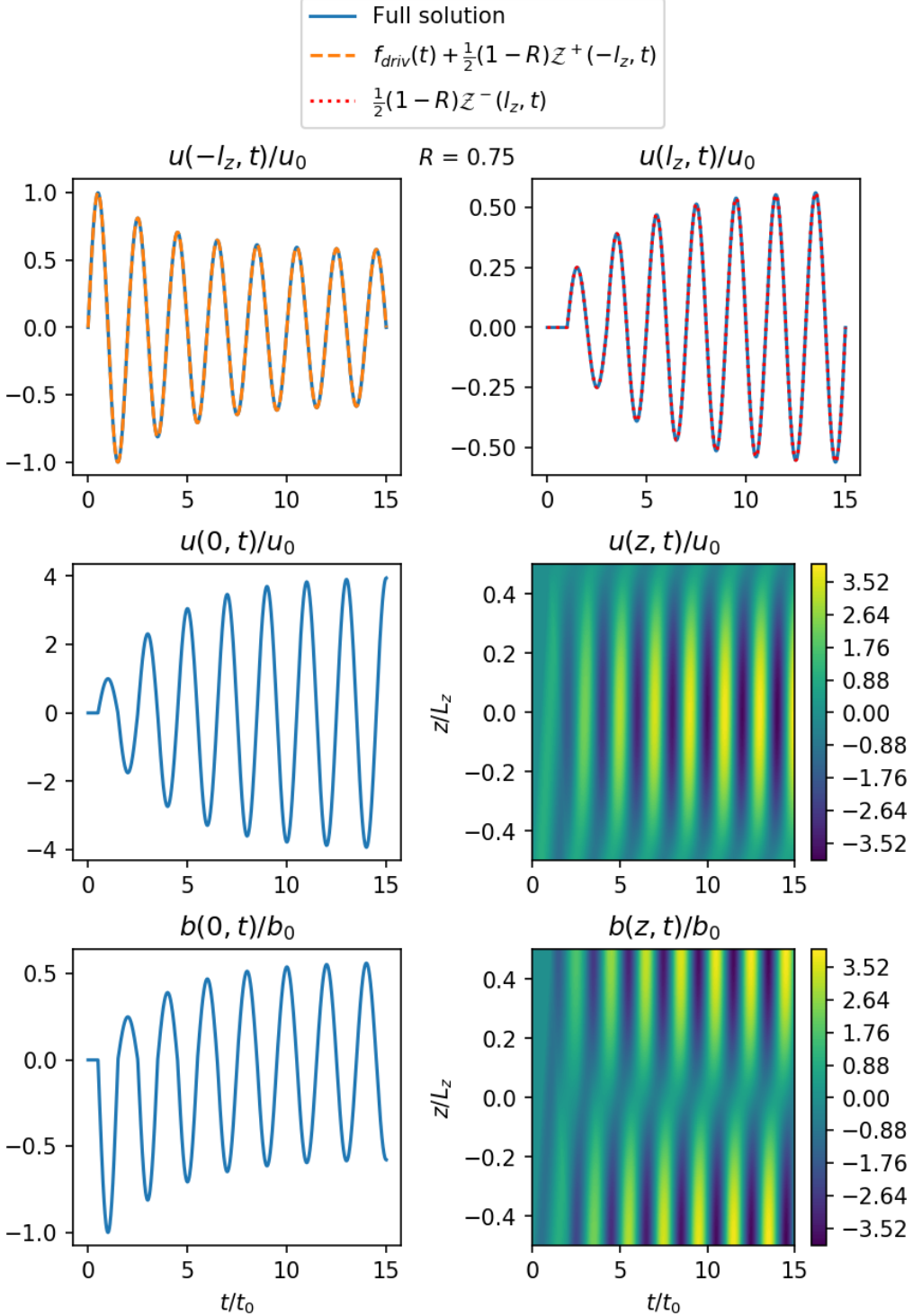


Figure 2.11: This figure plots u , b , \mathcal{Z}^+ , \mathcal{Z}^- for the case where $f_{driv}(t)$ is given by Equation (2.7.8) and this gives a continuous sinusoidal wave. Here the reflection coefficient is given by $R = 0.75$. The top row show plots at $z = -l_z$ (left) and $z = l_z$ (right) and they show that the boundary conditions given by Equation (2.7.4) are satisfied. The code used to make this figure is available on GitHub in the following directory:

→ [Python/Chapter2/leaky_wave.py](#)

given by

$$\begin{aligned} u(z, t) &= u_0 \sum_{k=0}^{\infty} (-1)^k R^k H(\theta_k) \exp(i\omega\theta_k) \\ &= u_0 \exp(i\omega[t - z/v_{A0} - l_z/v_{A0}]) \frac{1}{2} \sum_{k=0}^{\infty} (1 + (-1)^k) R^k \exp(-2i\omega l_z/v_{A0})^k - \\ &\quad u_0 \exp(i\omega[t + z/v_{A0} - l_z/v_{A0}]) \frac{1}{2} \sum_{k=0}^{\infty} (1 - (-1)^k) R^k \exp(-2i\omega l_z/v_{A0})^k. \end{aligned}$$

Using the formula for an infinite geometric series the steady state solution is given by,

$$u(z, t) = u_0 \exp(i\omega[t - l_z/v_{A0}]) \frac{\exp(-i\omega z/v_{A0}) - r \exp(i\omega z/v_{A0})}{1 - r^2}, \quad (2.8.1)$$

provided $R < 1$, where

$$r = R \exp(-2i\omega l_z/v_{A0}). \quad (2.8.2)$$

Using Equation (1.4.13) the magnetic field is given by

$$b = -\frac{B_0 u_0}{v_{A0}} \exp(i\omega[t - l_z/v_{A0}]) \frac{\exp(-i\omega z/v_{A0}) + r \exp(i\omega z/v_{A0})}{1 - r^2} \quad (2.8.3)$$

We can also calculate the steady-state solution via a numerical approach. This is useful to check that the analytic solution is correct. We seek the steady-state solution where the whole system oscillates at the driver frequency. Therefore, we can assume that the time dependence is given by $\exp(i\omega t)$. Assuming the time dependence implicitly, we can simplify the PDEs given by Equation (2.7.3) into the following ODEs,

$$\frac{dZ^\pm}{dz} = \pm i \frac{\omega}{v_{A0}} Z^\pm. \quad (2.8.4)$$

Note that this system of ODEs is coupled due to the boundary conditions given by Equation (2.7.4). We can solve this boundary value problem numerically using `solve_bvp` in [Virtanen et al. \(2020\)](#). In Figure 2.12 we plot the real and imaginary parts of the steady state velocity, u , and magnetic field, b as a function of z at $t = 0$. For each plot $R = 0.9$. The top-row plots the solution for $\omega = 0$. The second row plots the solution

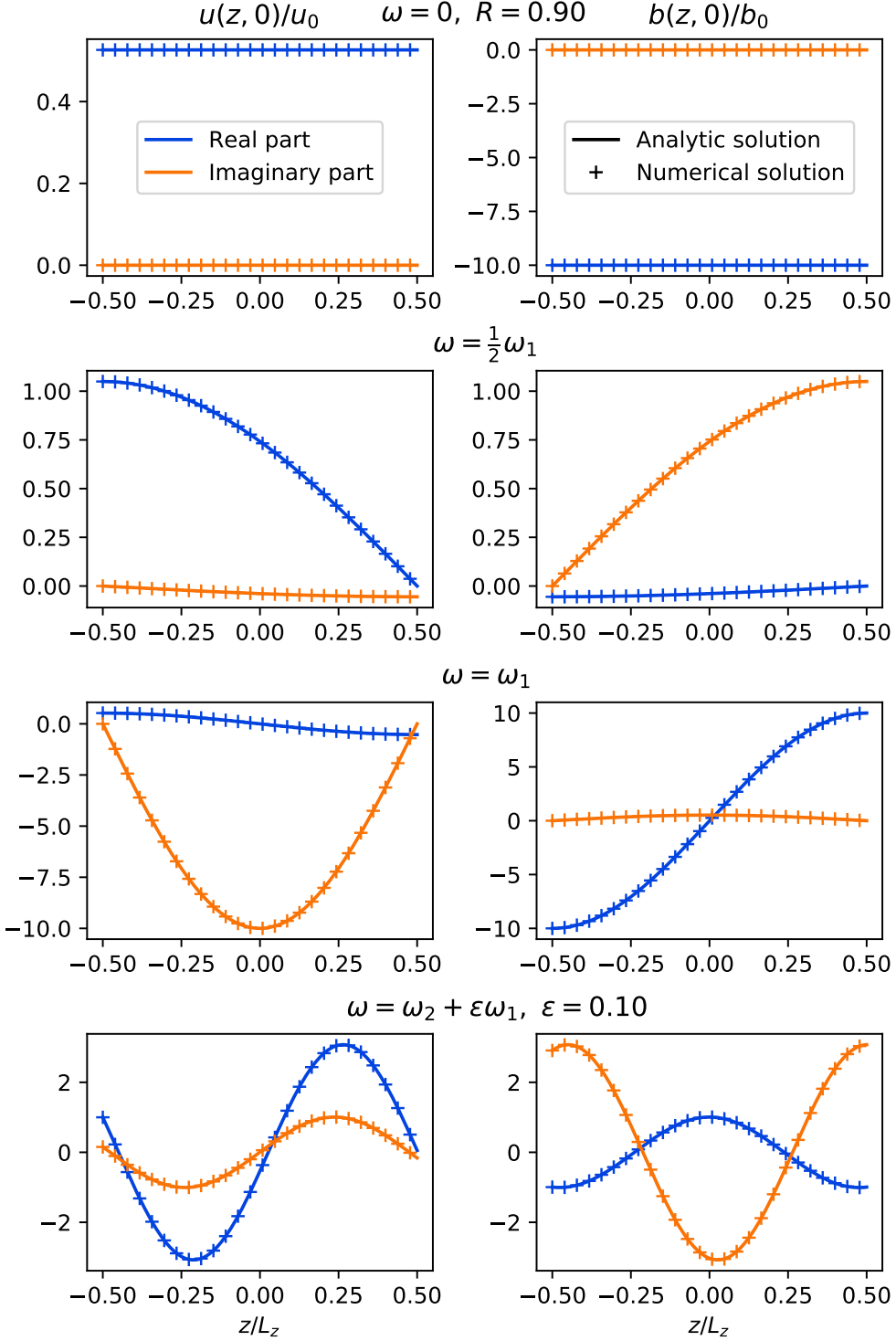


Figure 2.12: This figure shows plots of the steady state velocity (left) and magnetic field (right) along z . In each row a different frequency driver is used. The analytic solutions (solid line) were calculated using Equations (2.8.1) and (2.8.3). The numerical solutions (+ symbols) were calculated by solving the boundary value problem described by Equation (2.8.4) using `solve_bvp` in [Virtanen et al. \(2020\)](#).

The code used to make this figure is available on GitHub in the following directory:

→ [Python/Chapter2/steady_state_soln.py](#)

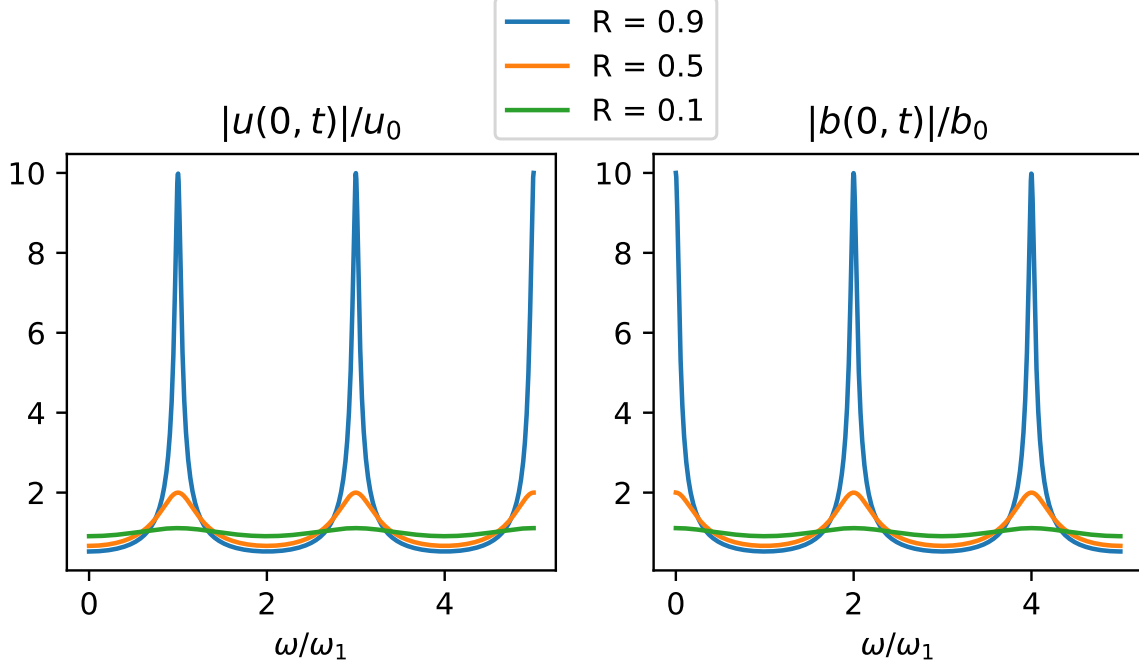


Figure 2.13: This figure shows plots of the absolute value of the velocity and magnetic field at $z = 0$ as a function of the driver frequency, ω , for $R = 0.9, 0.5$ and 0.1 . The absolute values were calculated using Equations (2.8.7) and (2.8.8). Note that b_0 is given by Equation (2.4.26). The code used to make this figure is available on GitHub in the following directory:

[→ Python/Chapter2/steady_state_soln_at_z=0.py](#)

for $\omega = \omega_1/2$, where ω_1 is the fundamental resonant frequency, see Equation (2.4.19). The third row plots the solution for $\omega = \omega_1$. Finally, the last row plots the solution for $\omega = \omega_2 + 0.1\omega_1$. They show that the numerical and analytic solutions agree and this suggests that Equations (2.8.1) and (2.8.3) are accurate.

At $z = 0$, Equation (2.8.1) can be simplified to give

$$u(0, t) = u_0 \exp(i\omega[t - l_z/v_{A0}]) \frac{1}{1+r}, \quad (2.8.5)$$

and Equation (2.8.3) gives

$$b(0, t) = -\frac{B_0 u_0}{v_{A0}} \exp(i\omega[t - l_z/v_{A0}]) \frac{1}{1-r}. \quad (2.8.6)$$

Therefore, the absolute value of $u(0, t)$ is given by

$$|u(0, t)| = \frac{u_0}{\sqrt{R^2 + 2R \cos(2\omega l_z/v_{A0}) + 1}}, \quad (2.8.7)$$

and the absolute value of $b(0, t)$ is given by

$$|b(0, t)| = \frac{B_0 u_0 / v_{A0}}{\sqrt{R^2 - 2R \cos(2\omega l_z / v_{A0}) + 1}}. \quad (2.8.8)$$

In Figure 2.13 we use Equations (2.8.7) and (2.8.8) to plot the absolute value of the steady state velocity, u and magnetic field b at $z = 0$ as function of the driver frequency, ω . The values are shown for $R = 0.9, 0.5$ and 0.1 . It shows that as $R \rightarrow 1$ then the absolute value goes to infinity at the resonant frequencies.

2.9 Open loop: phase mixing

This chapter has modelled the plasma as ideal, i.e. we have neglected resistivity and viscosity. We justify this because the Reynolds numbers for observed wavelengths is much greater than unity, see Equations (1.3.38) and (1.3.52). This section introduces a mechanism, namely phase mixing, that can generate very short length-scales, resulting in very small Reynolds numbers. Phase mixing is the process where gradients perpendicular to the field build-up due to Alfvén waves propagating on field lines with a spatial gradient in Alfvén travel time. Where the Alfvén travel time is the time it takes for Alfvén waves to propagate along the loop over a given distance. To illustrate phase mixing, we calculate the time evolution of driven Alfvén waves propagating in an open domain where $v_A = v_A(x)$.

We introduce an x -dependence, i.e. let

$$u = u(x, z, t), \quad b = b(x, z, t), \quad v_{A0} = v_A(x).$$

Note that the magnetic field is still given by Equation (1.4.6). We impose a driver at $z = 0$ and impose open boundary conditions. Hence, $\mathcal{Z}^+ = 0$, i.e. the solution can only contain solutions propagating in the positive z -direction. Therefore, $u = \mathcal{Z}^-/2$, and substituting this into Equation (2.7.3) gives

$$\frac{\partial u}{\partial t} + v_A(x) \frac{\partial u}{\partial z} = 0. \quad (2.9.1)$$

We aim to solve Equation (2.9.1) with the following initial condition

$$u(x, z, 0) = 0, \quad (2.9.2)$$

and boundary condition

$$u(x, 0, t) = f_{driv}(x, t). \quad (2.9.3)$$

This has the solution

$$u(x, z, t) = H\left(t - \frac{z}{v_A(x)}\right) f_{driv}\left(x, t - \frac{z}{v_A(x)}\right). \quad (2.9.4)$$

Consider the case where

$$f_{driv}(x, t) = u_0 \sin(\omega t), \quad (2.9.5)$$

and

$$v_A(x) = v_{A0} \left(1 + \frac{x}{L_x}\right), \quad (2.9.6)$$

where $x > -L_x$. Hence,

$$u(x, z, t) = u_0 H\left(t - \frac{z}{v_A(x)}\right) \sin\left[\omega\left(t - \frac{z}{v_A(x)}\right)\right]. \quad (2.9.7)$$

We plot this solution in Figure 2.14. It shows the velocity at different snapshots. Note that in Figure 2.14

$$T = \frac{2\pi}{\omega}, \quad L_x = \frac{2\pi}{\omega} v_{A0}.$$

The top row shows the solution at $t = T/4$, the second row is at $t = 11T/4$, the third row is at $t = 21T/4$ and the bottom row is at $t = 31T/4$. The left side shows plots along x at $z = z_0$ where z_0 is given by

$$z_0 = v_{A0} \left(t - \frac{T}{4}\right).$$

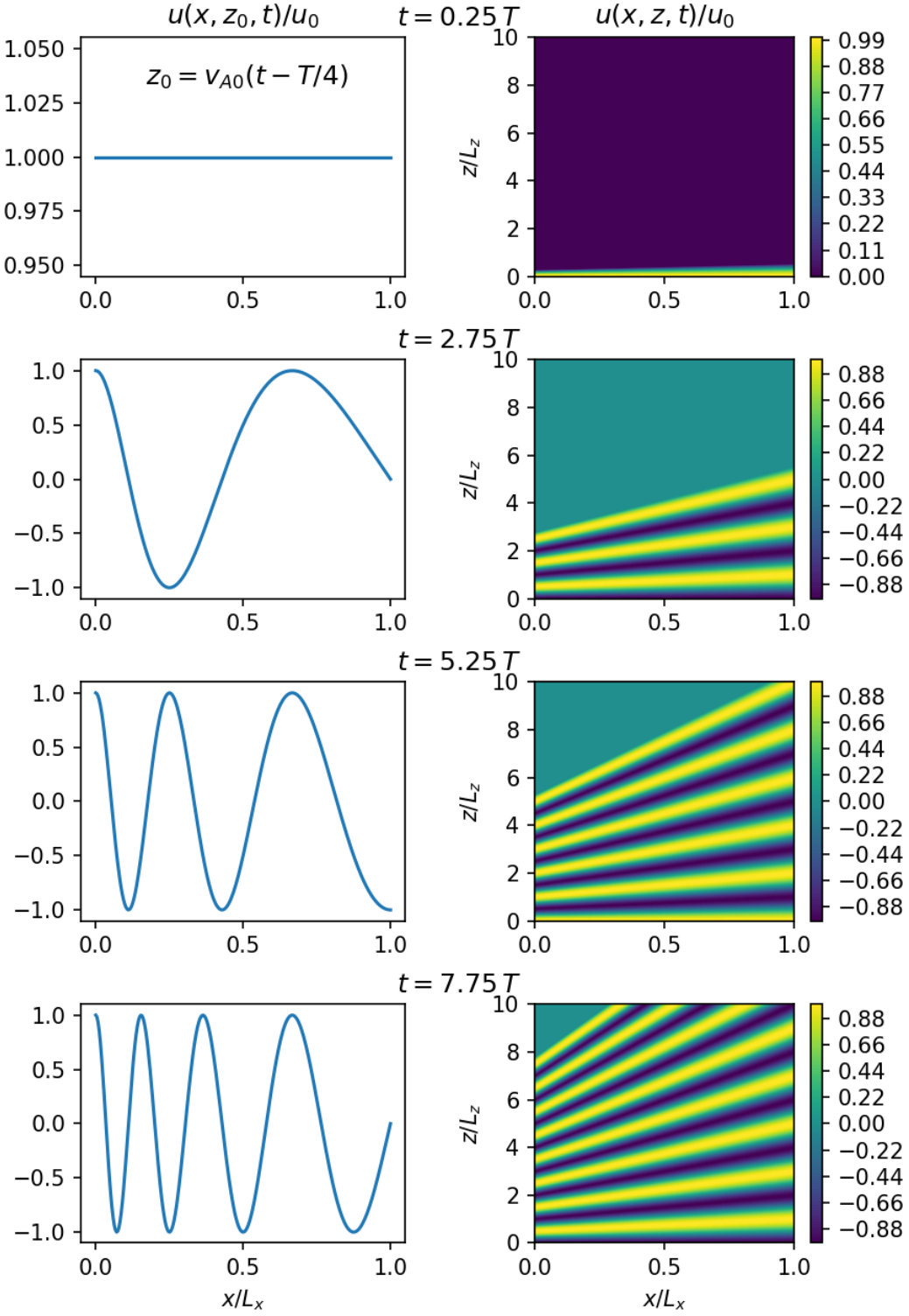


Figure 2.14: This figure shows snapshots of the velocity, where each row corresponds to a different time. The left side plots the velocity as a function of x at $z = z_0$, where z_0 is given by the expression in the top-left plot. The right side shows a contour plot of the velocity as a function of x and z .

The code used to make this figure is available on GitHub in the following directory:

→ [Python/Chapter2/phase_mixing.py](#)

The right side shows contour plots of the velocity as a function of x and z . They show that the length-scale in x gets shorter as the wave propagates further along. Consider the plots on the left side, the top plot is equal to a constant value in x , we think of this as a curve with only one peak, the second plot has two peaks, the third plot has three peaks, and the bottom plot has four peaks. To quantify the rate at which the length-scales decrease, consider the following. Assume, $t > z/v_A(x)$, hence,

$$u(x, z, t) = u_0 \sin \left[\omega \left(t - \frac{z}{v_A(x)} \right) \right]. \quad (2.9.8)$$

Taking the x -derivative gives

$$\frac{\partial u}{\partial x} = u_0 \omega \frac{dv_A}{dx} \frac{z}{v_A^2} \cos \left[\omega \left(t - \frac{z}{v_A(x)} \right) \right]. \quad (2.9.9)$$

This shows that the gradients in x grow linearly with z .

2.10 Discussion and conclusions

In this chapter, our goal was to introduce some key properties of ideal footpoint driven Alfvén waves relevant for the rest of this thesis. In Section 2.3 we showed how d'Alembert's formula and a method of images approach can be used to calculate the general solution in a closed loop. In Section 2.4 we showed that if the driver is of the form $\exp(i\omega t)$ then the general solution can be simplified using the geometric series formula. We showed that if the driving frequency is equal to one of the natural frequencies, i.e. $\omega = \omega_n$, (where ω_n is given by Equation 2.4.19), then the energy of the solution will grow quadratically and unbounded in time. If $\omega \neq \omega_n$ then the solution will oscillate about a finite value. We showed in Figures 2.1 and 2.2 that if the driver frequency equals the zeroth harmonic, $\omega = \omega_0 = 0$, then then only the magnetic energy grows to infinity and the kinetic energy oscillates about a finite value. Whereas, for the other harmonics, i.e. ω_n for $n \geq 1$, both the kinetic and magnetic kinetic energy grows to infinity. If $\omega = \omega_0$ then the velocity of the driver never changes sign, which stretches the magnetic field, resulting in a large build-up of magnetic energy for a small amount of kinetic energy. If $\omega = \omega_n$ for $n \geq 1$ then a standing wave is set up and this has approximately equal magnetic and kinetic energy (averaged over one wave period).

The sinusoidal driver is useful because it is relatively easy to calculate the exact solution. In reality, the photosphere will excite a range of frequencies, and this can be modelled by superimposing sinusoidal solutions via a Fourier series approach. In Section 2.5 we calculate the solution for a broadband driver, i.e. a driver which excites a broad range of frequencies. In Section 2.5.1 we assumed a Fourier series solution in z to convert the Alfvén wave equation, a PDE, into a set of ODEs for a driven harmonic oscillator. We calculated the exact solution for a red noise force and white noise force driver (in Section 2.5.3, we define red and white noise). We also estimated the solutions with a red and white noise force driver by approximating them with a finite Fourier series. Figure 2.7 compares the exact and approximate solutions and show they converge as the number of harmonics increases. The error shows a steep reduction if the resonant harmonic is excited. Note that red and white noise force drivers are unphysical because they have an infinite variance. However, they are still useful concepts because it is simple to calculate an exact analytic solution using a red and white noise force driver (see Section 2.5.3). Moreover, the approximate solutions in Figure 2.7 have a finite variance and show similar results. Results from Section 2.5 show that the variance and energy grow linearly when either a red noise or white noise force driver is used. Whereas in Section 2.4 we showed that if a sinusoidal driver is used with $\omega = \omega_n$, the energy grows quadratically with time.

In Sections 2.3-2.5 we used line-tied boundary conditions. These boundary conditions are motivated by the fact that the chromosphere is significantly denser than the corona. However, despite the large change in density, a small fraction of the waves will leak from the corona into the chromosphere. In Section 2.6 we calculate an estimate for the reflection coefficient using a similar model to that used in Hollweg (1984b). Figure 2.8 plots the reflection coefficient as a function of frequency. It shows that the higher the frequency (i.e. shorter wavelength), the more the waves leak out of the corona. In Section 2.7 we calculate the general solution for waves in a leaky loop. We show that the solution evolves towards a state where the whole system oscillates at the driver frequency, and this is called the steady-state solution. In Section 2.8 for a sinusoidal driver and confirm it numerically in Figure 2.12. Figure 2.13 shows that the steady-state solution's amplitude is largest at the resonant frequencies and tends to infinity as the reflection coefficient, R , goes to 1. Note that the timescale to reach steady-state also grows to infinity as $R \rightarrow 1$, and so we recover the closed-loop solution as $R \rightarrow 1$.

Finally, in Section 2.9 we introduce a phenomenon called phase mixing. Figure 2.14 shows if neighbouring field lines have different Alfvén speeds, this can result in Alfvén waves moving out of phase with their neighbours as they evolve. This results in the growth of steep gradients perpendicular to the field, which may be important in coronal heating, we discuss this further in the next chapter.

Chapter 3

Resistive phase-mixed Alfvén waves

This chapter contains work which has been adapted from [Prokopyszyn and Hood \(2019\)](#).

3.1 Introduction

At the end of the previous chapter, we introduced phase-mixing. We saw that very short-length-scales can build up when Alfvén waves propagate along field lines with different Alfvén travel times. Since each field line has different Alfvén travel times, this can lead to waves moving out of phase with their neighbours. This suggests that the ideal assumption we made in the previous chapter may no longer be valid. Moreover, it has been suggested in, for example, [Heyvaerts and Priest \(1983\)](#) that phase-mixed Alfvén waves could play a significant role in coronal heating.

Phase mixing has been researched extensively since [Heyvaerts and Priest \(1983\)](#) first proposed it as a coronal heating mechanism. For example, [Browning and Priest \(1984\)](#), expanded on the [Heyvaerts and Priest \(1983\)](#) work related to the Kelvin-Helmholtz instability. They show that standing phase-mixed Alfvén waves are unstable to the Kelvin-Helmholtz instability and will undergo a turbulent cascade, leading to enhanced dissipation of energy. In for example, [De Moortel et al. \(2000\)](#) and [Smith et al. \(2007\)](#) they study phase mixing in a stratified and divergent magnetic field. [Similon and Sudan \(1989\)](#) and [Howson et al. \(2019\)](#) study phase mixing in a complex magnetic field. [Hood et al. \(1997, 2002\)](#) investigate phase mixing in coronal holes and calculate a self-similar solution which enables them to analyse a more general class of solutions. They

find that a single pulse decays algebraically rather than exponentially. In McLaughlin et al. (2011); McLaughlin (2013); Prokopyszyn et al. (2019) they study phase mixing of nonlinear Alfvén waves near 2D x-type null points. In Nakariakov et al. (1997) they show that nonlinearities lead to the formation of fast waves which can help transport energy onto neighbouring field lines. Phase mixing has also been investigated in 3D (Magyar et al., 2017) and 3D coronal loops (Pagano and De Moortel, 2017; Pagano et al., 2018).

In this chapter, we aim to answer whether the phase-mixing of Alfvén waves plays an important or negligible role in coronal heating? To help answer this question, we introduce a term called the heating rate per unit of wave energy in a loop, denoted with γ . We define γ as the ratio of the integrated time-averaged heating rate along a loop over the wave energy of the loop, i.e.

$$\gamma = \frac{\left\langle \int_C \boldsymbol{\sigma}_{Brag} : \nabla u + j^2/\sigma dl \right\rangle}{\frac{1}{2} \left\langle \int_C \rho u^2 + b^2/\mu dl \right\rangle}, \quad (3.1.1)$$

where C is a contour of a given coronal loop and $\langle \rangle$ denotes the time average. Note that γ is closely related to the damping coefficient used in the equation to describe damped harmonic oscillators. The equation for a damped harmonic oscillator, with amplitude $x(t)$, is given by

$$\frac{d^2x}{dt^2} + \gamma_0 \frac{dx}{dt} + \omega_0^2 x = 0. \quad (3.1.2)$$

Multiplying through by dx/dt gives

$$\frac{d}{dt} \left[\frac{1}{2} \left(\frac{dx}{dt} \right)^2 + \frac{1}{2} \omega_0^2 x^2 \right] = -\gamma_0 \left(\frac{dx}{dt} \right)^2. \quad (3.1.3)$$

Note that the time average of the potential energy, $\langle \omega_0^2 x^2/2 \rangle$, is approximately equal to the time average of the kinetic energy, $\langle (\partial x/\partial t)^2/2 \rangle$, therefore, the heating rate over the kinetic and potential energy is given by

$$\gamma_0 \approx \frac{\gamma_0 \langle (\partial x/\partial t)^2 \rangle}{\frac{1}{2} \langle (\partial x/\partial t)^2 + \omega_0^2 x^2 \rangle}. \quad (3.1.4)$$

Therefore, γ and γ_0 satisfy very similar definitions, which explains why γ is closely related to the damping rate of the waves. Note that Hollweg (1984a,b) uses a very similar idea to γ except he uses a quantity called the quality factor, from resonance theory, which is approximately given by ω/γ , where ω is the angular frequency of a wave. We focus on using γ because it is easier to apply to a system in which multiple frequencies are excited. Arregui (2015) also discusses a similar idea. He argues (through an order magnitude analysis) that phase mixing could take too long to reach the required length scales for the heating rate to become important.

We can estimate the conductive and radiative losses (Withbroe and Noyes, 1977) and the wave energy (McIntosh et al., 2011; McIntosh and De Pontieu, 2012) in the corona. Using these values, we can approximate the value γ needs to satisfy for the conductive and radiative energy losses to be balanced by the viscous and Ohmic dissipation of the observed waves. This gives the required value of γ for coronal heating and we will compare it with the value of γ predicted by phase-mixing theory. This is how we will test if phase mixing can play a significant role in coronal heating. In Section 3.6 we estimate an upper bound for the γ predicted by phase-mixing theory by ensuring any simplifications made act to increase the value of γ . If our upper bound is too small, we can conclude that phase-mixing plays a negligible role in coronal heating. If the upper bound is equal to or larger than the required γ then this means phase-mixing could play an important role. However, we would need a more realistic model to know for sure. In this section, we will calculate the required value of γ in a closed loop.

We can estimate the conductive and radiative losses in a closed coronal loop via a theoretical and observational approach. We will first calculate the theoretical energy losses and then check them with the observations given by Withbroe and Noyes (1977). If we assume the radiative loss function can be approximated with

$$Q(T) = \chi T^{-1/2}, \quad (3.1.5)$$

where $\chi = 10^{-32} \text{ K}^{1/2} \text{ W m}^3$, then Priest (2014) shows that to maintain a loop with a

uniform pressure, p , with a uniform heating rate, H_c , then H_c must satisfy

$$\begin{aligned} H_c &= \frac{7}{8} \frac{\chi}{k_B^2} \frac{p^2}{T_{max}^{5/2}} \\ &\approx 4.59 \times 10^{-6} \left(\frac{\chi}{10^{-32} \text{ K}^{1/2} \text{ W m}^3} \right) \left(\frac{p}{10^{-2} \text{ Pa}} \right)^2 \left(\frac{10^6 \text{ K}}{T_{max}} \right)^{5/2} \text{ W m}^{-3} \end{aligned} \quad (3.1.6)$$

Table 1.1 shows the power losses due to conduction, radiation and solar wind per unit area in the corona. The table gives the power per unit area, whereas our theoretical calculation is per unit volume. Therefore, we need to integrate our theoretical calculation in the radial direction. We model the temperature as uniform in the radial direction and assume the pressure satisfies hydrostatic balance. In other words, we assume that

$$p = p_0 \exp(-r/h), \quad (3.1.7)$$

where h is the pressure scale height given by Equation (2.6.2). Note that for typical values ($m = m_p/2$, $g_\odot = 274 \text{ m}^2 \text{ s}^{-1}$) the pressure scale height is given by

$$h \approx 0.60 \times 10^8 \left(\frac{T}{10^6 \text{ K}} \right) \text{ m} \quad (3.1.8)$$

Most heating will occur within a height $2h$ of the solar surface, the radius of the Sun is about $0.70 \times 10^9 \text{ m}$ (Stanford Solar Center, 2019) which is greater than h . Therefore, the error associated with approximating the gravitational field strength as uniform will be small. We now need to integrate Equation (3.1.6) in the radial direction from r_0 to r_1 , where r_0 gives the radial coordinate of the base of the corona and r_1 gives the coordinate of the top of the corona. The height of the corona is not clearly defined, however, we know that $r_1 - r_0 \gg h$, therefore, we can approximate $r_1 \rightarrow \infty$. Hence, the integral of Equation (3.1.6) is given by

$$\begin{aligned} \int_{r_0}^{\infty} H_c dr &= \frac{h}{2} \frac{7}{8} \frac{\chi}{k_B^2} \frac{p(r_0)^2}{T_{max}^{5/2}} \\ &\approx 1.38 \times 10^2 \left(\frac{\chi}{10^{-32} \text{ K}^{1/2} \text{ W m}^3} \right) \left(\frac{p(r_0)}{10^{-2} \text{ Pa}} \right)^2 \left(\frac{10^6 \text{ K}}{T_{max}} \right)^{3/2} \text{ W m}^{-2}. \end{aligned} \quad (3.1.9)$$

Note that Table 1.1, shows that the energy losses are of the order $[10^2, 10^4] \text{ W m}^{-2}$ and

our calculation above lies in this range. Therefore, the theoretical and observational calculations are in approximate agreement.

In McIntosh et al. (2011); McIntosh and De Pontieu (2012), they observe velocity wave amplitudes, u_0 , in the quiet sun of around 20 km s^{-1} and in active regions of around 5 km s^{-1} . We can use this data to estimate the coronal wave energy by assuming the time-averaged kinetic energy associated with the waves equals the time-averaged magnetic perturbation energy. This gives a wave energy, E_{wave} , of approximately

$$\begin{aligned} E_{wave} &\approx \rho \langle u_0 \rangle^2 \\ &\approx 10^{-4} \left(\frac{\rho}{10^{-12} \text{ kg m}^{-3}} \right) \left(\frac{\langle u_0 \rangle}{10^4 \text{ m s}^{-1}} \right)^2 \text{ J m}^{-3}. \end{aligned} \quad (3.1.10)$$

Therefore, the value γ needs to satisfy for the conductive and radiative energy losses to be balanced by the viscous and Ohmic dissipation of the observed waves is given by

$$\begin{aligned} \gamma &= \frac{H_c}{E_{wave}} \\ &= \frac{7}{2} \frac{\chi}{m_p^2 T_{max}^{1/2}} \frac{\rho}{\langle u_0 \rangle^2} \\ &\approx 1.25 \times 10^{-1} \left(\frac{\rho}{10^{-12} \text{ kg m}^{-3}} \right) \left(\frac{10^6 \text{ K}}{T_{max}} \right)^{1/2} \left(\frac{10^4 \text{ m s}^{-1}}{\langle u_0 \rangle} \right)^2 \text{ s}^{-1}. \end{aligned} \quad (3.1.11)$$

Therefore, the γ predicted by phase-mixing needs to be of the order 10^{-1} s^{-1} for it to provide an important role in coronal heating.

3.2 Model and equations

This chapter will model perturbations on a background medium. We assume the system is linear and we make the same assumptions as described by Equations (1.4.3)-(1.4.5). We will model the background quantities as uniform in z . The background magnetic field points in the z -direction, i.e.

$$\mathbf{B}_0 = B_0 \hat{\mathbf{z}}. \quad (1.4.6)$$

We model the background Alfvén speed to be a function of x , i.e. $v_A = v_A(x)$.

If we assume $\mathbf{u} = u(x, y, z, t)\hat{\mathbf{y}}$ and $\mathbf{b} = b(x, y, z, t)\hat{\mathbf{y}}$ then the viscous heating associated with $\mathbf{W}^{(0)}$ becomes

$$\eta_0 \mathbf{W}^{(0)} : \nabla \mathbf{u} = \frac{\eta_0}{3} \left(\frac{\partial u}{\partial y} \right)^2, \quad (3.2.1)$$

where $\mathbf{W}^{(0)}$ is given by Equation (1.3.23). We assume the y -direction is invariant, i.e. $\partial/\partial y = 0$. This prevents mode coupling between u_x and u_y . Parker (1991) argues that this mode conversion is important and should not be neglected. However, in Chapter 4 we find that at resonant locations the mode conversion is one-way from fast to Alfvén waves. Therefore, the results presented in this chapter are relevant at these resonant locations (which are discussed in greater detail in Chapter 4). Some coronal arcades have an approximate invariant direction, and some flux tubes can be azimuthally invariant. Assuming $\partial/\partial y = 0$ prevents the development of MHD instabilities. In Heyvaerts and Priest (1983), they show that, for $\partial/\partial y \neq 0$, standing phase-mixed Alfvén waves are unstable to the Kelvin-Helmholtz and tearing instabilities. Hence we assume, $\partial/\partial y = 0$ which prevents viscous heating due to gradients in the y -direction (see Equation 3.2.1).

We solve for the y -component of the velocity, given by

$$\mathbf{u}(x, z, t) = u(x, z, t)\hat{\mathbf{y}}, \quad (2.2.2)$$

and the y -component of the perturbed magnetic field, given by

$$\mathbf{b}(x, z, t) = b(x, z, t)\hat{\mathbf{y}}. \quad (2.2.3)$$

The y -component of the linearised momentum equation, see Equation (1.3.18), is given by

$$\begin{aligned} \frac{\partial u}{\partial t} &= \frac{v_A^2(x)}{B_0} \frac{\partial b}{\partial z} + \frac{1}{\rho} \hat{\mathbf{y}} \cdot \nabla \cdot \boldsymbol{\sigma}_{Brag} \\ &\approx \frac{v_A^2(x)}{B_0} \frac{\partial b}{\partial z} + \frac{\eta_1}{\rho} \frac{\partial^2 u}{\partial x^2} + \frac{\eta_2}{\rho} \frac{\partial^2 u}{\partial z^2}. \end{aligned} \quad (3.2.2)$$

where $\boldsymbol{\sigma}_{Brag}$ is given by Equation (1.3.23), the plasma pressure and magnetic pressure terms are set to zero because the y -direction is invariant. Note that when calculating $\nabla \cdot \boldsymbol{\sigma}_{Brag}$, we ignored the derivatives associated with the coefficients, η_0, η_1, \dots etc. as

we expect our waves to phase mix and so we expect $|(\partial u / \partial x) / u| \gg |(\partial \eta_0 / \partial x) / \eta_0|$. The equations above show that after linearising the Braginskii viscous tensor, the contribution from the parallel component, $\eta_0 \mathbf{W}^{(0)}$, and the drift terms, $\eta_3 \mathbf{W}^{(3)}, \eta_4 \mathbf{W}^{(4)}$ is zero. This result and a discussion on the linearised Braginskii viscous stress tensor are given in, for example, Ruderman et al. (2000); Mocanu et al. (2008). Equations (1.3.31) to (1.3.33) show that η_0 is usually much greater than η_1 and η_2 . Equation (1.3.36) shows that we estimate η_0 to be a factor 10^{10} greater. By linearising the viscous stress tensor we could be neglecting the dominant term. However, this chapter aims to study linear waves only and in Section 3.6 we investigate the parameter space in which this linearization is justified. We intend to study phase mixing, which is a concept we introduced in Section 2.9, so we make another assumption which is to assume $\partial/\partial x \gg \partial/\partial z$. Therefore, we simplify Equation (3.2.2) further to give

$$\frac{\partial u}{\partial t} = \frac{v_A^2(x)}{B_0} \frac{\partial b}{\partial z} + \nu \frac{\partial^2 u}{\partial x^2}, \quad (3.2.3)$$

where we set $\nu = \eta_1/\rho$ to keep the notation tidy.

The y -component of the linearised induction equation, see Equation (1.3.48), is given by

$$\frac{\partial b}{\partial t} = B_0 \frac{\partial u}{\partial z} + \underbrace{\eta \nabla^2 b - \hat{\mathbf{y}} \cdot \nabla \times \left(\frac{1}{n_e e} \mathbf{j} \times \mathbf{B} \right)}_{\text{Hall term}}. \quad (3.2.4)$$

As above, we simplify this equation further by assuming that $\partial/\partial x \gg \partial/\partial z$ to give

$$\frac{\partial b}{\partial t} = B_0 \frac{\partial u}{\partial z} + \eta \frac{\partial^2 b}{\partial x^2}. \quad (3.2.5)$$

Note that we have neglected the Hall term because it is only dependent on derivatives which are parallel to the background magnetic field (for our system). In, for example, Threlfall et al. (2017) they investigate the effects of the Hall term on phase mixing. They find that introduction of the Hall terms results in wave dispersion which reduces the heating rate per unit of wave energy, γ . We aim to show that linear phase mixed Alfvén waves at observed wavelengths have an insufficient γ to heat the corona. Therefore, if γ is insufficient without the Hall term, we know it must be insufficient with the Hall

term.

Substituting Equation (3.2.5) into the time derivative of Equation (3.2.3) gives

$$\frac{\partial^2 u}{\partial t^2} = v_A^2(x) \frac{\partial^2 u}{\partial z^2} + v_A^2(x) \frac{\partial^2}{\partial x^2} \left(\frac{\eta}{B_0} \frac{\partial b}{\partial z} \right) + \nu \frac{\partial}{\partial t} \frac{\partial^2 u}{\partial x^2}.$$

Note that

$$\begin{aligned} \frac{\partial^2}{\partial x^2} \left(\frac{\eta}{B_0} \frac{\partial b}{\partial z} \right) &= \frac{\partial^2}{\partial x^2} \left[\frac{\eta}{v_A^2(x)} \left(\frac{\partial u}{\partial t} - \nu \frac{\partial^2 u}{\partial x^2} \right) \right] \\ &\approx \frac{\eta}{v_A^2(x)} \frac{\partial}{\partial t} \frac{\partial^2 u}{\partial x^2}, \end{aligned}$$

where we assume that η and ν are small factors such that their products are negligible. Moreover, we assume that $|(\partial u / \partial x) / u| \gg |(\partial v_A / \partial x) / v_A|$ and so we get the approximation above. Using the above two equations we get

$$\frac{\partial^2 u}{\partial t^2} - v_A^2(x) \frac{\partial^2 u}{\partial z^2} = (\eta + \nu) \frac{\partial}{\partial t} \frac{\partial^2 u}{\partial x^2}. \quad (3.2.6)$$

Equation (3.2.3) can be written as

$$\frac{\partial u}{\partial t} = v_A(x) \frac{\partial \hat{b}}{\partial z} + \nu \frac{\partial^2 u}{\partial x^2},$$

where

$$\hat{b}(x, z, t) = \frac{v_A(x)}{B_0} b(x, z, t). \quad (3.2.7)$$

Also if we assume $|(\partial b / \partial x) / b| \gg |(\partial v_A / \partial x) / v_A|$ then we can approximate Equation (3.2.5), multiplied by $v_A(x) / B_0$ as

$$\frac{\partial \hat{b}}{\partial t} = v_A(x) \frac{\partial u}{\partial z} + \eta \frac{\partial^2 \hat{b}}{\partial x^2}.$$

Combining the above equations gives

$$\frac{\partial Z^\pm}{\partial t} \mp v_A(x) \frac{\partial Z^\pm}{\partial z} = \nu_+ \frac{\partial^2 Z^\pm}{\partial x^2} + \nu_- \frac{\partial^2 Z^\mp}{\partial x^2}, \quad (3.2.8)$$

with \mathcal{Z}^\pm is given by

$$\mathcal{Z}^\pm(x, z, t) = u(x, z, t) \pm \frac{v_A(x)}{B_0} b(x, z, t), \quad (2.7.1)$$

and ν_\pm is given by

$$\nu_\pm = \frac{1}{2}(\eta \pm \nu). \quad (3.2.9)$$

In this chapter, we will solve the above equations for various boundary conditions. In Section 3.3 we solve the above equations for the case where the boundaries are open, in Section 3.4 we consider a closed-loop and in Section 3.5 we study a leaky loop. In all sections, we will have a driver at the bottom boundary ($z = 0$) given by

$$\begin{aligned} u(x, 0, t) &= f_{driv}(x, t) \\ &= f_0 \exp(i\omega t). \end{aligned} \quad (3.2.10)$$

We will impose Neumann boundary conditions in x , i.e.

$$\left. \frac{\partial u}{\partial x} \right|_{x=x_{min}} = \left. \frac{\partial u}{\partial x} \right|_{x=x_{max}} = 0. \quad (3.2.11)$$

Our initial conditions are

$$u(x, z, 0) = b(x, z, 0) = 0. \quad (3.2.12)$$

For our numerical solutions, the background Alfvén speed is given by

$$v_A(x) = v_{A0} \left[1 + \frac{x}{a_0} \right], \quad (3.2.13)$$

however, for our analytic solutions we will assume the more general form, namely, $v_A = v_A(x)$.

We seek the steady-state solution, where the solution oscillates at the driver frequency. Therefore, we assume a time-dependence of the form $\exp(i\omega t)$ implicitly.

Therefore, Equation (3.2.6) can be written as

$$-i\omega(\eta + \nu)\frac{\partial^2 u}{\partial x^2} = \omega^2 u + v_A^2 \frac{\partial^2 u}{\partial z^2}, \quad (3.2.14)$$

and Equation (3.2.8) gives

$$\frac{\partial \mathcal{Z}^\pm}{\partial z} = \frac{1}{v_A(x)} \left\{ \pm i\omega \mathcal{Z}^\pm + \nu_+ \frac{\partial^2 \mathcal{Z}^\pm}{\partial x^2} + \nu_- \frac{\partial^2 \mathcal{Z}^\mp}{\partial x^2} \right\}. \quad (3.2.15)$$

3.3 Open loop

This section aims to calculate solutions to Equations (3.2.14) and (3.2.15) analytically and numerically, for an open loop.

3.3.1 Analytic solution

To solve Equation (3.2.14) analytically we will use the method of multiple scales, where $\eta + \nu$ gives the small parameter. Dividing Equation (3.2.14) through by $v_A^2(x)$ gives

$$\frac{\partial^2 u}{\partial z^2} + k_z^2 u = -i(\eta + \nu) \frac{k_z}{v_A} \frac{\partial^2 u}{\partial x^2} \quad (3.3.1)$$

where

$$k_z(x) = \frac{\omega}{v_A(x)}. \quad (3.3.2)$$

We assume $u(x, z)$ takes the form of the following asymptotic series

$$u(x, z_0, z_1) = u_0(x, z, \epsilon z) + \epsilon u_1(x, z, \epsilon z) + \epsilon^2 u_2(x, z, \epsilon z) + \dots \quad (3.3.3)$$

where u has a shorter length-scale dependence, z_0 , given by

$$z_0 = z \quad (3.3.4)$$

and a longer length-scale dependence, z_1 , given by

$$z_1 = \epsilon z. \quad (3.3.5)$$

The zeroth order equation is given by

$$\frac{\partial^2 u_0}{\partial z^2} + k_z^2 u_0 = 0. \quad (3.3.6)$$

This has the general solution

$$u_0(x, z, z_1) = C_1(x, z_1) \exp[-ik_z(x)z] + C_2(x, z_1) \exp[ik_z(x)z]. \quad (3.3.7)$$

We apply the boundary condition that $\mathcal{Z}^+ = 0$ at $z = 0$, in other words the waves travelling in the negative z -direction have zero amplitude at $z = 0$ and this forces $C_2 = 0$. Applying the boundary condition given by Equation (3.2.10) gives

$$u_0(x, z, z_1) = f_0 C_3(z_1) \exp[-ik_z(x)z]. \quad (3.3.8)$$

Note that

$$\frac{\partial u}{\partial z} = \frac{\partial u}{\partial z_0} + \epsilon \frac{\partial u}{\partial z_1}, \quad (3.3.9)$$

$$\frac{\partial^2 u}{\partial z^2} = \frac{\partial^2 u}{\partial z_0^2} + 2\epsilon \frac{\partial^2 u}{\partial z_0 \partial z_1} + \epsilon^2 \frac{\partial^2 u}{\partial z_1^2}. \quad (3.3.10)$$

Hence, the first order equation is given by

$$\frac{\partial^2 u_1}{\partial z^2} + k_z^2 u_1 = -2 \frac{\partial^2 u_0}{\partial z \partial z_1} - i \frac{\eta + \nu}{\epsilon} \frac{k_z}{v_A} \frac{\partial^2 u_0}{\partial x^2}. \quad (3.3.11)$$

In order to eliminate secular terms we equate the right-hand side of the above equation to be zero which gives

$$\frac{\partial u_0}{\partial z_1} - \frac{(\eta + \nu)}{2\epsilon v_A} \frac{\partial^2 u_0}{\partial x^2} = 0. \quad (3.3.12)$$

Evaluating the x -derivative gives

$$\frac{\partial u_0}{\partial z_1} + \left(\frac{dk_z}{dx} \right)^2 \frac{(\eta + \nu)}{2\epsilon^3 v_A} z_1^2 u_0 = 0. \quad (3.3.13)$$

In order to make both terms the same order, we choose $\epsilon = (\eta + \nu)^{1/3}$. This has the general solution,

$$u_0(x, z, z_1) = C_4(x, z) \exp \left[- \left(\frac{dk_z}{dx} \right)^2 \frac{\eta + \nu}{6v_A} z_1^3 \right]. \quad (3.3.14)$$

Therefore, combining Equation (3.3.8) with (3.3.14) gives to leading order

$$\begin{aligned} u(x, z) &= f_0 \exp[-k_z(x)z] \exp \left[- \left(\frac{dk_z}{dx} \right)^2 \frac{\eta + \nu}{6v_A(x)} z^3 \right] \\ &= f_0 \exp[-k_z(x)z] \exp \left[- \left(\frac{dv_A}{dx} \right)^2 \frac{\eta + \nu}{6v_A^5(x)} \omega^2 z^3 \right] \\ &= f_0 \exp[-k_z(x)z] \exp \left[- \frac{\eta + \nu}{6\omega a^2(x)} k_z^3(x) z^3 \right], \end{aligned} \quad (3.3.15)$$

where

$$a(x) = \frac{v_A(x)}{dv_A/dx}, \quad (3.3.16)$$

which gives a measure of the length-scale of the Alfvén travel time. The magnetic field is given by

$$b(x, z) = B_0 \frac{f_0}{v_A(x)} \exp[i(\omega t - k_z(x)z)] \exp \left[- \frac{\eta + \nu}{6\omega a^2} k_z^3 z^3 \right], \quad (3.3.17)$$

to leading order. Note that the length-scale of the envelope, L_{ph} , is given by

$$L_{ph}(x) = \left[\frac{6\omega a^2}{\eta + \nu} \right]^{1/3} \frac{1}{k_z}. \quad (3.3.18)$$

In Section 2.9, Equation (2.9.9), we showed that the effective wavenumber in x , k_x^* , is given by

$$\begin{aligned} k_x^*(x) &= \omega \frac{dv_A}{dx} \frac{z}{v_A^2} \\ &= k_z z/a. \end{aligned} \quad (3.3.19)$$

Therefore, at $z = L_{ph}$, k_x^* is given by

$$k_x^* = \left[\frac{6\omega}{(\eta + \nu)a} \right]^{1/3}. \quad (3.3.20)$$

In Section 1.3.1 we showed that in the strong field limit, for collisional transport theory to be valid, Equation (1.3.2) needs to be satisfied. Therefore, we require

$$\frac{2\pi}{k_x^*} \gg \sqrt{\lambda_{Ti} r_e}. \quad (3.3.21)$$

For typical values, the phase-mixed length scale in x is given by

$$\frac{2\pi}{k_x^*} = 1.10 \left(\frac{\pi \times 10^{-2} \text{ Hz}}{\omega} \right) \left(\frac{\eta + \nu}{1 \text{ m}^2 \text{ s}^{-1}} \right)^{1/3} \left(\frac{a}{1 \text{ Mm}} \right)^{1/3} \text{ Mm.} \quad (3.3.22)$$

This shows Equation (1.3.2) is usually satisfied.

3.3.2 Numerical solution

Our goal now is to check the accuracy of Equation (3.3.15) by solving Equation (3.2.15) numerically. We discretize in x , i.e. we replace the x -derivatives in Equation (3.2.15) with finite difference approximations. This gives a set of ODEs in the z which we solve as an initial value problem using `solve_ivp` in [Virtanen et al. \(2020\)](#). To help simplify the code we consider the case where $\eta = \nu$ as this causes \mathcal{Z}^+ and \mathcal{Z}^- to decouple (see Equation 3.2.15). Setting $\mathcal{Z}^+ = 0$ at $z = 0$ forces $\mathcal{Z}^+ = 0 \forall z$. We choose the x -domain to be given by $x \in [-l_x, l_x]$, where

$$l_x = \frac{10}{k_x^*}.$$

The Alfvén speed is given by Equation (3.2.13) and the driver is given by Equation (3.2.10).

Our goal now is to check that the numerical solution agrees with the analytic solution. We test this via a graphical approach. In Figure 3.1 we plot the velocity perturbation u . The top-left shows the velocity along z at $x = 0$. The blue and orange curves show the real and imaginary parts, respectively. You can think of the imaginary part as showing what the real part will look like a quarter of a wave cycle later. The green curve shows the envelope, u_{env} which is given by

$$u_{env\pm}(x, z) = \pm f_0 \exp[-(z/L_{ph})^3], \quad (3.3.23)$$

which comes from Equation (3.3.15) and Heyvaerts and Priest (1983). It shows that at $x = 0$, to a good approximation, the wave decays with our predicted slope, given by Equation (3.3.15). The top-right plot shows the velocity along x at $z = L_{ph0}$, where we show the equation for L_{ph0} in the bottom-right of the figure. The solid line gives the numerical solution and the + symbols give the analytic solution, given by Equation (3.3.15). It shows that close to $x = 0$, the analytic and numerical solutions show good agreement. However, close to the boundaries, the agreement is poor, and this is because we impose Neumann boundary conditions, see Equation (3.2.11). Our analytic solution works well for open boundary conditions in x . However, these are difficult to implement numerically. The middle-row shows contour plots of the real and imaginary parts of the velocity as a function of x and z . Finally, the bottom-left shows the relative error between the numerical and analytic solutions at $x = 0$ and $z = L_{ph0}$ as a function of $\eta + \nu$. It shows that as we decrease $\eta + \nu$ the error reduces, despite L_{ph0} increasing. In the bottom-right, we show some of the parameters we use, including the grid resolution $n_x \times n_z$.

3.4 Closed loop

In this section we aim to solve Equation (3.2.14) for a closed loop, where we impose $u = 0$ at the top boundary, i.e.,

$$u(x, L_z) = 0, \quad (3.4.1)$$

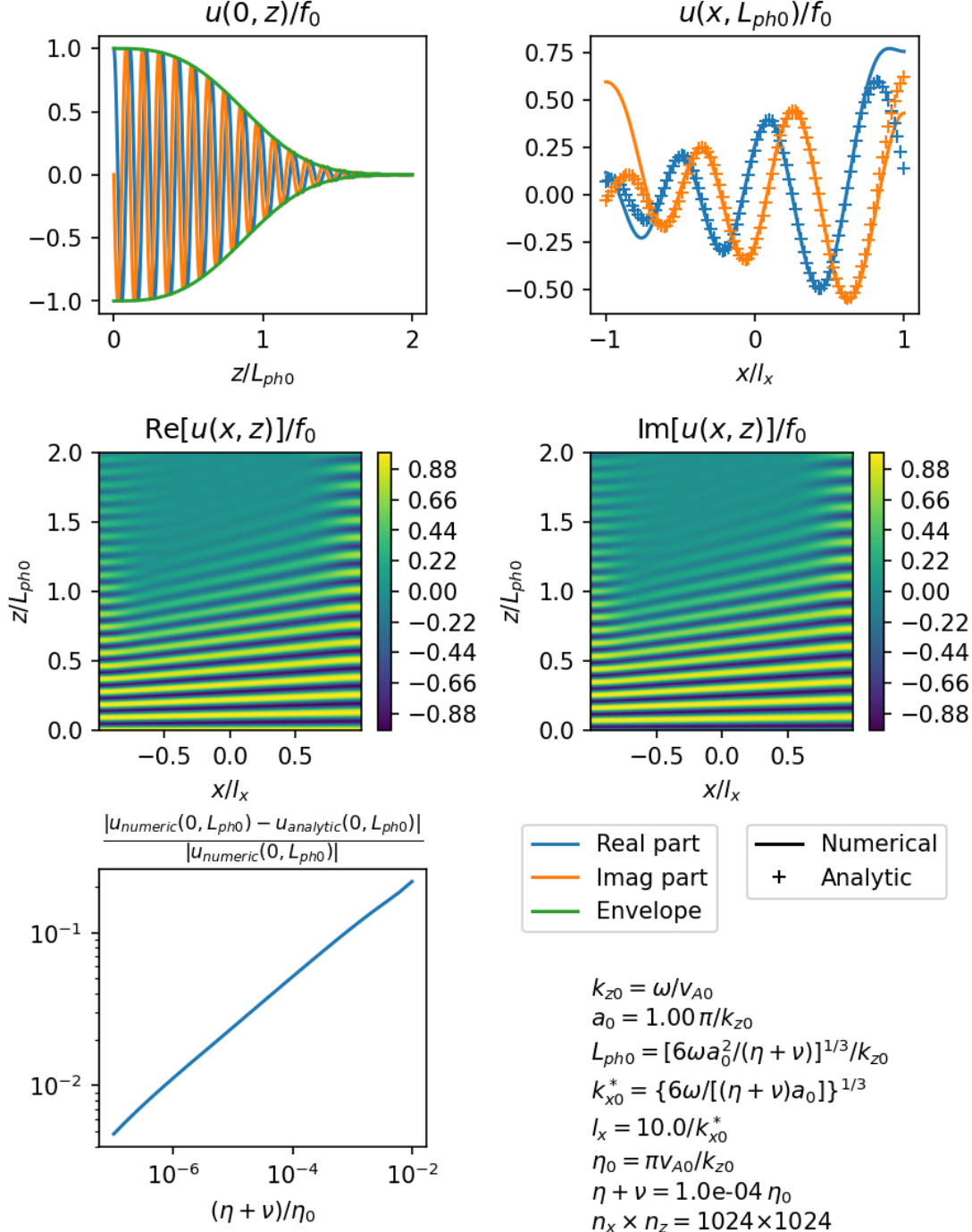


Figure 3.1: This figure shows plots of the velocity perturbation of phase-mixed Alfvén waves in an open loop. The top-left shows a plot along z at $x = 0$, where the green curve shows the envelope which we calculated using Equation (3.3.23). The top-right plot shows the analytic and numerical solutions along x at $z = L_{pho}$. The middle-row shows contour plots of the real and imaginary parts. The bottom-left plots the relative error between the analytic and numerical solutions at $x = 0$, $z = L_{pho}$ as a function of $\eta + \nu$. In the bottom-right, we show some of the parameters we used. The code used to make this figure is available on GitHub in the following directory:

→ [Python/Chapter3/open_loop.py](#)

where the domain is given by $z \in [0, L_z] = [0, 2l_z]$.

3.4.1 Analytic solution

Using a method of images approach, similar to that used in Section 2.4, as well as Equation (3.3.15), we calculate the steady-state solution to be

$$\begin{aligned} u(x, z) &= f_0 \sum_{k=0}^{\infty} (-1)^k \exp[-ik_z(x)z_k] \exp[-(z_k/L_{ph})^3] \\ &= f_0 A_{\infty}(x, z) \end{aligned} \quad (3.4.2)$$

where

$$z_k = (-1)^k(z - l_z) + (2k + 1)l_z, \quad (3.4.3)$$

and

$$A_{\infty}(x, z) = \sum_{k=0}^{\infty} (-1)^k \exp(-ik_z z_k) \exp[-(z_k/L_{ph})^3]. \quad (3.4.4)$$

Similarly, we calculate the magnetic field to be given by

$$\begin{aligned} b(x, z) &= -B_0 \frac{f_0}{v_A} \sum_{k=0}^{\infty} \exp[-k_z(x)z_k] \exp[-(z_k/L_{ph})^3] \\ &= -B_0 \frac{f_0}{v_A} B_{\infty}(x, z) \end{aligned} \quad (3.4.5)$$

where

$$B_{\infty}(x, z) = \sum_{k=0}^{\infty} \exp(-ik_z z_k) \exp[-(z_k/L_{ph})^3]. \quad (3.4.6)$$

We are not aware of any method to simplify the summations given by A_{∞} and B_{∞} further, however, we can approximate them numerically by truncating the series after N_a terms and then calculating the resulting summation numerically, provided $N_a \gg 1$.

3.4.2 Numerical solution

Our goal now is to verify Equations (3.4.2) numerically. We will convert Equation (3.2.14) into a set of ODEs, using the same approach used in Section 2.5.1. Let

$$u(x, z) = y(x, z) + f_0 \frac{L_z - z}{L_z}, \quad (3.4.7)$$

hence, the boundary conditions for y are

$$y(x, 0) = y(x, L_z) = 0. \quad (3.4.8)$$

We can write Equation (3.2.14) as

$$-i\omega(\eta + \nu) \frac{\partial^2 y}{\partial x^2} = \omega^2 y + v_A^2 \frac{\partial^2 y}{\partial z^2} + \omega^2 f_0 \frac{L_z - z}{L_z}.$$

Note that we can write the end term as the following Fourier series

$$\omega^2 f_0 \frac{L_z - z}{L_z} = 2\omega^2 f_0 \sum_{n=1}^{\infty} \frac{\sin(k_{zn}z)}{n\pi},$$

where

$$k_{zn} = \frac{n\pi}{L_z}. \quad (3.4.9)$$

Let

$$y(x, z) = \sum_{n=1}^{\infty} y_n(x) \sin(k_{zn}z). \quad (3.4.10)$$

Therefore, each y_n satisfies

$$\frac{d^2 y_n}{dx^2} = i \frac{\omega^2 - v_A^2(x) k_{zn}^2}{\omega(\eta + \nu)} y_n + \frac{2i\omega f_0}{n\pi(\eta + \nu)}. \quad (3.4.11)$$

We solve this set of ODEs using `solve_bvp` in [Virtanen et al. \(2020\)](#). We use the same Alfvén speed profile as the last section, namely Equation (3.2.13). We choose the driver

frequency, ω , to be given by

$$\omega = \frac{\pi v_{A0}}{L_z}, \quad (3.4.12)$$

this ensures the driving frequency is equal to the fundamental frequency of the loop at $x = 0$. Note that we approximate Equation (3.4.10) by truncating the series after N_h terms. We find that the error is small because the solution associated with the fundamental harmonic dominates due to the resonance being excited.

We can now verify Equations (3.4.2) via a graphical approach. In Figure 3.2 we plot the velocity perturbation, u . The top-left shows the velocity along z at $x = 0$. The blue and orange curves show the real and imaginary parts, respectively, see legend in bottom-right of the figure. It shows that the fundamental harmonic dominates the solution because we drive at the field line's fundamental frequency at $x = 0$. The top-right plot shows the velocity along x at $z = l_z$, i.e. the middle of the loop. The solid line gives the numerical solution and the + symbols give the analytic solution, given by Equation (3.3.15). The imaginary part shows a vertical velocity shear, giving rise to the Kelvin-Helmholtz instability (Heyvaerts and Priest, 1983). The middle-row shows contour plots of the real and imaginary parts of the velocity as a function of x and z . Finally, the bottom-left shows the relative error between the numerical and analytic solutions at $x = 0$ and $z = L_{ph0}$ as a function of $\eta + \nu$. It shows that as we decrease $\eta + \nu$, the error reduces.

3.4.3 Heating rate

In this section, we study the heating rate per unit of wave energy, γ . Using Equation (2.6.8) we know that the time-averaged Poynting flux in the z -direction, $\langle S_z \rangle$, is given by

$$\begin{aligned} \langle S_z \rangle &= -\frac{B_0}{4\mu}(u\bar{b} + \bar{u}b) \\ &= \frac{B_0^2 f_0^2}{2\mu v_A} \operatorname{Re}(A_\infty \bar{B}_\infty) \end{aligned} \quad (3.4.13)$$

At steady-state, the rate of change of energy in the loop is equal to the heating rate in the loop. Therefore, the heating rate is given by the Poynting flux at $z = 0$ as the

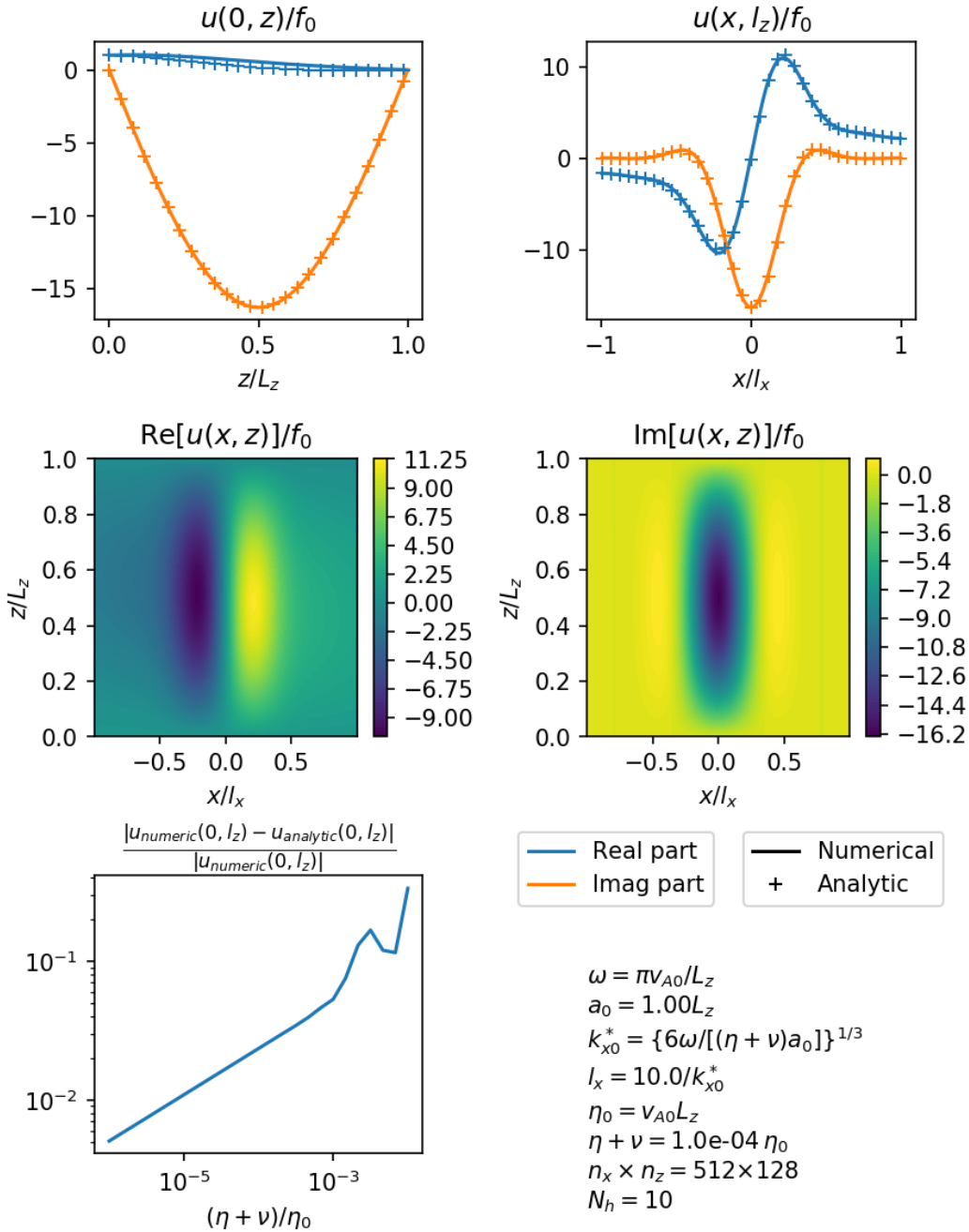


Figure 3.2: This figure shows plots of the velocity perturbation of phase-mixed Alfvén waves in a closed loop. The top-left shows a plot along z at $x = 0$. The top-right plot shows the analytic and numerical solutions along x at $z = l_z$. The middle-row shows contour plots of the real and imaginary parts. The bottom-left plots the relative error between the analytic and numerical solutions at $x = 0, z = l_z$ as a function of $\eta + \nu$. The code used to make this figure is available on GitHub in the following directory:
[→ Python/Chapter3/closed_loop.py](#)

Poynting flux at $z = L_z$ is zero. The time-averaged steady-state wave energy density, $\langle e_\infty \rangle$, is given by

$$\begin{aligned}\langle e_\infty \rangle &= \frac{\rho|u|^2}{4} + \frac{|b|^2}{4\mu} \\ &= \frac{B_0^2 f_0^2}{4\mu v_A^2} (|A_\infty|^2 + |B_\infty|^2).\end{aligned}\tag{3.4.14}$$

Therefore, the heating rate per unit of wave energy, γ , is given by

$$\begin{aligned}\gamma(x) &= \frac{\langle S_z \rangle|_{z=0}}{\int_0^{L_z} \langle e_\infty \rangle dz} \\ &= 2v_A \frac{\text{Re}(A_\infty \bar{B}_\infty)|_{z=0}}{\int_0^{L_z} |A_\infty|^2 + |B_\infty|^2 dz}.\end{aligned}\tag{3.4.15}$$

Equation (3.4.15), is quite obscure, it is difficult to see how γ changes with parameters such as ω or $\eta + \nu$. Our goal now is to calculate an approximation to Equation (3.4.15) which has a more convenient form. Let

$$B_\infty^*(x, z) = \sum_{k=0}^{\infty} \exp[-(ik_z + L_{ph}^{-1})z_k] \tag{3.4.16}$$

where B_∞^* is nearly the same as B_∞ except the cubic exponential has been replaced with a linear exponential. We postulate that $B_\infty^* \approx B_\infty$ at x provided $k_z(x)L_z = n\pi$ ($n \in \mathbb{Z}$). In other words, provided the field line at x is a resonant field line. Note that the form of B_∞^* is more convenient because we can evaluate the summation using the geometric series formula. We can write B_∞^* as

$$\begin{aligned}B_\infty^*(x, z) &= \exp[-(ik_z + L_{ph}^{-1})z] \frac{1}{2} \sum_{k=0}^{\infty} (1 + (-1)^k) \exp[-(ik_z + L_{ph}^{-1})L_z]^k \\ &\quad + \exp[-(ik_z + L_{ph}^{-1})(L_z - z)] \frac{1}{2} \sum_{k=0}^{\infty} (1 - (-1)^k) \exp[-(ik_z + L_{ph}^{-1})L_z]^k \\ &= \frac{\exp[-(ik_z + L_{ph}^{-1})z] + r \exp[-(ik_z + L_{ph}^{-1})(L_z - z)]}{1 - r^2} \\ &= \frac{\exp[-(ik_z + L_{ph}^{-1})z] + r^2 \exp[(ik_z + L_{ph}^{-1})z]}{1 - r^2},\end{aligned}$$

where

$$r = \exp[-(ik_z + L_{ph}^{-1})L_z]. \quad (3.4.17)$$

If we assume $L_z/L_{ph} \ll 1$ then we can approximate

$$r = \exp[-ik_z L_z](1 - L_z/L_{ph} + O[(L_z/L_{ph})^2]).$$

If $k_z L_z = n\pi$ then

$$r^2 = 1 - 2L_z/L_{ph} + O[(L_z/L_{ph})^2].$$

Hence, if $k_z L_z = n\pi$ then we can approximate B_∞^* as

$$B_\infty^*(x, 0) = \frac{L_{ph}}{L_z} + O[L_z/L_{ph}].$$

We assume that the energy, $\langle e_\infty \rangle$ is approximately uniformly distributed along z , therefore,

$$\begin{aligned} \int_0^{L_z} (|A_\infty|^2 + |B_\infty|^2) dz &\approx |B_\infty^*(x, 0)|^2 L_z \\ &= \frac{L_{ph}^2}{L_z} + O[L_z/L_{ph}]. \end{aligned}$$

To satisfy the boundary condition, Equation (3.2.10) we know that

$$A_\infty(x, 0) = 1.$$

Therefore, the heating rate per unit of wave energy, γ , is approximated by

$$\gamma(x) \approx \frac{2v_A}{L_{ph}} = \omega \left[\frac{4(\eta + \nu)}{3\omega a^2} \right]^{1/3}, \quad (3.4.18)$$

provided $k_z(x)L_z = n\pi$.

Our goal now is to verify that Equation (3.4.18) provides an approximation for Equation (3.4.15) on resonant field lines. Also, we aim to calculate γ for the non-

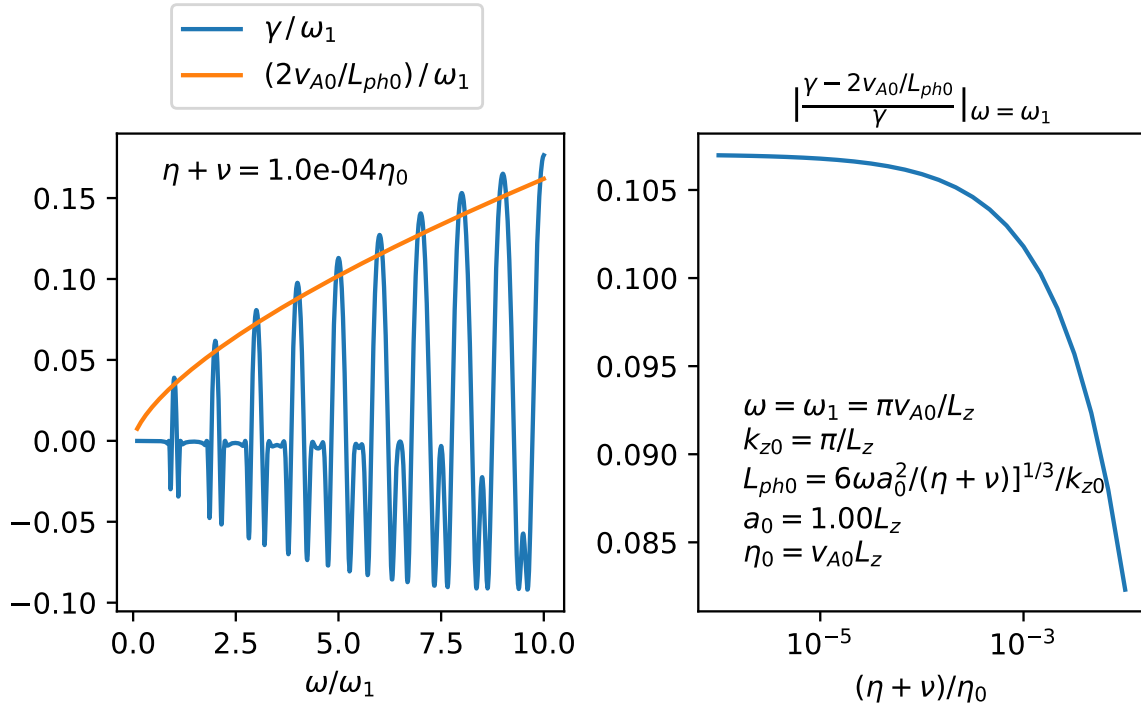


Figure 3.3: This figure shows plots of the heating rate per unit of wave energy, γ . The left-hand side shows γ as a function of frequency. The blue and orange curves were calculated using Equations (3.4.15) and (3.4.18) respectively. The right-hand side shows the relative error between these two equations as a function of $(\eta + \nu)$. The code used to make this figure is available on GitHub in the following directory:

[→ Python/Chapter3/closed_loop_gamma.py](#)

resonant field lines. To do this, we take a graphical approach. In Figure 3.3 we present γ . The blue and orange curves on the left-hand side show γ as a function of ω and were calculated using Equations (3.4.15) and (3.4.18) respectively. The blue curve shows that γ is largest at the resonant frequencies and is significantly smaller away from the resonance and can even be negative. The solution can be negative, and this is because we approximate γ here using the Poynting flux instead of the heating rate. Therefore the energy injected into a field line at $z = 0$ can be transferred to neighbouring field lines due to diffusion. At first, it may seem surprising that γ is so small at non-resonant frequencies because the wave energy, which appears on the denominator of Equation (3.4.15), decreases as the frequency moves away from the resonant frequencies. However, the numerator decreases to a greater degree as the frequency shifts away from the resonant frequencies. Typically, waves need to propagate within the loop for a long time before the length-scales in x become short enough for significant heating to occur. At non-resonant frequencies, waves cannot phase-mix to short enough length-scales before they are eliminated due to destructive interference. Note that the timescale for waves to be eliminated is characterised by the beating time, which we studied in Section 2.4.3. Comparing the blue and orange curves, we see that Equation (3.4.18) provides an approximation for Equation (3.4.15) at the resonant frequencies. The right-hand side presents the relative error between the two equations at $\omega = \omega_1$ and as a function of $\eta + \nu$. We see that the relative error remains within about 10%.

3.4.4 Multiple harmonics

We showed in Section 1.5 that velocity fluctuations oscillate at a broad range of frequencies. In this section, we aim to calculate the heating rate per unit of wave energy, γ , for the case where the driver excites a broad range of frequencies. In Section 2.5, we showed that the power spectrum in a closed loop with a broadband driver will on average have peaks at the resonant frequencies. Wright and Rickard (1995); Afanasyev et al. (2020) have also observed this. Therefore, for simplicity, our driver will only excite the resonant frequencies.

Let the bottom boundary condition be given by

$$\begin{aligned} u(x, 0, t) &= f_{driv}(t) \\ &= f_0 \sum_{n=-N}^N C_n \exp(i\omega_n t), \end{aligned} \tag{3.4.19}$$

where

$$C_n = \begin{cases} 0, & n = 0, \\ \frac{\sqrt{L_z} n^{-\alpha/2} \exp(i\varphi_n)}{\sqrt{\int_0^{L_z} |A_{\infty,n}|^2 + |B_{\infty,n}|^2 dz}}, & n > 0, \\ \bar{C}_{|n|}, & n < 0, \end{cases} \tag{3.4.20}$$

$$A_{\infty,n} = \sum_{k=0}^{\infty} (-1)^k \exp(-ik_{z,n} z_k) \exp[-(z_k/L_{ph,n})], \tag{3.4.21}$$

$$B_{\infty,n} = \sum_{k=0}^{\infty} \exp(-ik_{z,n} z_k) \exp[-(z_k/L_{ph,n})], \tag{3.4.22}$$

$$\omega_n = n \frac{\pi v_{A0}}{L_z}, \tag{3.4.23}$$

$$k_{z,n} = \frac{\omega_n}{v_{A0}}, \tag{3.4.24}$$

$$L_{ph,n} = \left[\frac{6\omega_n a^2}{\eta + \nu} \right]^{1/3} \frac{1}{k_{z,n}}. \tag{3.4.25}$$

Note that α controls the slope of the power spectrum, $\varphi_n \in \mathbb{R}$ gives an arbitrary phase, $\bar{C}_{|n|}$ denotes the complex conjugate and ensures the driver is real and N controls the number of harmonics which are excited. From Equations (3.4.2) and (3.4.5) we know that the steady-state solutions are given by

$$u(x, z, t) = f_0 \sum_{n=-N}^N A_{\infty,n} C_n \exp(i\omega_n t), \tag{3.4.26}$$

$$b(x, z, t) = -B_0 \frac{f_0}{v_A} \sum_{n=-N}^N B_{\infty,n} C_n \exp(i\omega_n t). \tag{3.4.27}$$

By Parseval's theorem, the time-averaged energy is given by

$$\begin{aligned}\langle e_\infty \rangle &= \frac{1}{P} \int_0^P \frac{\rho|u|^2}{4} + \frac{|b|^2}{4\mu} dt \\ &= \frac{B_0^2 f_0^2}{4\mu v_A^2} \sum_{n=-N}^N |A_{\infty,n} C_n|^2 + |B_{\infty,n} C_n|^2,\end{aligned}\tag{3.4.28}$$

where

$$P = \frac{2L_z}{v_{A0}}.\tag{3.4.29}$$

Therefore, the energy of the whole loop, $\langle E_\infty \rangle$, is given by

$$\begin{aligned}\langle E_\infty \rangle &= \frac{B_0^2 f_0^2}{4\mu v_A^2} \sum_{n=-N}^N |C_n|^2 \int_0^{L_z} |A_{\infty,n}|^2 + |B_{\infty,n}|^2 dz \\ &= \frac{B_0^2 f_0^2}{2\mu v_A^2} L_z \sum_{n=1}^N n^{-\alpha}.\end{aligned}\tag{3.4.30}$$

The above equations shows that our driver, Equation (3.4.19), ensures that the energy of the loop has a power spectrum with slope $\omega_n^{-\alpha}$.

Using Parseval's theorem, the average Poynting flux is given by

$$\begin{aligned}\langle S_z \rangle &= \frac{B_0^2 f_0^2}{2\mu v_A} \sum_{n=-N}^N |C_n|^2 \operatorname{Re}(A_{\infty,n} \bar{B}_{\infty,n}) \\ &= \frac{B_0^2 f_0^2}{\mu v_A} L_z \sum_{n=1}^N n^{-\alpha} \frac{\operatorname{Re}(A_{\infty,n} \bar{B}_{\infty,n})}{\int_0^{L_z} |A_{\infty,n}|^2 + |B_{\infty,n}|^2 dz}.\end{aligned}\tag{3.4.31}$$

Therefore, the heating rate per unit of wave energy, γ , is given by

$$\begin{aligned}\gamma &= \frac{\langle S_z \rangle|_{z=0}}{\langle E_\infty \rangle} \\ &= \frac{\sum_{n=1}^N n^{-\alpha} \gamma_n}{\sum_{n=1}^N n^{-\alpha}},\end{aligned}\tag{3.4.32}$$

where

$$\gamma_n = 2v_A \frac{\operatorname{Re}(A_{\infty,n} \bar{B}_{\infty,n})|_{z=0}}{\int_0^{L_z} |A_{\infty,n}|^2 + |B_{\infty,n}|^2 dz}. \quad (3.4.33)$$

Hence, γ takes the form of a weighted average of the set $\{\gamma_n\}$ with weights $n^{-\alpha}$.

Our goal now is to approximate Equation (3.4.32) in a more convenient form. We approximate γ_n by using Equation (3.4.18) to give

$$\begin{aligned} \gamma_n &\approx \omega_n \left[\frac{4(\eta + \nu)}{3\omega_n a^2} \right]^{1/3} \\ &= \omega_1 \left[\frac{4(\eta + \nu)}{3\omega_1 a^2} \right]^{1/3} n^{2/3}. \end{aligned} \quad (3.4.34)$$

Hence, Equation (3.4.32) can be approximated as

$$\begin{aligned} \gamma &\approx \gamma_1 \frac{\sum_{n=1}^N n^{2/3-\alpha}}{\sum_{n=1}^N n^{-\alpha}} \\ &= \gamma_1 \frac{H_N^{(\alpha-2/3)}}{H_N^{(\alpha)}}, \end{aligned} \quad (3.4.35)$$

where $H_N^{(p)}$ denotes the generalised harmonic number of order p of N . Note that

$$H_N^{(p)} = \begin{cases} \ln(N) + \gamma_{EM} + O(1/N), & p = 1 \\ N^{-p} \left[\frac{N}{1-p} + \frac{1}{2} + O(1/N) \right] + \zeta(p), & p \neq 1 \end{cases} \quad (3.4.36)$$

where $\zeta(p)$ denotes the Riemann zeta function (see right-side of Figure 3.4) and γ_{EM} is the Euler-Mascheroni constant. Hence, if $\alpha = 0$, then to leading order

$$\gamma \approx \gamma_1 \frac{3N^{2/3}}{5} + O(N^{-1/3}), \quad (3.4.37)$$

if $\alpha = 1$, then to leading order

$$\gamma \approx \gamma_1 \frac{3N^{2/3}/2 + \zeta(1/3) + O(N^{-1/3})}{\ln(N) + \gamma_{EM} + O(1/N)}, \quad (3.4.38)$$

if $\alpha = 5/3$, then to leading order

$$\gamma \approx \gamma_1 \frac{\ln(N) + \gamma_{EM} + O(1/N)}{\zeta(5/3) + O(N^{-2/3})}. \quad (3.4.39)$$

Our goal now is to check that γ , given by Equation (3.4.32), can be approximated with Equation (3.4.35) with $H_N^{(p)}$ approximated by Equation (3.4.36). We test this using a graphical approach. On the left-side of Figure 3.4 we plot the heating rate per unit of wave energy, γ , as a function of the number of excited harmonics, N , for different power spectra slopes, α . The exact solution (solid line) was calculated using Equation (3.4.35). The approximate solution ('+' symbols), was calculated using (3.4.32) with $H_N^{(p)}$ approximated by Equation (3.4.36). Note that to account for the error associated with approximating γ with Equation (3.4.18) we multiply our approximation by a factor 1.1. This factor comes from the fact that we noted an error of about 10% in Figure 3.3. We plot for the case where $\alpha = 0$ (blue), 1 (orange), and $5/3$ (green), these can be approximated with Equations (3.4.37)-(3.4.39) respectively. The plots suggest that our approximation is indeed accurate for $N \gg 1$. Note that if the power spectra are steep, $\alpha = 5/3$ say, then γ is weakly dependent on the number of harmonics. If the power spectra are flatter, $\alpha = 0$, then γ is highly dependent on the number of excited harmonics.

Figure 3.4 uses a range of α values including $5/3$ as this is one the values predicted from MHD turbulence theory (Bruno and Carbone, 2013). Morton et al. (2016); Kolotkov et al. (2016) provide observations of the power spectra of velocity fluctuations in the quiet sun, the active regions, and the coronal holes (see Figure 1.6). These latter authors find that the slope varies from $\alpha = 1$ to $\alpha = 1.53$ for higher frequencies, although they are only able to measure up to frequencies of around 10^{-2} Hz. Podesta et al. (2007) measure the power spectra in the solar wind and can measure up to 10^{-1} Hz and find the slope to be between $\alpha = 1.5$ and $\alpha = 5/3$.

3.5 Leaky loop

In Section 2.6, we showed that waves can leak out of the corona. In this section, we aim to study phase-mixed Alfvén waves in a leaky loop and calculate the effects of leakage on the value of γ . We use similar boundary conditions to those used in Section 2.7,

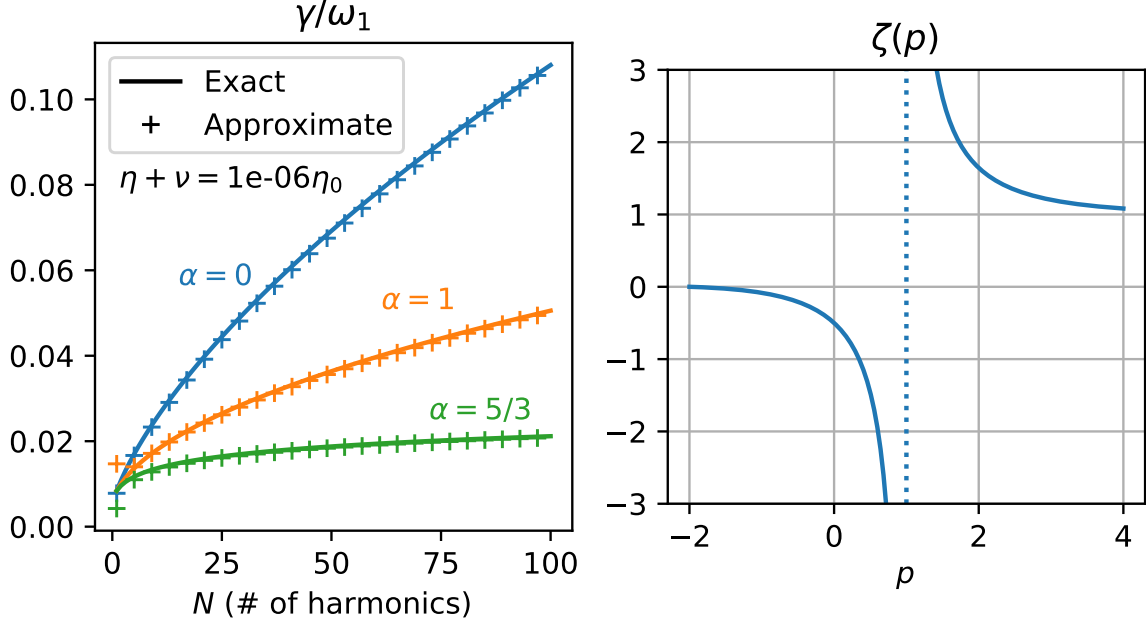


Figure 3.4: This figure shows line plots of the heating rate per unit of wave energy as a function of the number of excited harmonics, N , on the left. The right-side shows the Riemann zeta function along the real axis where the discontinuity at $p = 1$ is denoted with a dotted line. The code used to make this figure is available on GitHub in the following directory:

[→ Python/Chapter3/multiple_harmonics.py](#)

namely,

$$\begin{aligned}\mathcal{Z}^-(x, 0, t) &= 2f_{driv}(x, t) - R\mathcal{Z}^+(x, 0, t) \\ \mathcal{Z}^+(x, L_z, t) &= -R\mathcal{Z}^-(x, L_z, t),\end{aligned}\tag{2.7.4}$$

where R gives the reflection coefficient, which we approximate in Section 2.6. These boundary conditions ensure that each time a wave reaches a boundary a fraction R of the wave is reflected and a fraction $1 - R$ leaks out of the loop.

Our first goal is to calculate the timescale at which waves decay due to leakage. We will compare this with the resistive timescale to estimate the parameter space in which leakage plays a significant role in the decay of waves compared with resistive effects. Consider an ideal loop. The time taken for a wave to travel from $z = 0$ to $z = L_z$ (and vice versa) is the Alfvén travel time, τ_A , given by

$$\tau_A = \frac{L_z}{v_A}.\tag{3.5.1}$$

Therefore each time τ_A time units have elapsed the wave amplitude decreases by R .

Thus, the wave amplitude, u_0 , goes as

$$\begin{aligned} u_0 &\propto R^{\lfloor t/t_A \rfloor} \\ &= \exp\left(\left\lfloor \frac{t}{t_A} \right\rfloor \ln R\right) \\ &\approx \exp\left(-\frac{|\ln R|}{t_A} t\right). \end{aligned} \tag{3.5.2}$$

Hence, the leakage timescale, $\tau_{leakage}$, is given by,

$$\tau_{leakage} = \frac{L_z}{v_A |\ln R|}. \tag{3.5.3}$$

Each time a wave propagates a distance, L_{ph} , the wave decays by a factor $\exp(1)$ due to resistive effects. Therefore, the resistive timescale is given by

$$\begin{aligned} \tau_{resistive} &= \frac{L_{ph}}{v_A} \\ &= \left[\frac{6\omega^2 a^2}{\eta + \nu} \right]^{1/3} \frac{1}{\omega}. \end{aligned} \tag{3.5.4}$$

If $\tau_{resistive} \ll \tau_{leakage}$ then we expect leakage to play a negligible role and the solution to be well approximated by our calculation in Section 3.4. If $\tau_{resistive} \ll \tau_{leakage}$ then we expect resistivity and viscosity to play negligible role in determining the shape of the solution, however, any heating which occurs will still be Ohmic and viscous. To get an idea of the parameter space in which leakage plays an important role we plot $\tau_{resistive}$ and $\tau_{leakage}$ on the left-hand side of Figure 3.5 as a function of f in Hz. The plot shows that the leakage timescale is smaller than the resistive timescale for this parameter space. We show our choice of parameters in the figure, e.g. we assume a background Alfvén speed of 10^6 m s^{-1} , where we chose the parameters to represent typical values in coronal loops.

Extending Equations (3.4.2) and (3.4.5) to include leakage gives

$$\begin{aligned} u(x, z) &= f_0 \sum_{k=0}^{\infty} (-1)^k R^k \exp[-ik_z(x)z_k] \exp[-(z_k/L_{ph})^3] \\ &= f_0 A'_\infty(x, z), \end{aligned} \tag{3.5.5}$$

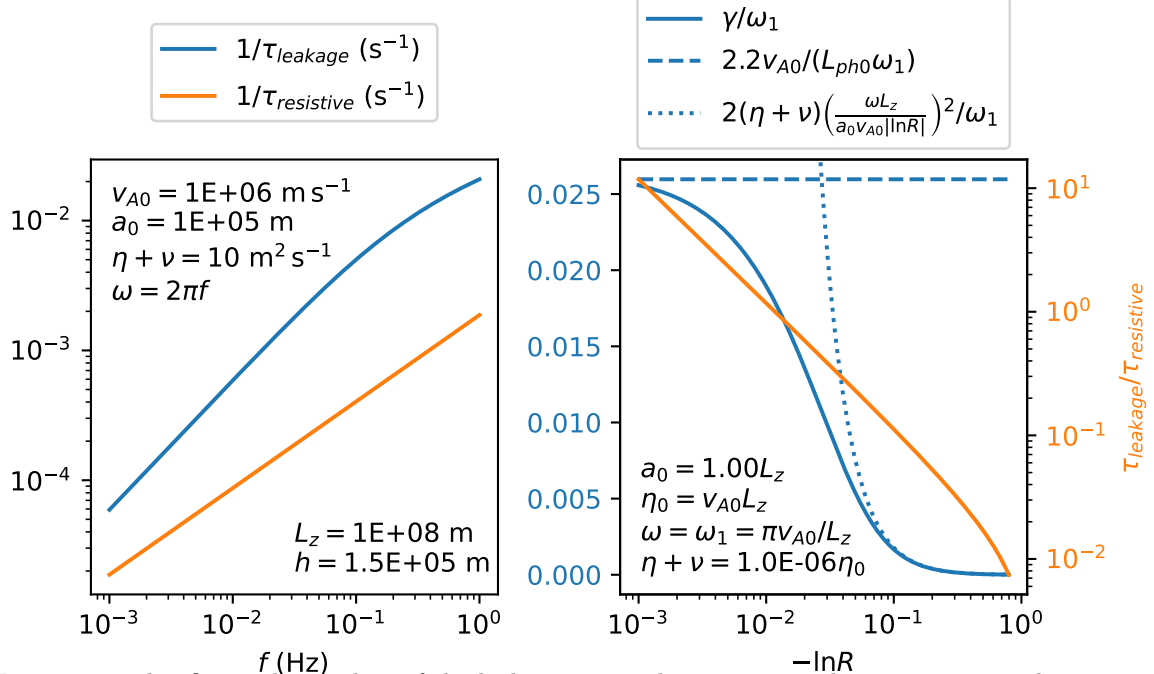


Figure 3.5: This figure shows plots of the leakage timescale, $\tau_{leakage}$, and resistive timescale, $\tau_{resistive}$ on the left as a function of the wave frequency. The right-side shows γ in blue and the ratio, $\tau_{leakage}/\tau_{resistive}$, in orange, as a function of the reflection coefficient, R . The code used to make this figure is available on GitHub in the following directory:

[→ Python/Chapter3/leaky_loop.py](#)

$$\begin{aligned} b(x, z) &= -B_0 \frac{f_0}{v_A} \sum_{k=0}^{\infty} R^k \exp[-ik_z(x)z_k] \exp[-(z_k/L_{ph})^3] \\ &= -B_0 \frac{f_0}{v_A} B'_{\infty}(x, z), \end{aligned} \quad (3.5.6)$$

where

$$A'_{\infty}(x, z) = \sum_{k=0}^{\infty} (-1)^k R^k \exp[-ik_z(x)z_k] \exp[-(z_k/L_{ph})^3], \quad (3.5.7)$$

$$B'_{\infty}(x, z) = \sum_{k=0}^{\infty} R^k \exp[-ik_z(x)z_k] \exp[-(z_k/L_{ph})^3]. \quad (3.5.8)$$

Introducing leakage means that the Poynting flux at $z = L_z$ is no longer necessarily equal to zero, therefore, the heating rate per unit of wave energy is given by

$$\gamma(x) = -2v_A \frac{[\operatorname{Re}(A'_{\infty} \bar{B}'_{\infty})]_{z=0}^{z=L_z}}{\int_0^{L_z} |A'_{\infty}|^2 + |B'_{\infty}|^2 dz}. \quad (3.5.9)$$

The above equation for γ is quite cumbersome because it is difficult to see its dependency on parameters such as ω or R . Our goal now is to calculate an approximate solution for the case where $\tau_{leakage} \ll \tau_{resistive}$. Note that Equation (3.4.18) gives an approximate solution for $\tau_{leakage} \gg \tau_{resistive}$. The heating rate per unit of wave energy, γ , is approximated by

$$\begin{aligned}\gamma &\approx \frac{\frac{1}{2}(\eta + \nu) \int_0^{L_z} \rho (\partial u / \partial x)^2 + (\partial b / \partial x)^2 / \mu dz}{\frac{1}{2} \int_0^{L_z} \rho u^2 + b^2 / \mu dz} \\ &\approx (\eta + \nu)(k_x^*)^2,\end{aligned}\quad (3.5.10)$$

where k_x^* gives a measure of the wavenumber in the x -direction. Substituting $z = v_A \tau_{leakage}$ into Equation (3.3.19), we estimate k_x^* in the strong leakage limit as

$$\begin{aligned}k_x^* &\approx \frac{\omega}{a} \tau_{leakage} \\ &= \frac{\omega L_z}{av_A |\ln R|}.\end{aligned}\quad (3.5.11)$$

Therefore, in the strong leakage limit,

$$\gamma \propto (\eta + \nu) \left(\frac{\omega L_z}{av_A |\ln R|} \right)^2.$$

Note that the dotted curve in Figure 3.5 uses

$$\gamma = 2(\eta + \nu) \left(\frac{\omega L_z}{av_A |\ln R|} \right)^2. \quad (3.5.12)$$

We now need to plot γ , given by Equation (3.5.9), as a function of R , to see how leakage affects γ and to check the accuracy of Equation (3.5.12). The solid blue curve on the right-hand side of Figure 3.5 shows γ as a function of the reflection coefficient $-\ln R$. The plot shows that increasing the leakage (decreasing R) causes γ to decrease. This is because the leakage reduces the development of short length-scales as waves leak out of the loop before they can phase-mix to the same length-scales that closed-loop waves can reach. The Figure shows that in the limit $\tau_{leakage}/\tau_{resistive} \ll 1$, then γ can be approximated with Equation (3.5.12), where the ratio $\tau_{leakage}/\tau_{resistive}$, is plotted in orange and the approximation is plotted with a dotted blue line. In the limit

$\tau_{leakage}/\tau_{resistive} \gg 1$ then γ can be well approximated by assuming the loop is closed.

3.6 Coronal heating discussion

In Section 3.1 we showed that we require $\gamma \approx 10^{-1} \text{ s}^{-1}$, see Equation (3.1.11), for phase mixing to play an important role in coronal heating. Our goal now is to use results from Sections 3.4-3.5 to estimate an upper bound for a typical value of γ in the closed corona using phase-mixing theory. We will first present our estimate. After that, we will discuss some of our simplifications and calculate if they increase or decrease our estimate of γ .

In Section 3.4.3 we showed that if a single harmonic is excited, then γ can be well approximated with Equation (3.4.18). Velocity fluctuations in the corona typically oscillate at a superposition of multiple frequencies, with a power spectrum approximated by Figure 1.6. In Section 3.4.4, we showed if multiple harmonics are excited and have a power spectrum proportional to $f^{-\alpha}$, where f denotes the frequency of the waves, then γ is approximated with Equation (3.4.35). Substituting for typical values, with $\alpha = 1$, $N = 100$, Equation (3.4.38) gives

$$\gamma \approx 1.43 \times 10^{-4} \left(\frac{\omega_1}{\pi \times 10^{-2} \text{ Hz}} \right)^{1/3} \left(\frac{\eta + \nu}{10 \text{ m}^2 \text{ s}^{-1}} \right)^{1/3} \left(\frac{1 \text{ Mm}}{a} \right)^{2/3} \text{ s}^{-1}. \quad (3.6.1)$$

Therefore, our upper bound for γ is significantly less than the required value of γ , by approximately three orders of magnitude. This implies that the $\mathbf{W}^{(1)}$ component of the viscosity tensor, $\boldsymbol{\sigma}_{Brag}$, plays a negligible role in coronal heating. This suggests that the direct dissipation of waves due to the steep gradients generated by phase-mixing play an insignificant role in coronal heating. However, phase mixing could still play an important but less direct role in coronal heating. For example, phase mixed Alfvén waves are susceptible to the Kelvin-Helmholtz and tearing mode instabilities, leading to a turbulent cascade to smaller scales. This would mean that the dissipation occurs primarily due to gradients parallel to the field or the velocity which are dissipated via the $\mathbf{W}^{(0)}$ component of the viscosity tensor. Note that $\mathbf{W}^{(0)}$ is not dependent on the gradients generated through phase-mixing since the x -direction is neither parallel to the field or the velocity. In Hillier and Arregui (2019) they show that the Kelvin-Helmholtz instability can lead to coronal cooling as a result of the fluid mixing together which

causes the temperature to become more uniform resulting in the total amount of radiation increases. To derive the above equations, we had to make several simplifications. The rest of this section justifies these simplifications and explains why we chose the values for the above parameters.

Increasing α acts to reduce γ . For our calculation we took $\alpha = 1$, which underestimates the single power-law fit to Figure 1.6. This helps ensure that our calculation for γ is an upper bound. We chose $N = 100$ because $100\omega_1 = \pi \text{ Hz}$ which is a higher than the maximum observed wave frequencies. We will also show later, in Equation (3.6.8), for high frequencies, phase mixing plays a negligible role in the dissipation of waves compared with the dissipation due to gradients parallel to the background field. The characteristic length of a coronal loop is about 100 Mm (O'Neill and Li, 2005) with an average Alfvén speed of about 1 Mm s^{-1} (McIntosh et al., 2011). This gives a fundamental angular frequency of $\omega_1 = \pi \times 10^{-2} \text{ Hz}$. Combining Equations (1.3.32) and (1.3.36) gives

$$\nu = \frac{\eta_1}{\rho} = 0.62 \left(\frac{10^{-3} \text{ Tesla}}{B_0} \right)^2 \left(\frac{10^6 \text{ K}}{T} \right)^{1/2} \left(\frac{\rho}{10^{-12} \text{ kg m}^{-3}} \right) \text{ m}^2 \text{ s}^{-1}, \quad (3.6.2)$$

where the Coulomb logarithm, $\log \Lambda$, has been set equal to 20. Therefore, Equations (1.3.50) and (3.6.2) show that $\eta + \nu < 10 \text{ m}^2 \text{ s}^{-1}$ for the given set of parameters. The parameter with the greatest level of uncertainty associated with it is the length-scale of the Alfvén travel times, a , given by Equation (3.3.16). We discuss a suitable value for a in the next paragraph.

Three factors determine the Alfvén travel time of a loop, the length of the loop, the plasma density, and the magnetic field strength. In Oliver et al. (1993), they calculate the Alfvén travel time in a potential coronal arcade with a uniform density profile. The flux function, A , is given by

$$A(x, z) = B_0 \Lambda_B \cos\left(\frac{x}{\Lambda_B}\right) \exp\left(-\frac{z}{\Lambda_B}\right), \quad (3.6.3)$$

where B_0 gives the field strength at $z = 0$, Λ_B gives the scale height of the field strength and is also related to the arcade's lateral extent. Note that lines of constant A provide the field lines and the associated magnetic field is given by $\mathbf{B} = \nabla A \times \hat{\mathbf{y}}$. We plot the field on the left side of Figure 3.6. In Oliver et al. (1993) they show that the

fundamental frequency of this arcade is given by

$$\omega_1 = \pi \frac{v_{A0}}{2x_0} \cos\left(\frac{x_0}{\Lambda_B}\right), \quad (3.6.4)$$

where v_{A0} gives the Alfvén speed at $z = 0$ and x_0 gives the x -coordinate of the field line at $z = 0$. Therefore, the length-scale of Alfvén travel time variations across the field lines can be approximated with

$$\begin{aligned} a(x_0) &= \left| \frac{\omega_1}{d\omega_1/dx_0} \right| \\ &= \frac{x_0 \Lambda_B \cos(x_0/\Lambda_B)}{\Lambda_B \cos(x_0/\Lambda_B) + x_0 \sin(x_0/\Lambda_B)}. \end{aligned} \quad (3.6.5)$$

Note that $a(x_0)$ is plotted on the right-side of Figure 3.6. The plot shows that $a = 0$ for $x_0 = 0$ and $x_0 = \pi\Lambda_B/2$. The magnetic field lines are highly divergent near $x_0 = \pi\Lambda_B/2$. In for example Ruderman et al. (1998); Smith et al. (2007), they show that a diverging flux tube can enhance the phase mixing. However, we are interested in an average value for a . The average value, $\langle a \rangle$ is given by

$$\begin{aligned} \langle a(x_0) \rangle &= \frac{2}{\pi\Lambda_B} \int_0^{\pi\Lambda_B/2} a(x_0) dx_0 \\ &= \frac{2}{\pi} \ln\left(\frac{\pi}{2}\right) \Lambda_B \\ &\approx 2.87 \left(\frac{\Lambda_B}{10 \text{ Mm}} \right) \text{ Mm}. \end{aligned} \quad (3.6.6)$$

For $x_0 \rightarrow 0$, $\omega_1 \rightarrow \infty$. Therefore, a resonance near $x_0 = 0$ must have a very high frequency. Figure 2.9 showed that very high frequencies can leak into the chromosphere more easily. This suggests imposing solid boundary conditions may not be appropriate here. The Alfvén travel time is also affected by the density of the plasma. Klimchuk (2015) shows that coronal loops have a characteristic diameter of approximately 1.5 Mm. If we assume a density contrast, $\rho_i/\rho_o = 2$, (Hood et al., 2013; Pascoe et al., 2013) where ρ_i gives the density inside a loop and ρ_o gives the density outside a loop then this gives a length-scale $a \approx 750$ km.

We modelled the system as linear. This meant the $\mathbf{W}^{(0)}$ component of the viscosity was neglected. If we assume $\mathbf{u} = u(x, z, t)\hat{\mathbf{y}}$ and $\mathbf{B} = B_0\hat{\mathbf{z}} + b(x, z, t)\hat{\mathbf{y}}$ and do not

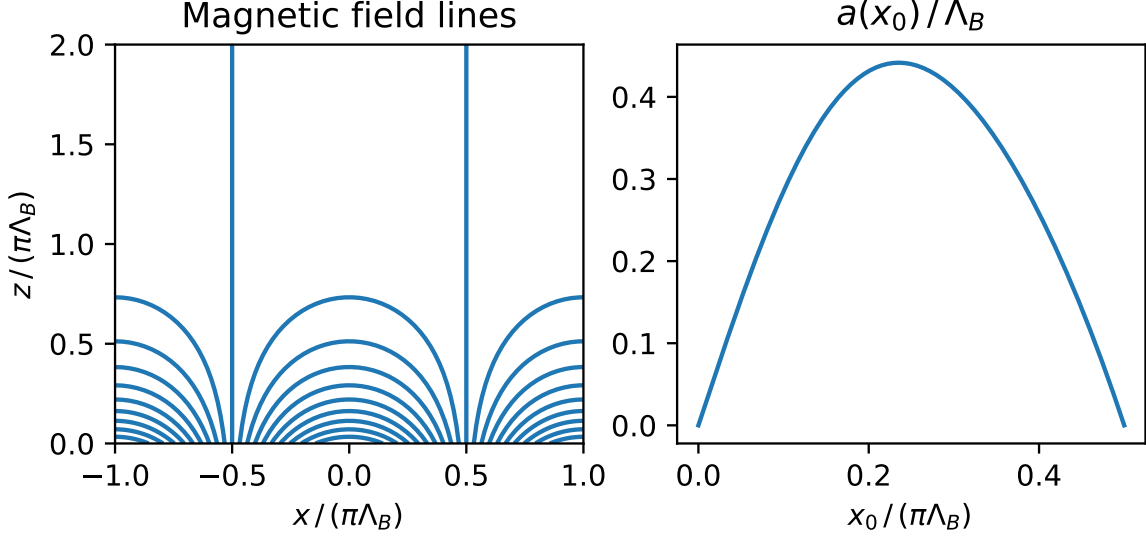


Figure 3.6: The left side of the figure shows a plot of the magnetic field lines where the flux function is given by Equation (3.6.3). The right side shows plots of a for the field lines as a function of the footpoint coordinate, x_0 . The code used to make this figure is available on GitHub in the following directory:

[→ Python/Chapter3/potential_arcade.py](#)

linearise, then

$$\eta_0 \mathbf{W}^{(0)} : \nabla \mathbf{u} = 3\eta_0 \epsilon^2 \left(\frac{\partial u}{\partial z} \right)^2 + O(\epsilon^3), \quad (3.6.7)$$

where $\epsilon = u/v_A$. Therefore, the ratio, $w_{0,1}$, between the heating generated by $\mathbf{W}^{(0)}$ and $\mathbf{W}^{(1)}$ can be estimated. For simplicity we choose $\eta = 0$, hence,

$$\begin{aligned} w_{0,1} &= \frac{\eta_0 \mathbf{W}^{(0)} : \nabla \mathbf{u}}{\eta_1 \mathbf{W}^{(1)} : \nabla \mathbf{u}} \\ &\approx 3\epsilon^2 \frac{\eta_0}{\eta_1} \left(\frac{k_z}{k_x^*} \right)^2 \\ &\approx 4.0471 \times 10^{-6} \frac{e^{2/3} \mu}{(\ln \Lambda)^{4/3}} \epsilon^2 \frac{T^{8/3} \omega^{4/3}}{\rho^{1/3} B_0^{4/3}} a^{2/3} \\ &\approx 0.59 \times 10^{-2} \left(\frac{\epsilon}{10^{-1}} \right)^2 \left(\frac{T}{10^6 \text{ K}} \right)^{8/3} \left(\frac{\omega}{\pi \times 10^{-2} \text{ Hz}} \right)^{4/3} \\ &\quad \times \left(\frac{10^{-12} \text{ kg m}^{-3}}{\rho} \right)^{1/3} \left(\frac{10^{-3} \text{ T}}{B_0} \right)^{4/3} \left(\frac{a}{10^5 \text{ m}} \right)^{2/3}, \end{aligned} \quad (3.6.8)$$

where k_x^* is given by Equation (3.3.20).

Another consequence of linearising the system is that it causes the Alfvén waves to become decoupled from the fast and slow waves. To see this, consider the y -component of the ideal momentum equation, Equation (1.3.18), with gravity neglected, $\partial/\partial y = 0$ and multiplied by $v_y = u$,

$$\rho \frac{\partial}{\partial t} \left(\frac{1}{2} v_y^2 \right) + \rho \mathbf{v} \cdot \nabla \left(\frac{1}{2} v_y^2 \right) = (\mathbf{B} \cdot \nabla) B_y, \quad (3.6.9)$$

where $B_y = b$. Consider the mass continuity equation, Equation (1.3.17), multiplied by $v_y^2/2$ to give

$$\frac{1}{2} v_y^2 \frac{\partial \rho}{\partial t} + \frac{1}{2} v_y^2 \nabla \cdot (\rho \mathbf{v}) = 0. \quad (3.6.10)$$

Combining the above equations gives the equation for the evolution of the Alfvén wave kinetic energy,

$$\frac{\partial}{\partial t} \left(\frac{1}{2} \rho v_y^2 \right) + \nabla \cdot \left(\frac{1}{2} \rho v_y^2 \mathbf{v} \right) = \frac{1}{\mu} v_y (\mathbf{B} \cdot \nabla) B_y. \quad (3.6.11)$$

Taking the dot product of Faraday's Law, Equation (1.3.8), with $\mathbf{B}_y/\mu = B_y/\mu \hat{\mathbf{y}}$, gives

$$\begin{aligned} \frac{\partial}{\partial t} \left(\frac{B_y^2}{2\mu} \right) &= -\frac{\mathbf{B}_y}{\mu} \cdot \nabla \times \mathbf{E} \\ &= -\nabla \cdot \left(\frac{\mathbf{E} \times \mathbf{B}_y}{\mu} \right) - \mathbf{E} \cdot \left(\frac{\nabla \times \mathbf{B}_y}{\mu} \right). \end{aligned} \quad (3.6.12)$$

Substituting the ideal Ohms law, Equation (1.3.13), gives the equation for the evolution of the Alfvén wave magnetic energy

$$\begin{aligned} \frac{\partial}{\partial t} \left(\frac{B_y^2}{2\mu} \right) + \nabla \cdot \left(\frac{\mathbf{E} \times \mathbf{B}_y}{\mu} \right) &= -\frac{1}{\mu} \mathbf{v} \cdot [(\nabla \times \mathbf{B}_y) \times \mathbf{B}] \\ &= -\frac{1}{\mu} v_y (\mathbf{B} \cdot \nabla) B_y + \mathbf{v} \cdot \nabla \left(\frac{B_y^2}{2\mu} \right) \end{aligned} \quad (3.6.13)$$

Superimposing Equations (3.6.11) and (3.6.13) gives the equation for the energy evolu-

tion of the Alfvén waves

$$\frac{\partial}{\partial t} \left(\frac{1}{2} \rho v_y^2 + \frac{B_y^2}{2\mu} \right) + \nabla \cdot \left(\frac{1}{2} \rho v_y^2 \mathbf{v} + \frac{\mathbf{E} \times \mathbf{B}_y}{\mu} \right) = \mathbf{v} \cdot \nabla \left(\frac{B_y^2}{2\mu} \right). \quad (3.6.14)$$

The above equation shows that the energy associated with perturbations in the y -direction (the Alfvén wave) is coupled to the perturbations in the x and z direction through the ponderomotive force, $-\nabla[B_y^2/(2\mu)]$. The ponderomotive force is defined as the magnetic pressure force associated with the Alfvén wave. In [Verwichte et al. \(1999\)](#) they show that each time nonlinear Alfvén pulses pass through each other, they generate a slow magnetoacoustic wave (in $\beta \ll 1$ plasma). They also show that for nonlinear Alfvén pulses, the Alfvén speed is dependent on the wave amplitude. They show that the evolution of an Alfvén pulse is described by the Cohen-Kulsrud equation ([Cohen and Kulsrud, 1974](#)), which is similar to Burger's equation. They show that shocks form and calculate the time at which the gradient of the solution becomes singular. [Nakariakov et al. \(1997\)](#); [Thurgood and McLaughlin \(2013a,b\)](#) shows that if there are gradients perpendicular to the field and the invariant direction then fast waves are produced by the ponderomotive force. [Terradas et al. \(2006\)](#) show that for a line-tied standing Alfvén wave, the ponderomotive force pushes plasma towards the antinodes and away from the nodes. They show that in a $\beta = 0$, isothermal, plasma, the amplitude of the density structures grows quadratically with time and this growth is limited by the pressure force if $\beta \neq 0$. In [Prokopyszyn et al. \(2019\)](#), we investigated standing nonlinear Alfvén waves in an X-type null point. We found that introducing nonlinearities had a relatively small effect (<10%) effect on γ . However, we used an unphysically large value for the diffusion constants to keep the system well resolved numerically.

Modelling the plasma as linear and modelling $\partial/\partial y = 0$ prevents the development of turbulence through the Kelvin-Helmholtz instability, tearing mode instability and by the nonlinear interaction of counter-propagating Alfvén waves ([Hollweg, 1986a](#); [van Ballegooijen et al., 2011](#); [Shoda et al., 2019](#)). Turbulence leads to the transfer of energy into higher wavenumbers/frequencies, which are then dissipated ([Karimabadi et al., 2013](#)), causing γ to increase. However, we showed in Equation (3.6.8) that for frequencies greater than about $\omega = \pi$ Hz the $\mathbf{W}^{(0)}$ component of the viscosity tensor starts to dominate. Therefore, our claim that the $\mathbf{W}^{(1)}$ component plays a negligible role in

coronal heating, in general, holds for a turbulent plasma.

Finally, we modelled the plasma as isothermal, and we discuss this in Section 1.3.9. In Cargill et al. (2016), they investigate the thermodynamic response of the plasma to the heating generated by phase-mixing. They find that the thermodynamics act to reduce the gradient in Alfvén speed which reduces γ . Also, including the thermodynamics will cause the natural frequencies of the system to change with time. Arregui (2015) argues that resonances could not last long enough for substantial heating from phase-mixing to occur. This suggests that including the thermodynamics in the model acts to reduce γ , which helps ensure Equation (3.6.1) is an upper bound for γ .

3.7 Conclusions

The results and discussions in this chapter suggest that the dissipation of the gradients produced by phase mixing plays a negligible role in coronal heating. However, it is possible that phase mixing could trigger the Kelvin-Helmholtz and tearing mode instabilities which cause a turbulent cascade. Then dissipation can occur primarily due to the $\mathbf{W}^{(0)}$ component of the viscosity tensor which dissipates gradients parallel to the magnetic and velocity fields. In Section 3.1 we showed that we require $\gamma \approx 10^{-1} \text{ s}^{-1}$ and Equation (3.6.1) shows that our upper bound for γ is too small by approximately 3 orders of magnitude. This upper bound was modelled to be an average upper bound across the whole corona. Phase mixing models can give a larger value of γ near, for example, null points or at highly divergent magnetic fields due to the greater presence of viscosity and the Alfvén speed-length scale, a , being larger.

In Section 3.3 we calculated the solution for a phase-mixed resistive Alfvén wave in an open-loop using the method of multiple scales. We then verified this numerically via a graphical approach, see Figure 3.1. We showed that the wave decays with a cubic Gaussian, $\exp[-(z/L_{ph})^3]$, in z with a length scale L_{ph} given by Equation (3.3.18). This shows that as the wave propagates the wave decays faster due to the wave phase mixing and the length-scales across the field getting shorter. We estimate at $z = L_{ph}$ the length scales in x are given by Equation (3.3.20), and we find this is still sufficiently long for collisional transport theory to be valid in the corona. Heyvaerts and Priest (1983) shows that propagating Alfvén waves are stable to the Kelvin-Helmholtz instability because the magnetic field and velocity perturbations are in phase with each other. For standing

Alfvén waves, the velocity and magnetic field perturbations are out of phase with each other in space and time. So the magnetic field cannot stabilise the velocity shear from the Kelvin-Helmholtz instability.

In Section 3.4 we extended our analytic solution from Section 3.3 to calculate an analytic solution for a closed-loop using a method of images approach. We then verified this numerically and plotted the results in Figure 3.2. After that, we calculated the solution for the case where multiple harmonics are excited. We showed that an upper bound for the heating rate per unit of wave energy, γ , can be well approximated with Equation (3.4.38) where this assumes a power spectrum with slope $\alpha = 1$. We use this formula in Section 3.6 to conclude that dissipation of the gradients produced by phase mixing plays a negligible role in coronal heating.

In Section 3.5, we calculate the solution for the case where waves can leak out of the corona. We find that this acts to reduce γ , and this is because waves leak out of the corona before they can phase-mix to short length scales where significant heating can occur. This means that our upper bound for γ can ignore the effects of leakage.

Finally, in Section 3.6 we brought results from the previous sections to conclude that the dissipation of the gradients produced by phase mixed Alfvén plays a negligible role in coronal heating. We then discussed the validity of this conclusion and whether we have missed any essential physics in our model, which might change our judgment. This included: whether our value for the characteristic Alfvén speed length-scale, a , was valid. Whether unobserved high-frequency waves could be significant. The importance of nonlinearities. The implications of assuming $\partial/\partial y = 0$. Finally, how including the thermodynamic response of the system may affect the results.

Chapter 4

Resonant absorption in an oblique field

This chapter contains work which has been adapted from [Prokopszyn et al. \(2021\)](#).

4.1 Introduction

In the previous chapter, we modelled the y -direction as invariant. This chapter builds on the last, by allowing for an $\exp(ik_y y)$ y -dependence. We will see that this enables mode conversion and a phenomenon called resonant absorption to occur. Resonant absorption is a process where magnetoacoustic waves mode convert to Alfvén waves resulting in a concentration of energy. In Section 4.4 we give a simple example of resonant absorption. It is analogous to a process which occurs in Barton’s pendulum experiment (see Figure 4.1). In Barton’s experiment, a heavy pendulum acts as a driver for a series of lighter pendula/oscillators. We choose one of these lighter oscillators, called the resonant pendulum, to have the same natural frequency as the driving frequency. Since all the oscillators connect to the same string, the heavy pendulum drives them all at the same frequency. After a while, the system reaches an approximate steady-state where the whole system oscillates at the driver frequency. At steady-state, the resonant pendulum oscillates at a significantly larger amplitude than the other oscillators. The string which connects the oscillators is analogous to magnetoacoustic waves, and the oscillators are analogous to standing Alfvén waves. In both cases, energy accumulates in a narrow

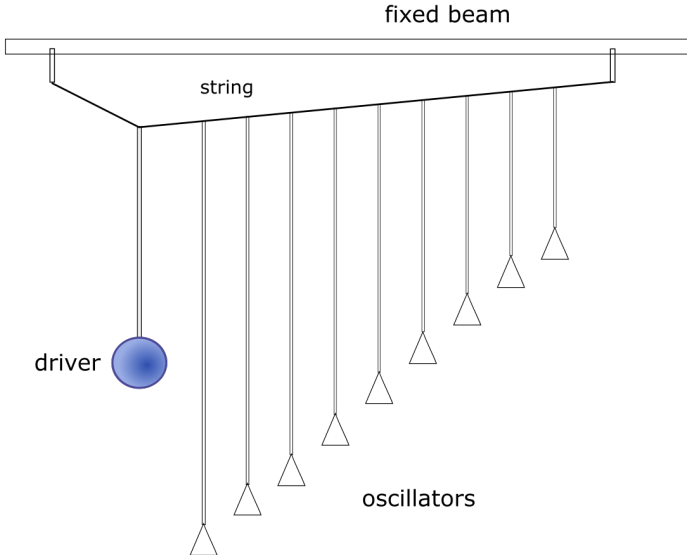


Figure 4.1: A diagram of the Barton's pendulums experiment (courtesy Wikipedia).

region due to resonance.

Resonant absorption is essential in the field of coronal seismology. Coronal seismology is a technique which enables solar physicists to infer coronal quantities (e.g. plasma density or magnetic field strength) by studying observed MHD waves ([Nakariakov and Verwiche, 2005](#)). The technique usually involves recording data that can be measured relatively easily, e.g. wave period, wavelength, amplitude, damping time and then using MHD wave theory to infer harder to measure quantities like the magnetic field strength or density gradient. Resonant absorption can play a key role in damping observed coronal loop oscillations ([Nakariakov et al., 1999](#); [Terradas et al., 2006](#)). [Ruderman and Roberts \(2002\)](#) shows that a kink wave in a plasma cylinder can mode convert to a torsional Alfvén wave. This results in the amplitude of the kink wave following a decay profile closely resembling that of observed decay profiles. Also, resonant absorption leads to the development of short length scales through phase mixing, leading to heating. [Poedts et al. \(1989\)](#); [Ofman et al. \(1995\)](#) suggest that resonant absorption could explain coronal heating. However, [Prokopszyn and Hood \(2019\)](#) argue that the heating rate is too slow for observed wave amplitudes and frequencies.

Previous chapters injected waves using a footpoint driver, whereas, this chapter drives from the side for mathematical convenience. These waves could be generated by, for example, a nearby flare. However, it is not our aim to investigate how the waves enter the corona, but instead, we study their dynamics once they are in the corona. The origin of coronal waves remains an open question. It is difficult for Alfvén waves

generated at the photosphere to enter the corona (Cranmer and van Ballegooijen, 2005), due to the rapid exponential decay of the density with height in the chromosphere and the steep jump in density at the transition region. Hollweg (1984b) suggests resonances in coronal loops and spicules provide enough energy flux to the corona to match the observed wave velocity amplitudes. Cally and Hansen (2011); Hansen and Cally (2012) suggest that mode conversion from fast waves to Alfvén waves at the transition region enables sufficient energy flux to enter the corona. It is also possible that the corona itself generates Alfvén waves via magnetic reconnection (Cranmer, 2018) and the energy released during reconnection partially feeds into the energy contained in the Alfvén waves.

This chapter closely follows the seminal work of Halberstadt and Goedbloed (1993); Goedbloed and Halberstadt (1994); Halberstadt and Goedbloed (1995). They modelled linear MHD waves and resonant absorption in a closed domain where the background magnetic field is tilted to be oblique to the solar surface. They showed that imposing line-tied boundary conditions causes the Alfvén waves and fast waves to couple. If the transverse length-scales are shorter than the Alfvén wavelength then evanescent fast waves/boundary layers form at the line-tied boundaries. Note that resonant absorption typically generates transverse length-scales, which are many times shorter than the Alfvén wavelength. Goedbloed and Halberstadt (1994) clearly shows the boundary layers in Figure 6c of their paper for the fast wave components of the Lagrangian displacements (ξ_F and η_F). We recommend reading Goedbloed and Halberstadt (1994) for an in-depth explanation of how the boundary layers form, but we also give a brief explanation in the penultimate paragraph of Section 4.5. Arregui et al. (2003) confirms the existence of these boundary layers via a numerical approach. One of the key differences between the work presented in this paper to that already in the literature is that we test the validity of imposing line-tied boundary conditions. To test the validity, we check if a model which includes the chromosphere instead of imposing line-tied boundary conditions can produce similar boundary layers. We model the corona and chromosphere using a piecewise constant background density profile with a discontinuous jump from the corona to the chromosphere.

The outline of this chapter is as follows; in Sections 4.2 and 4.3 we present the equations we will use to model the plasma and then discuss the applicability of some of the assumptions we make in the corona. Section 4.4 introduces some of the key and most

relevant properties of resonant absorption in a simple domain where the background magnetic field is perpendicular to the $z = z_{min}$ and $z = z_{max}$ boundaries. In Section 4.5, we calculate normal mode solutions in a domain where the Alfvén speed is uniform. We impose an incident Alfvén wave and calculate the unique solution which ensures the velocity is zero at $z = 0$. Since the Alfvén speed is uniform, resonant absorption cannot occur. However, we choose the length scales in x to be extremely short to simulate the conditions near a singularity in a resonant absorption experiment. Section 4.6 builds on Section 4.5 by using a background Alfvén speed which is piecewise constant in z . The regions $z > 0$ and $z < 0$ corresponds to the corona and chromosphere, respectively. We impose an incident Alfvén wave and calculate the unique solution which ensures continuity of the velocity and its derivative at $z = 0$. By comparing results from Sections 4.5 and 4.6, we can test how robust the boundary layers produced by line-tied boundary conditions are when we consider the finite nature of the jump in Alfvén speeds and the small length scales of a resonance layer. In Section 4.7 we use a background Alfvén speed which is a function of x and piecewise constant in z . Our goal here is to test if steep boundary layers form in a resonant absorption experiment. Finally, in Section 4.8, a summary of our results and conclusions are given.

4.2 Model and equations

In this section, we describe the most general model we will use. However, throughout this chapter, we will start with a simpler model. In subsequent sections, we will add complexity to the model as we head towards the most relevant description of resonance in coronal magnetic fields. For example, in Sections 4.5 and 4.6, the background Alfvén speed, v_A , will not depend on x but, in Section 4.7, we include a variation in x as well as a model chromosphere.

We model perturbations on a static background equilibrium and make the same assumptions as those described by Equation (1.4.3)-(1.4.5). The system is assumed to be ideal, i.e. we neglect viscosity and resistivity. We model the plasma as cold, i.e. $\beta = 0$, which means the gas pressure force is negligible. We assume the Lorentz force dominates and neglect the gravitational force. The background magnetic field is at an

angle α to the z -axis in the y - z plane, i.e.

$$\begin{aligned}\mathbf{B}_0 &= B_0(\sin \alpha \hat{\mathbf{y}} + \cos \alpha \hat{\mathbf{z}}) \\ &= B_0 \hat{\mathbf{B}}_0,\end{aligned}\tag{4.2.1}$$

The unit vectors, $\hat{\mathbf{B}}_0$ and $\hat{\perp}$, are defined as

$$\hat{\mathbf{B}}_0 = \sin \alpha \hat{\mathbf{y}} + \cos \alpha \hat{\mathbf{z}},\tag{4.2.2}$$

$$\hat{\perp} = \cos \alpha \hat{\mathbf{y}} - \sin \alpha \hat{\mathbf{z}},\tag{4.2.3}$$

where both unit vectors are in the y - z plane, $\hat{\mathbf{B}}_0$ is parallel to the background magnetic field and $\hat{\perp}$ is perpendicular to the background magnetic field. The background Alfvén speed is given by $v_A(x, z) = \hat{v}_A(x)v_A(0, z)$, where

$$v_A(0, z) = \begin{cases} v_{A-}, & z < 0, \\ v_{A+}, & z \geq 0, \end{cases}\tag{4.2.4}$$

and $\hat{v}_A(x)$ is an arbitrary function of x satisfying $\hat{v}_A(0) = 1$. The region $z < 0$ models the chromosphere and the region $z > 0$ models the corona, therefore, $v_{A+} > v_{A-}$ due to the higher density in the chromosphere.

The variables we solve for are the velocity, \mathbf{u} , given by

$$\mathbf{u}(x, y, z) = u_x \hat{\mathbf{x}} + u_\perp \hat{\perp}\tag{4.2.5}$$

and the magnetic field perturbations, \mathbf{b} , given by

$$\mathbf{b}(x, y, z) = b_x \hat{\mathbf{x}} + b_\perp \hat{\perp} + b_{||} \hat{\mathbf{B}}_0,\tag{4.2.6}$$

where

$$\begin{aligned}\hat{\mathbf{b}}(x, y, z) &= \hat{b}_x \hat{\mathbf{x}} + \hat{b}_\perp \hat{\perp} + \hat{b}_{||} \hat{\mathbf{B}}_0 \\ &= \frac{\mathbf{b}}{B_0}.\end{aligned}\tag{4.2.7}$$

The linearised momentum equation simplifies to

$$\frac{\partial \mathbf{u}}{\partial t} = \frac{1}{\mu\rho(x,z)}[(\mathbf{B}_0 \cdot \nabla)\mathbf{b} - \nabla(\mathbf{b} \cdot \mathbf{B}_0)], \quad (4.2.8)$$

and the induction equation simplifies to

$$\frac{\partial \mathbf{b}}{\partial t} = (\mathbf{B}_0 \cdot \nabla)\mathbf{u} - \mathbf{B}_0 \nabla \cdot \mathbf{u}. \quad (4.2.9)$$

Written out component-wise, the above equations become

$$\frac{\partial u_x}{\partial t} = v_A^2(x,z) \left[\nabla_{||} \hat{b}_x - \frac{\partial \hat{b}_{||}}{\partial x} \right], \quad (4.2.10)$$

$$\frac{\partial u_{\perp}}{\partial t} = v_A^2(x,z) \left[\nabla_{||} \hat{b}_{\perp} - \nabla_{\perp} \hat{b}_{||} \right], \quad (4.2.11)$$

$$\frac{\partial \hat{b}_x}{\partial t} = \nabla_{||} u_x, \quad (4.2.12)$$

$$\frac{\partial \hat{b}_{\perp}}{\partial t} = \nabla_{||} u_{\perp}, \quad (4.2.13)$$

$$\frac{\partial \hat{b}_{||}}{\partial t} = - \left[\frac{\partial u_x}{\partial x} + \nabla_{\perp} u_{\perp} \right], \quad (4.2.14)$$

where

$$\begin{aligned} \nabla_{\perp} &= \hat{\perp} \cdot \nabla \\ &= \cos \alpha \frac{\partial}{\partial y} - \sin \alpha \frac{\partial}{\partial z}, \end{aligned} \quad (4.2.15)$$

$$\begin{aligned} \nabla_{||} &= \hat{\mathbf{B}}_0 \cdot \nabla \\ &= \sin \alpha \frac{\partial}{\partial y} + \cos \alpha \frac{\partial}{\partial z}, \end{aligned} \quad (4.2.16)$$

are the derivatives perpendicular and parallel to the equilibrium magnetic field respectively.

In this chapter, we will derive exact analytic solutions to the equations. However, the formulae we derive are often cumbersome, and so our discussion will often focus on approximate (but less cumbersome) solutions in our narrower parameter space. The

parameter space we will focus on is

$$k_x \gg k_{\parallel+}, \quad (4.2.17)$$

$$k_{\parallel-} \gg k_{\parallel+}, \quad (4.2.18)$$

$$0 < k_y \leq O(k_{\parallel+}), \quad (4.2.19)$$

$$0 < \tan \alpha \leq O(1), \quad (4.2.20)$$

where

$$k_{\parallel\pm} = \frac{\omega}{v_{A\pm}}, \quad (4.2.21)$$

$$k_{\parallel 0} = \frac{\omega}{v_{A0}} \quad (4.2.22)$$

gives the Alfvén wavenumber and ω gives the wave frequency. We model $k_x \gg k_{\parallel+}$ as this approximates the conditions near a singularity in a resonant absorption experiment. The results should also apply to other cases where $k_x \gg k_{\parallel+}$, for example, during the nonlinear development of an instability. Our condition for α (Equation 4.2.20) prevents the background magnetic field from being tangential to the $z = 0$ plane. In for example, Vickers et al. (2018, 2020), they study the solutions where α is close to $\pi/2$.

4.3 Energy equations

Resonant absorption occurs when fast waves mode convert into Alfvén waves at a resonant field line. This can be better understood by considering how the oscillations in the x and $\hat{\mathbf{B}}_0$ direction couple to the fluctuations in the perpendicular (\perp) direction. Note that the x and parallel (\parallel) perturbation energy density is given by

$$\frac{1}{2}\rho u_x^2 + \frac{b_x^2}{2\mu} + \frac{b_\parallel^2}{2\mu},$$

and the \perp -energy density is given by

$$\frac{1}{2}\rho u_\perp^2 + \frac{b_\perp^2}{2\mu}.$$

Taking the dot product of Equation (4.2.8) with $\mathbf{u}_x = u_x \hat{\mathbf{x}}$ gives

$$\frac{\partial}{\partial t} \left(\frac{1}{2} \rho u_x^2 \right) = \frac{1}{\mu} [(\mathbf{B}_0 \cdot \nabla) b_x] u_x - \frac{B_0}{\mu} \frac{\partial b_{||}}{\partial x} u_x.$$

Taking the dot product of Equation (4.2.8) with $\mathbf{b}_x = b_x \hat{\mathbf{x}}$ gives

$$\frac{\partial}{\partial t} \left(\frac{b_x^2}{2\mu} \right) = \frac{1}{\mu} [(\mathbf{B}_0 \cdot \nabla) u_x] b_x.$$

Note that,

$$\nabla \cdot \left(\frac{\mathbf{E} \times \mathbf{b}_x}{\mu} \right) = -\frac{1}{\mu} \mathbf{B}_0 \cdot \nabla (u_x b_x),$$

hence,

$$\frac{\partial}{\partial t} \left(\frac{1}{2} \rho u_x^2 + \frac{b_x^2}{2\mu} \right) + \nabla \cdot \left(\frac{\mathbf{E} \times \mathbf{b}_x}{\mu} \right) = -\frac{B_0}{\mu} u_x \frac{\partial b_{||}}{\partial x}. \quad (4.3.1)$$

Similarly, we can show that

$$\frac{\partial}{\partial t} \left(\frac{1}{2} \rho u_{\perp}^2 + \frac{b_{\perp}^2}{2\mu} \right) + \nabla \cdot \left(\frac{\mathbf{E} \times \mathbf{b}_{\perp}}{\mu} \right) = -\frac{B_0}{\mu} u_{\perp} \nabla_{\perp} b_{||}, \quad (4.3.2)$$

$$\frac{\partial}{\partial t} \left(\frac{b_{||}^2}{2\mu} \right) + \nabla \cdot \left(\frac{\mathbf{E} \times \mathbf{b}_{||}}{\mu} \right) = \frac{B_0}{\mu} (\mathbf{u} \cdot \nabla) b_{||}. \quad (4.3.3)$$

Adding Equation (4.3.1) to (4.3.3) gives

$$\frac{\partial}{\partial t} \left(\frac{1}{2} \rho u_x^2 + \frac{b_x^2 + b_{||}^2}{2\mu} \right) + \nabla \cdot \left[\frac{\mathbf{E} \times (\mathbf{b}_x + \mathbf{b}_{||})}{\mu} \right] = \frac{B_0}{\mu} u_{\perp} \nabla_{\perp} b_{||}. \quad (4.3.4)$$

Equations (4.3.2) and (4.3.4) show that gradients in the magnetic pressure, $B_0 b_{||}/\mu$, are responsible for the mode conversion from oscillations in the x , $||$ directions to oscillations in the \perp direction. If $\nabla_{\perp} = 0$ then no mode conversion can occur between the fast and Alfvén waves and they are independent of one another. For example, this occurs when $\alpha = 0$ and $\partial/\partial y = 0$.

4.4 Normal field: Resonant absorption with line-tied BCs

This section aims to introduce resonant absorption by calculating the solution for the simple case where $\alpha = 0$. Therefore, the background magnetic field points in the z -direction. We aim to show how the waves can form very short length-scales if the system has a relatively small gradient in Alfvén travel time across the background magnetic field lines.

4.4.1 Equations

For simplicity, we will model the chromosphere as infinitely denser than the corona, i.e. $v_{A-} \rightarrow 0$. We will model the z -range as $0 \leq z \leq L_z$ and impose line-tied boundary conditions at $z = 0$ and $z = L_z$, i.e.

$$u_x|_{z=0} = u_x|_{z=L_z} = u_y|_{z=0} = u_y|_{z=L_z} = 0. \quad (4.4.1)$$

Therefore, $v_A = v_A(x)$. The x domain is given by $x \geq x_{min}$ and we impose a driver at $x = x_{min}$, of the form

$$u_x(x_{min}, y, z, t) = f_{driv}(y, z, t), \quad (4.4.2)$$

$$\left. \frac{\partial u_x}{\partial x} \right|_{x=x_{min}} = g_{driv}(y, z, t). \quad (4.4.3)$$

Since $\alpha = 0$, this means that $u_y = u_\perp$, $b_y = b_\perp$ and $b_z = b_{||}$. Also, $\nabla_\perp = \partial/\partial y$ and $\nabla_{||} = \partial/\partial z$. Therefore, Equations (4.2.10)-(4.2.14) can be written as

$$\frac{\partial u_x}{\partial t} = v_A^2(x) \left[\frac{\partial \hat{b}_x}{\partial z} - \frac{\partial \hat{b}_z}{\partial x} \right], \quad (4.4.4)$$

$$\frac{\partial u_y}{\partial t} = v_A^2(x) \left[\frac{\partial \hat{b}_y}{\partial z} - \frac{\partial \hat{b}_z}{\partial y} \right], \quad (4.4.5)$$

$$\frac{\partial \hat{b}_x}{\partial t} = \frac{\partial u_x}{\partial z}, \quad (4.4.6)$$

$$\frac{\partial \hat{b}_y}{\partial t} = \frac{\partial u_y}{\partial z}, \quad (4.4.7)$$

$$\frac{\partial \hat{b}_z}{\partial t} = - \left[\frac{\partial u_x}{\partial x} + \frac{\partial u_y}{\partial y} \right]. \quad (4.4.8)$$

4.4.2 Analytic solution

The problem is linear and the functions we need to solve for depend on just x . Therefore, by assuming a Fourier solution in y , z and t we can convert the PDEs, (4.4.4)-(4.4.8) into a set of ODEs. We assume the solutions are of the form

$$u_x(x, y, z, t) = \sum_{n=1}^{\infty} u_{xn}(x) \sin(k_{zn}z) \exp[i(k_y y + \omega t)], \quad (4.4.9)$$

$$u_y(x, y, z, t) = \sum_{n=1}^{\infty} u_{yn}(x) \sin(k_{zn}z) \exp[i(k_y y + \omega t)], \quad (4.4.10)$$

$$\hat{b}_x(x, y, z, t) = \sum_{n=1}^{\infty} \hat{b}_{xn}(x) \sin(k_{zn}z) \exp[i(k_y y + \omega t)], \quad (4.4.11)$$

$$\hat{b}_y(x, y, z, t) = \sum_{n=1}^{\infty} \hat{b}_{yn}(x) \sin(k_{zn}z) \exp[i(k_y y + \omega t)], \quad (4.4.12)$$

$$\hat{b}_z(x, y, z, t) = \sum_{n=1}^{\infty} \hat{b}_{zn}(x) \sin(k_{zn}z) \exp[i(k_y y + \omega t)], \quad (4.4.13)$$

where k_y , ω are constants (which can be complex),

$$k_{zn} = \frac{n\pi}{L_z}, \quad (4.4.14)$$

this ensures the line-tied boundary conditions in z are automatically satisfied. Substituting the above series into Equations (4.4.4)-(4.4.8), and multiplying by $\sin(k_{zm}z)$ and integrating from 0 to L_z gives.

$$i\omega u_{xm} = v_A^2(x) \left[ik_{zm} \hat{b}_{xm} - \frac{d\hat{b}_{zm}}{dx} \right], \quad (4.4.15)$$

$$i\omega u_{ym} = v_A^2(x) \left[ik_{zm} \hat{b}_{xm} - ik_y \hat{b}_{zm} \right], \quad (4.4.16)$$

$$i\omega \hat{b}_{xm} = ik_{zm} u_{xm}, \quad (4.4.17)$$

$$i\omega \hat{b}_{ym} = ik_{zm} u_{ym}, \quad (4.4.18)$$

$$i\omega \hat{b}_{zm} = - \left[\frac{du_{xm}}{dx} + ik_y u_{ym} \right]. \quad (4.4.19)$$

Let

$$\mathcal{L}_n(x) = \frac{\omega^2}{v_A^2(x)} - k_{zn}^2. \quad (4.4.20)$$

Eliminating \hat{b}_{xn} and \hat{b}_{yn} gives

$$\mathcal{L}_n(x)u_{xn}(x) = i\omega \frac{d\hat{b}_{zn}}{dx}, \quad (4.4.21)$$

$$\mathcal{L}_n(x)u_{yn}(x) = ik_y i\omega \hat{b}_{zn}. \quad (4.4.22)$$

Eliminating \hat{b}_{zn} gives

$$\frac{d^2u_{xn}}{dx^2} + \mathcal{L}_n(x)u_{xn}(x) = -ik_y \frac{du_{yn}}{dx}, \quad (4.4.23)$$

$$[\mathcal{L}_n(x) - k_y^2]u_{yn}(x) = -ik_y \frac{du_{xn}}{dx}. \quad (4.4.24)$$

Eliminating u_{yn} from Equation (4.4.23), using Equation (4.4.24), gives

$$\begin{aligned} \frac{d^2u_{xn}}{dx^2} + \mathcal{L}_n(x)u_{xn}(x) &= -ik_y \frac{d}{dx} \left[\frac{-ik_y}{\mathcal{L}_n(x) - k_y^2} \frac{du_{xn}}{dx} \right] \\ &= \frac{-k_y^2}{\mathcal{L}_n(x) - k_y^2} \left[\frac{d^2u_{xn}}{dx^2} - \frac{\mathcal{L}_x(x)}{\mathcal{L}_n(x) - k_y^2} \frac{du_{xn}}{dx} \right], \end{aligned}$$

where

$$\begin{aligned} \mathcal{L}_x(x) &= \frac{d\mathcal{L}_n}{dx} \\ &= -2 \frac{\omega^2}{v_A^3(x)} \frac{dv_A}{dx} \\ &= -\frac{2\omega^2}{v_A^2(x)a(x)}, \end{aligned} \quad (4.4.25)$$

$$a(x) = \frac{v_A(x)}{dv_A/dx}. \quad (3.3.16)$$

Rearranging gives

$$\mathcal{L}_n(x) \frac{d^2 u_{xn}}{dx^2} - \frac{k_y^2 \mathcal{L}_x(x)}{\mathcal{L}_n(x) - k_y^2} \frac{du_{xn}}{dx} + \mathcal{L}_n(x)[\mathcal{L}_n(x) - k_y^2] u_{xn}(x) = 0. \quad (4.4.26)$$

We can eliminate u_x to get an equation for u_\perp via the following procedure. Take the x -derivative of Equation (4.4.23) to give

$$u_{xn}(x) = -\frac{1}{\mathcal{L}'_n(x)} \left\{ \left[\frac{d^2}{dx^2} + \mathcal{L}_n \right] \frac{du_{xn}}{dx} + ik_y \frac{d^2 u_{yn}}{dx^2} \right\}.$$

Substitute this into Equation (4.4.23) to give

$$\frac{d^2 u_{xn}}{dx^2} - \frac{\mathcal{L}_n}{\mathcal{L}_x} \left\{ \left[\frac{d^2}{dx^2} + \mathcal{L}_n \right] \frac{du_{xn}}{dx} + ik_y \frac{d^2 u_{yn}}{dx^2} \right\} = -ik_y \frac{du_{yn}}{dx},$$

where we have assumed $\mathcal{L}_x(x) \neq 0$. See for example Thompson and Wright (1993) for a calculation of the solution in the case where $\mathcal{L}_n(x) = \mathcal{L}_x(x) = 0$. Multiply through by $-ik_y$ and eliminate u_{xn} using Equation (4.4.24) to give

$$\begin{aligned} & \frac{d}{dx} [(\mathcal{L}_n - k_y^2) u_{yn}] - \\ & \frac{\mathcal{L}_n}{\mathcal{L}_x(x)} \left\{ \left[\frac{d^2}{dx^2} + \mathcal{L}_n \right] [\mathcal{L}_n - k_y^2] u_{yn} + k_y^2 \frac{d^2 u_{yn}}{dx^2} \right\} = -k_y^2 \frac{du_{yn}}{dx}. \end{aligned}$$

This can be simplified to give

$$\mathcal{L}_n^2 \frac{d^2 u_{yn}}{dx^2} + \mathcal{L}_x \mathcal{L}_n \frac{du_{yn}}{dx} + (\mathcal{L}_n^3 + \mathcal{L}_{xx} \mathcal{L}_n - k_y^2 \mathcal{L}_n - \mathcal{L}_x^2) u_{yn} = 0, \quad (4.4.27)$$

where

$$\mathcal{L}_{xx} = \frac{d\mathcal{L}_x}{dx}. \quad (4.4.28)$$

Our goal now is to solve Equations (4.4.26) and (4.4.27) using the method of Frobenius. Assume that \mathcal{L}_n is an analytic function. Therefore, points where $\mathcal{L}_n(x) \neq 0$ are ordinary/regular points of Equation (4.4.27) and points where $\mathcal{L}_n(x) = 0$ are regular-singular points of the ODE. Let $x_{res,n}$ be defined as a point satisfying $\mathcal{L}_n(x_{res,n}) = 0$. If multiple points satisfy $\mathcal{L}_n(x) = 0$, then pick $x_{res,n}$ equal to one of these points ar-

bitrarily. Since we expect solutions u_{yn} to be singular at $x = x_{res,n}$, we will focus on studying solutions near this point.

Radius of convergence

Multiplying Equation (4.4.26) through by $(x - x_{res,n})^2 / \mathcal{L}_n(x)$ gives

$$(x - x_{res,n})^2 \frac{d^2 u_{xn}}{dx^2} + (x - x_{res,n}) p_n(x) \frac{du_{xn}}{dx} + q_n(x) u_{xn}(x) = 0, \quad (4.4.29)$$

where

$$p_n(x) = -\frac{k_y^2 \mathcal{L}_x(x)(x - x_{res,n})}{\mathcal{L}_n(x)(\mathcal{L}_n(x) - k_y^2)}, \quad (4.4.30)$$

$$q_n(x) = (\mathcal{L}_n(x) - k_y^2)(x - x_{res,n})^2. \quad (4.4.31)$$

The power series solution for u_{xn} about $x = x_{res,n}$ will have a radius of convergence at least as large as the radius of convergence for the power series of $p_n(x)$ and $q_n(x)$ about $x = x_{res,n}$. Since $\mathcal{L}_n(x)$ is analytic, we expect the radius of convergence for q_n to be infinite. The radius of convergence of $p_n(x)$ (denoted with R_n) is equal to the distance in the complex plane between $x_{res,n}$ and the nearest zero of $\mathcal{L}_n(x)(\mathcal{L}_n(x) - k_y^2)$ (excluding the point $x = x_{res,n}$). Hence, the radius of convergence for u_{xn} about $x = x_{res,n}$ is at least as large as R_n .

Indicial polynomial

To calculate the solution, via the method of Frobenius, we first need to calculate the indicial polynomial. Substituting

$$u_{xn}(x) = (x - x_{res,n})^\sigma \sum_{k=0}^{\infty} a_k (x - x_{res,n})^k,$$

into Equation (4.4.29) gives

$$\sum_{k=0}^{\infty} [(k + \sigma - 1)(k + \sigma) + (k + \sigma)p_n(x) + q_n(x)] a_k (x - x_{res,n})^k = 0.$$

We need to find values of σ where non-trivial solutions can exist. Taylor expanding $p(x)$ and $q(x)$ about $x = x_{res,n}$, we calculate the coefficient of the leading order power in $(x - x_{res,n})$ to be given by

$$I(\sigma) = (\sigma - 1)\sigma + p_n(x_{res,n})\sigma + q_n(x_{res,n}), \quad (4.4.32)$$

where $I(\sigma)$ is the indicial polynomial. Since $I(\sigma) = 0$, $p_n(x_{res,n}) = 1$ and $q_n(x_{res,n}) = 0$ we know that $\sigma^2 = 0$. Since we have repeated roots, the general solution is given by a linear combination of

$$u_{xn1}(x) = \sum_{k=0}^{\infty} a_k (x - x_{res,n})^k, \quad (4.4.33)$$

and

$$u_{xn2}(x) = u_{xn1}(x) \ln(x - x_{res,n}) + \sum_{k=1}^{\infty} b_k (x - x_{res,n})^k. \quad (4.4.34)$$

Recurrence relations

We will now calculate the recurrence relation for the a_k terms. Substituting $u_{xn1}(x)$ into Equation (4.4.29) and Taylor expanding $p_n(x)$ and $q_n(x)$ about $x = x_{res,n}$ gives

$$\sum_{k=0}^{\infty} \left[I(k)a_k + \sum_{j=0}^{k-1} \frac{jp_n^{(k-j)}(x_{res,n}) + q_n^{(k-j)}(x_{res,n})}{(k-j)!} a_j \right] (x - x_{res,n})^k = 0.$$

Equating the coefficient of $(x - x_{res,n})^k$ equal to zero gives the following recurrence relation,

$$a_k = -\frac{1}{I(k)} \sum_{j=0}^{k-1} \frac{jp_n^{(k-j)}(x_{res,n}) + q_n^{(k-j)}(x_{res,n})}{(k-j)!} a_j, \quad (4.4.35)$$

for $k \geq 1$, where we arbitrarily set $a_0 = 1$. Setting $a_0 = 1$ does not lose generality as u_{xn} is equal to a linear combination of u_{xn1} and u_{xn2} . Since $q'_n(x_{res,n}) = 0$ we know that $a_1 = 0$.

We will now calculate an expression for the b_k terms. Note that

$$\begin{aligned}\frac{du_{xn2}}{dx} &= \frac{du_{xn1}}{dx} \ln(x - x_{res,n}) + \frac{u_{xn1}}{x - x_{res,n}} + \sum_{k=1}^{\infty} kb_k(x - x_{res,n})^{k-1}, \\ \frac{d^2u_{xn2}}{dx^2} &= \frac{d^2u_{xn1}}{dx^2} \ln(x - x_{res,n}) + \frac{2}{x - x_{res,n}} \frac{du_{xn1}}{dx} - \frac{u_{xn1}}{(x - x_{res,n})^2} \\ &\quad + \sum_{k=1}^{\infty} k(k-1)b_k(x - x_{res,n})^{k-2}.\end{aligned}$$

Hence, substituting $u_{xn2}(x)$ into Equation (4.4.29) gives

$$\begin{aligned}2(x - x_{res,n}) \frac{du_{xn1}}{dx} + [p_n(x) - 1]u_{xn1}(x) + \\ \sum_{k=1}^{\infty} [k(k-1) + kp_n(x) + q_n(x)]b_k(x - x_{res,n})^k = 0.\end{aligned}$$

Substituting for $u_{xn1}(x)$ gives

$$\begin{aligned}\sum_{k=0}^{\infty} [2k + p_n(x) - 1]a_k(x - x_{res,n})^k + \\ \sum_{k=1}^{\infty} [k(k-1) + kp_n(x) + q_n(x)]b_k(x - x_{res,n})^k = 0.\end{aligned}$$

Taylor expanding $p_n(x)$, $q_n(x)$ about $x = x_{res,n}$ gives

$$\begin{aligned}\sum_{k=0}^{\infty} \left[(2k + p_n(0) - 1)a_k + \sum_{j=0}^{k-1} \frac{p_n^{(k-j)}(x_{res,n})}{(k-j)!} a_j \right] (x - x_{res,n})^k + \\ \sum_{k=1}^{\infty} \left[I(k)b_k + \sum_{j=1}^{k-1} \frac{j p_n^{(k-j)}(x_{res,n}) + q_n^{(k-j)}(x_{res,n})}{(k-j)!} b_j \right] (x - x_{res,n})^k = 0.\end{aligned}$$

Equating the coefficient of $(x - x_{res,n})^k$ equal to zero gives

$$\begin{aligned} -I(k)b_k &= (2k + p_n(0) - 1)a_k + \sum_{j=0}^{k-1} \frac{p_n^{(k-j)}(x_{res,n})}{(k-j)!} a_j \\ &\quad + \sum_{j=1}^{k-1} \frac{jp_n^{(k-j)}(x_{res,n}) + q_n^{(k-j)}(x_{res,n})}{(k-j)!} b_j, \end{aligned} \tag{4.4.36}$$

for $k \geq 1$. Since $a_1 = 0$ and $a_0 = 1$ we know that b_1 is given by

$$b_1 = -p'_n(x_{res,n}). \tag{4.4.37}$$

Singular solutions

Our goal now is to calculate the leading order singular solutions for u_{xn} , u_{yn} and b_{zn} . Note that if $\omega \in \mathbb{C}$ then $x_{res,n} \in \mathbb{C}$. Let $x_{res,n} = x_{r,n} + ix_{i,n}$, where $x_{r,n}, x_{i,n} \in \mathbb{R}$. We will assume that $|x_{i,n}| \ll R_n$. Let u_{xn} be given by

$$\begin{aligned} u_{xn}(x) &= -iu_0 x_{i,n} k_y [u_{xn2}(x) - u_{xn1}(x) \ln(x_{i,n})] \\ &= -iu_0 x_{i,n} k_y [\ln(X_n) + x_{i,n} b_1 X_n + O(X_n^2 \ln X_n, X_n^2)], \end{aligned} \tag{4.4.38}$$

where

$$X_n = \frac{x - x_{res,n}}{x_{i,n}}. \tag{4.4.39}$$

From Equation (4.4.24) we know that

$$\begin{aligned} u_{yn}(x) &= \frac{-ik_y}{\mathcal{L}_n(x) - k_y^2} \frac{du_{xn}}{dx} \\ &= u_0 \left\{ \frac{1}{X_n} + x_{i,n} b_1 + \frac{\mathcal{L}_x}{k_y^2} x_{i,n} + O(X_n \ln X_n, X_n) \right\}. \end{aligned} \tag{4.4.40}$$

Substituting Equation (4.4.40) into Equation (4.4.22) gives

$$\begin{aligned}\hat{b}_{zn}(x) &= \frac{-\mathcal{L}_n(x)}{\omega k_y} u_{yn}(x) \\ &= \frac{u_0}{v_A(x_{res,n})} \left[-\frac{v_A(x_{res,n}) \mathcal{L}_x}{\omega k_y} x_{i,n} + O(X_n^2 \ln X_n, X_n) \right] \\ &= \frac{u_0}{v_A(x_{r,n})} \left[\frac{2\omega x_{i,n}}{v_A(x_{r,n}) a_0 k_y} + O(X_n^2 \ln X_n, X_n) \right].\end{aligned}\quad (4.4.41)$$

Poynting flux

One of the most useful quantities in coronal seismology is the wave (e.g. kink wave) damping time (Ruderman and Roberts, 2002; Giagkiozis et al., 2016). This is related to the Poynting flux, which gives the energy flux (see Equation 1.4.42).

Using Equation (1.4.40), the Poynting flux in the x -direction is given by

$$\begin{aligned}S_x &= \frac{1}{\mu} \left\{ [\operatorname{Re}(\mathbf{b}) \cdot \mathbf{B}_0] \operatorname{Re}(\mathbf{u}) - [\operatorname{Re}(\mathbf{u}) \cdot \operatorname{Re}(\mathbf{b})] \mathbf{B}_0 \right\} \cdot \hat{x} \\ &= \frac{B_0^2}{\mu} \operatorname{Re}(u_x) \operatorname{Re}(\hat{b}_z) \\ &= \frac{B_0^2}{\mu} \left(\frac{u_x + u_x^*}{2} \right) \left(\frac{\hat{b}_z + \hat{b}_z^*}{2} \right),\end{aligned}\quad (4.4.42)$$

where u_x^* denotes the complex conjugate of u_x . Therefore, the component which is not zero when averaged over time is given by

$$\langle S_x \rangle = \frac{B_0^2}{4\mu} \left(u_x \hat{b}_z^* + u_x^* \hat{b}_z \right). \quad (4.4.43)$$

Integrating in z from 0 to L_z gives

$$\begin{aligned}\int_0^{L_z} \langle S_x \rangle dz &= \frac{L_z}{2} \sum_{n=1}^{\infty} \frac{B_0^2}{4\mu} \left(u_{xn} \hat{b}_{zn}^* + u_{xn}^* \hat{b}_{zn} \right) \\ &= \frac{L_z}{2} \sum_{n=1}^{\infty} \langle S_{xn} \rangle,\end{aligned}\quad (4.4.44)$$

where

$$\langle S_{xn} \rangle = \frac{B_0^2}{4\mu} \left(u_{xn} \hat{b}_{zn}^* + u_{xn}^* \hat{b}_{zn} \right). \quad (4.4.45)$$

Using Equations (4.4.38) and (4.4.41), we know,

$$\begin{aligned} u_{xn} \hat{b}_{zn}^* &= \left[-ik_y u_0 x_{i,n} \ln X_n \right] \left[2 \frac{u_0 x_{i,n} \omega}{k_y v_A^2(x_{r,n}) a(x_{r,n})} \right] \sin^2(k_{zn} z) + \dots \\ &= u_0 \left[-2i \frac{u_0 x_{i,n}^2 \omega}{v_A^2(x_{r,n}) a(x_{r,n})} \ln(X_n) + O(X_n \ln X_n, X_n) \right], \end{aligned} \quad (4.4.46)$$

and

$$u_{xn}^* \hat{b}_{zn} = u_0 \left[2i \frac{u_0 x_{i,n}^2 \omega}{v_A^2(x_{r,n}) a(x_{r,n})} \ln(X_n^*) + O(X_n \ln X_n, X_n) \right], \quad (4.4.47)$$

where we assume that $x \in \mathbb{R}$. Therefore,

$$\begin{aligned} \langle S_{xn} \rangle &= i \frac{B_0^2}{2\mu} \frac{u_0^2 x_{i,n}^2 \omega}{v_A^2(x_{r,n}) a_0} \left[\ln(x - x_{res,n}^*) - \ln(x - x_{res,n}) \right] + \dots \\ &= -\frac{B_0^2}{2\mu} \frac{u_0^2 x_{i,n}^2 \omega}{v_A^2(x_{r,n}) a(x_{r,n})} \left[\tan^{-1}(x_{i,n}, x - x_{r,n}) - \tan^{-1}(-x_{i,n}, x - x_{r,n}) \right] + O(X_n \ln X_n, X_n). \end{aligned} \quad (4.4.48)$$

Note that

$$\lim_{x \rightarrow \infty} \left\{ \tan^{-1}(x_{i,n}, x - x_{r,n}) - \tan^{-1}(-x_{i,n}, x - x_{r,n}) \right\} = 0,$$

$$\lim_{x \rightarrow -\infty} \left\{ \tan^{-1}(x_{i,n}, x - x_{r,n}) - \tan^{-1}(-x_{i,n}, x - x_{r,n}) \right\} = 2\pi \operatorname{sign}(x_{i,n}).$$

Hence, the jump in Poynting flux, ΔS_{xn} across $x_{res,n}$ for $\omega_i \ll \omega_r$ is given by

$$\langle \Delta S_{xn} \rangle = \pi \frac{B_0^2}{\mu} \frac{u_0^2 x_{i,n}^2 \omega_r}{v_A^2(x_{r,n}) a(x_{r,n})} \operatorname{sign}(x_{i,n}), \quad (4.4.49)$$

where $\operatorname{sign}(x_{i,m}) = x_{i,n}/|x_{i,n}|$.

4.4.3 Numerical solution

Our goal now is to verify our analytic solution numerically. We can solve Equation (4.4.29) by integrating in x using `solve_ivp` in [Virtanen et al. \(2020\)](#).

We choose the Alfvén speed to be given by

$$v_A(x) = v_{A0} \left(1 + \frac{x}{a_0} \right), \quad (4.4.50)$$

where we assume $x > -a_0$. The resonant locations, $x_{res,n}$ are given by

$$\mathcal{L}_n(x_{res,n}) = 0 \implies v_A(x_{res,n}) = \frac{\omega}{k_{zn}},$$

therefore,

$$x_{res,n} = a_0 \left[\frac{\omega}{v_{A0} k_{zn}} - 1 \right]. \quad (4.4.51)$$

This implies that

$$x_{r,n} = a_0 \left[\frac{\omega_r}{v_{A0} k_{zn}} - 1 \right], \quad (4.4.52)$$

$$x_{i,n} = \frac{a_0 \omega_i}{v_{A0} k_{zn}}. \quad (4.4.53)$$

We choose

$$\omega_r = v_{A0} k_{z1} \quad (4.4.54)$$

and this ensures that $x_{r,1} = 0$. We set the boundary conditions in x as

$$u_x|_{x=x_{min}} = -ik_y u_0 x_{i,1} \ln(X_1) \sin(k_{z1} z) \exp[i(k_y y + \omega t)], \quad (4.4.55)$$

$$\left. \frac{\partial u_x}{\partial x} \right|_{x=x_{min}} = -\frac{ik_y u_0}{X_1} \sin(k_{z1} z) \exp[i(k_y y + \omega t)]. \quad (4.4.56)$$

These boundary conditions ensure that $u_{xn} = u_{yn} = \hat{b}_{zn} = 0, \forall n \neq 1$.

To check the accuracy and give a visualisation of Equations (4.4.38), (4.4.40) and (4.4.48), we plot these solutions and compare them with solutions calculated numer-

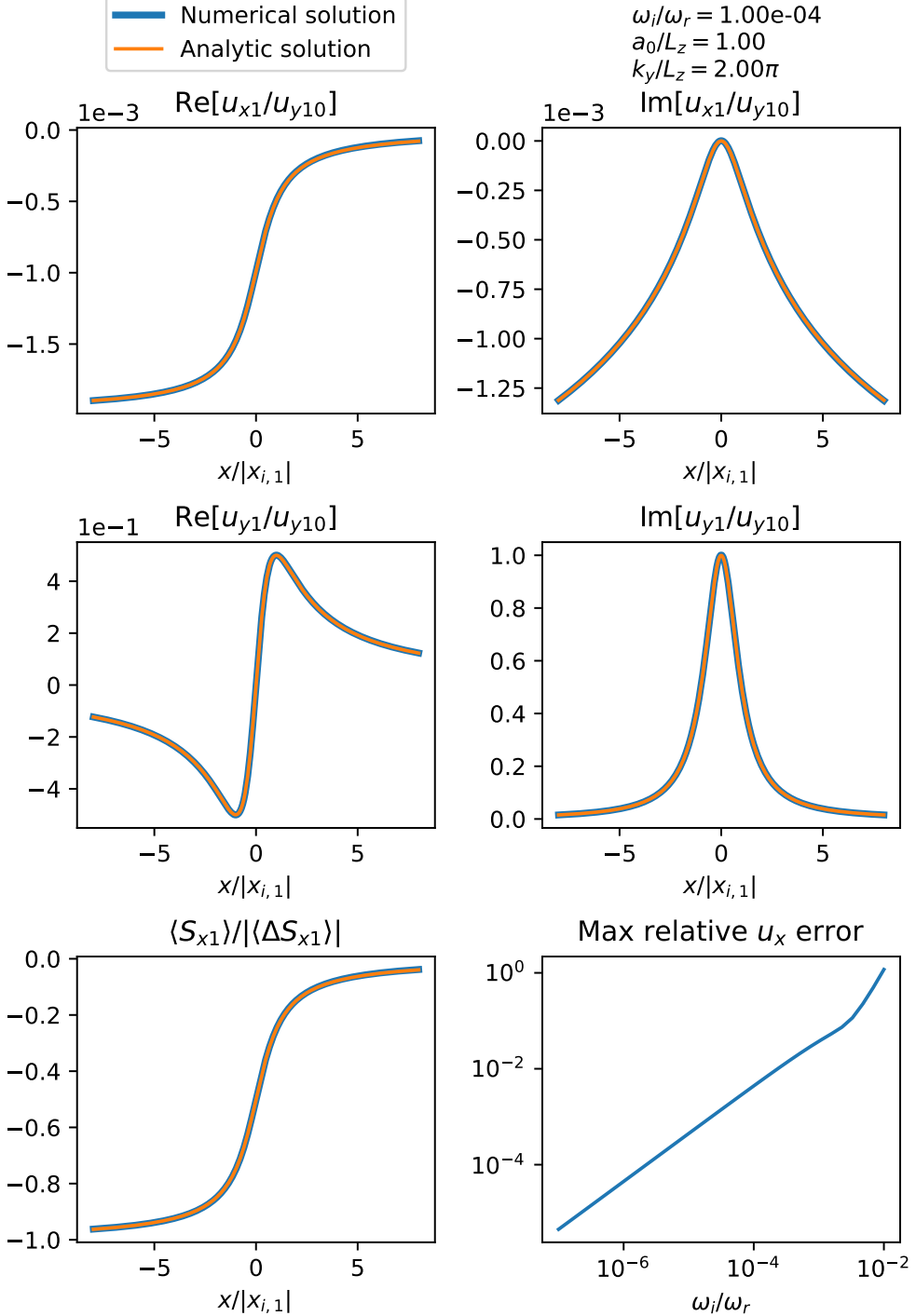


Figure 4.2: This figure shows the real and imaginary parts of $u_{x1}(x)$, $u_{y1}(x)$, as well as the Poynting flux, $\langle S_{x1} \rangle$ as a function of x . The bottom-right shows the maximum relative error between the numerical and analytic solutions for u_x against ω_i (see Equation 4.4.59). We calculated the blue curves numerically and calculated the orange curves analytically. Note that the Poynting flux is normalised by the absolute value of the jump, $|\langle \Delta S_{x1} \rangle|$, from Equation (4.4.49). The code used to make this figure is available on GitHub in the following directory:

[→ Python/Chapter4/normal_mode_along_x_alpha=0.py](#)

ically. In the top row of Figure 4.2 we show the real and imaginary parts of $u_{x1}(x)$. The analytic solution was calculated using Equation (4.4.38). The blue curve shows the numerical solution and the orange curve shows the analytic solution using Equation (4.4.38). The middle row shows the real and imaginary parts of $u_{y1}(x)$. The numerical solution was calculated by rearranging Equation (4.4.24), to give

$$u_{yn}(x) = \frac{-ik_y}{\mathcal{L}_n(x) - k_y^2} \frac{du_{xn}}{dx}. \quad (4.4.57)$$

The analytic solution was calculated using Equation (4.4.40). The bottom left plot shows the average Poynting flux directed in the x -direction. This was calculated using Equation (4.4.45) for $n = 1$. To calculate $\hat{b}_{z1}(x)$ numerically we used Equation (4.4.19) to give

$$\hat{b}_{zn}(x) = \frac{1}{i\omega} \left[\frac{\partial u_{xn}}{\partial x} + ik_y u_{yn} \right]. \quad (4.4.58)$$

The analytic solution was calculated using Equation (4.4.48). These plots show that the analytic and numerical solutions are in approximate agreement. However, this is for $\omega_i/\omega_r = 10^{-4}$. In the bottom right, we show the maximum relative error between the analytic and numerical solutions for u_x as a function of ω_i . The maximum relative error is given by

$$\text{Max relative } u_x \text{ error} = \max_{|x| \leq 8|x_{i,1}|} \left| \frac{u_{x,1}^{(num)} - u_{x,1}^{(ana)}}{u_{x,1}^{(num)}} \right|, \quad (4.4.59)$$

where $u_{x,1}^{(num)}$ denotes $u_{x,1}$ calculate numerically and $u_{x,1}^{(ana)}$ denotes $u_{x,1}$ calculated analytically using Equation (4.4.38). The bottom-right plot shows that as ω_i/ω_r increases, the error between the analytic and numerical solutions increases. Note that ω_i controls the rate of exponential growth (or decay) of the driver and should not be confused with the damping rate or the rate at which fast waves mode convert to Alfvén waves.

4.5 Oblique field: Uniform density profile

This section aims to show how boundary layers can form if the background magnetic field is oblique to the $z = z_{min}$ and $z = z_{max}$ boundaries, i.e. $\alpha \neq 0$. The solutions in the last section did not contain any boundary layers because $\alpha = 0$. For simplicity, we will model the background Alfvén speed as uniform, i.e. $v_A(x, z) = v_{A0}$ as this allows us to derive a simple algebraic dispersion relation. We will calculate the normal mode solution in a domain where we impose an incident Alfvén wave from $z > 0$ and line-tied boundary conditions at $z = 0$. Results from this section will be compared with results from Section 4.6 to test the validity of imposing line-tied boundary conditions.

4.5.1 Dispersion relation

Since the background Alfvén speed is uniform we can derive a dispersion relation using a method very similar to that used in Section 1.4. The derivation here is almost identical except $\partial/\partial y \rightarrow \nabla_\perp$ and $\partial/\partial z \rightarrow \nabla_\parallel$. Eliminating \hat{b}_x and \hat{b}_\parallel from Equations (4.2.10) and (4.2.11) gives

$$\left[\frac{\partial^2}{\partial t^2} - v_{A0}^2 \nabla_\parallel^2 \right] u_x = -v_{A0}^2 \frac{\partial^2 \hat{b}_\parallel}{\partial x \partial t}, \quad (4.5.1)$$

$$\left[\frac{\partial^2}{\partial t^2} - v_{A0}^2 \nabla_\parallel^2 \right] u_\perp = -v_{A0}^2 \nabla_\perp \frac{\partial \hat{b}_\parallel}{\partial t}. \quad (4.5.2)$$

Eliminating \hat{b}_\parallel gives

$$\left[\frac{\partial^2}{\partial t^2} - v_{A0}^2 \left(\frac{\partial^2}{\partial x^2} + \nabla_\parallel^2 \right) \right] u_x = v_A^2(z) \nabla_\perp \frac{\partial u_\perp}{\partial x}, \quad (4.5.3)$$

$$\left[\frac{\partial^2}{\partial t^2} - v_{A0}^2 (\nabla_\perp^2 + \nabla_\parallel^2) \right] u_\perp = v_A^2(z) \nabla_\perp \frac{\partial u_x}{\partial x}. \quad (4.5.4)$$

For $z \neq 0$,

$$\begin{aligned} & \left[\frac{\partial^2}{\partial t^2} - v_{A0}^2 (\nabla_\perp^2 + \nabla_\parallel^2) \right] \left[\frac{\partial^2}{\partial t^2} - v_{A0}^2 \left(\frac{\partial^2}{\partial x^2} + \nabla_\parallel^2 \right) \right] u_\perp = v_A^4 \nabla_\perp^2 \frac{\partial^2 u_\perp}{\partial x^2}, \\ & \Rightarrow \left[\frac{\partial^2}{\partial t^2} - v_{A0}^2 \nabla_\parallel^2 \right] \left[\frac{\partial^2}{\partial t^2} - v_{A0}^2 \left(\frac{\partial^2}{\partial x^2} + \nabla_\parallel^2 \right) \right] u_\perp - v_{A0}^2 \nabla_\perp^2 \left[\frac{\partial^2}{\partial t^2} - v_{A0}^2 \nabla_\parallel^2 \right] u_\perp = 0, \end{aligned}$$

$$\implies \left[\frac{\partial^2}{\partial t^2} - v_{A0}^2 \nabla_{||}^2 \right] \left[\frac{\partial^2}{\partial t^2} - v_{A0}^2 \left(\frac{\partial^2}{\partial x^2} + \nabla_{\perp}^2 + \nabla_{||}^2 \right) \right] u_{\perp} = 0. \quad (4.5.5)$$

To derive the dispersion relation, assume u_{\perp} is of the form

$$u_{\perp} = u_{\perp n} \exp[i(k_x x + k_y y + k_{zn} z + \omega t)]$$

Substituting this into Equation (4.5.5) gives the following dispersion relations

$$[\omega^2 + v_{A0}^2 \nabla_{||n}^2][\omega^2 - v_{A0}^2(k_x^2 + k_y^2 + k_{zn}^2)] = 0, \quad (4.5.6)$$

where

$$\nabla_{||n} = i(k_y \sin \alpha + k_{zn} \cos \alpha). \quad (4.5.7)$$

Hence, the possible values of k_{zn} are

$$\begin{pmatrix} k_{z1} \\ k_{z2} \\ k_{z3} \\ k_{z4} \end{pmatrix} = \begin{pmatrix} k_{||0}/\cos \alpha - k_y \tan \alpha \\ -k_{||0}/\cos \alpha - k_y \tan \alpha \\ i\sqrt{k_x^2 + k_y^2 - k_{||0}^2} \\ -i\sqrt{k_x^2 + k_y^2 - k_{||0}^2} \end{pmatrix}, \quad (4.5.8)$$

where $k_{||0}$ is given by Equation (4.2.22). The first two terms, k_{z1} , k_{z2} , correspond to Alfvén wave solutions and k_{z3} , k_{z4} correspond to fast wave solutions. Note that the fast wave solutions are evanescent for $k_x^2 + k_y^2 > k_{||0}^2$.

4.5.2 Normal mode solution

In this section, we will calculate the solution in an infinite domain where we impose an incident Alfvén wave from the right ($z > 0$) with $\mathbf{u} = 0$ at $z = 0$. We assume the

solutions are of the form

$$\begin{pmatrix} u_x \\ u_\perp \\ b_x \\ b_\perp \\ b_{||} \end{pmatrix} = \sum_{n=1}^4 \begin{pmatrix} u_{xn} \\ u_{\perp n} \\ b_{xn} \\ b_{\perp n} \\ b_{||n} \end{pmatrix} \exp[i(k_x x + k_y y + k_{zn} z + \omega t)], \quad (4.5.9)$$

where each k_{zn} is given by Equation (4.5.8).

We impose an incident Alfvén wave from the right by setting $u_{\perp 1} = u_0$, where u_0 gives the incident wave amplitude. We impose the amplitude of the incident fast waves to be zero, therefore, $u_{\perp 4} = 0$. From Equation (4.5.3) we know that

$$\begin{aligned} u_{xn} &= \frac{-ik_x \nabla_{\perp n}}{\mathcal{L}_n - k_x^2} u_{\perp n} \\ &= \hat{u}_{xn} u_{\perp n}, \end{aligned} \quad (4.5.10)$$

where

$$\hat{u}_{xn} = \frac{-ik_x \nabla_{\perp n}}{\mathcal{L}_n - k_x^2}, \quad (4.5.11)$$

$$\mathcal{L}_n = \nabla_{||n}^2 + k_{||0}^2, \quad (4.5.12)$$

$$\nabla_{\perp n} = i(k_y \cos \alpha - k_{zn} \sin \alpha), \quad (4.5.13)$$

$$\nabla_{||n} = i(k_y \sin \alpha + k_{zn} \cos \alpha). \quad (4.5.14)$$

We require $u_x(x, y, 0, t) = u_\perp(x, y, 0, t) = 0$, hence,

$$\begin{pmatrix} 1 & 1 \\ \hat{u}_{x2} & \hat{u}_{x3} \end{pmatrix} \begin{pmatrix} u_{\perp 2} \\ u_{\perp 3} \end{pmatrix} = -u_0 \begin{pmatrix} 1 \\ \hat{u}_{x1} \end{pmatrix}. \quad (4.5.15)$$

Hence,

$$\begin{pmatrix} u_{\perp 1} \\ u_{\perp 2} \\ u_{\perp 3} \end{pmatrix} = u_0 \begin{pmatrix} 1 \\ -(\hat{u}_{x1} - \hat{u}_{x3})/(\hat{u}_{x2} - \hat{u}_{x3}) \\ (\hat{u}_{x1} - \hat{u}_{x2})/(\hat{u}_{x2} - \hat{u}_{x3}) \end{pmatrix} \quad (4.5.16)$$

From Equations (4.2.12), (4.2.13) and (4.2.14), we know that

$$v_{A0}\hat{b}_{xn} = \frac{\nabla_{||n}}{ik_{||0}}u_{xn}, \quad (4.5.17)$$

$$v_{A0}\hat{b}_{\perp n} = \frac{\nabla_{||n}}{ik_{||0}}u_{\perp n}, \quad (4.5.18)$$

$$v_{A0}\hat{b}_{||n} = -\frac{1}{ik_{||0}}[ik_x u_{xn} + \nabla_{\perp n} u_{\perp n}]. \quad (4.5.19)$$

To help visualise the solutions and to check $u_x = u_{\perp} = 0$ at $z = 0$ we plot the solutions in Figure 4.3. We choose a large value of k_x , namely, $k_x = 50k_{||0}$, to simulate the conditions near a singularity in a resonant absorption experiment. This means that the fast wave terms are evanescent. The plots show that for \hat{b}_x and $\hat{b}_{||}$ the evanescent fast waves dominate near $z = 0$. For u_x and b_{\perp} the evanescent fast waves and Alfvén waves are of a similar order near $z = 0$. For u_{\perp} , the Alfvén waves dominate.

Equations (4.5.9)-(4.5.19) give the full set of solutions to the equations. However, we do not express the solutions in full here as they are cumbersome. We find the equations are easier to interpret if we construct series solutions by taking appropriate limits. Resonant absorption cannot occur because the background Alfvén speed is uniform. Therefore, singularities cannot form in our model. In Section 4.4, we showed that resonant absorption produces very short length-scales in x . Approaching resonant singularities, the length-scales in x shrink to zero. Therefore, we are interested in the limit $k_x/k_{||0} \rightarrow \infty$. Note that for $k_x \rightarrow \infty$ the fast wave solutions are evanescent. To help us understand the effects of line-tied boundary conditions, we will now calculate asymptotic expansions for u_{xn} , $u_{\perp n}$, b_{xn} , $b_{\perp n}$ and $b_{||n}$. The maple file we use to assist the algebra can be found in the following directory:

[→ Maple/Chapter4/uniform_in_x_vA0.pdf.](#)

To simplify the notation, let

$$\hat{k}_{y0} = \frac{k_y}{k_{||0}}. \quad (4.5.20)$$

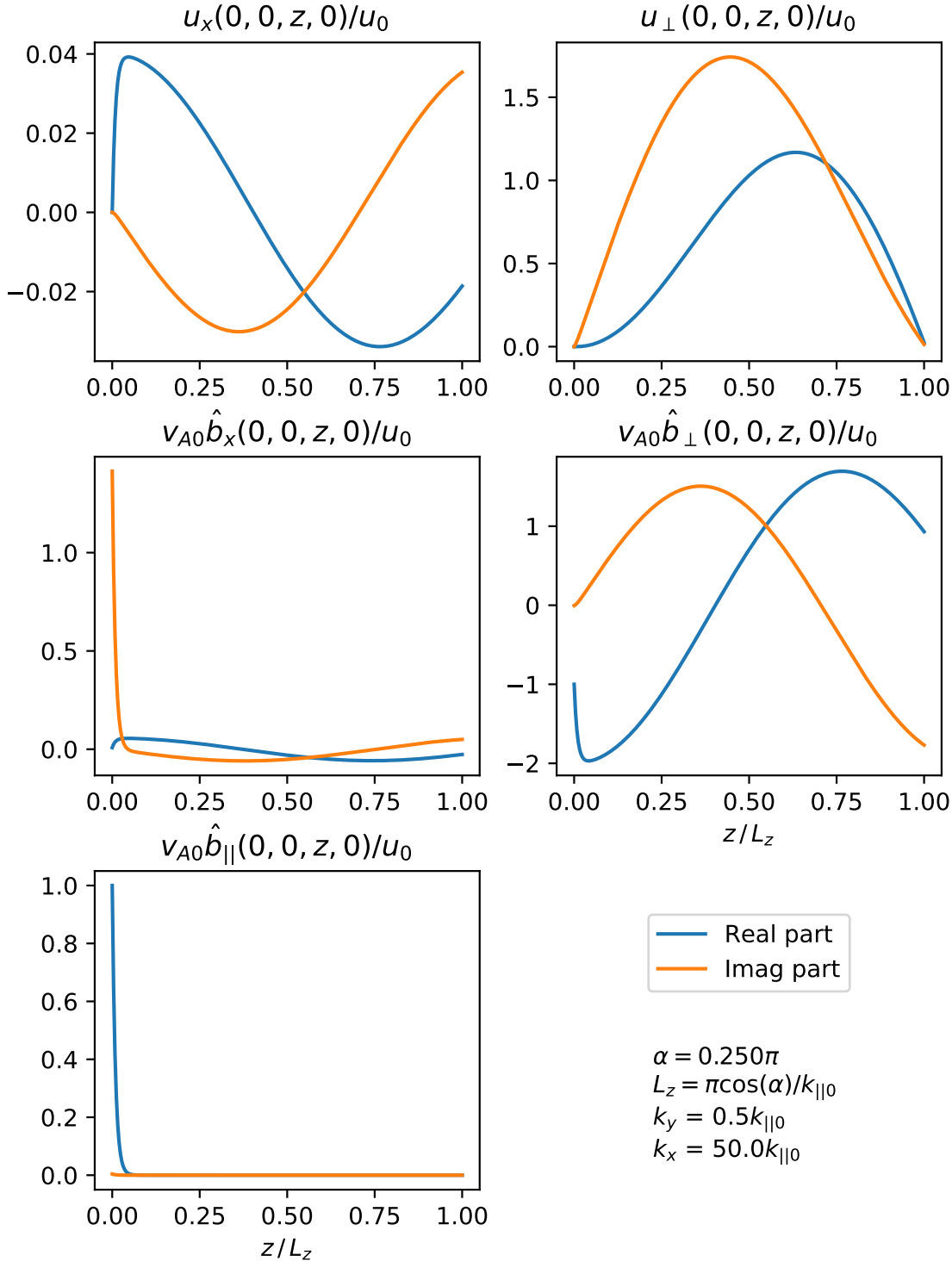


Figure 4.3: This figure shows plots of the real and imaginary parts of u_x , u_{\perp} , b_x , b_{\perp} and $b_{||}$ as a function of z . We calculated the solutions using Equations (4.5.9)-(4.5.19). The code used to make this figure is available on GitHub in the following directory:

→ [Python/Chapter4/uniform_density_profile.py](#)

The leading order asymptotic expansion for the u_x coefficients is given by

$$\frac{u_{x1}}{u_0} = -\frac{\hat{k}_{y0} - \sin \alpha}{\cos \alpha} \frac{k_{||0}}{k_x} + O\left(\frac{k_{||0}^2}{k_x^2}\right), \quad (4.5.21)$$

$$\frac{u_{x2}}{u_0} = \frac{\hat{k}_{y0} + \sin \alpha}{\cos \alpha} \frac{k_{||0}}{k_x} + O\left(\frac{k_{||0}^2}{k_x^2}\right), \quad (4.5.22)$$

$$\frac{u_{x3}}{u_0} = -2 \tan \alpha \frac{k_{||0}}{k_x} + O\left(\frac{k_{||0}^2}{k_x^2}\right). \quad (4.5.23)$$

The leading order asymptotic expansion for the u_\perp coefficients is given by

$$\frac{u_{\perp 1}}{u_0} = 1, \quad (4.5.24)$$

$$\frac{u_{\perp 2}}{u_0} = -1 + O\left(\frac{k_{||0}}{k_x}\right), \quad (4.5.25)$$

$$\frac{u_{\perp 3}}{u_0} = 2i \frac{\sin^2 \alpha}{\cos \alpha} \frac{k_{||0}}{k_x} + O\left(\frac{k_{||0}^2}{k_x^2}\right). \quad (4.5.26)$$

The \hat{b}_x coefficients are given by

$$\frac{v_{A0}\hat{b}_{x1}}{u_0} = -\frac{\hat{k}_{y0} - \sin \alpha}{\cos \alpha} \frac{k_{||0}}{k_x} + O\left(\frac{k_{||0}^2}{k_x^2}\right), \quad (4.5.27)$$

$$\frac{v_{A0}\hat{b}_{x2}}{u_0} = -\frac{\hat{k}_{y0} + \sin \alpha}{\cos \alpha} \frac{k_{||0}}{k_x} + O\left(\frac{k_{||0}^2}{k_x^2}\right), \quad (4.5.28)$$

$$\frac{v_{A0}\hat{b}_{x3}}{u_0} = -2i \sin \alpha + O\left(\frac{k_{||0}}{k_x}\right). \quad (4.5.29)$$

The \hat{b}_\perp coefficients are given by

$$\frac{v_{A0}\hat{b}_{\perp 1}}{u_0} = 1, \quad (4.5.30)$$

$$\frac{v_{A0}\hat{b}_{\perp 2}}{u_0} = 1 + O\left(\frac{k_{||0}}{k_x}\right), \quad (4.5.31)$$

$$\frac{v_{A0}\hat{b}_{\perp 3}}{u_0} = -2 \sin^2 \alpha + O\left(\frac{k_{||0}}{k_x}\right). \quad (4.5.32)$$

Finally, the $\hat{b}_{||}$ coefficients are given by

$$\frac{v_{A0}\hat{b}_{||1}}{u_0} = 0, \quad (4.5.33)$$

$$\frac{v_{A0}\hat{b}_{||2}}{u_0} = 0, \quad (4.5.34)$$

$$\frac{v_{A0}\hat{b}_{||3}}{u_0} = \sin(2\alpha) + O\left(\frac{k_{||0}}{k_x}\right). \quad (4.5.35)$$

For the Alfvén wave terms the associated magnetic pressure, $b_{||}$, equals zero and this was shown in Section 1.4. The above equations show that to leading order the u_x solution does include an evanescent fast wave term and this gives rise to the boundary layers seen in [Halberstadt and Goedbloed \(1993, 1995\)](#); [Arregui et al. \(2003\)](#). However, the leading order u_{\perp} solution does not contain any fast wave terms. Note that for b_x the boundary layer term dominates near $z = 0$.

Now, we give a brief explanation as to why the boundary layers form. Imposing $\mathbf{u} = 0$ at $z = 0$ forces the normal component of the magnetic field, b_z , to be zero. For proof, consider the z -component of the induction equation,

$$\frac{\partial b_z}{\partial t} = \hat{\mathbf{z}} \cdot \nabla \times (\mathbf{u} \times \mathbf{B}_0).$$

The curl in the z -direction only depends on derivatives in x and y . Since $\mathbf{u} = 0$ is constant at $z = 0$, the x and y derivatives are zero. Therefore, if b_z is initially zero, it will remain zero for all time. Therefore, at $z = 0$,

$$b_z = \cos \alpha b_{||} - \sin \alpha b_{\perp} = 0,$$

rearranging gives

$$b_{||} = \tan \alpha b_{\perp}.$$

Here, b_{\perp} gives the magnetic field component of the Alfvén wave and $b_{||}$ gives the magnetic pressure component of the fast wave. Hence, for $\alpha \neq 0$, if there is a large-amplitude Alfvén wave, then there must also be a large-amplitude fast wave (for $\alpha \neq 0$). If $v_A^2(k_x^2 + k_y^2) > \omega^2$, this forces the associated k_z to be imaginary, which means the fast

wave must be evanescent and so boundary layers will form.

Note that for $k_x \rightarrow \infty$, $k_{z3} \rightarrow ik_x$. Therefore, the time-averaged energy associated with the evanescent fast waves is proportional to $\exp(-2k_x z)$ and the total fast wave energy is proportional to

$$k_{||+} \int_0^\infty \exp(-2k_x z) dz = \frac{k_{||+}}{2k_x}. \quad (4.5.36)$$

Thus, the energy of the evanescent fast wave energy tends to 0 as $k_x \rightarrow \infty$, for u_0 fixed. Hence, the evanescent fast waves will have a limited effect on the rate of resonant absorption. Since the energy associated with the boundary layers does not grow as the length-scales in x get shorter, they cannot be absorbing energy. Moreover, the boundary layers cannot directly transport energy away as they are evanescent.

4.6 Oblique field: Piecewise constant density profile

This section aims to check if the boundary layers produced in Section 4.5 are physical or fictitious artefacts arising from the use of line-tied boundary conditions. Instead of imposing line-tied boundary conditions we use a piecewise constant density profile in z , i.e. the Alfvén speed is given by

$$v_A(z) = \begin{cases} v_{A-}, & z < 0 \\ v_{A+}, & z \geq 0. \end{cases} \quad (4.6.1)$$

Note that the region $z > 0$ models the corona and $z < 0$ models the chromosphere, therefore, $v_{A+} > v_{A-}$ as the density in the chromosphere is higher. We impose an incident Alfvén wave from the region $z > 0$ and then calculate the unique solution which ensures continuity of u_x , u_\perp , $\partial u_x / \partial z$, $\partial u_\perp / \partial z$ at $z = 0$.

We assume the solutions are of the form

$$\begin{pmatrix} u_x \\ u_\perp \\ \hat{b}_x \\ \hat{b}_\perp \\ \hat{b}_{||} \end{pmatrix} = \sum_{n=1}^4 \begin{pmatrix} u_{xn-} \\ u_{\perp n-} \\ \hat{b}_{xn-} \\ \hat{b}_{\perp n-} \\ \hat{b}_{||n-} \end{pmatrix} \exp[i(k_x x + k_y y + k_{zn-} z + \omega t)], \text{ for } z \leq 0, \quad (4.6.2)$$

and

$$\begin{pmatrix} u_x \\ u_\perp \\ \hat{b}_x \\ \hat{b}_\perp \\ \hat{b}_{||} \end{pmatrix} = \sum_{n=1}^4 \begin{pmatrix} u_{xn+} \\ u_{\perp n+} \\ \hat{b}_{xn+} \\ \hat{b}_{\perp n+} \\ \hat{b}_{||n+} \end{pmatrix} \exp[i(k_x x + k_y y + k_{zn+} z + \omega t)], \text{ for } z > 0, \quad (4.6.3)$$

where

$$\begin{pmatrix} k_{z1\pm} \\ k_{z2\pm} \\ k_{z3\pm} \\ k_{z4\pm} \end{pmatrix} = \begin{pmatrix} k_{||\pm}/\cos\alpha - k_y \tan\alpha \\ -k_{||\pm}/\cos\alpha - k_y \tan\alpha \\ i\sqrt{k_x^2 + k_y^2 - k_{||\pm}^2} \\ -i\sqrt{k_x^2 + k_y^2 - k_{||\pm}^2} \end{pmatrix}, \quad (4.6.4)$$

and $k_{||\pm}$ is given by Equation (4.2.21).

We impose an incident Alfvén wave from $z > 0$ by setting $u_{\perp 1+} = u_0$, where u_0 gives the incident wave amplitude. We impose the amplitude of the incident fast waves to be zero, therefore, $u_{\perp 4+} = 0$. There are no incident waves from the left, therefore, $u_{\perp 2-} = u_{\perp 3-} = 0$. From Equation (4.5.3) we know that

$$\begin{aligned} u_{xn\pm} &= \frac{-ik_x \nabla_{\perp n\pm}}{\mathcal{L}_{n\pm} - k_x^2} u_{\perp n\pm} \\ &= \hat{u}_{xn\pm} u_{\perp n\pm}, \end{aligned} \quad (4.6.5)$$

where

$$\hat{u}_{xn\pm} = \frac{-ik_x \nabla_{\perp n\pm}}{\mathcal{L}_{n\pm} - k_x^2}, \quad (4.6.6)$$

$$\mathcal{L}_{n\pm} = \nabla_{||n\pm}^2 + k_{||\pm}^2, \quad (4.6.7)$$

$$\nabla_{\perp n\pm} = i(k_y \cos\alpha - k_{zn\pm} \sin\alpha), \quad (4.6.8)$$

We require continuity of u_x , $\partial u_x / \partial z$, u_\perp and $\partial u_\perp / \partial z$ at $z = 0$. This gives the following

equations

$$\begin{aligned} \sum_{n \in \{1,4\}} u_{xn-} &= \sum_{n=1}^3 u_{xn+} \implies \sum_{n \in \{1,4\}} \hat{u}_{xn-} u_{\perp n-} = \sum_{n=1}^3 \hat{u}_{xn+} u_{\perp n+}, \\ \sum_{n \in \{1,4\}} k_{zn-} u_{xn-} &= \sum_{n=1}^3 k_{zn+} u_{xn+} \implies \sum_{n \in \{1,4\}} k_{zn-} \hat{u}_{xn-} u_{\perp n-} = \sum_{n=1}^3 k_{zn+} \hat{u}_{xn+} u_{\perp n+}, \\ \sum_{n \in \{1,4\}} u_{\perp n-} &= \sum_{n=1}^3 u_{\perp n+}, \\ \sum_{n \in \{1,4\}} k_{zn-} u_{\perp n-} &= \sum_{n=1}^3 k_{zn+} u_{\perp n+}. \end{aligned}$$

Written in matrix form, these become

$$\begin{pmatrix} \hat{u}_{x1-} & \hat{u}_{x4-} & -\hat{u}_{x2+} & -\hat{u}_{x3+} \\ k_{z1-}\hat{u}_{x1-} & k_{z4-}\hat{u}_{x4-} & -k_{z2+}\hat{u}_{x2+} & -k_{z3+}\hat{u}_{x3+} \\ 1 & 1 & -1 & -1 \\ k_{z1-} & k_{z4-} & -k_{z2+} & -k_{z3+} \end{pmatrix} \begin{pmatrix} u_{\perp 1-} \\ u_{\perp 4-} \\ u_{\perp 2+} \\ u_{\perp 3+} \end{pmatrix} = u_0 \begin{pmatrix} \hat{u}_{x1+} \\ k_{z1+}\hat{u}_{x1+} \\ 1 \\ k_{z1+} \end{pmatrix}.$$

We can solve this using symbolic and numerical computing environments e.g. Maple, see Github file:

[→ Maple/Chapter4/asymptotic_expansion_piecewise_constant_va_large_k_par_m.pdf](#).

From Equations (4.2.12), (4.2.13) and (4.2.14), we know that

$$v_{A+} \hat{b}_{xn\pm} = \frac{\nabla_{||n\pm}}{ik_{||+}} u_{xn\pm}, \quad (4.6.9)$$

$$v_{A+} \hat{b}_{\perp n\pm} = \frac{\nabla_{||n\pm}}{ik_{||+}} u_{\perp n\pm}, \quad (4.6.10)$$

$$v_{A+} \hat{b}_{||n\pm} = -\frac{1}{ik_{||+}} [ik_x u_{xn\pm} + \nabla_{\perp n\pm} u_{\perp n\pm}]. \quad (4.6.11)$$

To help check that solutions to the matrix above do indeed ensure continuity of u_x , $\partial u_x / \partial z$, u_\perp , $\partial u_\perp / \partial z$ we plot the velocities and their derivatives as a function of z in

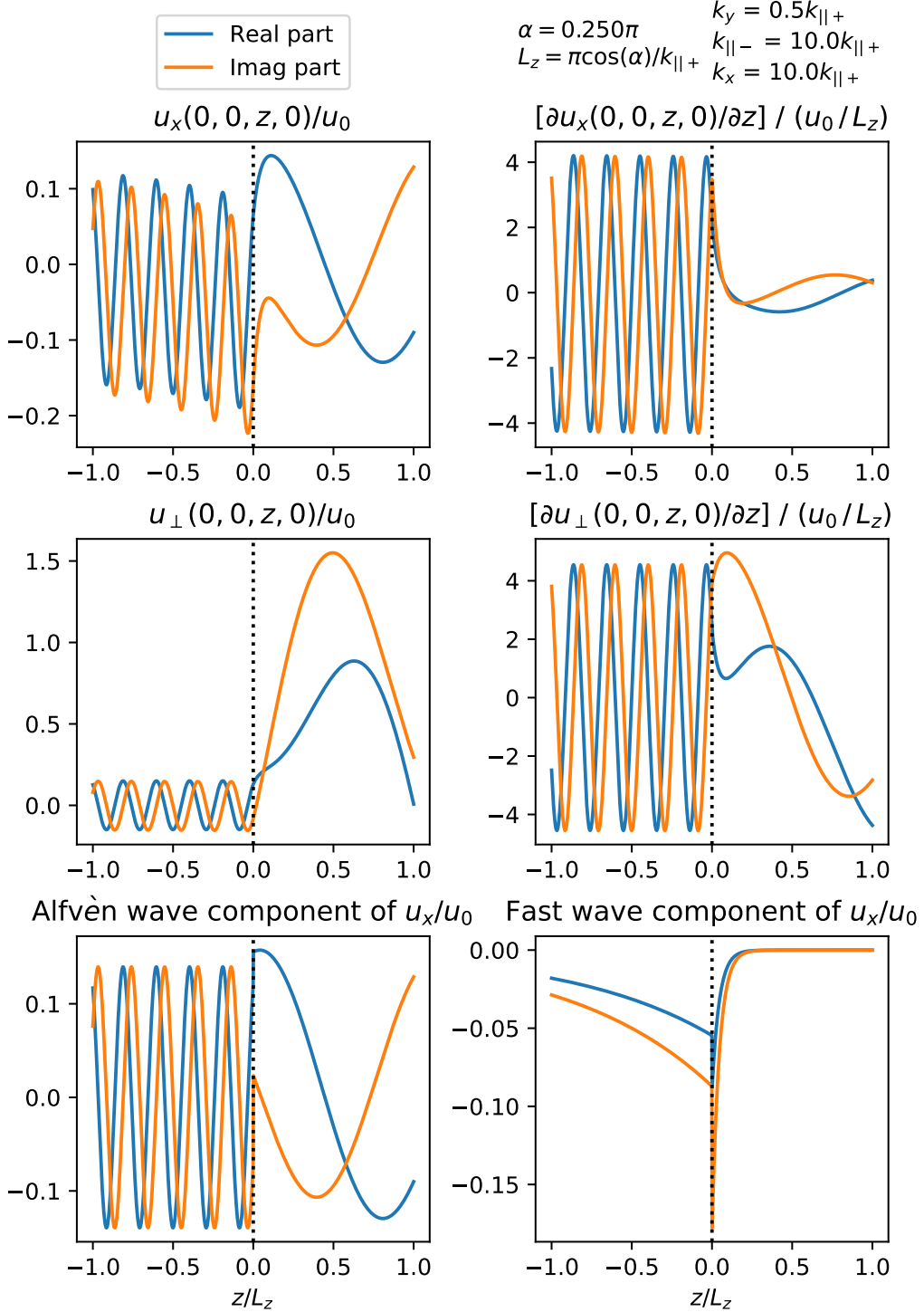


Figure 4.4: This figure shows plots of the velocity u_x , u_\perp and their z -derivatives as a function of z at $x = y = t = 0$. It shows that the velocities and their z -derivatives are continuous. The bottom row shows the Alfvén wave and fast components of u_x separately, where the Alfvén wave component have wavenumbers $k_{z1\pm}$, $k_{z2\pm}$ and the fast wave component have wavenumbers $k_{z3\pm}$, $k_{z4\pm}$. The code used to make this figure is available on GitHub in the following directory:

→ [Python/Chapter4/piecewise_constant_density_profile.py](#)

Figure 4.4. Also, to help visualise the solutions we plot the Alfvén wave component and fast wave component for u_x separately. Since $k_x^2 + k_y^2 > k_{\parallel\pm}^2$, the fast wave component is evanescent. We show the parameters we use in the top-right of each figure.

Equations (4.6.2)-(4.6.11) give the full solution to the equations. However, the solution is too cumbersome to present directly. To build our intuition for how the solutions change with k_x we plot the real/imaginary part of u_x , u_{\perp} and \hat{b}_{\parallel} as a function of z at $x = y = t = 0$ in Figure 4.5/4.6 respectively. The blue curve shows the solutions from Section 4.5 where line-tied boundary conditions ($\mathbf{u} = 0$) are imposed at $z = 0$. The dashed orange curve shows the solution where we impose continuity of \mathbf{u} and $\partial\mathbf{u}/\partial z$ at $z = 0$ with a piecewise constant background Alfvén speed. In the left-hand column, $k_x = 10k_{\parallel+}$, this means that the fast waves are evanescent for $z > 0$ and can propagate for $z < 0$. It shows that the solutions are in good agreement and suggests that line-tied boundary conditions give a good approximation for the solution where $z > 0$. The small disagreement occurs due to line-tied boundary conditions causing perfect reflection, whereas, a finite jump in the background Alfvén speed results in partial reflection. In the right column, $k_x = 1000k_{\parallel+}$, this means that the fast waves are evanescent everywhere. The plots show poor agreement near $z = 0$ and good agreement for $z \gg 0$. They show that the model with line-tied boundary conditions can significantly overestimate the amplitude of the evanescent fast waves/boundary layers.

We have seen that depending on the value of k_x , our models can sometimes agree on the amplitude of evanescent fast waves and sometimes disagree strongly. Our goal now is to quantify how well the model with line-tied boundary conditions approximates the amplitude of the evanescent fast wave/boundary layer as a function of k_x , for the parameter space given by Equations (4.2.17)-(4.2.20). Figure 4.7 plots the relative difference, given by,

$$\text{relative difference} = \left| \frac{u_{\perp 3} - u_{\perp 3+}}{u_{\perp 3+}} \right|, \quad (4.6.12)$$

where $u_{\perp 3}$ gives the amplitude of the fast wave component of u_{\perp} at $z = 0$ in the model where line-tied boundary conditions are imposed and $u_{\perp 3+}$ gives the amplitude in the model where a piecewise constant background Alfvén speed is used. Equations (4.5.10), (4.5.17), (4.5.18), (4.5.19) show that u_{xn} , b_{xn} , $b_{\perp n}$, $b_{\parallel n}$ are equal to scalar multiples

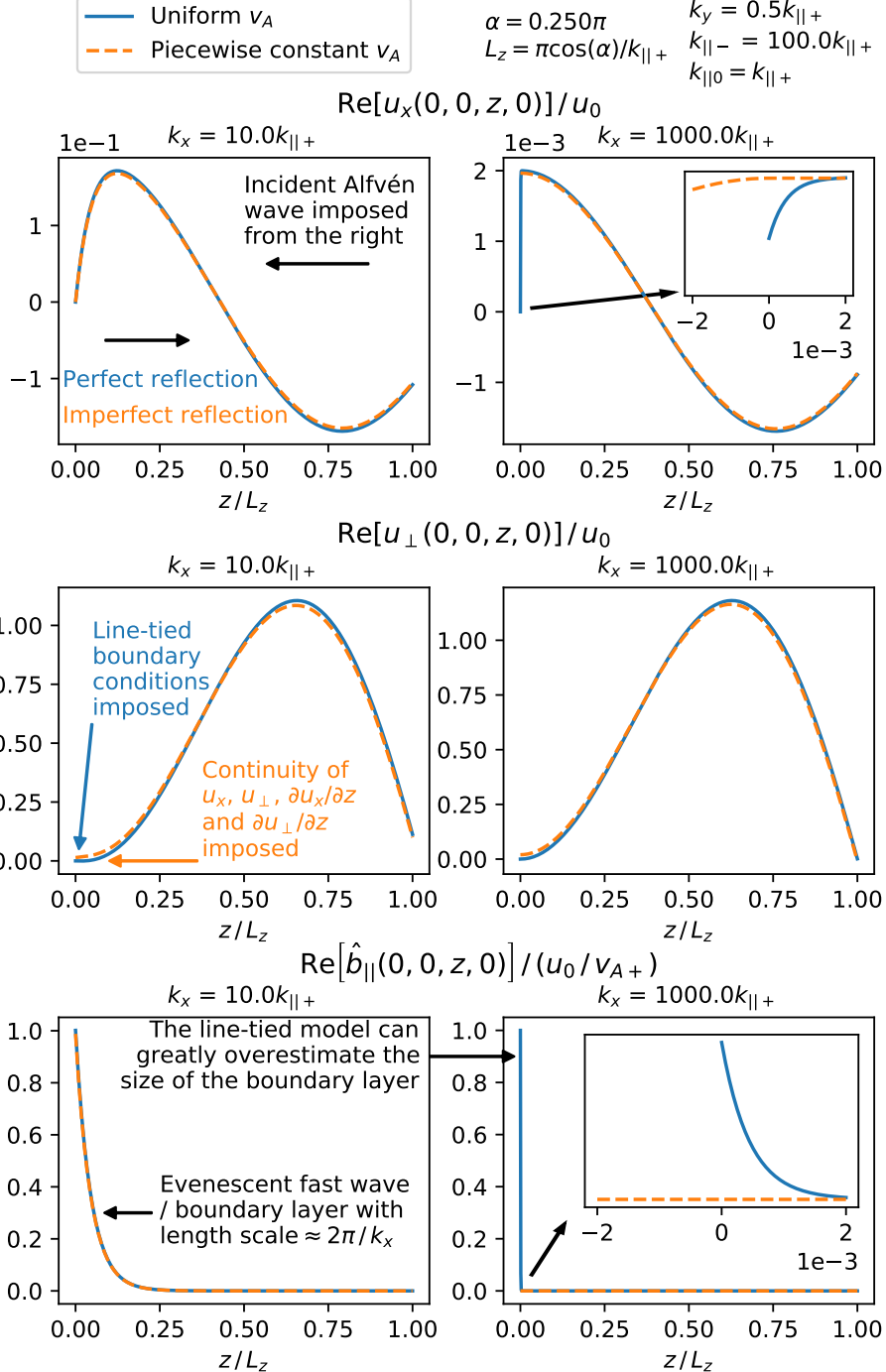


Figure 4.5: This figure shows plots of the real part of u_x (top row), u_{\perp} (middle row) and $\hat{b}_{||}$ (bottom row) at $x = y = t = 0$ as a function of z for $k_x = 10k_{||+}$ (left column) and $k_x = 1000k_{||+}$ (right column). The case where the background Alfvén speed is uniform and line-tied boundary conditions is imposed is shown in blue and the case where the Alfvén speed is piecewise constant and continuity of \mathbf{u} is imposed is shown in dashed orange. A description of this figure is continued in the caption of Figure 4.6. The code used to make this figure and Figure 4.6 is available on GitHub in the following directory:

→ [Python/Chapter4/piecewise_constant_vs_uniform.py](#)

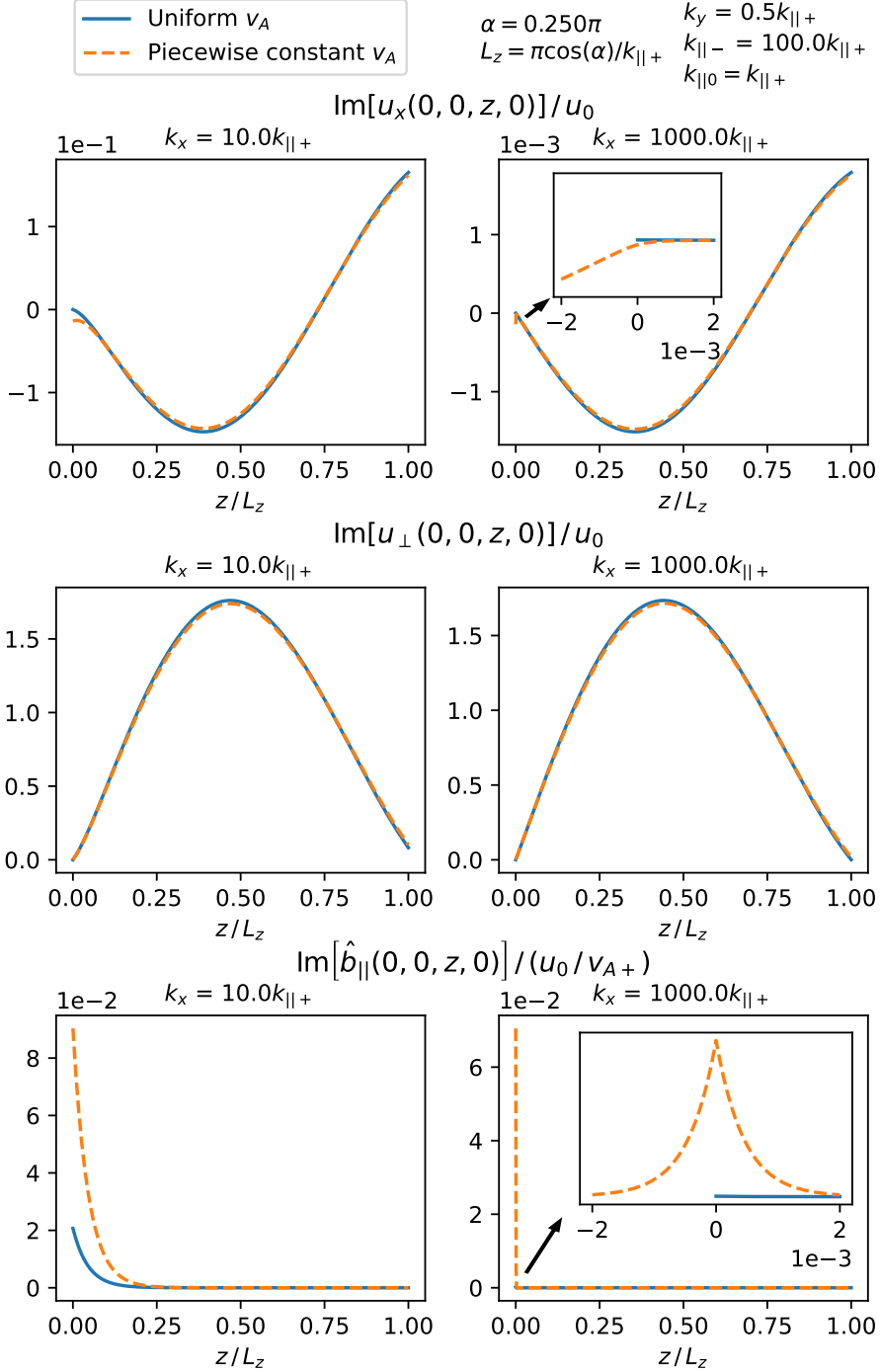


Figure 4.6: This figure is similar to Figure 4.5 except it plots the imaginary part of each variable instead. The blue and orange curves show good agreement in the left-hand column for both figures. The small differences occur due to the waves represented by the blue curve undergoing perfect reflection and the orange waves undergoing imperfect reflection at $z = 0$. The right-hand column shows less agreement between the plots, and this is because the fast waves are evanescent, whereas in the left-column the fast waves can propagate for $z < 0$. Equations (4.6.75)-(4.6.79) and (4.6.69)-(4.6.74) show that the fast wave terms in the blue solutions are of a higher order than the orange solutions.

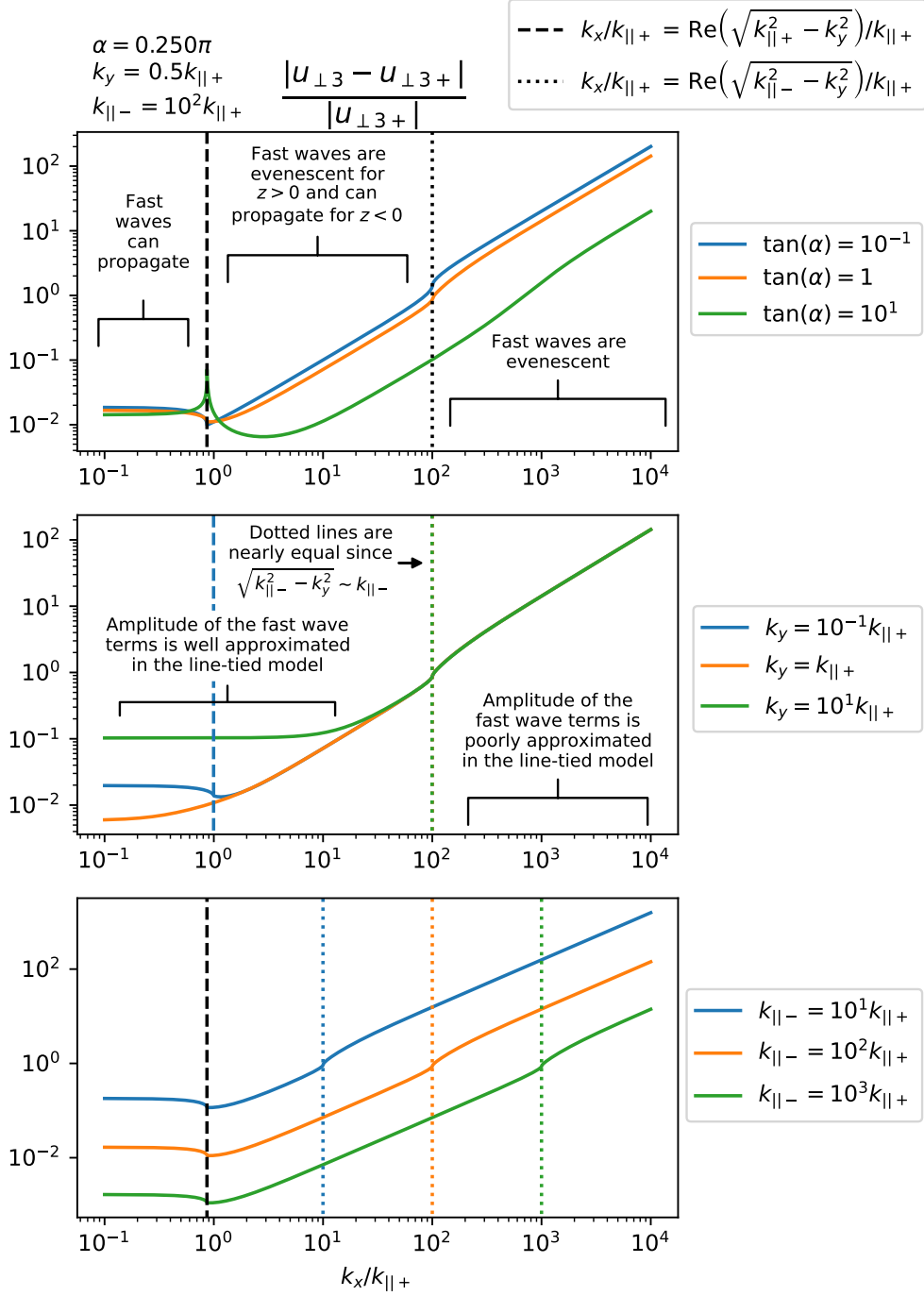


Figure 4.7: This figure plots the relative difference (see Equation 4.6.12) introduced by using line-tied boundary conditions to estimate the size of the boundary layers as a function of k_x . Unless stated otherwise, we use the parameters shown in the top-left. In the top plot, the different colours correspond to different values of α , in the middle plot they correspond to different values of k_y and in the bottom plot they correspond to different values of $k_{||-}$. If k_x is to the left/right of the vertical dashed lines, then the fast waves can propagate/are evanescent for $z > 0$ respectively. Similarly, if k_x is to the left/right of the vertical dotted lines, the fast waves can propagate/are evanescent for $z < 0$ respectively. The code used to make this figure is available on GitHub in the following directory:

→ Python/Chapter4/fast_wave_error_vs_kx.py

of $u_{\perp n}$, similarly, Equations (4.6.5), (4.6.9), (4.6.10), (4.6.11) show that u_{xn+} , b_{xn+} , $b_{\perp n+}$, $b_{||n+}$ are equal to the same scalar multiples of $u_{\perp n+}$ respectively (for $k_{||+} = k_{||0}$). Therefore,

$$\left| \frac{u_{\perp 3} - u_{\perp 3+}}{u_{\perp 3+}} \right| = \left| \frac{u_{x3} - u_{x3+}}{u_{x3+}} \right| = \dots = \left| \frac{b_{||3} - b_{||3+}}{b_{||3+}} \right|. \quad (4.6.13)$$

We show all the plots as functions of k_x , and the parameters take values shown in the top-left (unless stated otherwise). The vertical dashed lines show where

$$k_x = \operatorname{Re} \left(\sqrt{k_{||+}^2 - k_y^2} \right)$$

and the dotted lines show where

$$k_x = \operatorname{Re} \left(\sqrt{k_{||-}^2 - k_y^2} \right) = k_{||-} + O \left(\frac{k_{||+}}{k_{||-}} \right),$$

where we assume k_y satisfies Equation (4.2.19). If k_x is to the right of these vertical lines, then the fast waves are evanescent, and if k_x is to the left, then the fast waves can propagate. The plots show that the relative difference between the models is dependent on whether the fast waves are evanescent or propagating. If $k_x \gg k_{||-}$, then the models show poor agreement and the model with line-tied boundary conditions overestimates the size of the boundary layers. On the other hand, if $k_x \ll k_{||-}$ then the models show good agreement.

Since $k_{||-} \gg k_{||+}$ it is not clear if $k_x \gg k_{||-}$, even if the waves undergo resonant absorption. Our goal now is to check if it is possible for $k_x \gg k_{||-}$ in the corona by calculating the steady-state wavenumber, k_x^* , for driven standing phase-mixed Alfvén waves in a viscous and resistive domain (note that waves during resonant absorption undergo a similar phase-mixing process). In Section 3.3 we showed k_x^* is given by

$$\begin{aligned} k_x^* &= \left[\frac{6\omega}{(\eta + \nu)a} \right]^{1/3} \\ &\approx 1.82 \times 10^{-3} \left[\left(\frac{\omega}{10^{-2} \text{ s}^{-1}} \right) \left(\frac{10 \text{ m}^2 \text{ s}^{-1}}{\eta + \nu} \right) \left(\frac{10^6 \text{ m}}{a} \right) \right]^{1/3} \end{aligned} \quad (3.3.19)$$

for typical coronal values, where $\eta + \nu$ denotes the sum of the magnetic diffusivity and

kinematic viscosity coefficients and a is given by

$$a(x) = \frac{v_A(x)}{dv_A/dx}, \quad (3.3.16)$$

The Alfvén wavenumber parallel to the background magnetic field in the chromosphere, $k_{||-}$, is given by

$$k_{||-} = 10^{-5} \left(\frac{\omega}{10^{-2} \text{ s}^{-1}} \right) \left(\frac{10^3 \text{ m s}^{-1}}{v_{A-}} \right) \text{ m}^{-1}. \quad (4.6.14)$$

for typical values. Comparing Equations (3.3.19) and (4.6.14), they show that k_x^* can greatly exceed $k_{||-}$ for waves undergoing resonant absorption in the corona. However, it takes time for waves to phase-mix to such short length scales. Therefore, for early times $k_x \ll k_{||-}$ is valid and after the waves have sufficiently phase-mixed $k_x \gg k_{||+}$ is valid.

4.6.1 Asymptotic expansion: Case where $k_{||+} \ll k_x \ll k_{||-}$

Our goal now is to calculate the asymptotic expansions for the cases where $k_{||+} \ll k_x \ll k_{||-}$ and $k_{||-}, k_{||+} \ll k_x$ separately. In this section we calculate the asymptotic expansions for the case where $k_{||+} \ll k_x \ll k_{||-}$ and in the next section we calculate the solution for the case where $k_{||-}, k_{||+} \ll k_x$. Our line-tied boundary condition solutions from Section 4.5 provide a good approximation for the case where $k_x \ll k_{||-}$ as imposing line-tied boundary conditions is equivalent to modelling the chromosphere as infinitely denser than the corona which causes $k_{||-} \rightarrow \infty$.

To simplify the notation, let

$$\epsilon_- = \frac{k_x}{k_{||-}}, \quad (4.6.15)$$

$$\epsilon_+ = \frac{k_{||+}}{k_x}, \quad (4.6.16)$$

$$\hat{k}_{y+} = \frac{k_y}{v_{A+}} \quad (4.6.17)$$

To assist with the algebra we use a maple file which can be found on GitHub in the

following directory:

[→ Maple/Chapter4/asymptotic_expansion_piecewise_constant_va_large_k_par.m.pdf.](#)

We calculate the leading order multivariate Taylor expansions (assuming $\epsilon_-, \epsilon_+ \ll 1$). The u_x coefficients are given by

$$\frac{u_{x1-}}{u_0} = -2i \sin \alpha \epsilon_- \epsilon_+ + O(\epsilon_-^3, \epsilon_-^2 \epsilon_+, \epsilon_- \epsilon_+^2, \epsilon_+^3), \quad (4.6.18)$$

$$\frac{u_{x4-}}{u_0} = -2 \frac{\cos \alpha}{\sin \alpha} \epsilon_-^2 \epsilon_+ + O(\epsilon_-^4, \epsilon_-^3 \epsilon_+, \dots, \epsilon_+^4), \quad (4.6.19)$$

$$\frac{u_{x1+}}{u_0} = -\frac{\hat{k}_{y+} - \sin \alpha}{\cos \alpha} \epsilon_+ + O(\epsilon_-^2, \epsilon_- \epsilon_+, \epsilon_+^2), \quad (4.6.20)$$

$$\frac{u_{x2+}}{u_0} = \frac{\hat{k}_{y+} + \sin \alpha}{\cos \alpha} \epsilon_+ + O(\epsilon_-^2, \epsilon_- \epsilon_+, \epsilon_+^2), \quad (4.6.21)$$

$$\frac{u_{x3+}}{u_0} = -2 \tan \alpha \epsilon_+ + O(\epsilon_-^2, \epsilon_- \epsilon_+, \epsilon_+^2). \quad (4.6.22)$$

The u_\perp coefficients are given by

$$\frac{u_{\perp 1-}}{u_0} = -2i \cos \alpha \epsilon_-^2 \epsilon_+ + O(\epsilon_-^4, \epsilon_-^3 \epsilon_+, \dots, \epsilon_+^4) \quad (4.6.23)$$

$$\frac{u_{\perp 4-}}{u_0} = 2 \cos \alpha \epsilon_- \epsilon_+ + O(\epsilon_-^2, \epsilon_- \epsilon_+, \epsilon_+^2), \quad (4.6.24)$$

$$\frac{u_{\perp 1+}}{u_0} = 1, \quad (4.6.25)$$

$$\frac{u_{\perp 2+}}{u_0} = -1 + O(\epsilon_-, \epsilon_+), \quad (4.6.26)$$

$$\frac{u_{\perp 3+}}{u_0} = 2i \frac{\sin^2 \alpha}{\cos \alpha} \epsilon_+ + O(\epsilon_-^2, \epsilon_- \epsilon_+, \epsilon_+^2). \quad (4.6.27)$$

The b_x coefficients are given by

$$\frac{v_{A+} \hat{b}_{x1-}}{u_0} = -2i \sin \alpha + O(\epsilon_-, \epsilon_+), \quad (4.6.28)$$

$$\frac{v_{A+} \hat{b}_{x4-}}{u_0} = -2 \frac{\cos^2 \alpha}{\sin \alpha} \epsilon_- + O(\epsilon_-^2, \epsilon_- \epsilon_+, \epsilon_+^2), \quad (4.6.29)$$

$$\frac{v_{A+} \hat{b}_{x1+}}{u_0} = -\frac{\hat{k}_{y+} - \sin \alpha}{\cos \alpha} \epsilon_+ + O(\epsilon_-^2, \epsilon_- \epsilon_+, \epsilon_+^2), \quad (4.6.30)$$

$$\frac{v_{A+}\hat{b}_{x2+}}{u_0} = -\frac{\hat{k}_{y+} + \sin \alpha}{\cos \alpha} \epsilon_+ + O(\epsilon_-^2, \epsilon_- \epsilon_+, \epsilon_+^2), \quad (4.6.31)$$

$$\frac{v_{A+}\hat{b}_{x3+}}{u_0} = -2i \sin \alpha + O(\epsilon_-, \epsilon_+). \quad (4.6.32)$$

The b_\perp coefficients are given by

$$\frac{v_{A+}b_{\perp 1-}}{u_0} = -2i \cos \alpha \epsilon_- + O(\epsilon_-^2, \epsilon_- \epsilon_+, \epsilon_+^2), \quad (4.6.33)$$

$$\frac{v_{A+}b_{\perp 4-}}{u_0} = 2 \cos^2 \alpha + O(\epsilon_-, \epsilon_+), \quad (4.6.34)$$

$$\frac{v_{A+}b_{\perp 1+}}{u_0} = 1, \quad (4.6.35)$$

$$\frac{v_{A+}b_{\perp 2+}}{u_0} = 1 + O(\epsilon_-, \epsilon_+), \quad (4.6.36)$$

$$\frac{v_{A+}b_{\perp 3+}}{u_0} = -2 \sin^2 \alpha + O(\epsilon_-, \epsilon_+). \quad (4.6.37)$$

Finally, the $\hat{b}_{||}$ coefficients are given by

$$\frac{v_{A+}b_{||1-}}{u_0} = 0, \quad (4.6.38)$$

$$\frac{v_{A+}b_{||4-}}{u_0} = \sin(2\alpha) + O(\epsilon_-, \epsilon_+), \quad (4.6.39)$$

$$\frac{v_{A+}b_{||1+}}{u_0} = 0, \quad (4.6.40)$$

$$\frac{v_{A+}b_{||2+}}{u_0} = 0, \quad (4.6.41)$$

$$\frac{v_{A+}b_{||3+}}{u_0} = \sin(2\alpha) + O(\epsilon_-, \epsilon_+). \quad (4.6.42)$$

Taking the limit $\epsilon_- \rightarrow 0$ we do indeed recover the asymptotic expansions derived in Section 4.5 for $z > 0$ and $k_{||+} = k_{||0}$.

4.6.2 Asymptotic expansion: Case where $k_{||-}, k_{||+} \ll k_x$

Our goal now is to calculate the solution for the case where $k_x \gg k_{||-}, k_{||+}$, as this simulates the conditions for waves undergoing resonant absorption after they have phase-mixed to sufficiently short length scales. To assist with the algebra we use a maple file

which can be found on GitHub in the following directory:

[→ Maple/Chapter4/asymptotic_expansion_piecewise_constant_va_large_kx.pdf.](#)

To simplify the notation, let

$$r = \frac{k_{||+}}{k_{||-}}. \quad (4.6.43)$$

Assuming k_x is large, we calculate the leading order asymptotic expansions for the u_x coefficients as

$$\frac{u_{x1-}}{u_0} = -2r \frac{r\hat{k}_y - \sin \alpha}{(1+r)\cos \alpha} \frac{k_{||-}}{k_x} + O\left(\frac{k_{||-}^2}{k_x^2}\right), \quad (4.6.44)$$

$$\frac{u_{x4-}}{u_0} = -ir(1-r) \frac{\sin \alpha}{\cos^2 \alpha} \frac{k_{||-}^2}{k_x^2} + O\left(\frac{k_{||-}^3}{k_x^3}\right), \quad (4.6.45)$$

$$\frac{u_{x1+}}{u_0} = -r \frac{\hat{k}_y - \sin \alpha}{\cos \alpha} \frac{k_{||-}}{k_x} + O\left(\frac{k_{||-}^2}{k_x^2}\right), \quad (4.6.46)$$

$$\frac{u_{x2+}}{u_0} = r \frac{1-r}{1+r} \frac{\hat{k}_y + \sin \alpha}{\cos \alpha} \frac{k_{||-}}{k_x} + O\left(\frac{k_{||-}^2}{k_x^2}\right), \quad (4.6.47)$$

$$\frac{u_{x3+}}{u_0} = -ir(1-r) \frac{\sin \alpha}{\cos^2 \alpha} \frac{k_{||-}^2}{k_x^2} + O\left(\frac{k_{||-}^3}{k_x^3}\right). \quad (4.6.48)$$

The leading order asymptotic expansions for the u_\perp coefficients are given by

$$\frac{u_{\perp 1-}}{u_0} = \frac{2r}{r+1} + O\left(\frac{k_{||-}^2}{k_x^2}\right), \quad (4.6.49)$$

$$\frac{u_{\perp 4-}}{u_0} = r(r-1) \tan^2 \alpha \frac{k_{||-}^2}{k_x^2} + O\left(\frac{k_{||-}^3}{k_x^3}\right), \quad (4.6.50)$$

$$\frac{u_{\perp 1+}}{u_0} = 1, \quad (4.6.51)$$

$$\frac{u_{\perp 2+}}{u_0} = -\frac{1-r}{1+r} + O\left(\frac{k_{||-}^2}{k_x^2}\right), \quad (4.6.52)$$

$$\frac{u_{\perp 3+}}{u_0} = -r(1-r) \tan^2 \alpha \frac{k_{\parallel -}^2}{k_x^2} + O\left(\frac{k_{\parallel -}^3}{k_x^3}\right). \quad (4.6.53)$$

The leading order asymptotic expansions for the b_x coefficients are given by

$$\frac{v_{A+}\hat{b}_{x1-}}{u_0} = -2 \frac{r \hat{k}_y - \sin \alpha}{(1+r) \cos \alpha} \frac{k_{\parallel -}}{k_x} + O\left(\frac{k_{\parallel -}^2}{k_x^2}\right), \quad (4.6.54)$$

$$\frac{v_{A+}\hat{b}_{x4-}}{u_0} = -(1-r) \tan \alpha \frac{k_{\parallel -}}{k_x} + O\left(\frac{k_{\parallel -}^2}{k_x^2}\right), \quad (4.6.55)$$

$$\frac{v_{A+}\hat{b}_{x1+}}{u_0} = -r \frac{\hat{k}_y - \sin \alpha}{\cos \alpha} \frac{k_{\parallel -}}{k_x} + O\left(\frac{k_{\parallel -}^2}{k_x^2}\right), \quad (4.6.56)$$

$$\frac{v_{A+}\hat{b}_{x2+}}{u_0} = -r \frac{1-r}{1+r} \frac{\hat{k}_y + \sin \alpha}{\cos \alpha} \frac{k_{\parallel -}}{k_x} + O\left(\frac{k_{\parallel -}^2}{k_x^2}\right), \quad (4.6.57)$$

$$\frac{v_{A+}\hat{b}_{x3+}}{u_0} = (1-r) \frac{k_{\parallel -}}{k_x} + O\left(\frac{k_{\parallel -}^2}{k_x^2}\right). \quad (4.6.58)$$

The leading order asymptotic expansions for the b_{\perp} coefficients are given by

$$\frac{v_{A+}\hat{b}_{\perp 1-}}{u_0} = \frac{2}{1+r} + O\left(\frac{k_{\parallel -}^2}{k_x^2}\right), \quad (4.6.59)$$

$$\frac{v_{A+}\hat{b}_{\perp 4-}}{u_0} = -i(1-r) \frac{\sin^2 \alpha}{\cos \alpha} \frac{k_{\parallel -}}{k_x} + O\left(\frac{k_{\parallel -}^2}{k_x^2}\right), \quad (4.6.60)$$

$$\frac{v_{A+}\hat{b}_{\perp 1+}}{u_0} = 1, \quad (4.6.61)$$

$$\frac{v_{A+}\hat{b}_{\perp 2+}}{u_0} = \frac{1-r}{1+r} + O\left(\frac{k_{\parallel -}^2}{k_x^2}\right), \quad (4.6.62)$$

$$\frac{v_{A+}\hat{b}_{\perp 3+}}{u_0} = -i(1-r) \frac{\sin^2 \alpha}{\cos \alpha} \frac{k_{\parallel -}}{k_x} + O\left(\frac{k_{\parallel -}^2}{k_x^2}\right). \quad (4.6.63)$$

Finally, the leading order asymptotic expansions for the \hat{b}_{\parallel} coefficients are given by

$$\hat{b}_{\parallel 1-} = 0, \quad (4.6.64)$$

$$\frac{v_{A+}\hat{b}_{||4-}}{u_0} = ir(1-r)\sin\alpha \frac{k_{||-}}{k_x} + O\left(\frac{k_{||-}^2}{k_x^2}\right), \quad (4.6.65)$$

$$\hat{b}_{||1+} = 0, \quad (4.6.66)$$

$$\hat{b}_{||2+} = 0, \quad (4.6.67)$$

$$\frac{v_{A+}\hat{b}_{||3+}}{u_0} = ir(1-r)\sin\alpha \frac{k_{||-}}{k_x} + O\left(\frac{k_{||-}^2}{k_x^2}\right). \quad (4.6.68)$$

Equations (4.6.44)-(4.6.68) show that to leading order the Alfvén wave coefficients are given by

$$\hat{b}_{||1-} = \hat{b}_{||1+} = \hat{b}_{||2+} = 0, \quad (4.6.69)$$

$$\frac{u_{x1-}}{u_0}, \frac{u_{x1+}}{u_0}, \frac{u_{x2+}}{u_0}, \frac{v_{A+}\hat{b}_{x1-}}{u_0}, \frac{v_{A+}\hat{b}_{x1+}}{u_0}, \frac{v_{A+}\hat{b}_{x2+}}{u_0} = O\left(\frac{k_{||-}}{k_x}\right), \quad (4.6.70)$$

$$\frac{u_{\perp 1-}}{u_0}, \frac{u_{\perp 1+}}{u_0}, \frac{u_{\perp 2+}}{u_0}, \frac{v_{A+}\hat{b}_{\perp 1-}}{u_0}, \frac{v_{A+}\hat{b}_{\perp 1+}}{u_0}, \frac{v_{A+}\hat{b}_{\perp 2+}}{u_0} = O(1), \quad (4.6.71)$$

$$(4.6.72)$$

and the fast wave coefficients are given by

$$\frac{u_{x4-}}{u_0}, \frac{u_{x3+}}{u_0}, \frac{u_{\perp 4-}}{u_0}, \frac{u_{\perp 3+}}{u_0} = O\left(\frac{k_{||-}^2}{k_x^2}\right), \quad (4.6.73)$$

$$\hat{b}_{x4-}, \hat{b}_{x3+}, \hat{b}_{\perp 4-}, \hat{b}_{\perp 3+}, \hat{b}_{||4-}, \hat{b}_{||3+} = \frac{u_0}{v_{A+}} O\left(\frac{k_{||-}}{k_x}\right). \quad (4.6.74)$$

Similarly, Equations (4.5.21)-(4.5.35) show that to leading order the Alfvén wave coefficients are given by

$$\hat{b}_{||1} = \hat{b}_{||2} = 0, \quad (4.6.75)$$

$$\frac{u_{x1}}{u_0}, \frac{u_{x2}}{u_0}, \frac{v_{A+}\hat{b}_{x1}}{u_0}, \frac{v_{A+}\hat{b}_{x2}}{u_0} = O\left(\frac{k_{||+}}{k_x}\right), \quad (4.6.76)$$

$$\frac{u_{\perp 1}}{u_0}, \frac{u_{\perp 2}}{u_0}, \frac{v_{A+}\hat{b}_{\perp 1}}{u_0}, \frac{v_{A+}\hat{b}_{\perp 2}}{u_0} = O(1), \quad (4.6.77)$$

and the fast wave coefficients are given by

$$\frac{u_{x3}}{u_0}, \frac{u_{\perp 3}}{u_0} = O\left(\frac{k_{\parallel+}}{k_x}\right), \quad (4.6.78)$$

$$\frac{v_{A+}\hat{b}_{x3}}{u_0}, \frac{v_{A+}\hat{b}_{\perp 3}}{u_0}, \frac{v_{A+}\hat{b}_{\parallel 3}}{u_0} = O(1). \quad (4.6.79)$$

This shows that imposing line-tied boundary conditions does not change the order in k_x of the Alfvén wave terms, however, it can increase the order of the fast wave terms by a factor k_x . These results suggest that imposing line-tied boundary conditions can cause the model to significantly overestimate the amplitude of the evanescent fast waves/boundary layers for $\alpha \neq 0$. Equations (4.6.69)-(4.6.74) show that the leading order velocity does not contain any fast-wave terms. Compare this with Equations (4.6.75)-(4.6.79), which show that u_x does contain a fast wave component to leading order. Therefore, for a steady-state solution in a resonant absorption experiment, the fast wave components for u_x and u_\perp should be negligible compared with Alfvén wave components near the singularities, provided line-tied boundary conditions are not imposed. In the next section we verify this claim. It is quite counter-intuitive that the length-scales parallel to the chromosphere/corona interface, e.g. k_x , can have such a large effect on the validity of line-tied boundary conditions. Our goal now is to give an intuitive explanation for why this is. Imposing line-tied boundary conditions is in some sense equivalent to modelling the chromosphere as infinitely denser than the corona, i.e. setting $k_{\parallel -} \rightarrow \infty$. Therefore, imposing line-tied boundary conditions forces the fast waves in the chromosphere to be propagating waves. Propagating waves have a sinusoidal profile while evanescent waves have an exponential profile. This has important implications for ensuring continuity of velocity and its derivative at the chromosphere/corona interface and explains why the line-tied solution can be so different to the solution with a piecewise constant density profile at the interface.

4.7 Oblique field: Resonant absorption

In this section, we allow the Alfvén speed to be dependent on x as this enables resonant absorption to occur. Our goal in this section is to verify our claim, (see end of Section 4.6) that the velocity amplitude of the boundary layers should be negligible near the

singularity in a resonant absorption experiment.

4.7.1 Model and equations

The Alfvén speed is given by $v_A(x, z) = \hat{v}_A(x)v_A(0, z)$, where $v_A(0, z)$ is given by Equation (4.2.4) and $\hat{v}_A(x)$ is an arbitrary function of x satisfying $\hat{v}_A(x) = 1$.

We seek normal mode solutions and assume the variables are of the form

$$f(x, y, z, t) = f'(x, z) \exp\{i[k_\perp(\cos \alpha y - \sin \alpha z) + \omega t]\}.$$

Note that

$$\nabla_\perp f(x, y, z, t) = \exp\{i[k_\perp(\cos \alpha y - \sin \alpha z) + \omega t]\} \left(ik_\perp - \sin \alpha \frac{\partial}{\partial z} \right) f',$$

$$\nabla_\parallel f(x, y, z, t) = \exp\{i[k_\perp(\cos \alpha y - \sin \alpha z) + \omega t]\} \cos \alpha \frac{\partial f'}{\partial z}.$$

Therefore, Equations (4.2.10)-(4.2.14) can be simplified to

$$i\omega u'_x = v_A^2(x, z) \left[\nabla'_\parallel \hat{b}'_x - \frac{\partial \hat{b}'_\parallel}{\partial x} \right], \quad (4.7.1)$$

$$i\omega u'_\perp = v_A^2(x, z) \left[\nabla'_\parallel \hat{b}'_\perp - \nabla'_\perp \hat{b}'_\parallel \right], \quad (4.7.2)$$

$$i\omega \hat{b}'_x = \nabla'_\parallel u'_x, \quad (4.7.3)$$

$$i\omega \hat{b}'_\perp = \nabla'_\parallel u'_\perp, \quad (4.7.4)$$

$$i\omega \hat{b}'_\parallel = - \left[\frac{\partial u'_x}{\partial x} + \nabla'_\perp u'_\perp \right]. \quad (4.7.5)$$

where

$$\nabla'_\perp = \left(ik_\perp - \sin \alpha \frac{\partial}{\partial z} \right), \quad (4.7.6)$$

$$\nabla'_\parallel = \cos \alpha \frac{\partial}{\partial z}. \quad (4.7.7)$$

Eliminating \hat{b}'_x and \hat{b}'_\perp gives

$$\frac{\partial u'_x}{\partial x} = - \left[i\omega \hat{b}_{||} + \nabla'_\perp u'_\perp \right], \quad (4.7.8)$$

$$\frac{\partial \hat{b}'_{||}}{\partial x} = - \frac{i}{\omega} \mathcal{L}' u'_x, \quad (4.7.9)$$

$$\mathcal{L}' u'_\perp = i\omega \nabla'_\perp \hat{b}'_{||}, \quad (4.7.10)$$

where

$$\mathcal{L}' = \nabla'^2_{||} + \frac{\omega^2}{v_A^2(x, z)}. \quad (4.7.11)$$

Note that the z domain is given by $-L_z \leq z \leq L_z$. In this section, we impose periodic boundary conditions such that

$$u'_x(x, -L_z) = u'_x(x, L_z), \quad \frac{\partial u'_x}{\partial z} \Big|_{z=-L_z} = \frac{\partial u'_x}{\partial z} \Big|_{z=L_z}, \quad (4.7.12)$$

$$b'_{||}(x, -L_z) = b'_{||}(x, L_z), \quad \frac{\partial b'_{||}}{\partial z} \Big|_{z=-L_z} = \frac{\partial b'_{||}}{\partial z} \Big|_{z=L_z}, \quad (4.7.13)$$

$$u'_\perp(x, -L_z) = u'_\perp(x, L_z), \quad \frac{\partial u'_\perp}{\partial z} \Big|_{z=-L_z} = \frac{\partial u'_\perp}{\partial z} \Big|_{z=L_z}. \quad (4.7.14)$$

We choose these boundary conditions because they can be easily implemented both numerically and analytically without introducing fictitious boundary layers. Our model approximates a loop in the corona which goes into the chromosphere then back into the corona and so on.

4.7.2 Eigenfunctions and eigenfrequencies

To help solve Equations (4.7.8)-(4.7.10) we assume the solutions are of the form

$$u'_x(x, z) = u_{x0}^{(1)}(x)\phi_0(z) + \sum_{n=1}^{\infty} u_{xn}^{(1)}(x)\phi_n(z) + u_{xn}^{(2)}(x)\varphi_n(z), \quad (4.7.15)$$

$$b'_{||}(x, z) = b_{||0}^{(1)}(x)\phi_0(z) + \sum_{n=1}^{\infty} b_{||n}^{(1)}(x)\phi_n(z) + b_{||n}^{(2)}(x)\varphi_n(z), \quad (4.7.16)$$

$$u'_\perp(x, z) = u_{\perp 0}^{(1)}(x)\phi_0(z) + \sum_{n=1}^{\infty} u_{\perp n}^{(1)}(x)\phi_n(z) + u_{\perp n}^{(2)}(x)\varphi_n(z), \quad (4.7.17)$$

where ϕ_n, φ_n are eigenfunctions, with eigenfrequencies, ω_n, ϖ_n , respectively. The eigenfunctions satisfy the following Sturm-Liouville equations,

$$\left[\nabla_{||}^{\prime 2} + \frac{\omega_n^2}{v_A^2(0, z)} \right] \phi_n(z) = 0,$$

$$\left[\nabla_{||}^{\prime 2} + \frac{\varpi_n^2}{v_A^2(0, z)} \right] \varphi_n(z) = 0,$$

as well as the periodic boundary conditions, see Equation (4.7.12).

By symmetry, we assume the eigenfunctions are of the form

$$\phi_n(z) = A_n \begin{cases} a_n \cos[k_{zn-}(z + l_z)], & z < 0, \\ c_n \cos[k_{zn+}(z - l_z)], & z \geq 0, \end{cases} \quad (4.7.18)$$

$$\varphi_n(z) = B_n \begin{cases} b_n \sin[\bar{k}_{zn-}(z + l_z)], & z < 0, \\ d_n \sin[\bar{k}_{zn+}(z - l_z)], & z \geq 0, \end{cases} \quad (4.7.19)$$

where a_n, b_n, c_n, d_n are constants, $L_z = 2l_z$ and

$$k_{zn\pm} = \frac{\omega_n}{v_{A\pm} \cos \alpha}, \quad (4.7.20)$$

$$\bar{k}_{zn\pm} = \frac{\varpi_n}{v_{A\pm} \cos \alpha}. \quad (4.7.21)$$

Hence

$$\frac{d\phi_n}{dz} = A_n \begin{cases} -a_n k_{zn-} \sin[k_{zn-}(z + l_z)], & z < 0, \\ -c_n k_{zn+} \sin[k_{zn+}(z - l_z)], & z \geq 0, \end{cases} \quad (4.7.22)$$

$$\frac{d\varphi_n}{dz} = B_n \begin{cases} b_n \bar{k}_{zn+} \cos[\bar{k}_{zn+}(z + l_z)], & z < 0, \\ d_n \bar{k}_{zn+} \cos[\bar{k}_{zn+}(z - l_z)], & z \geq 0. \end{cases} \quad (4.7.23)$$

We require continuity of $\phi_n, \varphi_n, d\phi_n/dz, d\varphi_n/dz$ at $z = 0$ and $z = \pm L_z$, this gives the

following equations

$$\begin{pmatrix} \cos(k_{zn}-l_z) & -\cos(k_{zn}+l_z) \\ k_{zn-}\sin(k_{zn}-l_z) & k_{zn+}\sin(k_{zn}+l_z) \end{pmatrix} \begin{pmatrix} a_n \\ c_n \end{pmatrix} = \begin{pmatrix} 0 \\ 0 \end{pmatrix}, \quad (4.7.24)$$

$$\begin{pmatrix} \sin(\bar{k}_{zn}-l_z) & \sin(\bar{k}_{zn}+l_z) \\ \bar{k}_{zn-}\cos(\bar{k}_{zn}-l_z) & -\bar{k}_{zn+}\cos(\bar{k}_{zn}+l_z) \end{pmatrix} \begin{pmatrix} b_n \\ d_n \end{pmatrix} = \begin{pmatrix} 0 \\ 0 \end{pmatrix}. \quad (4.7.25)$$

For non-trivial solutions to exist, ω_n, ϖ_n must satisfy

$$k_{zn+}\sin(k_{zn}+l_z)\cos(k_{zn}-l_z) + k_{zn-}\sin(k_{zn}-l_z)\cos(k_{zn}+l_z) = 0, \quad (4.7.26)$$

$$\bar{k}_{zn+}\sin(\bar{k}_{zn}+l_z)\cos(\bar{k}_{zn}-l_z) + \bar{k}_{zn-}\sin(\bar{k}_{zn}-l_z)\cos(\bar{k}_{zn}+l_z) = 0. \quad (4.7.27)$$

These equations define, ω_n, ϖ_n and we order them such that

$$\omega_0 < \omega_1 < \omega_2 \dots, \quad \varpi_0 < \varpi_1 < \varpi_2 \dots, \quad (4.7.28)$$

where $\omega_0 = \varpi_0 = 0$.

Note that if $l_z = n\pi/k_{zn+}$ and $l_z = n\pi/\bar{k}_{zn+}$ the above equations simplify to

$$k_{zn-}\sin\left(n\pi\frac{k_{zn-}}{k_{zn+}}\right)(-1)^n = 0, \quad \bar{k}_{zn+}\sin\left(n\pi\frac{\bar{k}_{zn-}}{\bar{k}_{zn+}}\right)(-1)^n = 0,$$

which is satisfied for $v_{A+}/v_{A-} = m$, where m is an integer. If $l_z = (2n+1)\pi/(2k_{zn+})$ and $l_z = (2n+1)\pi/(2\bar{k}_{zn+})$ the above equations simplify to

$$k_{zn+}(-1)^n \cos\left(\frac{1}{2}(2n+1)\pi\frac{k_{zn-}}{k_{zn+}}\right) = 0, \quad \bar{k}_{zn-}(-1)^n \cos\left(\frac{1}{2}(2n+1)\pi\frac{k_{zn-}}{\bar{k}_{zn+}}\right) = 0.$$

which is satisfied for $v_{A+}/v_{A-} = m$, where m is an odd integer. Therefore, for $v_{A+}/v_{A-} = m$, where m is an odd positive integer, a subset of the eigenvalues are given by

$$\omega_j = \varpi_j = k\pi\frac{v_{A+}}{L_z} \cos\alpha, \quad (4.7.29)$$

where $j = [(m-1)/2+1]k$ and $k \in \mathbb{N}$.

If ω_n, ϖ_n satisfy Equations (4.7.26) and (4.7.27), then the boundary conditions and

continuity conditions are ensured if

$$a_n = \begin{cases} \cos(k_{zn+}l_z), & \cos(k_{zn+}l_z) \neq 0, \\ k_{zn+} \sin(k_{zn+}l_z), & \cos(k_{zn+}l_z) = 0, \end{cases} \quad (4.7.30)$$

$$c_n = \begin{cases} \cos(k_{zn-}l_z), & \cos(k_{zn-}l_z) \neq 0, \\ -k_{zn-} \sin(k_{zn-}l_z), & \cos(k_{zn-}l_z) = 0, \end{cases} \quad (4.7.31)$$

$$b_n = \begin{cases} \sin(\bar{k}_{zn+}l_z), & \sin(\bar{k}_{zn+}l_z) \neq 0, \\ \bar{k}_{zn+} \cos(\bar{k}_{zn+}l_z), & \sin(\bar{k}_{zn+}l_z) = 0, \end{cases} \quad (4.7.32)$$

$$d_n = \begin{cases} -\sin(\bar{k}_{zn-}l_z), & \sin(\bar{k}_{zn-}l_z) \neq 0, \\ \bar{k}_{zn-} \cos(\bar{k}_{zn-}l_z), & \sin(\bar{k}_{zn-}l_z) = 0. \end{cases} \quad (4.7.33)$$

Let $\langle f_n(z), f_m(z) \rangle$ denote the following inner product

$$\langle f_n(z), f_m(z) \rangle = \frac{v_{A+}^2}{L_z} \int_{-L_z}^{L_z} \frac{f_n(z)f_m(z)}{v_A^2(0, z)} dz. \quad (4.7.34)$$

By Sturm–Liouville theory, the eigenfunctions are orthogonal to each other over this inner product, hence,

$$\langle \phi_n(z), \varphi_m(z) \rangle = 0. \quad (4.7.35)$$

We normalise such that

$$\langle \phi_n(z), \phi_m(z) \rangle = \langle \varphi_n(z), \varphi_m(z) \rangle = \delta_{nm}, \quad (4.7.36)$$

where δ_{nm} is the Kronecker delta. Note that

$$\begin{aligned} \frac{L_z}{v_{A+}^2} \frac{\langle \phi_n, \phi_n \rangle}{A_n^2} &= 2 \int_0^{l_z} \frac{a_n^2}{v_{A-}^2} \cos^2(k_{zn-}z) + \frac{c_n^2}{v_{A+}^2} \cos^2(k_{zn+}z) dz \\ &= \left\{ \frac{a_n^2}{2v_{A-}^2 k_{zn-}} \left[2k_{zn-}z + \sin(2k_{zn-}z) \right] \right. \\ &\quad \left. + \frac{c_n^2}{2v_{A+}^2 k_{zn+}} \left[2k_{zn+}z + \sin(2k_{zn+}z) \right] \right\}_0^{l_z} \\ &= \frac{a_n^2}{2v_{A-}^2 k_{zn-}} \left[2k_{zn-}l_z + \sin(2k_{zn-}l_z) \right] \\ &\quad + \frac{c_n^2}{2v_{A+}^2 k_{zn+}} \left[2k_{zn+}l_z + \sin(2k_{zn+}l_z) \right], \end{aligned} \quad (4.7.37)$$

$$\begin{aligned} \frac{L_z}{v_{A+}^2} \frac{\langle \varphi_n, \varphi_n \rangle}{B_n^2} &= \frac{b_n^2}{2v_{A-}^2 \bar{k}_{zn-}} \left[2\bar{k}_{zn-}l_z - \sin(2\bar{k}_{zn-}l_z) \right] \\ &\quad + \frac{b_n^2}{2v_{A-}^2 \bar{k}_{zn-}} \left[2\bar{k}_{zn-}l_z - \sin(2\bar{k}_{zn-}l_z) \right]. \end{aligned} \quad (4.7.38)$$

Hence,

$$A_n = \frac{\sqrt{L_z}}{v_{A+}} \left(\frac{a_n^2}{2v_{A-}^2 k_{zn-}} \left[2k_{zn-}l_z + \sin(2k_{zn-}l_z) \right] + \frac{c_n^2}{2v_{A+}^2 k_{zn+}} \left[2k_{zn+}l_z + \sin(2k_{zn+}l_z) \right] \right)^{-1/2}, \quad (4.7.39)$$

$$B_n = \frac{\sqrt{L_z}}{v_{A+}} \left(\frac{b_n^2}{2v_{A-}^2 \bar{k}_{zn-}} \left[2\bar{k}_{zn-}l_z - \sin(2\bar{k}_{zn-}l_z) \right] + \frac{b_n^2}{2v_{A-}^2 \bar{k}_{zn-}} \left[2\bar{k}_{zn-}l_z - \sin(2\bar{k}_{zn-}l_z) \right] \right)^{-1/2}. \quad (4.7.40)$$

To help visualise the eigenfunctions, we plot the first 3 normalised eigenfunctions (excluding the 0th eigenfunction) in Figure 4.8 for $v_{A-} = v_{A+}/5$. They show that the amplitude of the eigenfunctions in the chromosphere can be as large as the amplitude in the corona, although it never exceeds the coronal amplitudes. The bottom-left of Figure 4.8 shows the first 5 eigenfrequencies as a function of $1/v_{A-}$. They show that

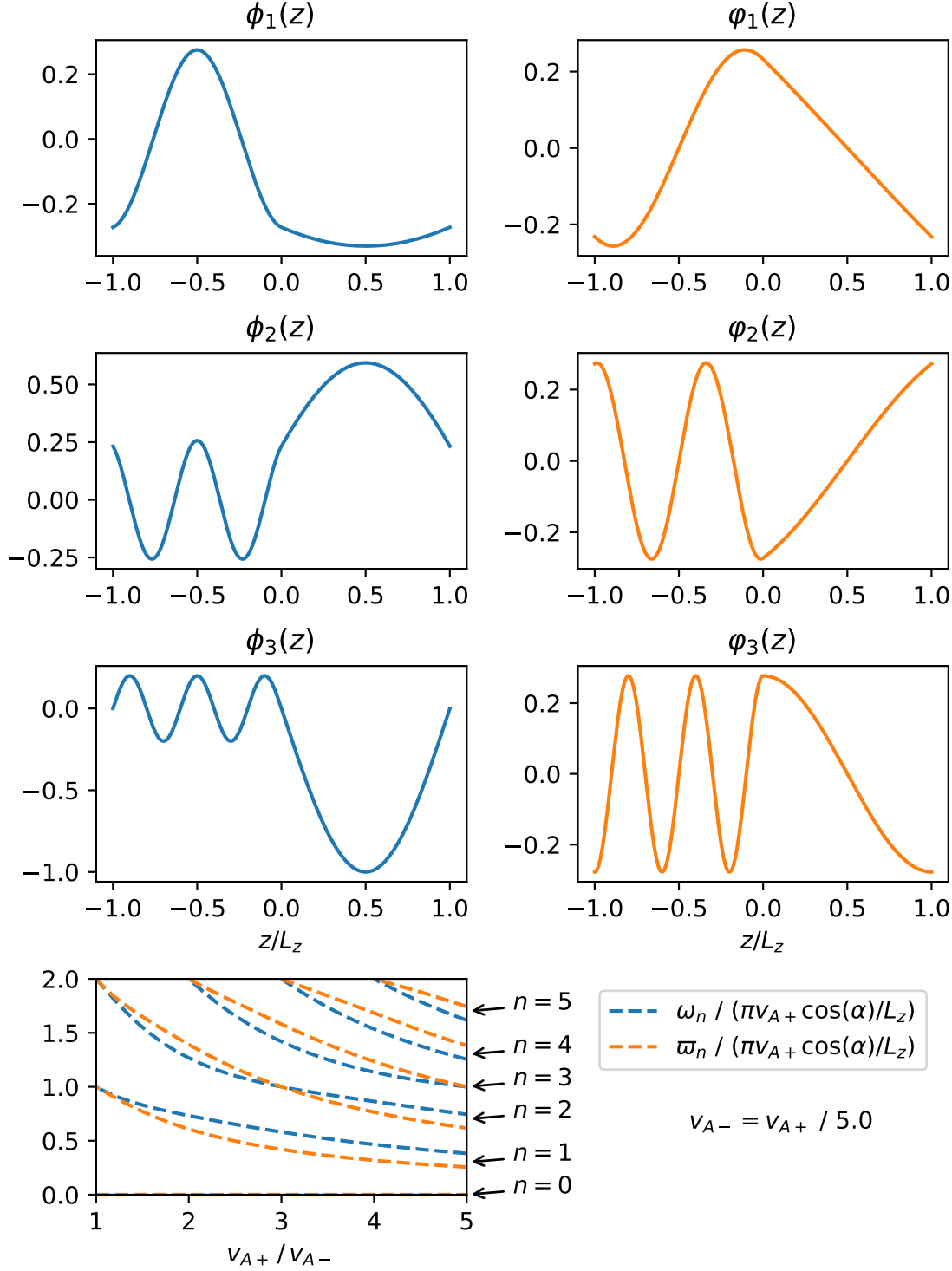


Figure 4.8: The 1st, 2nd and 3rd rows of this Figure show the 1st, 2nd and 3rd eigenfunctions, $\phi_n(z)$, $\varphi_n(z)$, respectively, where $v_{A-} = v_{A+}/5$. In the bottom-left plot we show the first 5 eigenfrequencies, ω_n , w_n as a function of v_{A+}/v_{A-} . The code we used to make this figure is available on GitHub in the following directory:

→ [Python/Chapter4/eigenfunction_eigenfrequency_plots.py](#)

decreasing v_{A-} causes ω_n and ϖ_n to decrease because this lowers the Alfvén travel time of the loop. This plot can also be used to check that for $v_{A+}/v_{A-} = m$, where m is an odd integer, a subset of the eigenfrequencies are given by Equation (4.7.29).

4.7.3 Analytic resonant solution

Deriving a PDE for $u_\perp(x, z)$

Our goal now is to calculate the leading order resonant/singular solution analytically. We will verify our result numerically in the next section. Eliminating \hat{b}'_\parallel from Equations (4.7.8)-(4.7.10) gives

$$\left[\mathcal{L}' + \frac{\partial^2}{\partial x^2} \right] u'_x = -\frac{\partial}{\partial x} \nabla'_\perp u'_\perp, \quad (4.7.41)$$

$$[\mathcal{L}' + \nabla'^2_\perp] u'_\perp = -\frac{\partial}{\partial x} \nabla'_\perp u'_x \quad (4.7.42)$$

We can eliminate u'_x with the following procedure. Take the x -derivative of the Equation (4.7.41)

$$\begin{aligned} \mathcal{L}'_x u'_x + \left[\mathcal{L}' + \frac{\partial^2}{\partial x^2} \right] \frac{\partial u'_x}{\partial x} &= -\nabla'_\perp \frac{\partial^2 u'_\perp}{\partial x^2}, \\ \implies u'_x &= -\frac{1}{\mathcal{L}'_x} \left\{ \left[\mathcal{L}' + \frac{\partial^2}{\partial x^2} \right] \frac{\partial u'_x}{\partial x} + \nabla'_\perp \frac{\partial^2 u'_\perp}{\partial x^2} \right\}. \end{aligned}$$

where

$$\mathcal{L}'_x = \frac{\partial \mathcal{L}'}{\partial x} = \frac{-2\omega^2}{a(x)v_A^2(x, z)}. \quad (4.7.43)$$

Substitute this into Equation (4.7.41) to give

$$-\frac{\mathcal{L}'}{\mathcal{L}'_x} \left\{ \left[\mathcal{L}' + \frac{\partial^2}{\partial x^2} \right] \frac{\partial u'_x}{\partial x} + \nabla'_\perp \frac{\partial^2 u'_\perp}{\partial x^2} \right\} + \frac{\partial^2 u'_x}{\partial x^2} = -\nabla'_\perp \frac{\partial u'_\perp}{\partial x},$$

Applying $-\nabla'_\perp$ to both sides, substituting for u'_x and assuming $z \neq 0, -L_z, L_z$ gives

$$-\frac{\mathcal{L}'}{\mathcal{L}'_x} \left\{ \left[\mathcal{L}' + \frac{\partial^2}{\partial x^2} \right] [\mathcal{L}' + \nabla'^2_\perp] u'_\perp - \nabla'^2_\perp \frac{\partial^2 u'_\perp}{\partial x^2} \right\} + \frac{\partial}{\partial x} [\mathcal{L}' + \nabla'^2_\perp] u'_\perp = \nabla'^2_\perp \frac{\partial u'_\perp}{\partial x}.$$

This can be simplified to give

$$\mathcal{L}'^2 \frac{\partial^2 u'_\perp}{\partial x^2} +' \mathcal{L}'_x \mathcal{L}' \frac{\partial u'_\perp}{\partial x} + \mathcal{M}' u'_\perp = 0, \quad (4.7.44)$$

where

$$\mathcal{M}' = \mathcal{L}'^3 + \mathcal{L}'^2 \nabla_\perp'^2 + \mathcal{L}'_{xx} \mathcal{L}' - \mathcal{L}'_x^2 \quad (4.7.45)$$

From the literature (e.g. Thompson and Wright 1993; Wright and Allan 1996) and Section 4.4, we know that the formation of singularities in x usually accompany resonant absorption. Equation (4.7.44) shows that the coefficient of the leading order x -derivative goes to zero if $\mathcal{L}'(x, z) = 0$. Let

$$x_{res,m} = x_{r,m} + ix_{i,m},$$

be defined as a location which satisfies

$$\mathcal{L}'(x_{res,m}, z)\phi_m(z) = 0. \quad (4.7.46)$$

We postulate that singularities can form at locations, $x_{res,m}$, which are locations where a resonance can occur.

Deriving an ODE for $u_{\perp m}^{(1)}(x)$

Our goal now is to convert this PDE into an ODE for $u_{\perp m}^{(1)}(x)$ using the expansion given by Equation (4.7.17). Note that

$$\begin{aligned} \mathcal{L}'(x, z)\phi_n(z) &= [\omega^2/\hat{v}_A^2(x) - \omega_n^2] \frac{\phi_n(z)}{v_A^2(0, z)} = 0 \\ &= \left[\mathcal{L}'_x(x_{res,m}, z)(x - x_{res,m}) + \frac{1}{2}\mathcal{L}'_{xx}(x_{res,m}, z)(x - x_{res,m})^2 + \dots \right] \phi_n(z). \end{aligned}$$

Multiplying Equation (4.7.17) thorough by $\kappa_m^2(x, z)\phi_m v_{A+}^2/[L_z v_A^2(0, z)]$ where

$$\begin{aligned}\kappa_m(x, z) &= (x - x_{res,m}) \frac{v_A^2(0, z)}{\omega^2/\hat{v}_A^2(x) - \omega_m^2} \\ &= (x - x_{res,m}) \left[\mathcal{L}'_x(x_{res,m}, z)(x - x_{res,m}) + \frac{1}{2} \mathcal{L}'_{xx}(x_{res,m}, z)(x - x_{res,m})^2 + \dots \right]^{-1} \\ &= \frac{1}{\mathcal{L}'_x(x_{res,m}, z)} \left[1 - \frac{1}{2} \frac{\mathcal{L}'_{xx}(x_{res,m}, z)}{\mathcal{L}'_x(x_{res,m}, z)} (x - x_{res,m}) + \dots \right],\end{aligned}\tag{4.7.47}$$

and integrating from $-L_z$ to L_z gives

$$(x - x_{res,m})^2 \frac{d^2 u_{\perp m}^{(1)}}{dx^2} + (x - x_{res,m}) p_m(x) \frac{du_{\perp m}^{(1)}}{dx} + q_m(x) u_{\perp m}^{(1)}(x) = f_m(x),\tag{4.7.48}$$

where

$$p_m(x) = \mathcal{L}'_x(x, z) \kappa_m(x, z),\tag{4.7.49}$$

$$q_m(x) = \langle \mathcal{M}' \phi_m(z), \kappa_m^2(x, z) \phi_m(z) \rangle,\tag{4.7.50}$$

$$\begin{aligned}f_m(x) &= - \left\langle \mathcal{M}' u_{\perp m}^{(2)}(x) \varphi_m(z), \kappa_m^2(x, z) \phi_m(z) \right\rangle \\ &\quad - \sum_{\substack{n=0 \\ n \neq m}}^{\infty} \left\langle \mathcal{M}' \left[u_{\perp n}^{(1)}(x) \phi_n(z) + u_{\perp n}^{(2)}(x) \varphi_n(z) \right], \kappa_m^2(x, z) \phi_m(z) \right\rangle.\end{aligned}\tag{4.7.51}$$

Complementary function and particular integral

To solve Equation (4.7.48) we will first calculate the complementary function by solving the homogeneous equation given by

$$(x - x_{res,m})^2 \frac{d^2 u_{\perp m}^{(1)}}{dx^2} + (x - x_{res,m}) p_m(x) \frac{du_{\perp m}^{(1)}}{dx} + q_m(x) u_{\perp m}^{(1)}(x) = 0.\tag{4.7.52}$$

We can solve this equation by using the method of Frobenius using an approach very similar to that used in, for example, Thompson and Wright (1993); Wright and Rickard (1995); Soler et al. (2013). We first need to calculate the indicial equation by assuming

the solutions are of the form

$$u_{\perp m}^{(1)}(x) = (x - x_{res,m})^\sigma \sum_{n=0}^{\infty} a_n (x - x_{res,m})^n,$$

to give

$$\sum_{n=0}^{\infty} a_n [\sigma(\sigma - 1) + \sigma p_m(x) + q_m(x)] (x - x_{res,m})^{n+\sigma}.$$

Hence, the indicial equation is given by

$$I(\sigma) = \sigma(\sigma - 1) + p_m(x_{res,m})\sigma + q_m(x_{res,m}). \quad (4.7.53)$$

For non-trivial solution to exist we require $I(\sigma) = 0$. Since $p_m(x_{res,m}) = -q_m(x_{res,m}) = 1$ we know that $\sigma = \pm 1$. Note that the allowed values of σ differ by an integer. Therefore, the general complementary solution for $u_{\perp m}^{(1)}(x)$ is given by a linear combination of

$$u_{\perp m1}^{(1)}(x) = \sum_{n=1}^{\infty} a_n (x - x_{res,m})^n, \quad (4.7.54)$$

and

$$u_{\perp m2}^{(1)}(x) = C u_{\perp m1}^{(1)}(x) \ln(x - x_{res,m}) + \sum_{n=-1}^{\infty} b_n (x - x_{res,m})^n, \quad (4.7.55)$$

where a_n, b_n, C are constants.

If we know the power series in x for $f_m(x)$ then we can calculate the particular integral to Equation (4.7.48) by using the method of undetermined coefficients. Since $f_m(x)$ is proportional to $u_{\perp n}^{(1)}(x), u_{\perp n}^{(2)}(x)$, we know that the leading order term can be at most order $(x - x_{res,m})^{-1}$.

Singular solution

Our goal now is to calculate a leading order singular solution for u'_x, u'_{\perp} and $\hat{b}'_{||}$ which we can verify numerically. Assume that $x_{i,m} \ll R$ where R is the radius of convergence

for the power series solution of $u'_\perp(x, z)$ in x . We will assume that to leading order $u_{\perp n}^{(1)} = u_{\perp n}^{(2)} = u_{\perp m}^{(2)} = 0$ for all $n \neq m$. This ensures that the leading order solution for $u_{\perp m}(x)$ is given by the leading term of the complementary solution. Let u'_\perp be given by

$$u'_\perp(x, z) = u_0 \left[\frac{\phi_m(z)}{X_m} + O(X_m \ln X_m, X_m) \right], \quad (4.7.56)$$

where

$$X_m = \frac{x - x_{res,m}}{x_{i,m}}, \quad (4.7.57)$$

and we choose the boundary conditions such that the terms of order X_m^0 equal zero.

From Equation (4.7.42) we know that u_x is given by

$$u'_x(x, z) = -u_0 [x_{i,m} \ln(X_m) \nabla'_\perp \phi_m(z) + O(X_m, X_m^2 \ln X_m)], \quad (4.7.58)$$

where we impose the boundary condition that terms of order X_m^0 equal zero. From Equation (4.7.10), we know that to leading order $\hat{b}'_{||}$ satisfies

$$\begin{aligned} \nabla'_\perp \hat{b}'_{||}(z) &= u_0 \frac{\mathcal{L}'_x(x_{r,m}, z) x_{i,m}}{i\omega_r} \phi_m(z) + \frac{O(X_m \ln X_m, X_m)}{L_z} \\ &= 2iu_0 \frac{\omega_r x_{i,m}}{a(x_{r,m}) v_A^2(x_{r,m}, z)} \phi_m(z) + \frac{O(X_m \ln X_m, X_m)}{L_z}, \end{aligned} \quad (4.7.59)$$

assuming $\omega_i \ll \omega_r$. Our goal now is to solve Equation (4.7.59) for $\hat{b}'_{||}$. For $\sin \alpha = 0$, $\hat{b}'_{||}$ is given by

$$\hat{b}'_{||}(x, z) = \frac{2u_0 \omega_r x_{i,m}}{a(x_{r,m}) v_A^2(x_{r,m}, z) k_\perp} \phi_m(z) + O(X_m \ln X_m, X_m). \quad (4.7.60)$$

For $\sin \alpha \neq 0$, we can calculate $b'_{||}(x, z)$ by using an integrating factor. However, if $k_\perp L_z / \sin \alpha = j\pi$ for $j \in \mathbb{Z}$ then $\hat{b}'_{||}(x, z)$ is not uniquely defined by the boundary conditions in z . To see this, assume $\hat{b}'_{||}(x, z)$ is of the form

$$\hat{b}'_{||}(x, z) = \sum_{n=-\infty}^{\infty} \hat{b}_{||n}(x) \exp\left(in \frac{\pi}{L_z} z\right),$$

This ensures that $\hat{b}_{||}(x, z)$ is periodic in z with period $2L_z$. Substituting this into Equation (4.7.59), multiplying by $\exp(ij\pi z/L_z)/(2L_z)$ and integrating from $-L_z$ to L_z gives

$$i\left(k_{\perp} - \sin \alpha j \frac{\pi}{L_z}\right) \hat{b}'_{||j}(x) = \frac{1}{2L_z} \int_{-L_z}^{L_z} \hat{b}'_{||}(x, z) \exp\left(ij \frac{\pi}{L_z} z\right) dz.$$

Hence, if $k_{\perp} L_z / \sin \alpha = j\pi$ for $j \in \mathbb{Z}$ then $\hat{b}'_{||j}(x)$ and consequently $\hat{b}'_{||}(x, z)$ is not uniquely defined by the boundary conditions in z .

Poynting flux

Finally, we aim to calculate the Poynting flux near the resonant location, $x_{res,n}$. Using Equation (1.4.40) the Poynting flux in the x -direction is given by

$$\begin{aligned} S_x &= \frac{1}{\mu} \left\{ [\operatorname{Re}(\mathbf{b}) \cdot \mathbf{B}_0] \operatorname{Re}(\mathbf{u}) - [\operatorname{Re}(\mathbf{u}) \cdot \operatorname{Re}(\mathbf{b})] \mathbf{B}_0 \right\} \cdot \hat{\mathbf{x}} \\ &= \frac{B_0^2}{\mu} \operatorname{Re}(u_x) \operatorname{Re}(\hat{b}_{||}) \\ &= \frac{B_0^2}{\mu} \left(\frac{u_x + u_x^*}{2} \right) \left(\frac{\hat{b}_{||} + \hat{b}_{||}^*}{2} \right), \end{aligned} \quad (4.7.61)$$

where u_x^* denotes the complex conjugate of u_x . Therefore, the component which does not average to zero in y is given by

$$\langle S_x \rangle = \frac{B_0^2}{4\mu} \left(u_x \hat{b}_{||}^* + u_x^* \hat{b}_{||} \right). \quad (4.7.62)$$

Substituting Equation (4.7.58) gives

$$\langle S_x \rangle = -\frac{B_0^2}{4\mu} u_0 \left[x_{i,n} \left(\ln(X_m) \nabla'_{\perp} \phi_n \hat{b}_{||}^* + \ln(X_m^*) \nabla'^*_\perp \phi_n \hat{b}'_{||} \right) + O(X_m, X_m^2 \ln X_m) \right], \quad (4.7.63)$$

for x sufficiently close to $x_{res,n}$. Note that

$$\lim_{x \rightarrow \infty} \ln(X_m) - \lim_{x \rightarrow -\infty} \ln(X_m) = -i\pi \operatorname{sign}(x_{i,m}),$$

$$\lim_{x \rightarrow \infty} \ln(X_m^*) - \lim_{x \rightarrow -\infty} \ln(X_m^*) = i\pi \operatorname{sign}(x_{i,m}),$$

where $\text{sign}(x_{i,m}) = x_{i,m}/|x_{i,m}|$. We define the jump in Poynting flux, $\langle \Delta S_x \rangle$, across $x = x_{r,m}$ as

$$\langle \Delta S_x \rangle = i\pi u_0 x_{i,m} \frac{B_0^2}{4\mu} \text{sign}(x_{i,m}) \left(\nabla'_\perp \phi_n \hat{b}_\parallel^* - \nabla'^*_\perp \phi_n \hat{b}_\parallel \right). \quad (4.7.64)$$

4.7.4 Numerical solution

Our goal now is to verify Equations (4.7.56)-(4.7.59) by solving Equations (4.7.8)-(4.7.10) numerically. To solve the system numerically, we use Equations (4.7.15)-(4.7.17) and convert Equations (4.7.8)-(4.7.10) from a set of PDEs into a set of ODEs which we then solve as an initial value problem in x using `solve_ivp` in [Virtanen et al. \(2020\)](#).

For $z \neq 0, -L_z, L_z$, taking ∇'_\perp of Equation (4.7.10) gives

$$\mathcal{L}' \nabla'_\perp u'_\perp = i\omega \nabla'^2_\perp \hat{b}'_\parallel. \quad (4.7.65)$$

Let

$$\nabla'_\perp u'_\perp(x, z) = \Delta_{\perp 0}^{(1)}(x) \phi_0(z) + \sum_{n=1}^{\infty} \Delta_{\perp n}^{(1)}(x) \phi_n(z) + \Delta_{\perp n}^{(2)}(x) \varphi_n(z). \quad (4.7.66)$$

Note that

$$\mathcal{L}'(x, z) \phi_n(z) = [\omega^2/\hat{v}_A^2(x) - \omega_n^2] \frac{\phi_n(z)}{v_A^2(0, z)}, \quad (4.7.67)$$

$$\mathcal{L}'(x, z) \varphi_n(z) = [\omega^2/\hat{v}_A^2(x) - \varpi_n^2] \frac{\varphi_n(z)}{v_A^2(0, z)}. \quad (4.7.68)$$

Substituting Equations (4.7.15), (4.7.16), (4.7.66) into (4.7.8), (4.7.9), (4.7.65), gives

$$\begin{aligned} \sum_{n=0}^{\infty} \frac{du_{xn}^{(1)}}{dx} \phi_n + \frac{du_{xn}^{(2)}}{dx} \varphi_n &= - \sum_{n=0}^{\infty} i\omega [b_{||n}^{(1)} \phi_n(z) + b_{||n}^{(2)} \varphi_n] + \\ &\quad \Delta_{\perp n}^{(1)} \phi_n + \Delta_{\perp n}^{(2)} \varphi_n, \end{aligned} \quad (4.7.69)$$

$$\sum_{n=0}^{\infty} \frac{d\hat{b}_{||n}^{(1)}}{dx} \phi_n + \frac{db_{||n}^{(2)}}{dx} \varphi_n = -\frac{i}{\omega} \sum_{n=0}^{\infty} u_{xn}^{(1)} [\omega^2 / \hat{v}_A^2(x) - \omega_n^2] \frac{\phi_n(z)}{v_A^2(x, z)} + u_{xn}^{(2)} [\omega^2 / \hat{v}_A^2(x) - \varpi_n^2] \frac{\varphi_n(z)}{v_A^2(x, z)}, \quad (4.7.70)$$

$$i\omega \nabla_{\perp}^{\prime 2} \sum_{n=0}^{\infty} b_{||n}^{(1)} \phi_n + b_{||n}^{(2)} \varphi_n = \sum_{n=0}^{\infty} \Delta_{\perp n}^{(1)} [\omega^2 / \hat{v}_A^2(x) - \omega_n^2] \frac{\phi_n(z)}{v_A^2(0, z)} + \Delta_{\perp n}^{(2)} [\omega^2 / \hat{v}_A^2(x) - \varpi_n^2] \frac{\varphi_n(z)}{v_A^2(0, z)}, \quad (4.7.71)$$

where $u_{x0}^{(2)} = b_{||0}^{(2)} = u_{\perp 0}^{(2)} = 0$. Taking the inner product of the above equations with ϕ_m and φ_m gives

$$\frac{du_{xm}^{(1)}}{dx} = -[i\omega b_{||m}^{(1)} + \Delta_{\perp m}^{(1)}], \quad (4.7.72)$$

$$\frac{du_{xm}^{(2)}}{dx} = -[i\omega b_{||m}^{(2)} + \Delta_{\perp m}^{(2)}], \quad (4.7.73)$$

$$\frac{db_{||m}^{(1)}}{dx} = -\frac{i}{\omega} \sum_{n=0}^{\infty} u_{xn}^{(1)} [\omega^2 / \hat{v}_A^2(x) - \omega_n^2] \left\langle \frac{\phi_n(z)}{v_A^2(0, z)}, \phi_m(z) \right\rangle, \quad (4.7.74)$$

$$\frac{db_{||m}^{(2)}}{dx} = -\frac{i}{\omega} \sum_{n=0}^{\infty} u_{xn}^{(2)} [\omega^2 / \hat{v}_A^2(x) - \varpi_n^2] \left\langle \frac{\varphi_n(z)}{v_A^2(0, z)}, \varphi_m(z) \right\rangle, \quad (4.7.75)$$

$$\Delta_{\perp m}^{(1)} = \frac{i\omega}{\omega^2 / \hat{v}_A^2 - \omega_m^2} \sum_{n=0}^{\infty} b_{||n}^{(1)} \left\langle v_A^2(0, z) \nabla_{\perp}^{\prime 2} \phi_n, \phi_m \right\rangle + b_{||n}^{(2)} \left\langle v_A^2(0, z) \nabla_{\perp}^{\prime 2} \varphi_n, \phi_m \right\rangle, \quad (4.7.76)$$

$$\Delta_{\perp m}^{(2)} = \frac{i\omega}{\omega^2 / \hat{v}_A^2 - \varpi_m^2} \sum_{n=0}^{\infty} b_{||n}^{(1)} \left\langle v_A^2(0, z) \nabla_{\perp}^{\prime 2} \phi_n, \varphi_m \right\rangle + b_{||n}^{(2)} \left\langle v_A^2(0, z) \nabla_{\perp}^{\prime 2} \varphi_n, \varphi_m \right\rangle. \quad (4.7.77)$$

This is a set of ODEs which we can solve as an initial value problem in x using `solve_ivp` in [Virtanen et al. \(2020\)](#). However, for numerical reasons only a finite number of terms can be calculated. Therefore, we truncate the summations after a finite number of terms/harmonics, N_h .

The Alfvén speed x -dependence is given by

$$\hat{v}_A(x) = 1 + \frac{x}{a_0}. \quad (4.7.78)$$

where $a_0 = a(0)$ is a constant which controls the Alfvén speed length scale in x . From Equation (4.7.46), we can calculate $x_{res,m}$ locations using

$$\hat{v}_A(x_{res,m}) = \frac{\omega}{\omega_m}. \quad (4.7.79)$$

This implies that

$$x_{r,m} = a_0 \left(\frac{\omega_r}{\omega_m} - 1 \right), \quad (4.7.80)$$

$$x_{i,m} = a_0 \frac{\omega_i}{\omega_m}. \quad (4.7.81)$$

We set $v_{A-} = v_{A+}/21$ and $\omega_r = \omega_{11}$. Using Equation (4.7.29) we know that

$$\omega_{11} = \pi \frac{v_{A+}}{L_z} \cos \alpha. \quad (4.7.82)$$

Hence, $x_{r,11} = 0$ and $x_{i,11} = a_0 \omega_i / \omega_{11}$.

The boundary conditions in x are

$$u'_x(x_{min}, z) = -u_0 x_{i,11} \ln(X_{11}) \nabla'_\perp \phi_{11}(z), \quad (4.7.83)$$

$$\nabla'_\perp \hat{b}'_{||}(x_{min}, z) = 2iu_0 \frac{\omega x_{i,11}}{a_0 v_A^2(0, z)} \phi_{11}(z), \quad (4.7.84)$$

where

$$X_{11} = \frac{x_{i,11}}{x - ix_{i,11}}, \quad (4.7.85)$$

$k_\perp L_z / \sin \alpha \neq n\pi$ for $n \in \mathbb{Z}$ to ensure $\hat{b}'_{||}(x_{min}, z)$ is uniquely determined by Equation (4.7.84). To calculate $u_{xn}^{(1)}(x_{min})$, $u_{xn}^{(2)}(x_{min})$, $b_{||n}^{(1)}(x_{min})$, $b_{||n}^{(2)}(x_{min})$, for $n = 0, 1, 2, \dots, N_h$ we take the inner product of $u'_x(x_{min}, z)$ and $\hat{b}'_{||}(x_{min}, z)$ with ϕ_n and φ_n .

To check that the numerical solutions agree with the analytic solutions given by Equations (4.7.56), (4.7.58) and (4.7.63) and to help visualise the solutions, we plot the

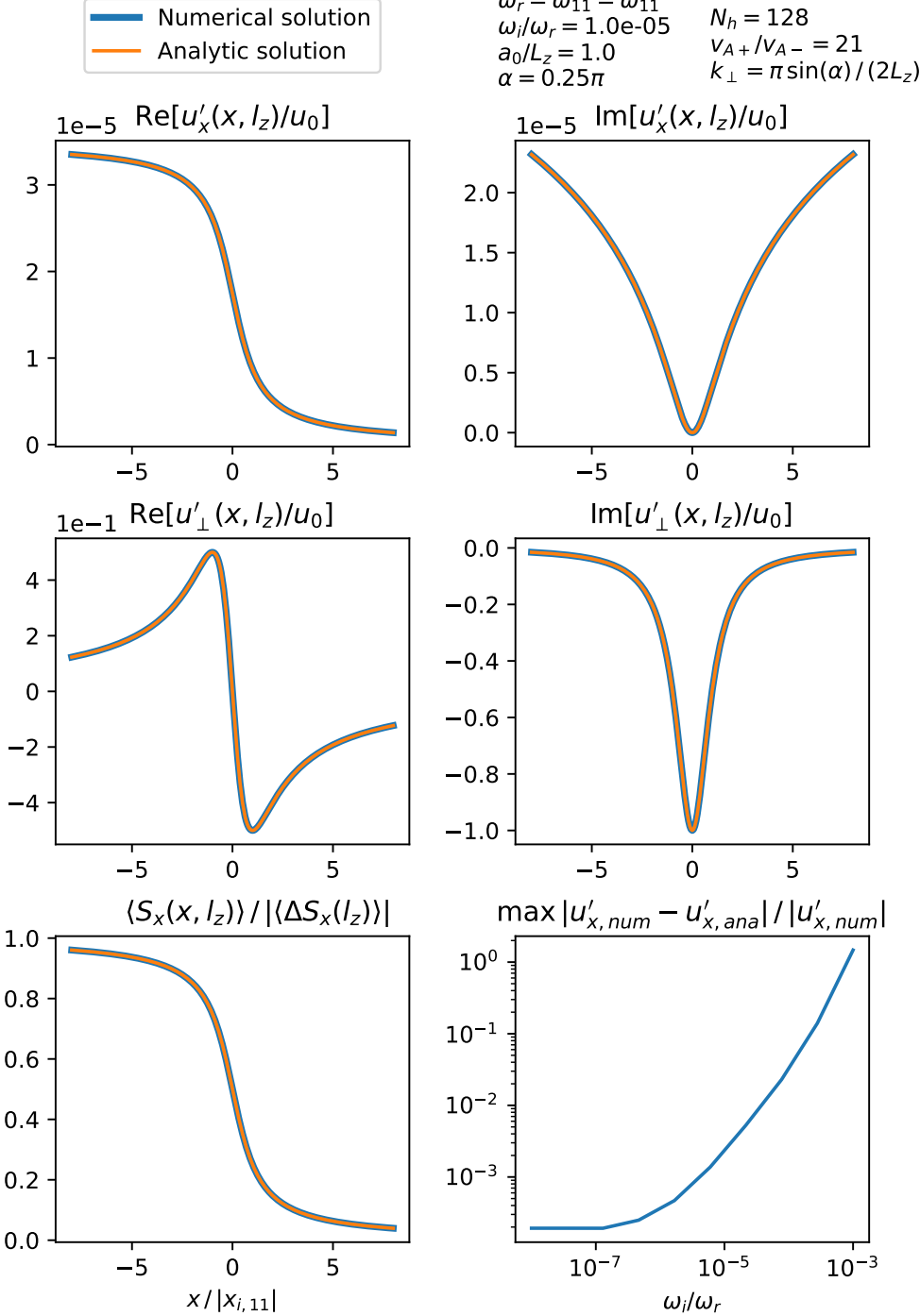


Figure 4.9: This figure shows plots of the real and imaginary parts of u'_x (top row), u'_\perp (middle row) and $\langle S'_x \rangle$ (bottom left) as a function of x at $z = l_z$. We calculated the blue curves numerically and the orange curves plot Equations (4.7.56), (4.7.58) and (4.7.63). The bottom right plot shows the relative error between the numerical and analytic solutions for u_x as a function of ω_i/ω_r . The velocity curves are normalised by u_0 which gives the amplitude of u_\perp at $x = 0$. The Poynting flux is normalised by $|\langle \Delta S'_x \rangle|$ at $z = l_z$ (see Equation (4.7.64)). The code used to make this figure is available on GitHub in the following directory:

→ [Python/Chapter4/spectral_code/line_along_x.py](#)

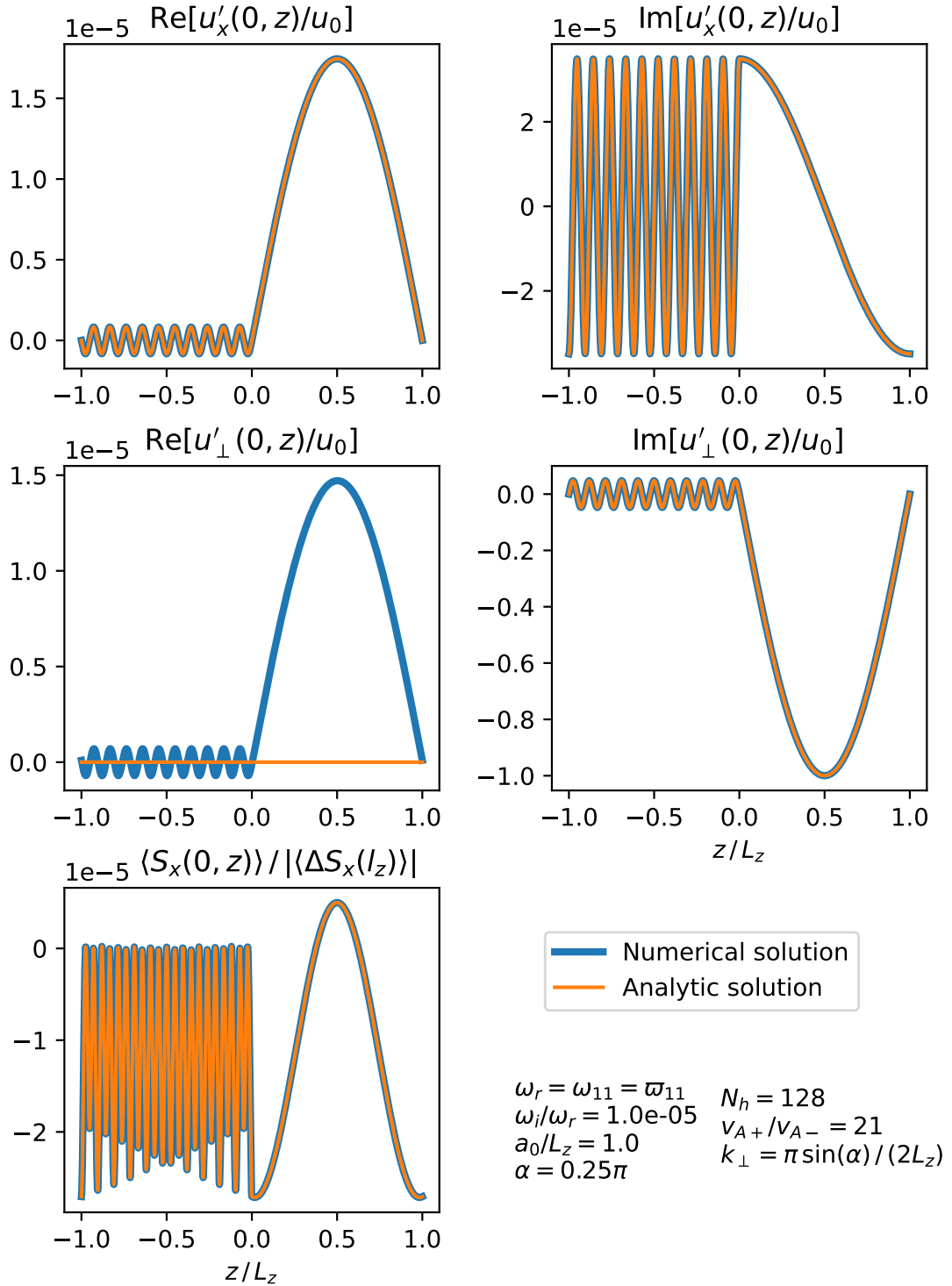


Figure 4.10: This figure is similar to Figure 4.9 except it plots the variables as function of z at $x = 0$ instead. The code used to make this figure is available on GitHub in the following directory:

→ [Python/Chapter4/spectral_code/line_along_z.py](#)

solutions in Figure 4.9 and 4.10. They show that the analytic and numerical solutions do agree provided ω_i/ω_r is small enough. The bottom right of the Figure 4.9 shows the maximum relative error between the numerical and analytic solutions for u_x' , which is given by

$$\text{max relative } u_x' \text{ error} = \max_{\substack{-8|x_{i,11}| \leq x \leq 8|x_{i,11}| \\ -L_z \leq z \leq L_z}} \left| \frac{u_{x,num}' - u_{x,ana}'}{u_{x,num}'} \right|, \quad (4.7.86)$$

where $u_{x,num}'$ denotes the u_x' solution which was calculated numerically and $u_{x,ana}'$ was calculated analytically using Equation (4.7.58). The bottom right of the Figure 4.9 shows that decreasing ω_i/ω_r causes the error to decrease. This plot appears to be converging to a non-zero value and this is because the numerical solution only uses a finite number of harmonics N_h . Increasing N_h acts to reduce the error further. Figure 4.10 shows that although the amplitude of u_\perp may decrease significantly in the chromosphere, this is not necessarily true for u_x . Equation (4.6.44) also shows that u_x in the chromosphere will not necessarily go to zero, even if $v_{A-} \rightarrow 0$. This suggests that imposing line-tied ($\mathbf{u} = 0$) boundary conditions at the edge of the corona will lead to the generation of unphysical structures. The usual justification for imposing line-tied boundary conditions is that the chromosphere is significantly denser than the corona and so it acts like a solid wall. Here, $v_{A+}/v_{A-} = 21$ and yet u_x is showing no signs of going to zero in the chromosphere. Although u_x does not go to zero, the kinetic energy and magnetic energy is dominated by u_\perp and b_\perp , therefore, the kinetic and magnetic energy is approximately uniformly distributed along z .

4.8 Summary and conclusions

The first results we presented in this chapter were shown in Section 4.3. We showed that oscillations in the x and $\hat{\mathbf{B}}_0$ directions couple to the oscillations in the \perp -direction due to gradients in the magnetic pressure perturbation, $B_0 b_{\parallel}/(2\mu)$. Resonant absorption occurs where the mode conversion is one-way from fast wave perturbations to Alfvén waves.

In Section 4.4 our goal was to introduce resonant absorption by using a model which was as simple as possible whilst complex enough to show some of its key properties.

For simplicity, we chose the background magnetic field to be at right-angles to the $z = \text{constant}$ plane, i.e. $\alpha = 0$ and the background Alfvén speed to be a function of just x . We calculated the normal mode solutions and derived a single ODE which u_y satisfies, see Equation (4.4.27). To solve the ODE we used method of Frobenius and showed that the solution can become singular at resonant locations $x_{res,n}$ where $\mathcal{L}_n(x_{res,n}) = 0$, i.e. at locations where the Alfvén wave equation is satisfied. This shows that resonant absorption occurs at locations where the frequency of the driver equals the natural Alfvén frequency of a field line. We calculated the leading order approximations of the singular solutions and verified these numerically via a graphical approach in Figure 4.2.

In Section 4.5 we showed how Alfvén waves propagating from the corona to the chromosphere mode convert at the transition region to form fast waves. If

$$k_x \geq \text{Re} \left(\sqrt{k_{\parallel 0}^2 - k_y^2} \right),$$

then the fast waves are evanescent in the corona and will form boundary layers at the transition region (see Figures 4.5 and 4.6). This phenomenon has been shown in for example, [Halberstadt and Goedbloed \(1993, 1995\)](#); [Arregui et al. \(2003\)](#). To simulate the conditions near a singularity in a resonant absorption experiment, we calculated asymptotic expansions for $k_x/k_{\parallel+} \rightarrow \infty$ (see Equations 4.5.21-4.5.35). They show that the boundary layers do not form if the magnetic field is normal to the transition region, i.e. if $\alpha = 0$.

After that, we tested the validity of line-tied boundary conditions by checking if these boundary layers still form if a piecewise constant background Alfvén speed with continuity of \mathbf{u} and $d\mathbf{u}/dz$ is imposed instead (see Section 4.6). We believe we are the first authors to test line-tied boundary conditions in this way. The results (see Figures 4.5-4.7) suggest that line-tied boundary conditions provide a good approximation provided the fast waves can propagate in the chromosphere, i.e.

$$k_x \leq \text{Re}(\sqrt{k_{\parallel-}^2 - k_y^2}).$$

However, if the fast waves are evanescent in the chromosphere, i.e.

$$k_x \geq \text{Re}(\sqrt{k_{\parallel-}^2 - k_y^2}).$$

then line-tied boundary conditions will overestimate the size of the boundary layers by a factor of the order $k_x/k_{\parallel-}$. If $k_x \gg k_{\parallel-}$ then Equations (4.6.44)-(4.6.68) approximate the solution, however, if $k_{\parallel+} \ll k_x \ll k_{\parallel-}$ then the line-tied solutions (Equations 4.5.21-4.5.35) provide a better approximation. We estimated that if the Alfvén waves are able to phase-mix to the shortest length scales allowed by the resistivity and viscosity in the corona then the $k_x \gg k_{\parallel-}$ is usually most appropriate limit. However, during the early stages, before the waves have phase-mixed, $k_x \ll k_{\parallel-}$ is the most valid limit. Future work could investigate the solutions with an exponential background density instead of our piecewise-constant background density. This may allow us to calculate a condition which k_x must satisfy which is dependent on the pressure scale height rather than on $k_{\parallel-}$.

The results from Section 4.6 suggest that the fast wave component of the velocity should go to zero near singular locations in a resonant absorption experiment since $k_x \rightarrow \infty$ approaching the singularity. In the final section (Section 4.7), we tested this by calculating the normal mode resonant absorption solution in a domain where the background Alfvén speed is a function of x and piecewise constant in z . We used periodic boundary condition in z for convenience and because this simulates a loop which goes from the corona to the chromosphere then back to the corona and so on. In Section 4.7.3 we calculated the leading order singular solutions near a resonant location analytically. In Figures 4.9 and 4.10 we plot the analytic and numerical solutions together and show that they agree. We verified that to leading order, u_x and u_{\perp} do not contain any boundary layers near the singularity. This confirms that imposing line-tied boundary conditions can cause the model to significantly overestimate the amplitude of the boundary layers. However, in Section 4.6 we showed as $k_x \rightarrow \infty$ the amplitude of the boundary layers does not increase. This suggests that the boundary layers have a limited effect on the rate at which the resonant absorption occurs. Moreover, since the boundary layers are evanescent, they cannot directly transport energy away.

In conclusion, Alfvén waves will (in general) mode convert to form fast waves at the transition region. The fast waves can be evanescent or can propagate depending on the value of $\mathbf{k} \cdot \mathbf{k} - \omega^2/v_A^2$. We have demonstrated that line-tied boundary conditions can be more problematic than many authors realise. If k_x grows large enough such that it causes the fast waves in the chromosphere to be evanescent, then the line-tied model will fail to reduce the size of the boundary layers accurately. We believe that

few authors are aware of this because it is quite counter-intuitive that k_x (which gives the length-scales in a direction tangential to the chromosphere/corona interface) can be important in determining the validity of line-tied boundary conditions. Increasing k_x can result in the line-tied model greatly overestimating the amplitude of the boundary layers by approximately a factor $k_x/k_{\parallel -}$. With that in mind, we believe authors should continue to use line-tied boundary conditions for their simplicity and ability to reduce computation time, provided that their flaws are understood. For example, we have shown that line-tied boundary conditions provide a good approximation (with an error of the order v_{A-}/v_{A+}) if the fast waves can propagate in the chromosphere. If the fast waves are evanescent in the chromosphere, then line-tied boundary conditions are less useful. However, sometimes this won't be important. For example, when studying energetics, as the boundary layers are evanescent and cannot transport energy away. Moreover, we showed in Section 4.5 that their energy does not grow as $k_x \rightarrow \infty$.

Chapter 5

Conclusions and future work

This thesis used mathematical models to develop our understanding of MHD waves in the solar corona. We chose our models to be complex enough to allow the phenomena we are interested in to be studied and simple enough to be easily understood. We calculated analytic solutions and then verified many of these results numerically by comparing them side-by-side using graphs. The work presented here may play a role in solving the coronal heating problem and developing coronal seismology.

Chapter 2 introduced some of the key concepts relevant to the rest of this thesis. We modelled linear ideal Alfvén waves which we injected into the corona by using a footpoint driver. The waves were modelled as perturbations on a uniform background magnetic field and Alfvén speed. To begin with, we used a sinusoidal driver in a closed loop and found that the form of the solution was highly dependent on the driver frequency. If the driver frequency equalled one of the natural Alfvén frequencies of the loop, then resonance occurred. This meant that the energy grew quadratically with time. If the driver frequency was not equal to a natural frequency, then the energy oscillated about a finite value at the beating frequency (which goes to zero as the driver frequency tends towards natural frequencies). We showed that a white and red noise force driver causes the energy to grow linearly with time on average. A white noise driver is a random driver which excites all frequencies with equal force, and a red noise driver has a power spectrum which goes as f^{-2} , where f denotes frequency. In Section 2.5.3 we give a more precise definitions. Observational evidence (see Figure 1.6) suggests the power spectrum slope for waves in the corona lies somewhere in between f^{-2} and f^0 . We also considered the case where the waves were partially confined in a leaky

loop where a fraction $R < 1$ of the incident wave amplitude reflects at the boundary. We used a sinusoidal driver and found that leakage prevents energy of the system from growing to infinity, and the system converges towards a steady-state. At steady-state, the amplitude of the waves is fixed, and the system oscillates at the driver frequency. Note that a system will also converge towards a steady-state if resistivity or viscosity is included in the model.

In Chapter, 3 our goal was to answer whether the dissipation of phase-mixed Alfvén waves plays an essential or negligible role in coronal heating. To achieve this goal, we introduced a term called the damping rate per unit of wave energy which we denote γ . We estimated that for phase mixing to be a viable heating mechanism then our phase mixing model needs to have a γ of about 10^{-1} s^{-1} . We are careful to ensure any simplifications we make act to increase γ , which means our calculation for γ is an upper bound. For example, we assume the system is at steady-state which acts to increase γ , in Arregui (2015) they argue that Alfvén waves may not have time to reach steady-state due to thermodynamic changes in the loop. We first introduced phase mixing in an open-loop and calculated the analytic solution using the method of multiple scales. Neighbouring field lines had different natural frequencies, which meant steep gradients formed perpendicular to the velocity and magnetic fields. After that, we modelled a closed-loop and extended our solution for the open-loop using a method of images approach to calculate the analytic solution. We included leakage into the model and found that this acts to reduce γ . The results from this chapter suggest that the dissipation of the gradients produced by phase mixing plays a negligible role in coronal heating. However, it is possible that phase mixing plays a less direct role; for example, it could trigger the Kelvin-Helmholtz and tearing mode instabilities which cause a turbulent cascade. In this case, the dissipation will occur primarily due to gradients parallel to the velocity and magnetic fields because the $\mathbf{W}^{(0)}$ component of the viscosity tensor will dominate. Note that the gradients formed by phase mixing are perpendicular to the velocity field and magnetic field.

In the resonant absorption literature, authors typically assume the background magnetic field is perpendicular to the transition region. Halberstadt and Goedbloed (1993, 1995); Arregui et al. (2003) use line-tied boundary conditions in their resonant absorption models to show that if the background magnetic field is oblique to the transition region then steep boundary layers/evanescent fast waves can form. The goal in Chapter

4 was to check that these boundary layers are physical and not a result of approximating the steep jump in density from the corona to the chromosphere with line-tied boundary conditions. To test this, we first introduced resonant absorption in a model where the background field is normal to the transition region and the Alfvén speed was purely a function of x to show some of the key properties of resonant absorption. We showed resonant absorption occurs where the frequency of the incoming fast waves equals the natural Alfvén frequency of a resonant field line resulting in the formation of singularities at discrete x -coordinates. At the singularities, the mode conversion from fast waves to Alfvén waves is one-way and is caused by gradients in the magnetic pressure. After that, we modified the model to let the background Alfvén speed be uniform in x and piecewise constant in z , where $z > 0$ models the corona and $z < 0$ corresponds to the chromosphere. This meant resonant absorption could not occur. However, we derived dispersion relations and simulated the singularities which would form in a resonant absorption experiment by letting $k_x \rightarrow \infty$. We used an asymptotic expansion to express the solutions in a simpler form for $k_x \rightarrow \infty$. If line-tied boundary conditions are used then u_x to leading order contains a steep evanescent fast wave/boundary layer term to leading order. However, if the chromosphere is included in the model then the steep boundary layers do not appear in the leading order expansion for u_x . This suggests that imposing line-tied boundary conditions can cause the model to significantly overestimate the amplitude of the boundary layers. Finally, we extended the model to let the Alfvén speed have an x -dependence. By using an eigenfunction approach we showed that near singularity/resonant location the boundary layers are not present to leading order. This helps to confirm that line-tied boundary conditions can cause significant overestimation of the size of the boundary layers. However, line-tied boundary conditions can still be useful in future models for their simplicity, provided their limitations are understood. In the future, we would like to compare resonant absorption experiments where line-tied boundary conditions and where the chromosphere is included in the model to precisely quantify the effects of imposing line-tied boundary conditions in a resonant absorption experiment. Also, we would like to extend our results from the Cartesian coordinate system to a cylindrical coordinate system as this can more easily be applied to coronal loops.

This thesis focused on improving our understanding of MHD waves and pushing the boundaries of our current knowledge. We hope that results from the work presented

here lead to developments in coronal seismology. In the future, we aim to apply contemporary MHD wave theory to observational data to infer approximate values for difficult to measure quantities, e.g. the magnetic field strength and density (see [Mathioudakis et al. 2013](#)). Calculating the values of quantities in the corona could lead to significant developments in explaining the observed dynamics and may present us with new puzzles to solve. With ever-improving computational power and observational instruments, coronal seismology is becoming an increasingly important and relevant area of research. For coronal seismology to become more widely used, we need to develop more user-friendly code and software to automate much of the process. We hope to create software and code that enables users to estimate quantities using coronal seismology quickly. Ideally, the code and software would be easy to use such that the user does not need extensive knowledge of MHD wave theory to estimate the desired quantities.

Another suggestion for future work is to investigate if the viscous dissipation of fast waves plays a significant role in the quiet sun. In [Withbroe and Noyes \(1977\)](#); [Parker \(1991\)](#) they suggest that the waves need to dissipate over a length scale of 1 or 2 solar radii to heat the corona. In Appendix A, we use a simple toy model to show that the fast waves can dissipate over short enough length-scales. However, we make many simplifications and so a more extensive analysis is required.

It has been a privilege to have had this opportunity to contribute towards solar physics research. We hope that the readers found this thesis interesting and useful for developing their understanding of solar/plasma physics. Acquiring a better knowledge of solar/plasma physics at a theoretical level may play a key role in solving problems such as the coronal heating problem which could reveal new and exciting problems which need to be solved. Developments in coronal heating could lead to results in other areas such as nuclear fusion due to our improved understanding of plasma physics. Finally, it could be relevant for space weather prediction, which is increasingly important with our ever-increasing dependence on orbital satellites.

Appendix A

Coronal heating by viscous fast waves

In this appendix, we expand upon a proposed topic for further research mentioned in Chapter 5. Namely, the possibility that the viscous dissipation of fast waves plays a major role in coronal heating. We will present a simple toy model to show our proposal's plausibility and then discuss how to investigate this rigorously in the future.

A.1 Model and assumptions

In this section, we will describe the model we will use. Our domain is designed to approximate the quiet sun conditions near the equator. We model perturbations on a static background equilibrium and make the same assumptions as those described by Equation (1.4.3)-(1.4.5). The plasma is modelled as cold, i.e. $\beta = 0$, which means the magnetic pressure force is negligible. We assume the Lorentz force dominates and neglect the gravitational force. Our background quantities are assumed to be uniform with the background magnetic field pointing south to north and approximately tangential to the solar surface at the equator,

$$\mathbf{B}_0 = B_0 \hat{\mathbf{z}}, \tag{A.1.1}$$

The $\hat{\mathbf{x}}$ direction points radially outwards from the solar surface.

We model the linearised momentum equation as

$$\frac{\partial \mathbf{u}}{\partial t} = v_A^2 \left[\frac{\partial \hat{\mathbf{b}}}{\partial z} - \nabla \cdot \hat{\mathbf{b}}_z \right] + \frac{1}{\rho} \nabla \cdot \boldsymbol{\pi}_0, \quad (\text{A.1.2})$$

and the linearised induction equations as

$$\frac{\partial \hat{\mathbf{b}}}{\partial t} = \frac{\partial \mathbf{u}}{\partial z} - \nabla \cdot \mathbf{u} \hat{\mathbf{z}}, \quad (\text{A.1.3})$$

where $\boldsymbol{\pi}_0$ denotes the linearised viscosity tensor (see Equation 1.3.23) and

$$\hat{\mathbf{b}} = \frac{\mathbf{b}}{B_0}. \quad (\text{A.1.4})$$

We assume $\omega_{ci}/\nu_i \ll 1$ and neglect the $\mathbf{W}^{(1)}, \mathbf{W}^{(2)}, \mathbf{W}^{(3)}, \mathbf{W}^{(4)}$ terms. Mocanu et al. (2008) shows that the linearised viscosity tensor is given by

$$\begin{aligned} \boldsymbol{\pi}_0 &= \eta_0 \left(\hat{\mathbf{B}}_0 \otimes \hat{\mathbf{B}}_0 - \frac{1}{3} \mathbf{I} \right) Q \\ &= \frac{\eta_0}{3} \begin{pmatrix} -1 & 0 & 0 \\ 0 & -1 & 0 \\ 0 & 0 & 2 \end{pmatrix} Q, \end{aligned} \quad (\text{A.1.5})$$

where η_0 is given by Equation (1.3.31) and

$$\hat{\mathbf{B}}_0 = \frac{\mathbf{B}_0}{B_0}, \quad (\text{A.1.6})$$

$$Q = 3 \hat{\mathbf{B}}_0 \cdot \nabla (\hat{\mathbf{B}}_0 \cdot \mathbf{u}) - \nabla \cdot \mathbf{u} \quad (\text{A.1.7})$$

We will assume our variables are of the form

$$f(x, t) = f_0 \exp[i(k_x x + \omega t)], \quad (\text{A.1.8})$$

where $\omega \in \mathbb{R}^+$ and $k_x \in \mathbb{C}$. This simulates waves, propagating/decaying radially outwards/inwards from the solar surface at the equator. Enforcing $\partial/\partial y = \partial/\partial z = 0$

causes

$$\frac{\partial}{\partial t} \mathbf{u} \cdot \hat{\mathbf{y}} = \frac{\partial}{\partial t} \mathbf{u} \cdot \hat{\mathbf{z}} = \frac{\partial}{\partial t} \hat{\mathbf{b}} \cdot \hat{\mathbf{z}} = \frac{\partial}{\partial t} \hat{\mathbf{b}} \cdot \hat{\mathbf{y}} = 0$$

and we let

$$\mathbf{u} = u_x \hat{\mathbf{x}}, \quad (\text{A.1.9})$$

$$\hat{\mathbf{b}} = \hat{b}_z \hat{\mathbf{z}}. \quad (\text{A.1.10})$$

Hence,

$$Q = -\frac{\partial u_x}{\partial x}, \quad (\text{A.1.11})$$

$$\frac{\partial u_x}{\partial t} = -v_A^2 \frac{\partial \hat{b}_z}{\partial x} + \nu_0 \frac{\partial^2 u_x}{\partial x^2}, \quad (\text{A.1.12})$$

$$\frac{\partial \hat{b}_z}{\partial t} = -\frac{\partial u_x}{\partial x}. \quad (\text{A.1.13})$$

We model the system as weakly viscous and assume that

$$\begin{aligned} \epsilon &= \frac{\nu_0 \omega}{v_A^2} \\ &\approx 1.13 \times 10^{-1} \left(\frac{\ln \Lambda}{20} \right)^{-1} \left(\frac{T}{3 \times 10^6 \text{ K}} \right)^{5/2} \left(\frac{\rho}{10^{-13} \text{ kg m}^{-3}} \right)^{-1} \\ &\quad \left(\frac{\omega}{\pi \times 10^{-2} \text{ s}^{-1}} \right) \left(\frac{v_A}{4 \times 10^5 \text{ m s}^{-1}} \right)^{-2} \end{aligned} \quad (\text{A.1.14})$$

$\ll 1$.

A.2 Damping length

In Withbroe and Noyes (1977); Parker (1991) they suggest that the waves need to decay on a length scale of $1-2R_\odot$ to play a significant role in coronal heating, where R_\odot denotes the solar radius. This section aims to derive a dispersion relation for the waves in our model to calculate a damping length. Taking the time derivative of

(A.1.12) to eliminate \hat{b}_z gives

$$\frac{\partial^2 u_x}{\partial t^2} = v_A^2 \frac{\partial^2 u_x}{\partial x^2} + \nu_0 \frac{\partial}{\partial t} \frac{\partial^2 u_x}{\partial x^2}. \quad (\text{A.2.1})$$

Dividing through by v_A^2 and assuming u_x is of the form given by Equation (A.1.8) gives

$$\frac{\omega^2}{v_A^2} = (1 + i\epsilon)k_x^2. \quad (\text{A.2.2})$$

Using the binomial expansion gives

$$k_x^2 = \frac{\omega^2}{v_A^2} [1 - i\epsilon + O(\epsilon^2)]. \quad (\text{A.2.3})$$

We assume k_x is given by the negative root as the waves propagate away from the solar surface in the positive x -direction. Hence,

$$k_x = -\frac{\omega}{v_A} \left[1 - \frac{1}{2}i\epsilon + O(\epsilon^2) \right]. \quad (\text{A.2.4})$$

The decay length-scale is given by

$$\begin{aligned} L_d &= \frac{2\pi}{\text{Im}(k_x)} \\ &\approx 4\pi \frac{1}{\epsilon} \frac{v_A}{\omega} \\ &= 4\pi \left(\frac{1}{\nu_0} \right) \frac{v_A^3}{\omega^2} \\ &= 4\pi \left(\frac{3}{2.21} \times 10^{16} \ln \Lambda T^{-5/2} \rho \right) \frac{v_A^3}{\omega^2} \\ &\approx 1.42 \times 10^9 \left(\frac{\ln \Lambda}{20} \right) \left(\frac{T}{3 \times 10^6 \text{ K}} \right)^{-5/2} \left(\frac{\rho}{10^{-13} \text{ kg m}^{-3}} \right) \left(\frac{v_A}{4 \times 10^5 \text{ m s}^{-1}} \right)^3 \\ &\quad \left(\frac{\omega}{\pi \times 10^{-2} \text{ s}^{-1}} \right)^{-2} \text{ m}, \end{aligned} \quad (\text{A.2.5})$$

Equation (A.2.5) suggests that for typical coronal values, it is possible for fast waves to decay on a length-scale of about 2 solar radii, $R_\odot \approx 7 \times 10^8 \text{ m}$. Our values for the

density and Alfvén speed were chosen by using mean observed values and were taken from Table 1 in Morton et al. (2016). Figure 1.6 shows that we chose a high frequency (where $\omega = 2\pi f$) and we discuss this further in the next section.

A.3 Discussion

We have shown that our model can dissipate fast waves on a length-scale of about 2 solar radii, and this suggests that this mechanism could play a significant role in coronal heating. However, we made many simplifications in our analysis, and it is unclear if relaxing these assumptions will increase or decrease the damping length. For example, we modelled the quantities as uniform and linear. This meant waves could not reflect and prevents reflection-driven turbulence (Hollweg, 1986a; van Ballegooijen et al., 2011; Shoda et al., 2019). Authors typically study Alfvén wave turbulence, but we think it could be interesting to investigate fast wave turbulence as these are compressible and therefore dissipate via viscosity more easily. We used a high frequency in (A.2.5) to account for the fact that waves may be able to cascade to higher frequencies due to turbulence. Including a more complex field can lead to several effects such as fast wave refraction towards null points (McLaughlin and Hood, 2006; McLaughlin et al., 2011; McLaughlin, 2016), the triggering of reconnection (McLaughlin et al., 2009) and enhanced phase mixing (Similon and Sudan, 1989; Howson et al., 2020). We modelled the fast waves as propagating perpendicular to the field, in reality a component will propagate parallel and this could decrease the heating. Therefore, we would expect less heating at coronal holes where the field is approximately normal to the solar surface. In summary, the results provided here suggest further study could be fruitful. However, a more extensive analysis is needed to determine if the viscous dissipation of fast waves plays a significant role in coronal heating.

Bibliography

- Afanasyev, A. N., T. Van Doorsselaere, and V. M. Nakariakov (2020, January). Excitation of decay-less transverse oscillations of coronal loops by random motions. *Astronomy & Astrophysics* 633, L8.
- Alfvén, H. (1942, October). Existence of Electromagnetic-Hydrodynamic Waves. *Nature* 150(3805), 405–406.
- Antiochos, S. K., P. J. MacNeice, and D. S. Spicer (2000, Jun). The Thermal Nonequilibrium of Prominences. *The Astrophysical Journal* 536(1), 494–499.
- Antolin, P., I. De Moortel, T. Van Doorsselaere, and T. Yokoyama (2016, October). Modeling Observed Decay-less Oscillations as Resonantly Enhanced Kelvin-Helmholtz Vortices from Transverse MHD Waves and Their Seismological Application. *The Astrophysical Journal Letters* 830(2), L22.
- Antolin, P., D. Schmit, T. M. D. Pereira, B. De Pontieu, and I. De Moortel (2018, March). Transverse Wave Induced Kelvin-Helmholtz Rolls in Spicules. *The Astrophysical Journal* 856(1), 44.
- Antolin, P. and K. Shibata (2010, March). The Role Of Torsional Alfvén Waves in Coronal Heating. *The Astrophysical Journal* 712(1), 494–510.
- Arregui, I. (2015, April). Wave heating of the solar atmosphere. *Philosophical Transactions of the Royal Society of London Series A* 373(2042), 20140261–20140261.
- Arregui, I., R. Oliver, and J. L. Ballester (2003, May). Coupling of fast and Alfvén waves in a straight bounded magnetic field with density stratification. *Astronomy & Astrophysics* 402, 1129–1143.

BIBLIOGRAPHY

- Banerjee, D., R. Erdélyi, R. Oliver, and E. O’Shea (2007, November). Present and Future Observing Trends in Atmospheric Magnetoseismology. *Solar Physics* 246(1), 3–29.
- Braginskii, S. I. (1965). Transport processes in a plasma. *Reviews of Plasma Physics* 1, 205–311.
- Browning, P. K. and E. R. Priest (1984, February). Kelvin-Helmholtz instability of a phased-mixed Alfvén wave. *Astronomy & Astrophysics* 131(2), 283–290.
- Bruno, R. and V. Carbone (2013, May). The Solar Wind as a Turbulence Laboratory. *Living Reviews in Solar Physics* 10(1), 2.
- Cally, P. S. and S. C. Hansen (2011, September). Benchmarking Fast-to-Alfvén Mode Conversion in a Cold Magnetohydrodynamic Plasma. *The Astrophysical Journal* 738(2), 119.
- Cargill, P. and I. De Moortel (2011, July). Solar physics: Waves galore. *Nature* 475, 463–464.
- Cargill, P. J., I. De Moortel, and G. Kiddie (2016, May). Coronal Density Structure and its Role in Wave Damping in Loops. *The Astrophysical Journal* 823(1), 31.
- Cohen, R. H. and R. M. Kulsrud (1974, December). Nonlinear evolution of parallel-propagating hydromagnetic waves. *Physics of Fluids* 17, 2215–2225.
- Cranmer, S. R. (2018, July). Low-frequency Alfvén Waves Produced by Magnetic Reconnection in the Sun’s Magnetic Carpet. *The Astrophysical Journal* 862(1), 6.
- Cranmer, S. R. and A. A. van Ballegooijen (2005, February). On the Generation, Propagation, and Reflection of Alfvén Waves from the Solar Photosphere to the Distant Heliosphere. *The Astrophysical Journal Supplement Series* 156(2), 265–293.
- De Moortel, I., A. W. Hood, and T. D. Arber (2000, February). Phase mixing of Alfvén waves in a stratified and radially diverging, open atmosphere. *Astronomy & Astrophysics* 354, 334–348.

BIBLIOGRAPHY

- De Moortel, I. and V. M. Nakariakov (2012, July). Magnetohydrodynamic waves and coronal seismology: an overview of recent results. *Philosophical Transactions of the Royal Society of London Series A* 370(1970), 3193–3216.
- Dere, K. P., E. Landi, P. R. Young, G. Del Zanna, M. Landini, and H. E. Mason (2009, May). CHIANTI - an atomic database for emission lines. IX. Ionization rates, recombination rates, ionization equilibria for the elements hydrogen through zinc and updated atomic data. *Astronomy & Astrophysics* 498(3), 915–929.
- Elsden, T. and A. N. Wright (2017, March). The theoretical foundation of 3-D Alfvén resonances: Time-dependent solutions. *Journal of Geophysical Research (Space Physics)* 122(3), 3247–3261.
- Elsden, T. and A. N. Wright (2018, January). The Broadband Excitation of 3-D Alfvén Resonances in a MHD Waveguide. *Journal of Geophysical Research (Space Physics)* 123(1), 530–547.
- Feynman, J. and S. B. Gabriel (2000, May). On space weather consequences and predictions. *Journal of Geophysical Research* 105(A5), 10543–10564.
- Gary, G. A. (2001, Oct). Plasma Beta above a Solar Active Region: Rethinking the Paradigm. *Solar Physics* 203(1), 71–86.
- Giagkiozis, I., M. Goossens, G. Verth, V. Fedun, and T. Van Doorsselaere (2016, June). Resonant Absorption of Axisymmetric Modes in Twisted Magnetic Flux Tubes. *The Astrophysical Journal* 823(2), 71.
- Goedbloed, J. P. and G. Halberstadt (1994, June). Magnetohydrodynamic waves in coronal flux tubes. *Astronomy & Astrophysics* 286, 275–301.
- Goossens, M., R. Erdélyi, and M. S. Ruderman (2011, July). Resonant MHD Waves in the Solar Atmosphere. *Solar Science Reviews* 158, 289–338.
- Halberstadt, G. and J. P. Goedbloed (1993, December). The continuous Alfvén spectrum of line-tied coronal loops. *Astronomy & Astrophysics* 280(2), 647–660.
- Halberstadt, G. and J. P. Goedbloed (1995, September). Alfvén wave heating of coronal loops: photospheric excitation. *Astronomy & Astrophysics* 301, 559.

BIBLIOGRAPHY

- Hansen, S. C. and P. S. Cally (2012, May). Benchmarking Fast-to-Alfvén Mode Conversion in a Cold MHD Plasma. II. How to Get Alfvén Waves through the Solar Transition Region. *The Astrophysical Journal* 751(1), 31.
- Heyvaerts, J. and E. R. Priest (1983, January). Coronal heating by phase-mixed shear Alfvén waves. *Astronomy & Astrophysics* 117, 220–234.
- Hillier, A. and I. Arregui (2019, November). Coronal Cooling as a Result of Mixing by the Nonlinear Kelvin-Helmholtz Instability. *The Astrophysical Journal* 885(2), 101.
- Hogan, J. T. (1984, Sep). Collisional transport of momentum in axisymmetric configurations. *Physics of Fluids* 27(9), 2308–2312.
- Hollweg, J. V. (1984a, April). Alfvénic resonant cavities in the solar atmosphere: Simple aspects. *Solar Physics* 91(2), 269–288.
- Hollweg, J. V. (1984b, February). Resonances of coronal loops. *The Astrophysical Journal* 277, 392–403.
- Hollweg, J. V. (1986a, April). Transition region, corona, and solar wind in coronal holes. *Journal of Geophysical Research* 91(A4), 4111–4125.
- Hollweg, J. V. (1986b, Jul). Viscosity and the Chew-Goldberger-Low Equations in the Solar Corona. *The Astrophysical Journal* 306, 730.
- Hood, A. W., S. J. Brooks, and A. N. Wright (2002, October). Coronal heating by the phase mixing of individual pulses propagating in coronal holes. *Proceedings of the Royal Society of London Series A* 458(2026), 2307.
- Hood, A. W., J. Ireland, and E. R. Priest (1997, February). Heating of coronal holes by phase mixing. *Astronomy & Astrophysics* 318, 957–962.
- Hood, A. W., M. Ruderman, D. J. Pascoe, I. De Moortel, J. Terradas, and A. N. Wright (2013, March). Damping of kink waves by mode coupling. I. Analytical treatment. *Astronomy & Astrophysics* 551, A39.
- Howson, T. A., I. De Moortel, and L. E. Fyfe (2020, November). The effects of driving time scales on heating in a coronal arcade. *Astronomy & Astrophysics* 643, A85.

BIBLIOGRAPHY

- Howson, T. A., I. De Moortel, and J. Reid (2020, April). Phase mixing and wave heating in a complex coronal plasma. *Astronomy & Astrophysics* 636, A40.
- Howson, T. A., I. De Moortel, J. Reid, and A. W. Hood (2019, September). Magnetohydrodynamic waves in braided magnetic fields. *Astronomy & Astrophysics* 629, A60.
- Ionson, J. A. (1982, March). Resonant electrodynamic heating of stellar coronal loops - an LRC circuit analog. *The Astrophysical Journal* 254, 318–334.
- Johnston, C. D., P. J. Cargill, P. Antolin, A. W. Hood, I. De Moortel, and S. J. Bradshaw (2019, May). The effects of numerical resolution, heating timescales and background heating on thermal non-equilibrium in coronal loops. *Astronomy & Astrophysics* 625, A149.
- Karimabadi, H., V. Roytershteyn, M. Wan, W. H. Matthaeus, W. Daughton, P. Wu, M. Shay, B. Loring, J. Borovsky, E. Leonardis, S. C. Chapman, and T. K. M. Nakamura (2013, January). Coherent structures, intermittent turbulence, and dissipation in high-temperature plasmas. *Physics of Plasmas* 20(1), 012303.
- Kelly, P. A. (2020). Mechanics lecture notes: An introduction to solid mechanics. [Online; accessed 28-Aug-2020].
- Klimchuk, J. A. (2015, April). Key aspects of coronal heating. *Philosophical Transactions of the Royal Society of London Series A* 373, 20140256–20140256.
- Klimchuk, J. A., S. Patourakos, and P. J. Cargill (2008, Aug). Highly Efficient Modeling of Dynamic Coronal Loops. *The Astrophysical Journal* 682(2), 1351–1362.
- Kolotkov, D. Y., S. A. Anfinogentov, and V. M. Nakariakov (2016, August). Empirical mode decomposition analysis of random processes in the solar atmosphere. *Astronomy & Astrophysics* 592, A153.
- Kudoh, T. and K. Shibata (1999, March). Alfvén Wave Model of Spicules and Coronal Heating. *The Astrophysical Journal* 514(1), 493–505.
- Lide, D. R. (2003). Handbook of chemistry and physics.

BIBLIOGRAPHY

- Lockheed Martin Solar and Astrophysics Laboratory (2019). Images of the sun taken by the transition region and coronal explorer. [Online; accessed 03-Nov-2019].
- MacTaggart, D., L. Vergori, and J. Quinn (2017, September). Braginskii magnetohydrodynamics for arbitrary magnetic topologies: coronal applications. *Journal of Fluid Mechanics* 826, 615–635.
- Magyar, N., T. Van Doorsselaere, and M. Goossens (2017, November). Generalized phase mixing: Turbulence-like behaviour from unidirectionally propagating MHD waves. *Scientific Reports* 7, 14820.
- Martens, P. C. H. (2010, May). Scaling Laws and Temperature Profiles for Solar and Stellar Coronal Loops with Non-uniform Heating. *The Astrophysical Journal* 714(2), 1290–1304.
- Mathioudakis, M., D. B. Jess, and R. Erdélyi (2013, June). Alfvén Waves in the Solar Atmosphere. From Theory to Observations. *Space Science Reviews* 175(1-4), 1–27.
- McIntosh, S. W. and B. De Pontieu (2012, December). Estimating the “Dark” Energy Content of the Solar Corona. *The Astrophysical Journal* 761, 138.
- McIntosh, S. W., B. de Pontieu, M. Carlsson, V. Hansteen, P. Boerner, and M. Goossens (2011, July). Alfvénic waves with sufficient energy to power the quiet solar corona and fast solar wind. *Nature* 475, 477–480.
- McLaughlin, J. A. (2013, September). Phase Mixing of Alfvén Waves Near a 2D Magnetic Null Point. *Journal of Astrophysics and Astronomy* 34(3), 223–246.
- McLaughlin, J. A. (2016, March). Behaviour of Magnetoacoustic Waves in the Neighbourhood of a Two-Dimensional Null Point: Initially Cylindrically Symmetric Perturbations. *Journal of Astrophysics and Astronomy* 37, 2.
- McLaughlin, J. A., I. de Moortel, and A. W. Hood (2011, March). Phase mixing of nonlinear visco-resistive Alfvén waves. *Astronomy & Astrophysics* 527, A149.
- McLaughlin, J. A., I. De Moortel, A. W. Hood, and C. S. Brady (2009, January). Nonlinear fast magnetoacoustic wave propagation in the neighbourhood of a 2D magnetic X-point: oscillatory reconnection. *Astronomy & Astrophysics* 493(1), 227–240.

BIBLIOGRAPHY

- McLaughlin, J. A. and A. W. Hood (2006, November). MHD mode coupling in the neighbourhood of a 2D null point. *Astronomy & Astrophysics* *459*, 641–649.
- McLaughlin, J. A., A. W. Hood, and I. de Moortel (2011, July). Review Article: MHD Wave Propagation Near Coronal Null Points of Magnetic Fields. *Space Science Reviews* *158*, 205–236.
- Mocanu, G., A. Marcu, I. Ballai, and B. Orza (2008, October). The problem of phase mixed shear Alfvén waves in the solar corona revisited. *Astronomische Nachrichten* *329*(8), 780.
- Morton, R. J., S. Tomczyk, and R. F. Pinto (2016, September). A Global View of Velocity Fluctuations in the Corona below $1.3 R_{\odot}$ with CoMP. *The Astrophysical Journal* *828*(2), 89.
- Morton, R. J., M. J. Weberg, and J. A. McLaughlin (2019, January). A basal contribution from p-modes to the Alfvénic wave flux in the Sun’s corona. *Nature Astronomy* *3*, 223.
- Nakariakov, V. M. and D. Y. Kolotkov (2020, August). Magnetohydrodynamic Waves in the Solar Corona. *Annual Review of Astronomy and Astrophysics* *58*, 441–481.
- Nakariakov, V. M., L. Ofman, E. E. Deluca, B. Roberts, and J. M. Davila (1999, August). TRACE observation of damped coronal loop oscillations: Implications for coronal heating. *Science* *285*, 862–864.
- Nakariakov, V. M., B. Roberts, and K. Murawski (1997, September). Alfvén Wave Phase Mixing as a Source of Fast Magnetosonic Waves. *Solar Physics* *175*(1), 93–105.
- Nakariakov, V. M. and E. Verwichte (2005, May). Coronal Waves and Oscillations. *Living Reviews in Solar Physics* *2*(1), 3.
- Ofman, L., J. M. Davila, and R. S. Steinolfson (1995, May). Coronal Heating by the Resonant Absorption of Alfvén Waves: Wavenumber Scaling Laws. *The Astrophysical Journal* *444*, 471.

BIBLIOGRAPHY

- Oliver, R., J. L. Ballester, A. W. Hood, and E. R. Priest (1993, June). Magnetohydrodynamic waves in a potential coronal arcade. *Astronomy & Astrophysics* *273*, 647.
- O'Neill, I. and X. Li (2005, June). Coronal loops heated by turbulence-driven Alfvén waves: A two fluid model. *Astronomy & Astrophysics* *435*(3), 1159–1167.
- Pagano, P. and I. De Moortel (2017, May). Contribution of mode-coupling and phase-mixing of Alfvén waves to coronal heating. *Astronomy & Astrophysics* *601*, A107.
- Pagano, P. and I. De Moortel (2019, March). Contribution of observed multi frequency spectrum of Alfvén waves to coronal heating. *Astronomy & Astrophysics* *623*, A37.
- Pagano, P., D. J. Pascoe, and I. De Moortel (2018, August). Contribution of phase-mixing of Alfvén waves to coronal heating in multi-harmonic loop oscillations. *Astronomy & Astrophysics* *616*, A125.
- Parker, E. N. (1991, Jul). The Phase Mixing of Alfvén Waves, Coordinated Modes, and Coronal Heating. *The Astrophysical Journal* *376*, 355.
- Pascoe, D. J., A. W. Hood, I. De Moortel, and A. N. Wright (2013, March). Damping of kink waves by mode coupling. II. Parametric study and seismology. *Astronomy & Astrophysics* *551*, A40.
- Podesta, J. J., D. A. Roberts, and M. L. Goldstein (2007, July). Spectral Exponents of Kinetic and Magnetic Energy Spectra in Solar Wind Turbulence. *The Astrophysical Journal* *664*(1), 543–548.
- Poedts, S., M. Goossens, and W. Kerner (1989, March). Numerical simulation of coronal heating by resonant absorption of Alfvén waves. *Solar Physics* *123*(1), 83–115.
- Priest, E. (2014, May). *Magnetohydrodynamics of the Sun*. Cambridge University Press.
- Prokopszyn, A. P. K. and A. W. Hood (2019, December). Investigating the damping rate of phase-mixed Alfvén waves. *Astronomy & Astrophysics* *632*, A93.
- Prokopszyn, A. P. K., A. W. Hood, and I. De Moortel (2019, April). Phase mixing of nonlinear Alfvén waves. *Astronomy & Astrophysics* *624*, A90.

BIBLIOGRAPHY

- Prokopyszyn, A. P. K., A. N. Wright, and A. W. Hood (2021, April). Line-tied boundary conditions can cause resonant absorption models to generate unphysically large boundary layers. *arXiv e-prints* Ø, arXiv:2104.10497.
- Richardson, A. (2019). 2019 nrl plasma formulary.
- Roberts, B. (2019). *MHD Waves in the Solar Atmosphere*. Cambridge University Press.
- Rosner, R., W. H. Tucker, and G. S. Vaiana (1978, Mar). Dynamics of the quiescent solar corona. *The Astrophysical Journal* 220, 643–645.
- Ruderman, M. S., V. M. Nakariakov, and B. Roberts (1998, October). Alfvén wave phase mixing in two-dimensional open magnetic configurations. *Astronomy & Astrophysics* 338, 1118–1124.
- Ruderman, M. S., R. Oliver, R. Erdélyi, J. L. Ballester, and M. Goossens (2000, February). Slow surface wave damping in plasmas with anisotropic viscosity and thermal conductivity. *Astronomy & Astrophysics* 354, 261–276.
- Ruderman, M. S. and B. Roberts (2002, September). The Damping of Coronal Loop Oscillations. *The Astrophysical Journal* 577(1), 475–486.
- Shimizu, T., S. Imada, and M. Kubo (2018). *First Ten Years of Hinode Solar On-Orbit Observatory*, Volume 449. Springer.
- Shoda, M., T. K. Suzuki, M. Asgari-Targhi, and T. Yokoyama (2019, July). Three-dimensional Simulation of the Fast Solar Wind Driven by Compressible Magnetohydrodynamic Turbulence. *The Astrophysical Journal Letters* 880(1), L2.
- Similon, P. L. and R. N. Sudan (1989, January). Energy Dissipation of Alfvén Wave Packets Deformed by Irregular Magnetic Fields in Solar-Coronal Arches. *The Astrophysical Journal* 336, 442.
- Smith, P. D., D. Tsiklauri, and M. S. Ruderman (2007, December). Enhanced phase mixing of Alfvén waves propagating in stratified and divergent coronal structures. *Astronomy & Astrophysics* 475(3), 1111–1123.

BIBLIOGRAPHY

- Soler, R., M. Goossens, J. Terradas, and R. Oliver (2013, November). The Behavior of Transverse Waves in Nonuniform Solar Flux Tubes. I. Comparison of Ideal and Resistive Results. *The Astrophysical Journal* 777(2), 158.
- Spitzer, L. (1965). *Physics of fully ionized gases*. Courier Corporation.
- Stanford Solar Center (2019). The sun's vital statistics. [Online; accessed 20-Oct-2019].
- Terradas, J., R. Oliver, and J. L. Ballester (2006, May). Damped Coronal Loop Oscillations: Time-dependent Results. *The Astrophysical Journal* 642(1), 533–540.
- Thompson, M. J. and A. N. Wright (1993, September). Resonant Alfvén wave excitation in two-dimensional systems: Singularities in partial differential equations. *Journal of Geophysical Research* 98(A9), 15541–15552.
- Threlfall, J., I. De Moortel, and T. Conlon (2017, November). Above the Noise: The Search for Periodicities in the Inner Heliosphere. *Solar Physics* 292(11), 165.
- Thurgood, J. O. and J. A. McLaughlin (2013a, July). Nonlinear Alfvén wave dynamics at a 2D magnetic null point: ponderomotive force. *Astronomy & Astrophysics* 555, A86.
- Thurgood, J. O. and J. A. McLaughlin (2013b, November). On Ponderomotive Effects Induced by Alfvén Waves in Inhomogeneous 2.5D MHD Plasmas. *Solar Physics* 288(1), 205–222.
- Tomczyk, S., S. W. McIntosh, S. L. Keil, P. G. Judge, T. Schad, D. H. Seeley, and J. Edmondson (2007, August). Alfvén Waves in the Solar Corona. *Science* 317(5842), 1192.
- van Ballegooijen, A. A., M. Asgari-Targhi, S. R. Cranmer, and E. E. DeLuca (2011, July). Heating of the Solar Chromosphere and Corona by Alfvén Wave Turbulence. *The Astrophysical Journal* 736(1), 3.
- Van Doorsselaere, T., J. Andries, and S. Poedts (2007, August). Observational evidence favors a resistive wave heating mechanism for coronal loops over a viscous phenomenon. *Astronomy & Astrophysics* 471(1), 311–314.

BIBLIOGRAPHY

- van Doorsselaere, T., E. Verwichte, and J. Terradas (2009, December). The Effect of Loop Curvature on Coronal Loop Kink Oscillations. *Space Science Reviews* 149(1-4), 299–324.
- Vernazza, J. E., E. H. Avrett, and R. Loeser (1981, April). Structure of the solar chromosphere. III - Models of the EUV brightness components of the quiet-sun. *The Astrophysical Journal Supplement Series* 45, 635–725.
- Verwichte, E., V. M. Nakariakov, and A. W. Longbottom (1999, August). On the evolution of a nonlinear Alfvén pulse. *Journal of Plasma Physics* 62(2), 219–232.
- Vickers, E., I. Ballai, and R. Erdélyi (2018, October). Propagation of Leaky MHD Waves at Discontinuities with Tilted Magnetic Field. *Solar Physics* 293(10), 139.
- Vickers, E., I. Ballai, and R. Erdélyi (2020, February). Magnetic Rayleigh-Taylor instability at a contact discontinuity with an oblique magnetic field. *Astronomy & Astrophysics* 634, A96.
- Virtanen, P., R. Gommers, T. E. Oliphant, M. Haberland, T. Reddy, D. Cournapeau, E. Burovski, P. Peterson, W. Weckesser, J. Bright, S. J. van der Walt, M. Brett, J. Wilson, K. Jarrod Millman, N. Mayorov, A. R. J. Nelson, E. Jones, R. Kern, E. Larson, C. Carey, İ. Polat, Y. Feng, E. W. Moore, J. VanderPlas, D. Laxalde, J. Perktold, R. Cimrman, I. Henriksen, E. A. Quintero, C. R. Harris, A. M. Archibald, A. H. Ribeiro, F. Pedregosa, P. van Mulbregt, and S. . . Contributors (2020). SciPy 1.0: Fundamental Algorithms for Scientific Computing in Python. *Nature Methods* 17, 261–272.
- Williams, B. M. (2018). *The dynamic topology of the solar corona: mapping the Sun's three dimensional magnetic skeleton*. Ph. D. thesis, University of St Andrews.
- Withbroe, G. L. and R. W. Noyes (1977). Mass and energy flow in the solar chromosphere and corona. *Annual Review of Astronomy & Astrophysics* 15, 363–387.
- Wright, A. N. and W. Allan (1996, August). Structure, phase motion, and heating within Alfvén resonances. *Journal of Geophysical Research* 101(A8), 17399–17408.
- Wright, A. N. and T. Elsden (2016, December). The Theoretical Foundation of 3D Alfvén Resonances: Normal Modes. *The Astrophysical Journal* 833(2), 230.

BIBLIOGRAPHY

Wright, A. N. and G. J. Rickard (1995, May). A Numerical Study of Resonant Absorption in a Magnetohydrodynamic Cavity Driven by a Broadband Spectrum. *The Astrophysical Journal* 444, 458.